(NASA-CR-161254) SUBSCALE SOLID MOTOR NOZZLE TESTS, PHASE 4 AND NOZZLE MATERIALS SCREENING AND THERMAL CHARACTERIZATION, PHASE 5 Final Report, Feb. 1976 - Mar. 1979 (Aerotherm Acurex Corp., Mountain View) N79-29226 Unclas G3/20 31725

NASA CONTRACTOR
REPORT

NASA CR-161254

SUBSCALE SOLID MOTOR NOZZLE TESTS--PHASE IV AND NOZZLE MATERIALS SCREENING AND THERMAL CHARACTERIZATION--PHASE V

By J. Arnold, J. Dodson, and B. Laub
Acurex Corporation/Aerotherm
485 Clyde Avenue
Mountain View, California 94042

Final Report

June 1979

Prepared for

NASA-George C. Marshall Space Flight Center
Marshall Space Flight Center, Alabama 35812

TECHNICAL REPORT STANDARD TITLE PAGE

1. REPORT NO.	2. GOVERNMENT ACCESSION NO.	3. RECIPIENT'S CATALOG NO.
NASA CR-161254		

4. TITLE AND SUBTITLE	5. REPORT DATE
Subscale Solid Motor Nozzle Tests--Phase IV--and Nozzle Materials Screening and Thermal Characterization--Phase V	June 1979
	6. PERFORMING ORGANIZATION CODE
7. AUTHOR(S)	8. PERFORMING ORGANIZATION REPORT #
J. Arnold, J. Dodson, and B. Laub	TM-79-255
9. PERFORMING ORGANIZATION NAME AND ADDRESS	10. WORK UNIT NO.
Acurex Corporation/Aerotherm 485 Clyde Avenue Mountain View, California 94042	11. CONTRACT OR GRANT NO. NAS8-30264
	13. TYPE OF REPORT & PERIOD COVERED Contractor Report
12. SPONSORING AGENCY NAME AND ADDRESS National Aeronautics and Space Administration Washington, DC 20546	14. SPONSORING AGENCY CODE

15. SUPPLEMENTARY NOTES

This work was done under the technical supervision of Mr. Harold Blevins, George C. Marshall Space Flight Center.

16. ABSTRACT

This document contains data generated under Phases IV and V of NAS8-30264. Phase IV consisted of the fabrication and testing of four 2.5-inch throat diameter nozzles and one 7-inch throat diamter nozzle consisting of the baseline material and low cost materials to be considered as potential replacements for the baseline. Phase V consisted of the screening, thermo-physical, and thermo-chemical characterization of new candidate low cost materials for the Shuttle solid motor nozzles.

17. KEY WORDS	18. DISTRIBUTION STATEMENT
	Unclassified-Unlimited A. A. McCOOL Dir, Structures and Propulsion Laboratory

19. SECURITY CLASSIF. (of this report)	20. SECURITY CLASSIF. (of this page)	21. NO. OF PAGES	22. PRICE
Unclassified	Unclassified	217	NTIS

FOREWORD

This document is a final report prepared by the Aerospace Systems Division of Acurex Corporation/Aerotherm, Mountain View, California and contains data generated under Phases IV and V of NASA Contract NAS8-30264. Phase IV consisted of the fabrication and testing of four 2.5-inch throat diameter nozzles and one 7-inch throat diameter nozzle consisting of the baseline material and low cost materials to be considered as potential replacements for the baseline. Phase V consisted of the screening, thermophysical, and thermochemical characterization of new candidate low cost materials for the Shuttle solid motor nozzles.

The NASA Program Manager was Mr. Ben Powers; the NASA Technical Monitor was Mr. Harold Blevins. Mr. Roger Bedard and Mr. Duane Baker were the overall Acurex Program Managers and were assisted by Mr. Philip Johnson. Mr. John Arnold was the Acurex Project Engineer.

The authors wish to acknowledge the contributions of: (1) Mr. Joe Barry of JPL, Edwards, California, who coordinated the acquisition of the propellants for the HIPPO and CHAR motor nozzle tests, as well as provided onsite test support; (2) Mr. Tom Kinsel of AFRPL, Edwards, California, who was the USAF Project Engineer in support of the HIPPO and CHAR motor tests; (3) Mr. Bruce Whitfield of HITCO Corporation, who was the Project Engineer for the fabrication of the 7-inch nozzle; and (4) the Fiberite and U.S. Polymeric Corporations for their cooperation in supplying materials for the Phase V screening program.

This report covers work conducted during the period of February, 1976 through March, 1979 and was submitted in June, 1979.

TABLE OF CONTENTS

Section		Page
1	INTRODUCTION AND SUMMARY	1-1
2	SUBSCALE NOZZLE TEST PROGRAM	2-1
	2.1 2.5-Inch Hippo Motor Nozzles	2-1
	2.1.1 Design and Fabrication	2-1
	2.1.2 Test Program	2-2
	2.1.3 Test Results	2-4
	2.2 7-INCH CHAR MOTOR NOZZLE	2-51
	2.2.1 Design and Fabrication	2-51
	2.2.2 Test Program	2-78
	2.2.3 Test Results	2-82
	2.3 Subscale Nozzle Test Summary	2-103
3	SURVEY, SELECTION, AND CHARACTERIZATION OF ALTERNATE LOW COST NOZZLE MATERIALS	3-1
	3.1 Material Survey	3-1
	3.1.1 Survey Scope	3-2
	3.1.2 Screening and Selection	3-5
	3.1.3 Projected Costs	3-10
	3.2 Materials Screening Tests	3-14
	3.2.1 Test Conditions	3-19
	3.2.2 Model and Test Configurations -- Test Matrix	3-19
	3.2.3 Test Results	3-24
	3.3 Materials Full Characterization Program	3-33
	3.3.1 Decomposition Kinetics	3-46
	3.3.2 Elemental Composition	3-52
	3.3.3 Heat of Formation	3-53
	3.3.4 Density	3-54
	3.3.5 Specific Heat Capacity	3-54
	3.3.6 Thermal Conductivity	3-58
	3.3.7 Characterization Summary	3-68
4	PROGRAM SUMMARY	4-1
	4.1 Phase IV Subscale Nozzle Tests	4-1
	4.2 Phase V: Low Cost Materials Screening and Characterization Program	4-3

LIST OF ILLUSTRATIONS

Figure		Page
2-1	Schematic of 2.5-Inch Throat Diameter HIPPO Motor Nozzles	2-3
2-2	HIPPO Motor Chamber Pressure Histories	2-5
2-3	2.5-Inch HIPPO Motor Nozzles, Axial and Circumferential Measurement Locations	2-7
2-4	2.5-Inch HIPPO Nozzle Pre- and Post-Test Profiles	2-17
2-5	Nozzle 1 Throat Recession Profile	2-52
2-6	Nozzle 2 Throat Recession Profile	2-53
2-7	Nozzle 3 Throat Recession Profile	2-54
2-8	Nozzle 4 Throat Recession Profile	2-55
2-9	Schematic of 7-Inch Throat Diameter CHAR Motor Nozzle	2-56
2-10	Stations for CHAR Motor Analysis	2-58
2-11	Propellant Freestream Properties	2-64
2-12	Nondimensional Mass Loss for MX4926 at Station 1	2-67
2-13	Nondimensional Mass Loss for MX4926 at Station 2	2-68
2-14	Heat Transfer Coefficient	2-70
2-15	Carbon Phenolic Thermal Performance at Station 1	2-76
2-16	Carbon Phenolic Thermal Performance at Station 2	2-77
2-17	Liner Thickness Requirements Versus Firing Time	2-80
2-18	CHAR Motor Chamber Pressure History, 7-Inch Nozzle	2-81
2-19	7-Inch CHAR Motor Nozzle, Axial and Circumferential Measurement Locations	2-83
2-20	7-Inch CHAR Motor Nozzle Pre- and Post-Test Profiles	2-87

LIST OF ILLUSTRATIONS (Continued)

Figure		Page
2-21	7-Inch Nozzle Recession Profile at Station 15 -- Exit Cone	2-97
2-22	7-Inch Nozzle Recession Profile at Station 16.1 -- Throat Ring	2-98
2-23	7-Inch Nozzle Recession Profile at Station 17 -- Throat Ring	2-99
2-24	7-Inch Nozzle Recession Profile at Station 18 -- Throat Ring	2-100
2-25	7-Inch Nozzle Recession Profile at Station 19.6 -- Throat Center	2-101
2-26	7-Inch Nozzle Recession Profile at Station 21.0 -- Throat Ring	2-102
2-27	Post-Test Condition of 7-Inch Nozzle Components Following Disassembly from Steel Shell	2-105
2-28	Post-Test Surface Condition of 7-Inch Nozzle Throat Ring Following Disassembly from Steel Shell	2-107
2-29	Post-Test Condition of 7-Inch Nozzle Throat and Exit Cone Sections	2-109
2-30	Post-Test Condition of 7-Inch Nozzle Rayon Fabric Throat Sections A and H	2-111
2-31	Post-Test Condition of 7-Inch Nozzle Throat Section at Junction of Pitch Fabric and Rayon Fabric	2-113
2-32	Post-Test Condition of 7-Inch Nozzle Pitch Fabric Throat Section and Corresponding Nose Ring Section	2-115
3-1	Basic Rayon or PAN Precursor Fabric Production Approaches	3-8
3-2	Basic Pitch Fabric Production Sequence	3-9
3-3	Cost Effects of Alternate Processing on High Volume Production	3-12

LIST OF ILLUSTRATIONS (Continued)

Figure		Page
3-4	Effect of Fabric Production Method on Cost	3-13
3-5	Cost Projections for Typical PAN Fabric (Stackpole SWB-8)	3-15
3-6	Cost Projections for Pitch Precursor Fabrics (Union Carbide VC-0149)	3-16
3-7	Projected Costs for Staple Rayon Precursor Fabrics (HITCO CCA-28)	3-17
3-8	Comparison of Projected Costs	3-18
3-9	Typical Screening Test Model	3-21
3-10	Acurex Constrictor Arc, Rocket Simulator Configuration	3-22
3-11	Test Configuration	3-23
3-12	Summary of Recession Rate Data from Screening Tests for 90° Ply Orientation	3-29
3-13	Summary of Recession Rate Data from Screening Tests for 20° Ply Orientation	3-30
3-14	Summary of Mass Loss Rate Data from Screening Tests for 90° Ply Orientation	3-31
3-15	Summary of Mass Loss Rate Data from Screening Tests for 20° Ply Orientation	3-32
3-16	Typical Post-Test Photographs of APG Screening Material Specimens	3-35
3-17	Comparison of TGA Data and CMA Prediction for Karbon 408P	3-49
3-18	Comparison of TGA Data and CMA Prediction for Karbon 411	3-50
3-19	Ice Calorimeter Data for Karbon 408P	3-56
3-20	Ice Calorimeter Data for Karbon 411	3-57
3-21	Virgin Conductivity for Karbon 408P	3-60

LIST OF ILLUSTRATIONS (Concluded)

Figure		Page
3-22	Virgin Conductivity for Karbon 411	3-61
3-23	Control Volumes for In-Depth Energy and Mass Balances	3-62
3-24	Typical Instrumented Duct Flow Test Section	3-65
3-25	Typical Test Model with In-Depth Thermocouples	3-67
3-26	Char Conductivity for Karbon 408P	3-69
3-27	Char Conductivity for Karbon 411	3-70
3-28	Comparison of In-Depth Thermocouple Measurements and CMA Predictions for Karbon 408P (90°)	3-71
3-29	Comparison of In-Depth Thermocouple Measurements and CMA Predictions for Karbon 408P (20°)	3-72
3-30	Comparison of In-Depth Thermocouple Measurements and CMA Predictions for Karbon 411 (90°)	3-73
3-31	Comparison of In-Depth Thermocouple Measurements and CMA Predictions for Karbon 411 (20°)	3-74

LIST OF TABLES

Table		Page
2-1	HIPPO Nozzle Post-test Throat Measurements Taken at RPL After Firing	2-6
2-2	HIPPO Nozzle Measurement Locations	2-8
2-3	HIPPO Nozzle Number 1 -- Recession Measurements	2-9
2-4	HIPPO Nozzle Number 2 -- Recession Measurements	2-10
2-5	HIPPO Nozzle Number 3 -- Recession Measurements	2-11
2-6	HIPPO Nozzle Number 4 -- Recession Measurements	2-12
2-7	HIPPO Nozzle Number 1 -- Char Depth Measurements	2-13
2-8	HIPPO Nozzle Number 2 -- Char Depth Measurements	2-14
2-9	HIPPO Nozzle Number 3 -- Char Depth Measurements	2-15
2-10	HIPPO Nozzle Number 4 -- Char Depth Measurements	2-16
2-11	Propellant Constituents and Properties	2-59
2-12	Constituent Elemental Composition	2-60
2-13	Propellant Elemental Composition	2-61
2-14	Average Chamber Conditions	2-63
2-15	Local Freestream Conditions	2-63
2-16	Gas Phase Elemental Composition	2-66
2-17	MX4926 Elemental Composition (By Mass)	2-66
2-18	Surface Boundary Conditions	2-71
2-19	MX4926 Chemical Properties	2-74
2-20	MX4926 Thermophysical Properties	2-75
2-21	Carbon Phenolic Response at 50 Seconds -- 7-Inch Nozzle Design Criteria	2-79
2-22	7-Inch Char Motor Nozzle Measurement Locations	2-84
2-23	7-Inch Char Motor Nozzle -- Recession Measurements	2-85

LIST OF TABLES (Continued)

Table		Page
2-24	7-Inch Char Motor Nozzle -- Char Depth Measurements	2-86
3-1	Shuttle Nozzle Candidate Materials	3-3
3-2	Companies Surveyed	3-4
3-3	Fabrics Eliminated Due to Availability Criteria	3-6
3-4	Comparison of Rocket Motor and APG Environments	3-20
3-5	Comparison of APG Test Gas and Typical Nozzle Exhaust Gas Equilibrium Composition	3-20
3-6	Prepreg and Cured Resin Content Data	3-25
3-7	Nozzle Material Screening Test Matrix	3-26
3-8	Materials Screening Test Results	3-28
3-9	Cost and Design Comparison of Selected Alternate Materials and Baseline Material	3-45
3-10	Decomposition Constants for Karbon 408P and Karbon 411	3-51
3-11	Elemental Composition of Pyrolysis Gas	3-53
3-12	Virgin Heats of Formation	3-53
3-13	Densities of Candidate Materials	3-54
3-14	Virgin Material Specific Heat Capacity	3-55
3-15	Location of In-Depth Thermocouples by X-Ray	3-75
3-16	Thermal and Physical Properties of Karbon 408P	3-76
3-17	Thermal and Physical Properties of Karbon 411	3-77

LIST OF SYMBOLS

A	Area
A/A^*	Local-to-throat area ratio
B	Frequency factor
B'_c	Normalized mass loss rate -- char
B'_g	Normalized pyrolysis gas injection
C	Stanton number
C_p	Specific heat
D	Local diameter
D^*	Throat diameter
E_a	Activation energy
H	Enthalpy
H_f	Heat of formation
ΔH_f	Heat of formation
K	Elemental mass fraction
$\tilde{K}$	Total mass fraction
L_e	Lewis number
MW	Molecular weight
P	Pressure
Pr	Prandtl number
R	Radius
R	Gas constant
$\dot{S}$	Surface recession rate
T	Temperature
U	Velocity parallel to surface
h	Enthalpy
k	Thermal conductivity

$\dot{m}$	Mass flowrate
p	Pressure
$\dot{q}$	Heat flux
$\dot{q}_{CW}$	Cold wall heat flux
$\dot{q}_{RAD}$	Radiation heat flux
r_c	Throat radius of curvature
t	Time
u	Velocity parallel to surface
y	Distance

Greek

ρ	Density
υ	Stoichiometric coefficient
$\rho_e U_e C_H$	Heat transfer coefficient
ε	Emissivity
μ	Viscosity
δ	Thickness
λ	Stream distance
θ	Time
ψ	Reaction order
Γ	Volume fraction of resin
σ	Stefan-Boltzmann constant
χ	Mass fraction of virgin material

Subscripts

am	Arithmetic mean
c	Chamber conditions
c	Char, carbon

e	At boundary layer edge
e	Erosion
eff	Effective
g	Pyrolysis gas
H	Heat transfer
i	Element (or constituent) i
i	Initial
j	Element (or constituent) j
M	Mass
o	Stagnation conditions
o	Original
P	Penetration
Py	Pyrolysis gas
R	Recovery
r	Residual, residual mass fraction
react	Reaction
sf	Safety factor
v	Virgin material
w	At the surface (wall)

SECTION 1

INTRODUCTION AND SUMMARY

Rocket nozzles for the NASA Space Shuttle SRM have been designed using materials proven successful by many years of testing. However, the Shuttle philosophy of providing an economical means of placing material and personnel into earth orbit requires a continued effort to reduce mission costs. One area in which significant cost reductions can be realized is in the area of the SRM nozzle ablative liners. The primary high heat load material for the current nozzle design is a rayon precursor carbon phenolic. The material for lower heating conditions in the exit cone is also a rayon precursor carbon phenolic.

Over the past several years, a number of low cost materials have been proposed as substitutes for the above precursor materials; these consist primarily of continuous filament pitch carbon fabrics, pitch carbon mats, staple polyacrylonitrile (PAN) precursor fabrics, and staple rayon precursor fabrics. An advantage, in addition to the lower costs for these materials (other than rayon), is their availability. The future availability of the baseline continuous filament rayon into the 1980's is highly uncertain.

The level to which the proposed new materials have been characterized was insufficient to allow a thermal analysis for a full-scale Shuttle SRM nozzle design. A need, therefore, existed to

obtain the thermophysical and thermochemical properties of the promising low cost materials and to demonstrate the acceptability of these materials by exposing them to actual subscale motor firing conditions. To satisfy this need, several test programs were conducted for NASA in five separate phases. Phases I through III have been completed, and the results reported under separate cover (Reference 1). The results from Phases IV and V are contained in this report.

The objectives of Phase IV, "Design and Test Subscale Nozzles," were to develop and establish design techniques for low cost ablative materials, to determine the behavior of these materials under actual subscale motor firing environments, and to validate the use of these materials for application in the full-scale solid rocket nozzles for the Shuttle motor.

Under the Phase IV program, five nozzles were designed, fabricated, and successfully tested in the AFRPL facilities at Edwards AFB, California. These included four 2.5-inch throat diameter and one 7-inch throat diameter nozzles. The purpose of the 2.5-inch throat diameter test nozzle firings using the HIPPO motor configuration was to provide an experimental performance comparison of pitch fabric and pitch mat carbon phenolic with the baseline rayon (both FMC and ENKA precursor fabrics) carbon phenolic. The purpose of the 7-inch throat diameter nozzle, fired with the 84-inch CHAR motor, was to provide a larger subscale test firing for material performance verification. The results from these test firings showed that the pitch fabric and pitch mat are acceptable for use in the Shuttle SRM nozzle throat and exit cone, respectively.

The objectives of Phase V, "Alternative Carbon Fabric Phenolic Ablatives," were to define alternate precursor ablative materials, in

addition to those defined in Phase III and tested in Phase IV, based on cost, long-term availability, and ablation performance. The objectives also included the development of rocket nozzle design data for two alternate precursor ablative materials selected on the basis of performance from the list of candidate materials. The program plan for accomplishing the above objectives of Phase V included the following tasks.

Task 1 -- Material Survey

A matrix of alternate precursor ablative materials was prepared, following a vendor survey and request for samples. Thirteen types of materials were selected, along with the rayon baseline, for testing under Task 2.

Task 2 -- Screening Tests

The materials selected under Task 1 were subjected to thermal and erosion screening tests in Acurex's 1.0-MW Arc Plasma Generator. The materials were exposed to heat flux levels and chemical environments that are similar to those experienced in an actual rocket nozzle firing. Two of the most promising materials for application to the Shuttle motor nozzle were selected based on ablation performance and subjected to thermal characterization testing under Task 3.

Task 3 -- Thermal Characterization

Thermophysical and thermochemical material property experiments which are required for making erosion and in-depth transient temperature predictions (using ACE and CMA computer codes) were performed for the two materials selected under Task 2.

Task 4 -- Design Computer Code Coefficients

The input coefficients required for the ACE and CMA computer programs were generated from analyses of the data obtained during

Task 3. These data will provide the capability for designing and analyzing the performance of the two alternate precursor carbon ablative materials in rocket nozzle applications.

The generic class of materials selected for screening were:

- Staple PAN
- Staple rayon
- Pitch (continuous plus one staple)
- Continuous filament rayon (baseline reference)

The two selected for characterization were a staple PAN fabric and a continuous pitch fabric.

SECTION 2

SUBSCALE NOZZLE TEST PROGRAM

This section describes the design, fabrication, and testing of the five subscale nozzle tests performed under Phase IV. The four 2.5-inch throat diameter HIPPO motor nozzles are discussed in Section 2.1, and the 7-inch throat diameter CHAR motor nozzle is discussed in Section 2.2. A nozzle test summary is presented in Section 2.3.

2.1 2.5-INCH HIPPO MOTOR NOZZLES

2.1.1 Design and Fabrication

As a result of the Arc Plasma Generator (APG) screening tests conducted under Phase III of the overall program, the pitch fabric and the pitch mat carbon ablatives were found to be very desirable, from a performance standpoint as well as for their low cost and availability, when compared to the baseline rayon precursor fabric. Therefore, to further verify the performance of these materials as Shuttle nozzle candidates, both materials were subjected to an actual rocket motor firing environment. For this verification, four 2.5-inch throat diameter nozzles were designed and fabricated for testing in the HIPPO motor assembly. Two of the nozzles were fabricated with rayon precursor carbon cloth phenolic, designated as baseline nozzles. The other two nozzles were fabricated with pitch fabric phenolic and pitch mat phenolic, respectively.

The design and construction of the four nozzles were the same for each and were compatible with existing steel shells. The nozzle assembly is shown schematically in Figure 2-1, with the nozzles numbered and identified according to material. The two rayon fabric nozzles were fabricated from both ENKA and FMC rayon fabrics for comparison of the two fabric sources.

The four nozzle assemblies were composed of four components:

1. Forward throat ring
2. Throat ring
3. Forward exit cone
4. Aft exit cone

Fabric or mat orientation for all components was 90^{0} to the nozzle centerline. Internal contours and component geometry of all the nozzles were identical to provide comparable postfire performance data.

The nozzle components were fabricated in billet form, debulked under pressure, cured to final density, and final-machined to drawing specifications. The machined components were then bonded to the shell and to each other using an epoxy adhesive (EA 913). Bondlines were held between 0.005 inch to 0.030 inch to provide adequate structural support and thermal expansion gaps.

2.1.2 Test Program

Each nozzle assembly was sent to Area 1-42 of the Rocket Propulsion Laboratory (RPL), Edwards AFB, California for testing in the HIPPO motor configuration. Upon receipt of each nozzle, a detailed dimensional and visual inspection was conducted at the test site. Each nozzle was then mounted into the aft closure assembly which was in turn mounted, following

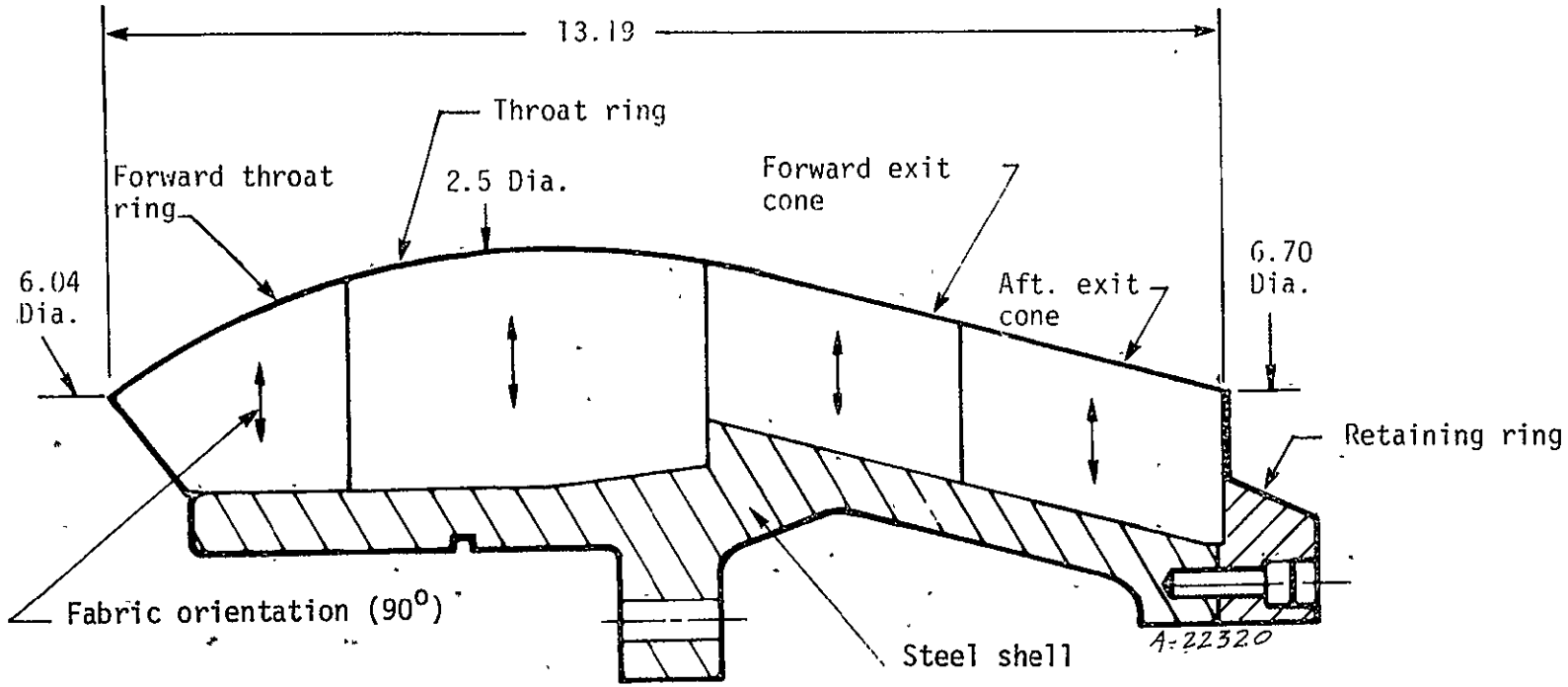

Nozzle No. 1:	MX-4926 (FMC rayon fabric precursor)
Nozzle No. 2:	MXG-1033F (Union Carbide pitch fabric precursor)
Nozzle No. 3:	MX-4929 (Union Carbide pitch mat precursor)
Nozzle No. 4:	MX-4926 (ENKA rayon fabric precursor)

Figure 2-1. Schematic of 2.5-inch throat diameter HIPPO motor nozzles.

propellant loading, onto the motor case. The nozzles were tested in the order and on the dates listed below:

Nozzle Number	Date Fired
MX-4926 (FMC)	July 26, 1976
MXG-1033F	July 29, 1976
MX-4929	August 26, 1976
MX-4926 (ENKA)	October 28, 1976

Figure 2-2 presents the HIPPO motor chamber pressure (P_c) histories for the four nozzles tested. Peak pressure was fairly uniform for all four firings at approximately 800 psig. Tailoff and total test times varied according to the nozzle tested. As an indicator of performance, the chamber pressure history for the two rayon fabric nozzles (1 and 4) remained higher toward and during tailoff, as opposed to the somewhat lower history for the pitch fabric nozzle (2). The pressure history for the pitch mat fabric nozzle (3) was considerably lower than both the rayon and pitch fabric nozzles.

2.1.3 Test Results

Following the HIPPO motor firing of the four 2.5-inch throat diameter nozzles at the RPL test site, each was measured at the throat with a dial micrometer and then shipped to Acurex for a thorough post-test characterization. The throat measurements made at the test site are presented in Table 2-1 and represent only an average throat diameter.

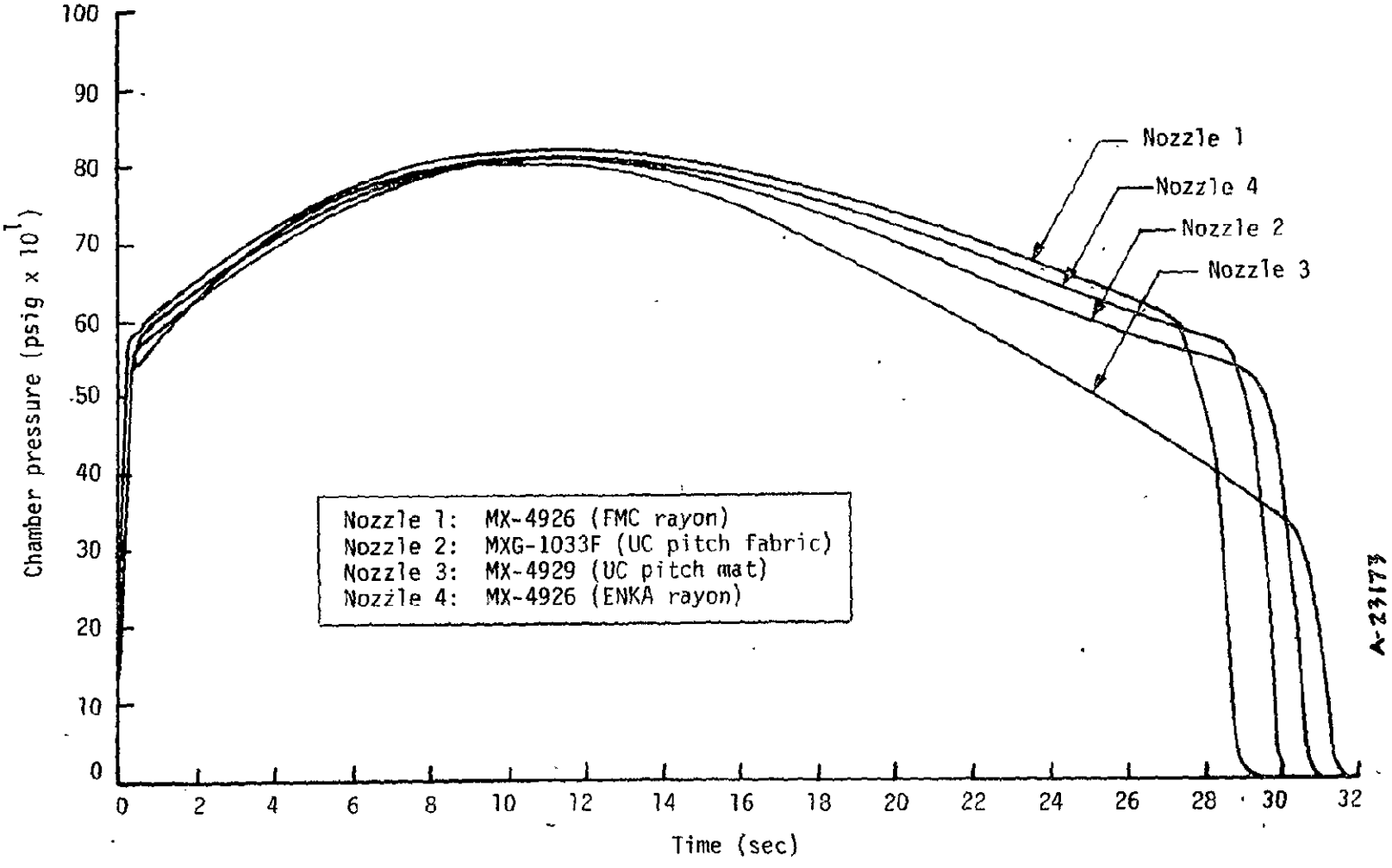

Figure 2-2. HIPPO motor chamber pressure histories.

TABLE 2-1. HIPPO NOZZLE POST-TEST THROAT MEASUREMENTS TAKEN AT RPL AFTER FIRING

Nozzle Number	Radial Recession[a] (inch)
1	0.212
2	0.255
3	0.382
4	0.239

[a]Measurements were taken with a dial micrometer which gives an average based on a surface of three pads (prongs) with the throat.

At Acurex, each nozzle was sliced into eight sections which were designated A through H. These sections are shown in Figure 2-3. The angle of each section with respect to 0^{o} (pre- and post-test marking) was chosen according to the ablated shape of the throat in order to map the contour effectively with detailed measurements. The axial locations selected for measurement are also shown in Figure 2-3. The end of the aft exit cone was designated as station 0.0 inches. The forward end is station 14.244 inches, and the throat center is station 9.00 inches. The local nozzle slope with respect to the nozzle centerline at each axial location is given in Table 2-2.

Detailed measurements were made of the recession and char depth at each axial location (or station). These measurements are presented in Tables 2-3 through 2-10. They are also compared in Figure 2-4 as profiles with the original nozzle contour. These profiles are plotted for each nozzle section and provide a visual examination of the nozzle's performance. For nozzles 3 and 4, an additional measurement was taken of

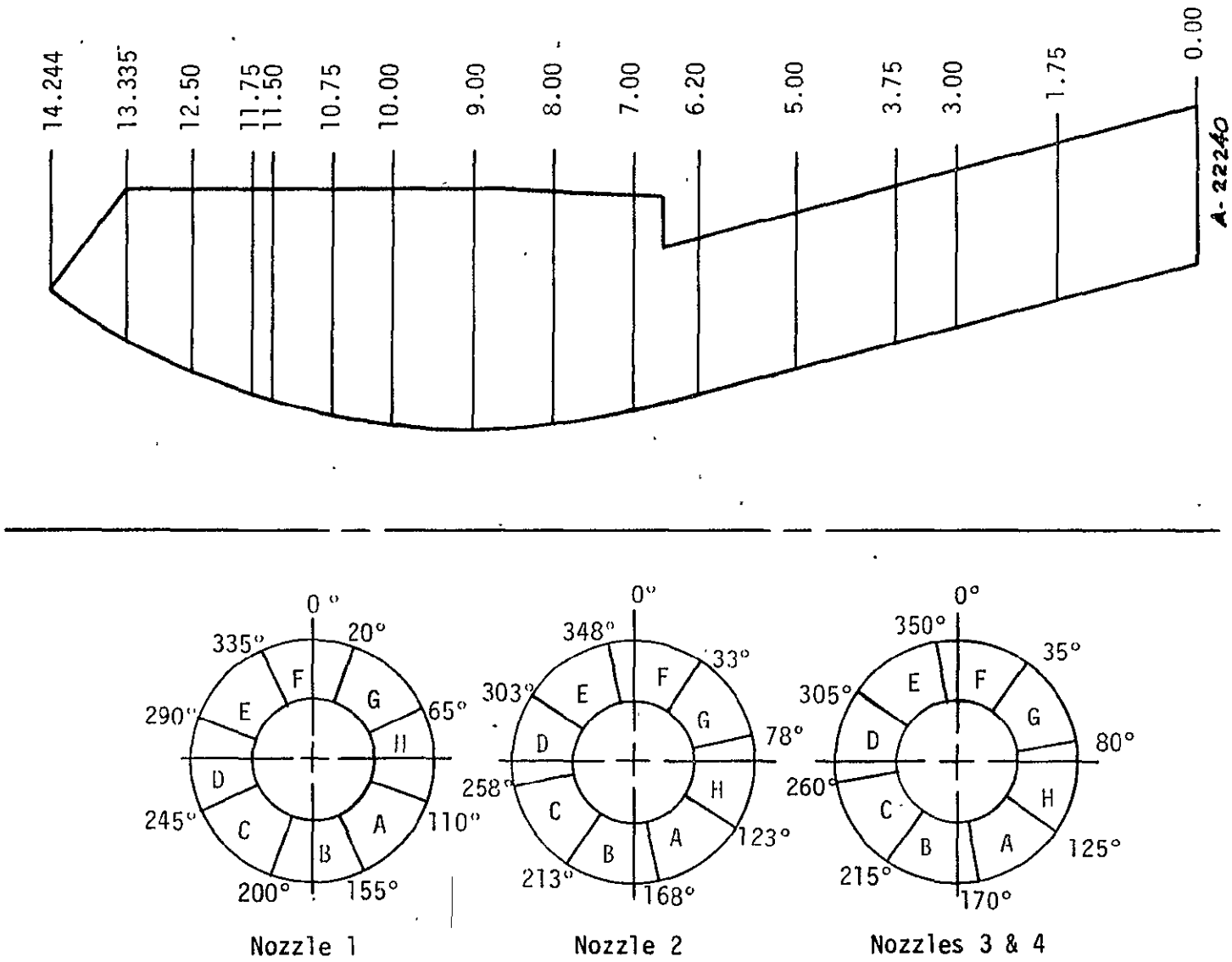

Figure 2-3. 2.5-inch HIPPO motor nozzles, axial and circumferential measurement locations.

TABLE 2-2. HIPPO NOZZLE MEASUREMENT LOCATIONS

Axial Location[a]	Local Nozzle Slope
0	15^0
1.75	15^0
3.00	15^0
3.87	15^0
5.00	15^0
6.20	15^0
7.00	13^0
8.00	7^0
9.00	0^0
10.00	$5^0 30'$
10.75	12^0
11.50	15^0
11.75	$18^0 30'$
12.50	24^0
13.335	28^0
14.244	37^0

[a]Refer to Figure 2-3

TABLE 2-3. HIPPO NOZZLE NUMBER 1 -- RECESSION MEASUREMENTS

Axial Location[a] (in)	CIRCUMFERENTIAL LOCATION[a]															
	20°		65°		110°		155°		200°		245°		290°		335°	
	⊥[b] to ℄	⊥ to Surface	⊥ to ℄	⊥ to Surface	⊥ to ℄	⊥ to Surface	⊥ to ℄	⊥ to Surface	⊥ to ℄	⊥ to Surface	⊥ to ℄	⊥ to Surface	⊥ to ℄	⊥ to Surface	⊥ to ℄	⊥ to Surface
5.00	0.044	0.043	0.025	0.024	0.019	0.018	0.012	0.012	0.014	0.014	0.005	0.005	0.021	0.020	0.003	0.002
6.20	0.065	0.063	0.093	0.090	0.072	0.070	0.046	0.044	0.048	0.046	0.042	0.041	0.056	0.054	0.043	0.042
7.00	0.137	0.133	0.174	0.170	0.117	0.114	0.106	0.103	0.102	0.100	0.113	0.110	0.094	0.091	0.122	0.119
8.00	0.185	0.184	0.225	0.224	0.175	0.175	0.165	0.165	0.205	0.204	0.175	0.175	0.161	0.160	0.165	0.165
9.00	0.217	0.217	0.282	0.282	0.207	0.207	0.203	0.203	0.194	0.194	0.235	0.235	0.208	0.208	0.216	0.216
10.00	0.201	0.199	0.284	0.282	0.193	0.191	0.197	0.195	0.183	0.181	0.219	0.217	0.233	0.231	0.182	0.180
10.75	0.186	0.181	0.258	0.253	0.168	0.164	0.176	0.172	0.158	0.155	0.208	0.203	0.195	0.191	0.164	0.160
11.50	0.133	0.128	0.216	0.209	0.137	0.132	0.133	0.128	0.122	0.118	0.177	0.171	0.141	0.136	0.112	0.108
11.75	0.098	0.093	0.187	0.177	0.084	0.079	0.108	0.102	0.084	0.080	0.145	0.137	0.188	0.178	0.073	0.069
12.50	0.035	0.032	0.096	0.088	0.006	0.005	0.042	0.039	0.038	0.035	0.081	0.074	0.065	0.051	0.001	0.001
13.335	0.073	0.064	0.086	0.076	0.058	0.060	0.061	0.053	0.067	0.059	0.097	0.086	0.068	0.060	0.061	0.054

[a] Refer to Figure 2-3; locations 0 through 3.75-inch omitted since recession was negligible

[b] ⊥ denotes perpendicular

TABLE 2-4. HIPPO NOZZLE NUMBER 2 -- RECESSION MEASUREMENTS

Axial Location[a] (in)	CIRCUMFERENTIAL LOCATION[a]															
	33°		78°		123°		168°		213°		258°		303°		348°	
	⊥[b] to ℄	⊥ to Surface	⊥ to ℄	⊥ to Surface	⊥ to ℄	⊥ to Surface	⊥ to ℄	⊥ to Surface	⊥ to ℄	⊥ to Surface	⊥ to ℄	⊥ to Surface	⊥ to ℄	⊥ to Surface	⊥ to ℄	⊥ to Surface
5.00	0.010	0.010	0.016	0.016	0.000	0.000	0.000	0.000	0.008	0.008	0.003	0.003	0.005	0.005	0.005	0.005
6.20	0.070	0.068	0.047	0.044	0.097	0.094	0.027	0.026	0.049	0.047	0.032	0.031	0.370	0.036	0.031	0.030
7.00	0.104	0.102	0.157	0.153	0.107	0.105	0.111	0.108	0.101	0.099	0.164	0.160	0.139	0.135	0.152	0.148
8.00	0.216	0.215	0.237	0.236	0.225	0.224	0.242	0.241	0.203	0.202	0.232	0.231	0.245	0.244	0.232	0.231
9.00	0.310	0.310	0.297	0.297	0.262	0.262	0.328	0.328	0.281	0.281	0.322	0.322	0.277	0.277	0.296	0.296
10.00	0.288	0.286	0.265	0.262	0.250	0.248	0.310	0.307	0.242	0.240	0.270	0.267	0.249	0.246	0.278	0.276
10.75	0.282	0.275	0.259	0.259	0.244	0.239	0.290	0.284	0.235	0.230	0.232	0.227	0.211	0.207	0.250	0.245
11.50	0.205	0.198	0.110	0.106	0.149	0.144	0.170	0.165	0.156	0.151	0.113	0.109	0.113	0.109	0.131	0.126
11.75	0.153	0.145	0.096	0.091	0.099	0.094	0.107	0.102	0.113	0.107	0.079	0.075	0.089	0.084	0.095	0.090
12.50	0.082	0.075	0.002	0.002	0.001	0.001	0.021	0.019	0.025	0.023	0.000	0.000	0.007	0.007	0.033	0.030
13.335	0.034	0.033	0.006	0.005	0.039	0.034	0.000	0.000	0.039	0.034	0.000	0.000	0.027	0.024	0.022	0.020

[a] Refer to Figure 2-3; locations 0 through 3.75-inch omitted since recession was negligible

[b] ⊥ denotes perpendicular

TABLE 2-5. HIPPO NOZZLE NUMBER 3 -- RECESSION MEASUREMENTS

Axial Location[a] (in)	CIRCUMFERENTIAL LOCATION[a]															
	35°		80°		125°		170°		215°		260°		305°		350°	
	⊥[b] to ℄	⊥ to Surface	⊥ to ℄	⊥ to Surface	⊥ to ℄	⊥ to Surface	⊥ to ℄	⊥ to Surface	⊥ to ℄	⊥ to Surface	⊥ to ℄	⊥ to Surface	⊥ to ℄	⊥ to Surface	⊥ to ℄	⊥ to Surface
5.00	0.000	0.000	0.000	0.000	0.012	0.017	0.000	0.000	0.016	0.015	0.026	0.026	0.030	0.029	0.033	0.032
6.20	0.127	0.123	0.068	0.066	0.089	0.086	0.098	0.095	0.109	0.105	0.165	0.160	0.162	0.157	0.154	0.149
7.00	0.246	0.239	0.144	0.141	0.156	0.152	0.177	0.172	0.177	0.173	0.291	0.284	0.362	0.353	0.304	0.296
8.00	0.353	0.352	0.279	0.276	0.273	0.272	0.307	0.306	0.310	0.308	0.516	0.513	0.494	0.492	0.481	0.479
9.00	0.399	0.399	0.252	0.252	0.333	0.333	0.303	0.303	0.381	0.381	0.479	0.479	0.530	0.530	0.509	0.509
10.00	0.366	0.363	0.233	0.231	0.259	0.257	0.279	0.276	0.339	0.336	0.434	0.432	0.474	0.470	0.424	0.421
10.75	0.311	0.304	0.166	0.162	0.189	0.185	0.261	0.252	0.279	0.273	0.372	0.364	0.393	0.384	0.378	0.370
11.50	0.174	0.168	0.129	0.124	0.112	0.109	0.167	0.161	0.147	0.142	0.291	0.282	0.300	0.290	0.271	0.262
11.75	0.124	0.118	0.074	0.070	0.060	0.056	0.113	0.107	0.101	0.095	0.200	0.190	0.259	0.246	0.223	0.211
12.50	0.053	0.049	0.000	0.000	0.032	0.030	0.047	0.043	0.029	0.027	0.116	0.106	0.134	0.123	0.114	0.104
13.335	0.040	0.035	0.045	0.044	0.024	0.021	0.028	0.022	0.049	0.043	0.093	0.082	0.087	0.077	0.120	0.106

[a] Refer to Figure 2-3; locations 0 through 3.75-inch omitted since recession was negligible

[b] ⊥ denotes perpendicular

TABLE 2-6. HIPPO NOZZLE NUMBER 4 -- RECESSION MEASUREMENTS

Axial Location[a] (in)	CIRCUMFERENTIAL LOCATION[a]															
	35°		80°		125°		170°		215°		260°		305°		350°	
	⊥[b] to ℄	⊥ to Surface	⊥ to ℄	⊥ to Surface	⊥ to ℄	⊥ to Surface	⊥ to ℄	⊥ to Surface	⊥ to ℄	⊥ to Surface	⊥ to ℄	⊥ to Surface	⊥ to ℄	⊥ to Surface	⊥ to ℄	⊥ to Surface
5.00	0.000	0.000	0.010	0.009	0.012	0.012	0.002	0.002	0.003	0.003	0.007	0.007	0.020	0.019	0.000	0.000
6.20	0.044	0.042	0.051	0.049	0.059	0.057	0.041	0.040	0.063	0.061	0.061	0.059	0.047	0.045	0.008	0.008
7.00	0.094	0.091	0.089	0.087	0.115	0.112	0.081	0.079	0.088	0.086	0.094	0.092	0.081	0.079	0.077	0.075
8.00	0.172	0.171	0.183	0.183	0.191	0.190	0.178	0.177	0.185	0.184	0.192	0.191	0.169	0.168	0.181	0.181
9.00	0.228	0.228	0.247	0.247	0.249	0.249	0.241	0.241	0.249	0.249	0.262	0.262	0.219	0.219	0.214	0.214
10.00	0.216	0.214	0.243	0.241	0.261	0.259	0.251	0.249	0.244	0.242	0.267	0.265	0.208	0.207	0.205	0.204
10.75	0.196	0.192	0.218	0.213	0.246	0.240	0.241	0.236	0.239	0.233	0.253	0.248	0.221	0.216	0.186	0.182
11.50	0.152	0.147	0.190	0.183	0.184	0.178	0.201	0.194	0.189	0.182	0.213	0.206	0.177	0.171	0.170	0.165
11.75	0.120	0.114	0.144	0.137	0.146	0.138	0.170	0.162	0.176	0.167	0.174	0.165	0.136	0.129	0.126	0.119
12.50	0.058	0.053	0.078	0.072	0.076	0.069	0.099	0.090	0.128	0.117	0.118	0.108	0.097	0.089	0.063	0.058
13.225	0.000	0.000	0.000	0.000	0.000	0.000	0.005	0.005	0.000	0.000	0.003	0.002	0.008	0.007	0.015	0.013

[a] Refer to Figure 2-3; locations 0 through 3.75-inch omitted since recession was negligible

[b] ⊥ denotes perpendicular.

TABLE 2-7. HIPPO NOZZLE NUMBER 1 -- CHAR DEPTH MEASUREMENTS

Axial Location[a] (in)	CIRCUMFERENTIAL LOCATIONS															
	20°		65°		110°		155°		200°		245°		290°		335°	
	⊥[b] to ℄	⊥ to Surface	⊥ to ℄	⊥ to Surface	⊥ to ℄	⊥ to Surface	⊥ to ℄	⊥ to Surface	⊥ to ℄	⊥ to Surface	⊥ to ℄	⊥ to Surface	⊥ to ℄	⊥ to Surface	⊥ to ℄	⊥ to Surface
0.00	0.365	0.353	0.333	0.322	0.349	0.337	0.346	0.334	0.344	0.332	0.375	0.362	0.297	0.287	0.342	0.330
1.75	0.496	0.479	0.433	0.418	0.407	0.393	0.443	0.428	0.390	0.377	0.399	0.385	0.410	0.396	0.401	0.387
3.00	0.424	0.410	0.433	0.418	0.421	0.407	0.431	0.416	0.364	0.352	0.442	0.427	0.403	0.389	0.437	0.422
3.75	0.451	0.436	0.477	0.461	0.438	0.423	0.457	0.441	0.440	0.425	0.452	0.437	0.450	0.435	0.438	0.423
5.00	0.470	0.454	0.497	0.480	0.487	0.470	0.421	0.407	0.487	0.470	0.475	0.459	0.464	0.448	0.421	0.407
6.20	0.485	0.468	0.476	0.460	0.444	0.429	0.413	0.399	0.436	0.421	0.439	0.424	0.420	0.406	0.455	0.439
7.00	0.497	0.480	0.451	0.439	0.443	0.432	0.405	0.395	0.469	0.457	0.386	0.376	0.433	0.422	0.443	0.432
8.00	0.414	0.411	0.384	0.381	0.418	0.415	0.394	0.391	0.387	0.384	0.376	0.373	0.434	0.431	0.410	0.407
9.00	0.387	0.387	0.357	0.357	0.400	0.400	0.370	0.370	0.384	0.384	0.314	0.314	0.363	0.363	0.377	0.377
10.00	0.352	0.350	0.349	0.347	0.378	0.476	0.354	0.352	0.370	0.368	0.345	0.343	0.325	0.324	0.359	0.357
10.75	0.372	0.364	0.321	0.314	0.358	0.350	0.375	0.367	0.414	0.405	0.351	0.308	0.384	0.376	0.337	0.330
11.50	0.341	0.329	0.299	0.289	0.348	0.336	0.335	0.324	0.337	0.326	0.327	0.316	0.328	0.317	0.333	0.322
11.75	0.354	0.336	0.315	0.299	0.398	0.377	0.343	0.325	0.395	0.375	0.309	0.293	0.369	0.350	0.369	0.350
12.50	0.341	0.312	0.349	0.319	0.399	0.365	0.410	0.375	0.395	0.361	0.328	0.300	0.368	0.336	0.369	0.337
13.335	0.394	0.348	0.405	0.358	0.411	0.363	0.492	0.434	0.425	0.375	0.400	0.353	0.440	0.388	0.488	0.431

[a] Refer to Figure 2-3

[b] ⊥ denotes perpendicular

TABLE 2-8. HIPPO NOZZLE NUMBER 2 -- CHAR DEPTH MEASUREMENTS

Axial Location[a] (in)	CIRCUMFERENTIAL LOCATION[a]															
	33°		78°		123°		168°		213°		258°		303°		348°	
	⊥[b] to ℄	⊥ to Surface	⊥ to ℄	⊥ to Surface	⊥ to ℄	⊥ to Surface	⊥ to ℄	⊥ to Surface	⊥ to ℄	⊥ to Surface	⊥ to ℄	⊥ to Surface	⊥ to ℄	⊥ to Surface	⊥ to ℄	⊥ to Surface
0.00	0.412	0.398	0.457	0.441	0.397	0.383	0.443	0.428	0.363	0.351	0.473	0.457	0.469	0.453	0.460	0.444
1.75	0.503	0.486	0.547	0.528	0.493	0.476	0.499	0.482	0.501	0.484	0.563	0.544	0.575	0.555	0.513	0.496
3.00	0.554	0.535	0.565	0.546	0.568	0.549	0.507	0.490	0.531	0.513	0.594	0.574	0.556	0.537	0.546	0.527
3.75	0.639	0.617	0.614	0.593	0.661	0.638	0.535	0.517	0.546	0.527	0.622	0.601	0.651	0.629	0.557	0.537
5.00	0.663	0.640	0.616	0.595	0.692	0.668	0.582	0.562	0.576	0.556	0.635	0.613	0.650	0.628	0.638	0.616
6.20	0.587	0.567	0.618	0.597	0.646	0.624	0.542	0.524	0.585	0.565	0.654	0.632	0.679	0.656	0.635	0.613
7.00	0.573	0.558	0.603	0.582	0.575	0.560	0.542	0.528	0.595	0.580	0.598	0.583	0.644	0.627	0.604	0.589
8.00	0.624	0.619	0.588	0.568	0.523	0.519	0.500	0.496	0.515	0.511	0.570	0.566	0.574	0.570	0.596	0.592
9.00	0.465	0.465	0.479	0.479	0.504	0.504	0.506	0.506	0.436	0.436	0.489	0.489	0.525	0.525	0.535	0.535
10.00	0.475	0.473	0.530	0.528	0.554	0.551	0.465	0.463	0.478	0.576	0.465	0.449	0.524	0.522	0.557	0.554
10.75	0.468	0.458	0.516	0.505	0.542	0.530	0.460	0.450	0.472	0.462	0.510	0.499	0.536	0.524	0.544	0.532
11.50	0.490	0.473	0.590	0.570	0.581	0.561	0.489	0.472	0.512	0.495	0.534	0.516	0.559	0.540	0.570	0.551
11.75	0.529	0.502	0.584	0.554	0.648	0.615	0.570	0.541	0.578	0.548	0.580	0.560	0.625	0.593	0.632	0.599
12.50	0.615	0.562	0.640	0.585	0.652	0.596	0.615	0.562	0.624	0.570	0.649	0.593	0.668	0.610	0.681	0.622
13.335	0.668	0.590	0.752	0.664	0.673	0.594	0.679	0.600	0.671	0.592	0.725	0.640	0.689	0.608	0.736	0.650

[a] Refer to Figure 2-3

[b] ⊥ denotes perpendicular

TABLE 2-9. HIPPO NOZZLE NUMBER 3 -- CHAR DEPTH MEASUREMENTS

Axial Location[a] (in)	CIRCUMFERENTIAL LOCATION[a]															
	35°		80°		125°		170°		215°		260°		305°		350°	
	⊥[b] to ℄	⊥ to Surface	⊥ to ℄	⊥ to Surface	⊥ to ℄	⊥ to Surface	⊥ to ℄	⊥ to Surface	⊥ to ℄	⊥ to Surface	⊥ to ℄	⊥ to Surface	⊥ to ℄	⊥ to Surface	⊥ to ℄	⊥ to Surface
0.00	0.279	0.269	0.204	0.197	0.308	0.298	0.220	0.212	0.294	0.284	0.302	0.291	0.293	0.283	0.267	0.258
1.75	0.495	0.478	0.421	0.407	0.420	0.405	0.367	0.354	0.426	0.411	0.446	0.431	0.462	0.446	0.436	0.422
3.00	0.526	0.508	0.475	0.461	0.494	0.477	0.471	0.455	0.521	0.503	0.522	0.504	0.475	0.459	0.502	0.485
3.75	0.432	0.417	0.403	0.389	0.424	0.409	0.406	0.392	0.448	0.433	0.426	0.412	0.415	0.401	0.404	0.390
5.00	0.455	0.439	0.430	0.416	0.423	0.409	0.443	0.428	0.454	0.438	0.426	0.412	0.451	0.401	0.437	0.422
6.20	0.444	0.429	0.446	0.430	0.457	0.442	0.409	0.395	0.415	0.401	0.371	0.358	0.401	0.387	0.395	0.381
7.00	0.367	0.366	0.438	0.427	0.399	0.388	0.409	0.398	0.422	0.411	0.360	0.350	0.300	0.292	0.351	0.342
8.00	0.310	0.307	0.358	0.355	0.340	0.338	0.370	0.367	0.339	0.337	0.258	0.256	0.253	0.251	0.240	0.238
9.00	0.277	0.277	0.371	0.371	0.277	0.277	0.327	0.327	0.330	0.330	0.294	0.294	0.273	0.273	0.303	0.303
10.00	0.283	0.282	0.366	0.365	0.336	0.335	0.346	0.345	0.335	0.333	0.281	0.280	0.288	0.286	0.292	0.290
10.75	0.330	0.322	0.409	0.400	0.390	0.381	0.346	0.339	0.385	0.376	0.300	0.293	0.302	0.296	0.270	0.265
11.50	0.430	0.415	0.400	0.386	0.409	0.395	0.389	0.375	0.419	0.404	0.329	0.317	0.308	0.297	0.336	0.325
11.75	0.386	0.366	0.420	0.399	0.416	0.394	0.408	0.386	0.426	0.404	0.367	0.292	0.319	0.302	0.331	0.314
12.50	0.433	0.396	0.449	0.410	0.455	0.416	0.442	0.404	0.445	0.407	0.378	0.345	0.366	0.335	0.367	0.335
12.335	0.512	0.452	0.467	0.412	0.554	0.489	0.488	0.431	0.530	0.468	0.470	0.415	0.495	0.437	0.484	0.427

[a] Refer to Figure 2-3

[b] ⊥ denotes perpendicular

TABLE 2-10. HIPPO NOZZLE NUMBER 4 -- CHAR DEPTH MEASUREMENTS

Axial Location[a] (in)	CIRCUMFERENTIAL LOCATION[a]															
	35°		80°		125°		170°		215°		260°		305°		350°	
	⊥[b] to ℄	⊥ to Surface	⊥ to ℄	⊥ to Surface	⊥ to ℄	⊥ to Surface	⊥ to ℄	⊥ to Surface	⊥ to ℄	⊥ to Surface	⊥ to ℄	⊥ to Surface	⊥ to ℄	⊥ to Surface	⊥ to ℄	⊥ to Surface
0.0	0.383	0.370	0.304	0.294	0.360	0.348	0.337	0.325	0.329	0.318	0.321	0.310	0.342	0.330	0.313	0.302
1.75	0.459	0.443	0.446	0.430	0.430	0.415	0.421	0.406	0.410	0.396	0.439	0.424	0.402	0.388	0.413	0.399
3.00	0.467	0.452	0.467	0.451	0.428	0.414	0.419	0.405	0.427	0.413	0.421	0.407	0.418	0.404	0.447	0.432
3.75	0.483	0.466	0.470	0.454	0.435	0.420	0.449	0.434	0.440	0.425	0.465	0.449	0.440	0.425	0.470	0.454
5.00	0.482	0.466	0.504	0.486	0.456	0.441	0.465	0.449	0.465	0.449	0.488	0.471	0.456	0.441	0.509	0.492
6.20	0.479	0.463	0.503	0.485	0.459	0.444	0.445	0.449	0.365	0.352	0.405	0.391	0.419	0.404	0.490	0.473
7.00	0.469	0.457	0.439	0.428	0.446	0.435	0.457	0.445	0.426	0.415	0.405	0.395	0.440	0.429	0.439	0.428
8.00	0.459	0.456	0.425	0.422	0.427	0.423	0.380	0.377	0.348	0.345	0.384	0.381	0.412	0.409	0.398	0.395
9.00	0.416	0.416	0.368	0.368	0.404	0.404	0.340	0.340	0.300	0.300	0.343	0.343	0.399	0.399	0.340	0.340
10.00	0.341	0.340	0.333	0.332	0.352	0.350	0.331	0.329	0.353	0.351	0.320	0.319	0.392	0.391	0.332	0.330
10.75	0.333	0.326	0.377	0.369	0.348	0.341	0.342	0.334	0.379	0.370	0.332	0.325	0.378	0.370	0.343	0.336
11.50	0.390	0.377	0.431	0.417	0.377	0.364	0.339	0.327	0.337	0.326	0.343	0.331	0.374	0.361	0.363	0.351
11.75	0.402	0.382	0.431	0.409	0.377	0.357	0.357	0.338	0.356	0.338	0.330	0.313	0.402	0.382	0.399	0.378
12.50	0.438	0.401	0.449	0.410	0.402	0.367	0.449	0.410	0.395	0.360	0.394	0.360	0.412	0.377	0.403	0.368
13.335	0.531	0.469	0.551	0.486	0.514	0.434	0.569	0.503	0.533	0.471	0.511	0.451	0.518	0.458	0.572	0.505

[a] Refer to Figure 2-3

[b] ⊥ denotes perpendicular

Figure 2-4. 2.5-inch HIPPO nozzle pre- and post-test profiles.
(Pages 2-19 through 2-50)

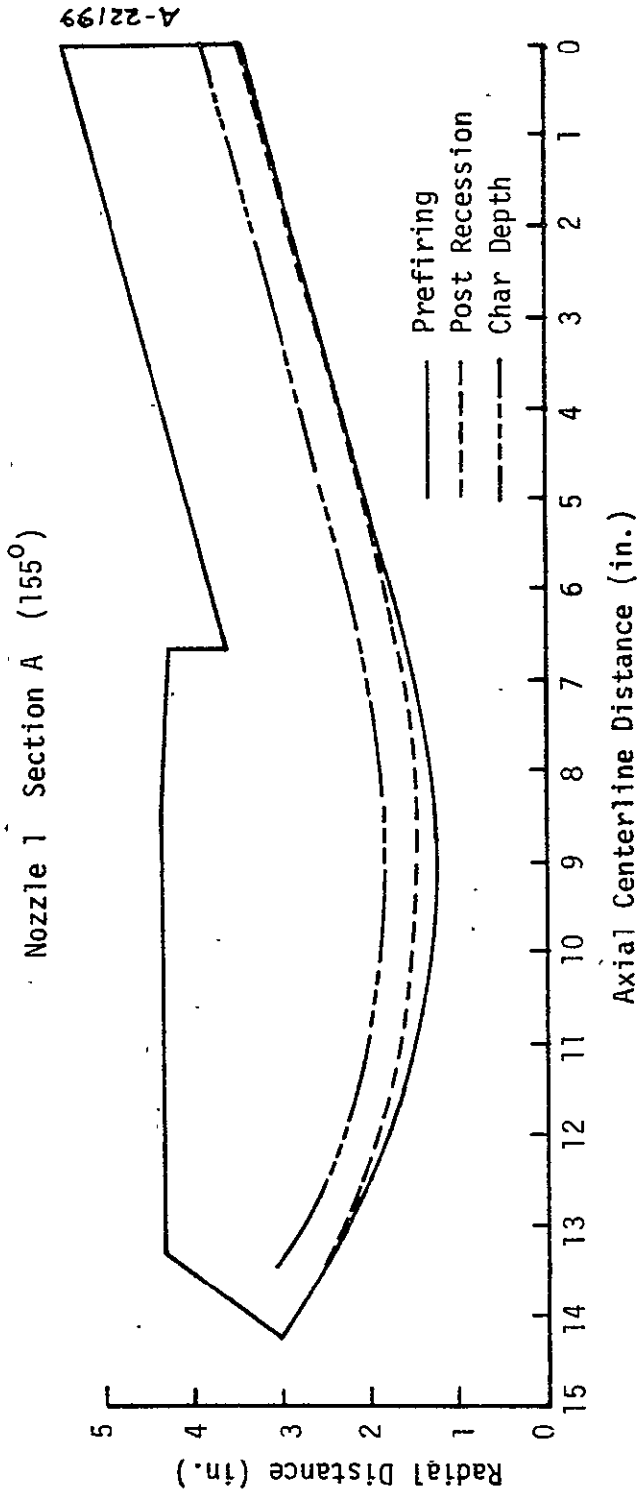

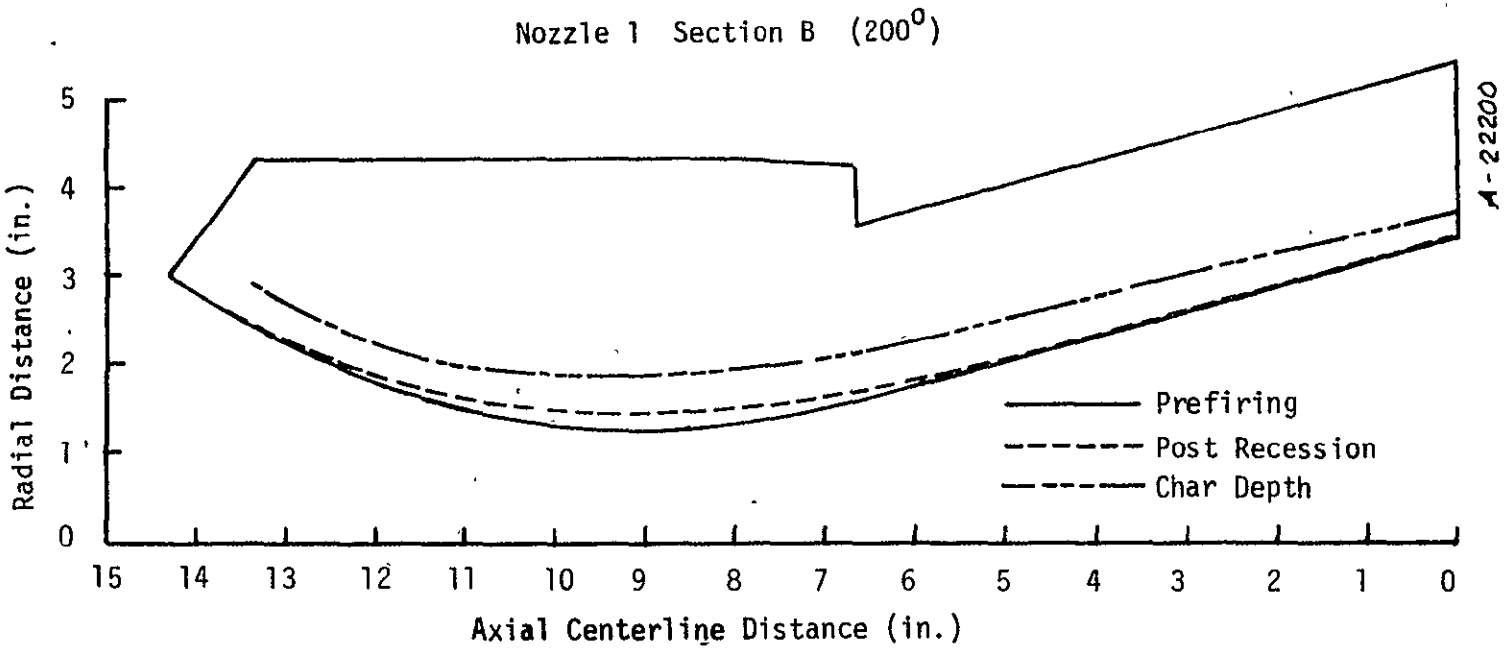
Nozzle 1 Section B (200°)
Radial Distance (in.)
5
4
3
2
1
0
15 14 13 12 11 10 9 8 7 6 5 4 3 2 1 0
Axial Centerline Distance (in.)
Prefiring
Post Recession
Char Depth
A-22200

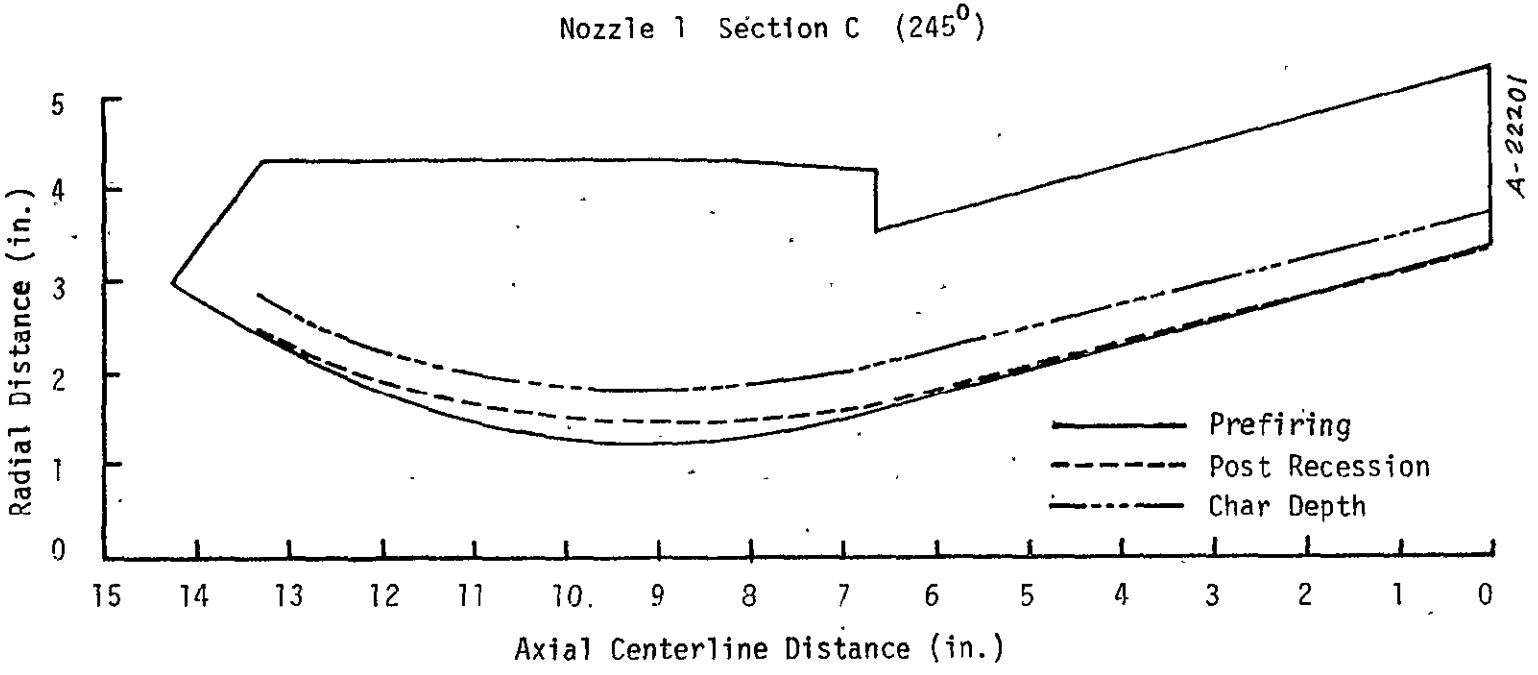
Nozzle 1 Section C (245°)
Radial Distance (in.)
5
4
3
2
1
0
15 14 13 12 11 10 9 8 7 6 5 4 3 2 1 0
Axial Centerline Distance (in.)
Prefiring
Post Recession
Char Depth
A-22201

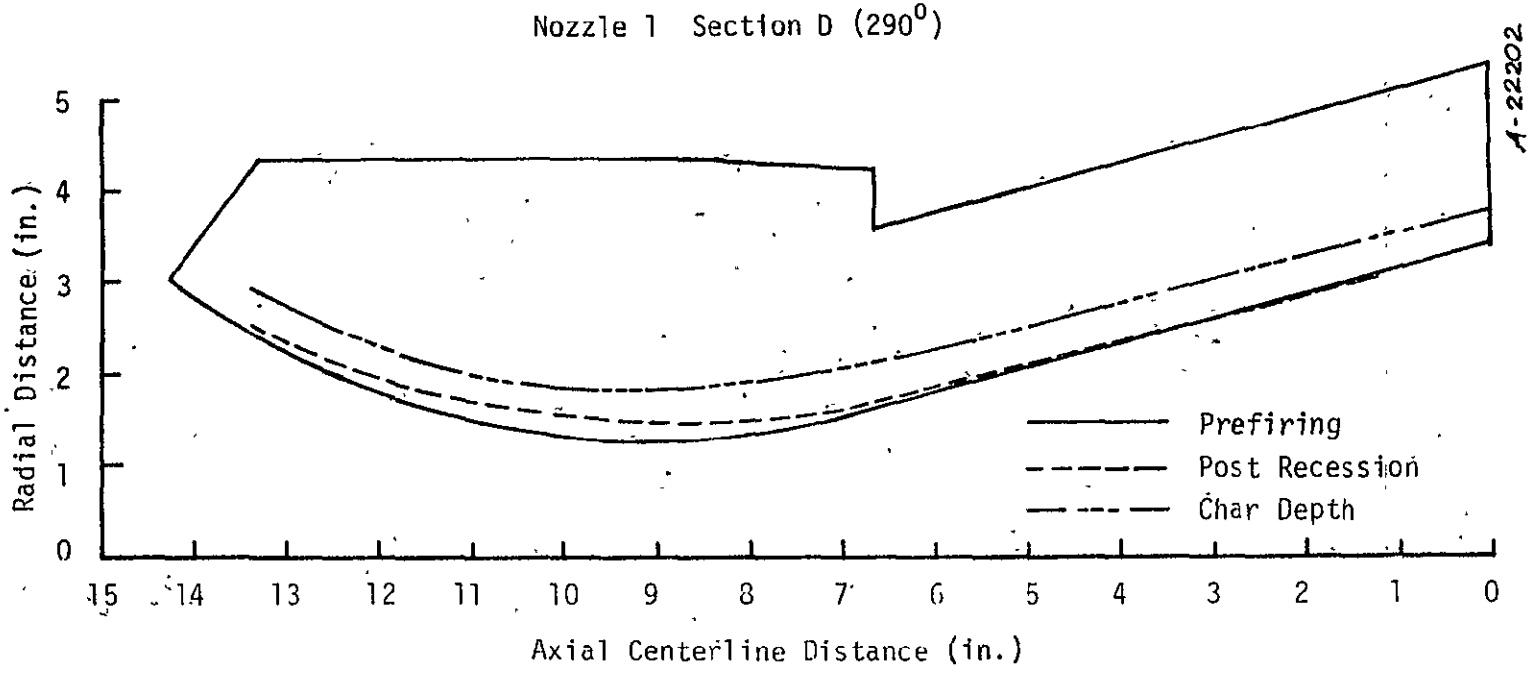
Nozzle 1 Section D (290°)
A-22202
Radial Distance (in.)
5
4
3
2
1
0
15
14
13
12
11
10
9
8
7
6
5
4
3
2
1
0
Axial Centerline Distance (in.)
Prefiring
Post Recession
Char Depth

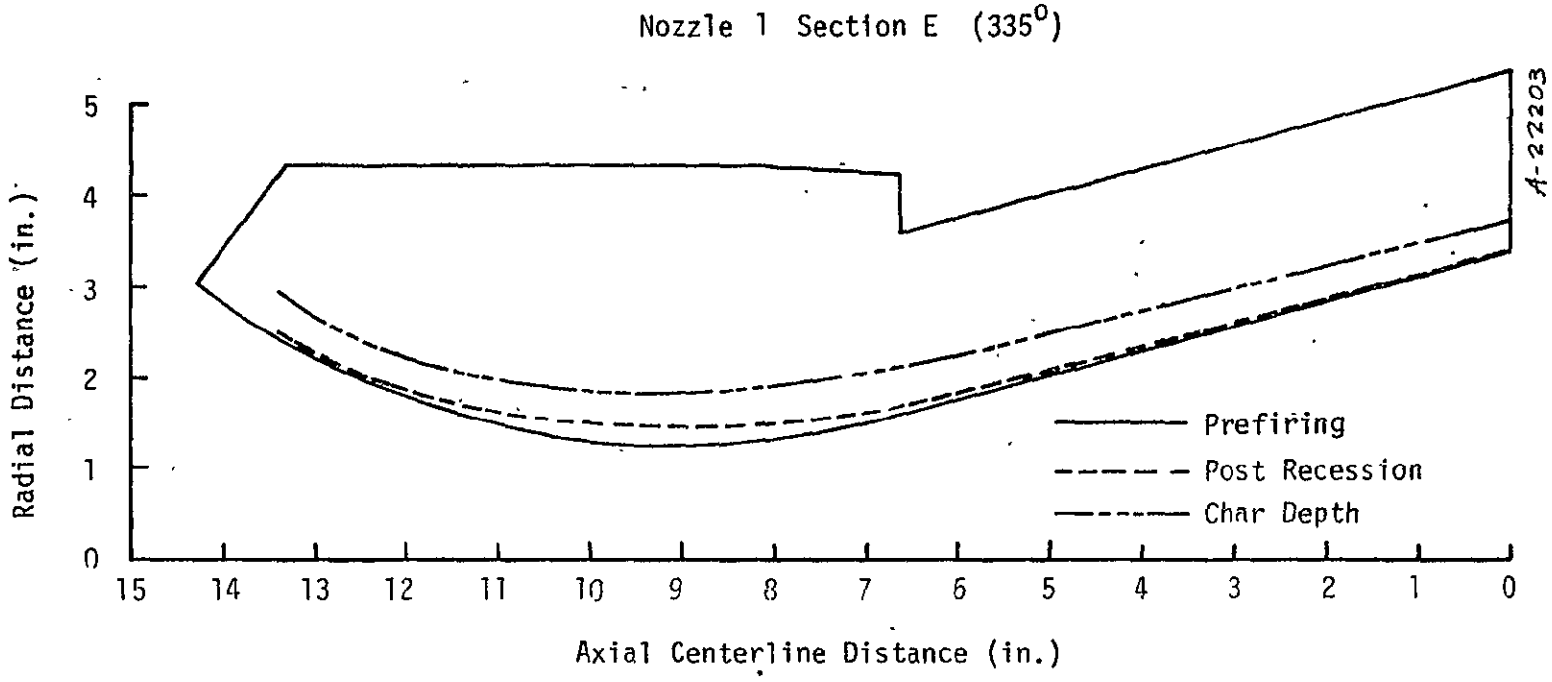
Nozzle 1 Section E (335°)
Radial Distance (in.)
5
4
3
2
1
0
15
14
13
12
11
10
9
8
7
6
5
4
3
2
1
0
Axial Centerline Distance (in.)
Prefiring
Post Recession
Char Depth
A-22203

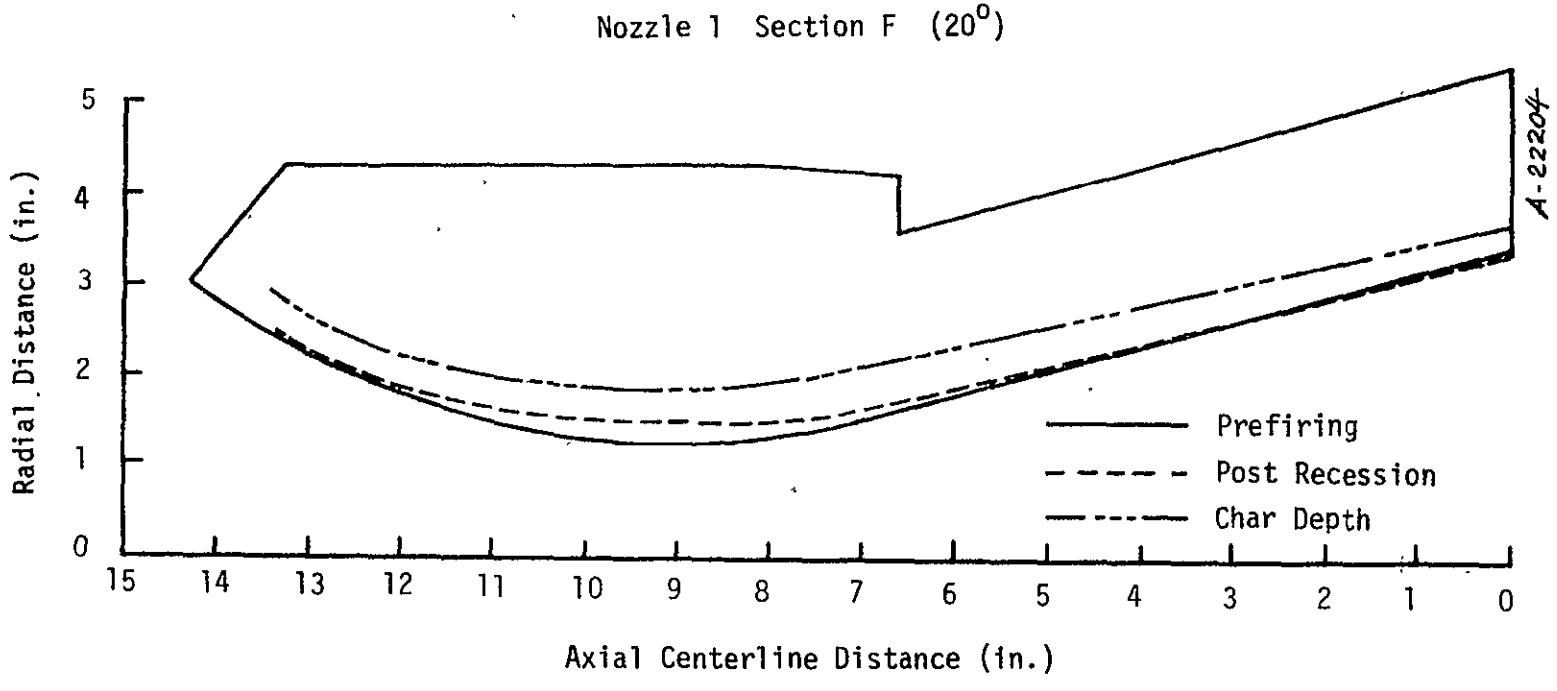
Nozzle 1 Section F (20°)
Radial Distance (in.)
5
4
3
2
1
0
15
14
13
12
11
10
9
8
7
6
5
4
3
2
1
0
Axial Centerline Distance (in.)
Prefiring
Post Recession
Char Depth
A-22204

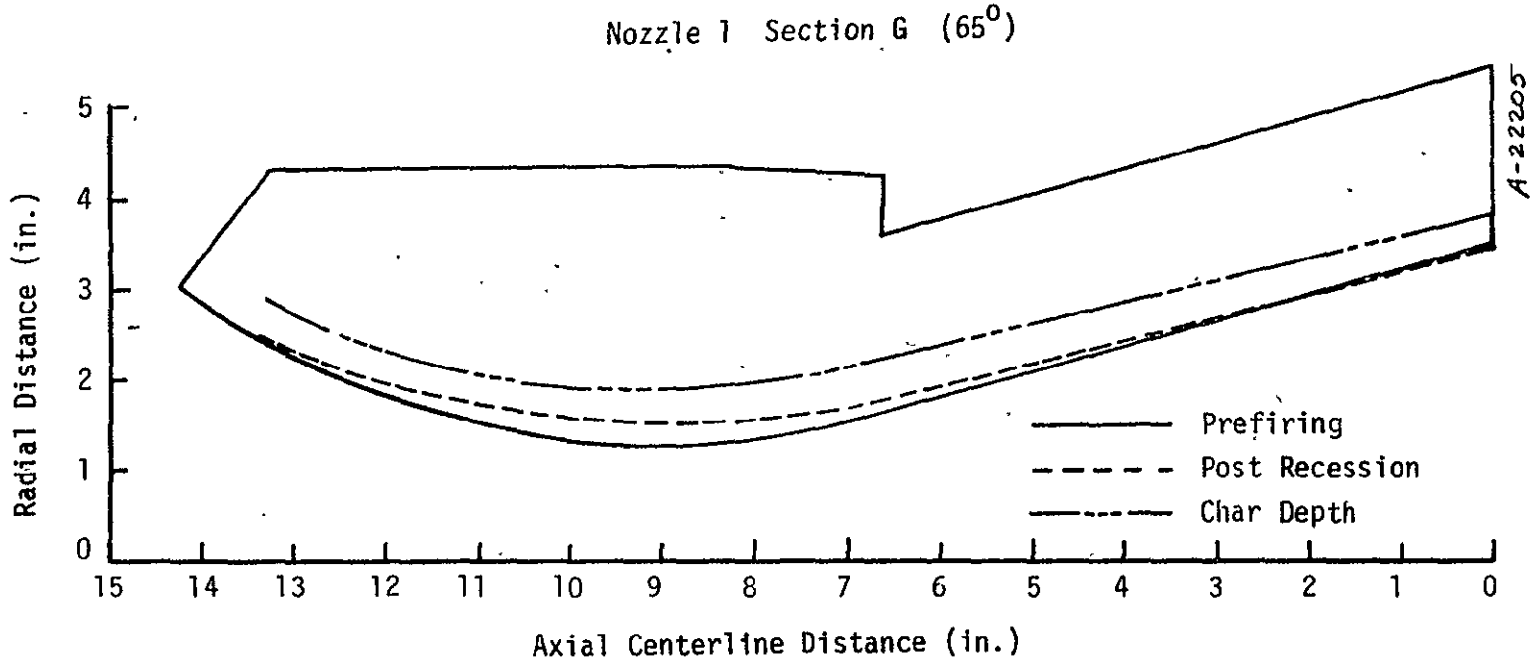
Nozzle 1 Section G (65°)
A-22205
Radial Distance (in.)
5
4
3
2
1
0
15
14
13
12
11
10
9
8
7
6
5
4
3
2
1
0
Axial Centerline Distance (in.)
Prefiring
Post Recession
Char Depth

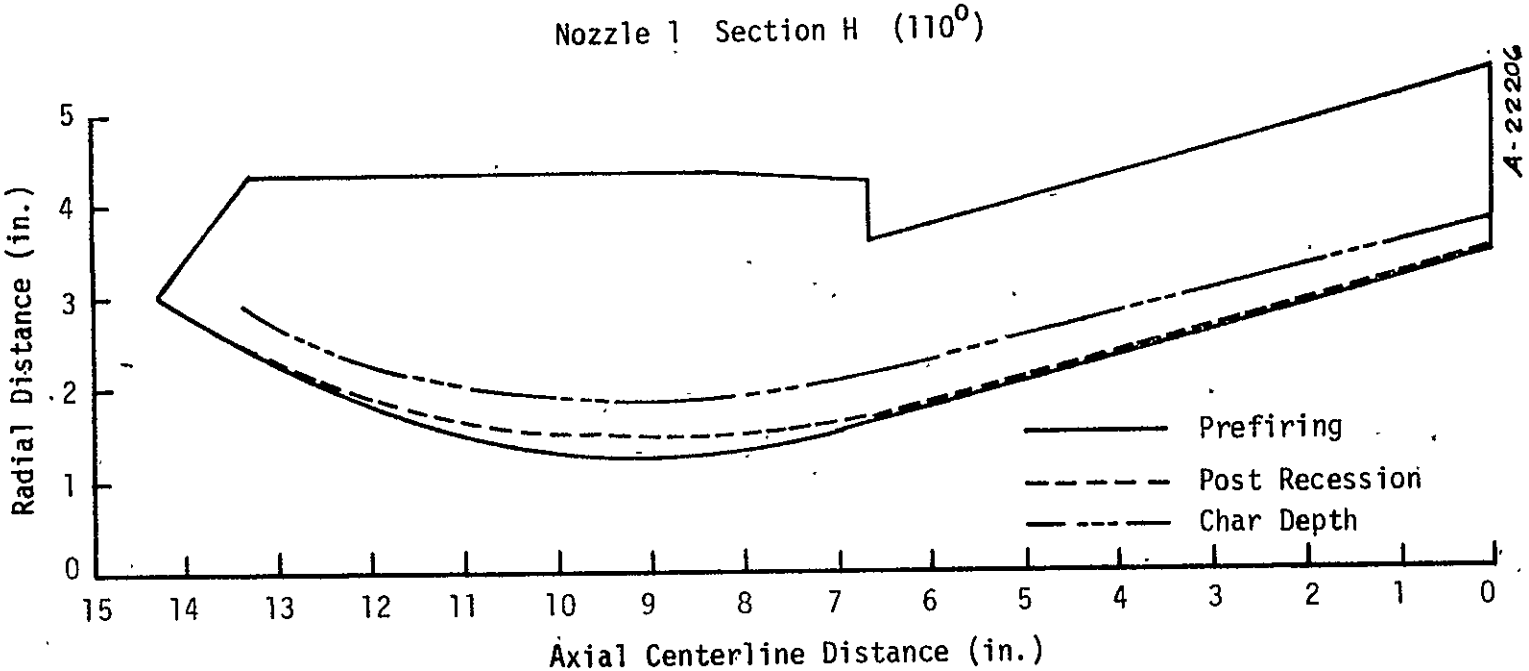
Nozzle 1 Section H (110°)
A-22206
Radial Distance (in.)
5
4
3
2
1
0
15 14 13 12 11 10 9 8 7 6 5 4 3 2 1 0
Axial Centerline Distance (in.)
Prefiring
Post Recession
Char Depth

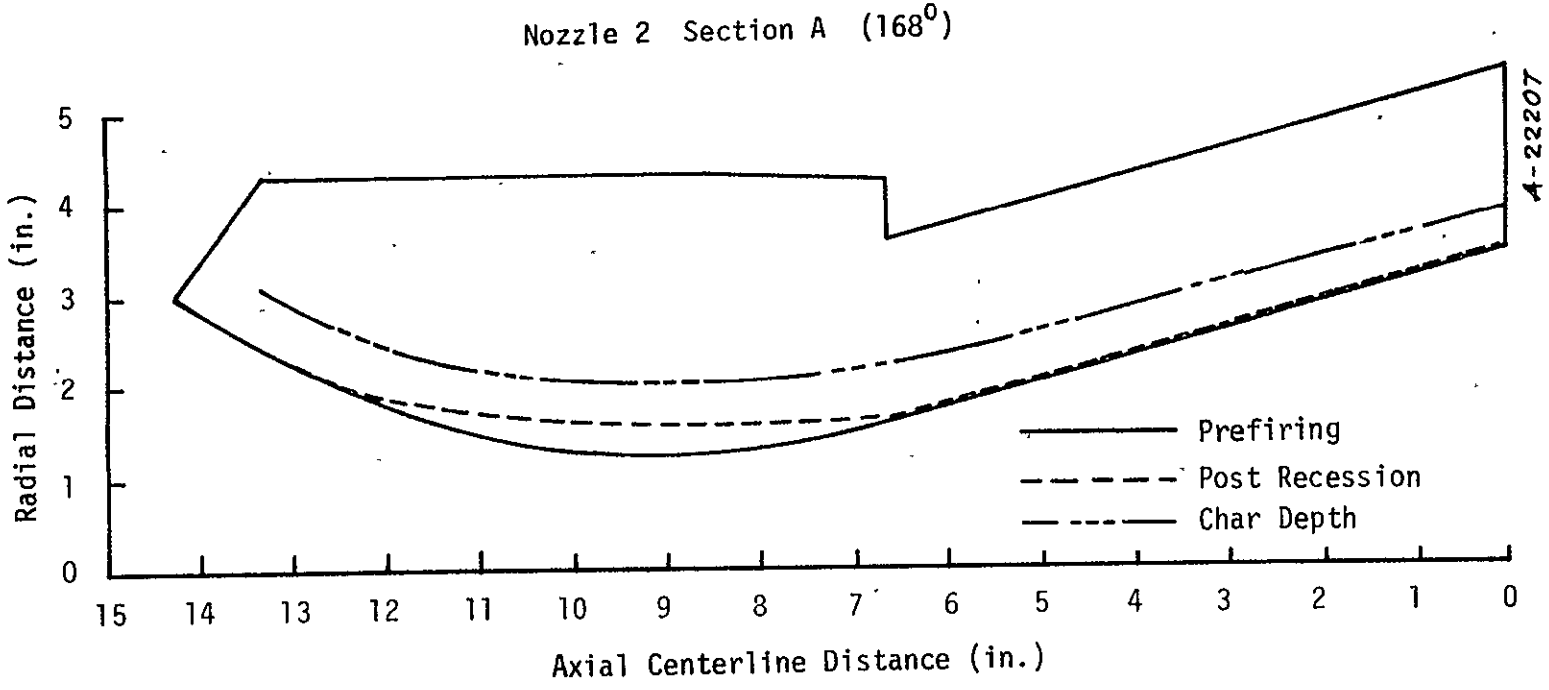
Nozzle 2 Section A (168°)
Radial Distance (in.)
Axial Centerline Distance (in.)
Prefiring
Post Recession
Char Depth
4-22207

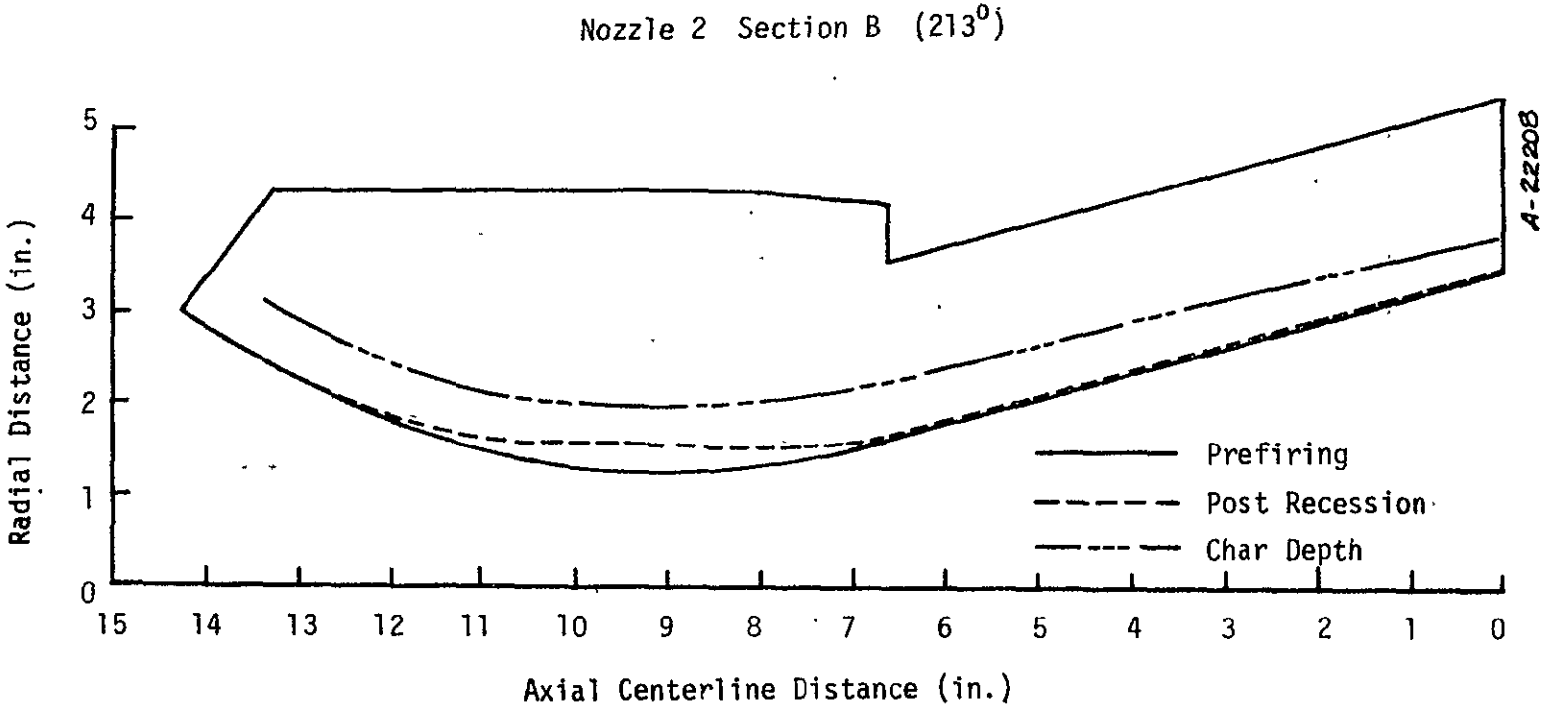
Nozzle 2 Section B (213°)
Radial Distance (in.)
5
4
3
2
1
0
15 14 13 12 11 10 9 8 7 6 5 4 3 2 1 0
Axial Centerline Distance (in.)
Prefiring
Post Recession
Char Depth
A-22208

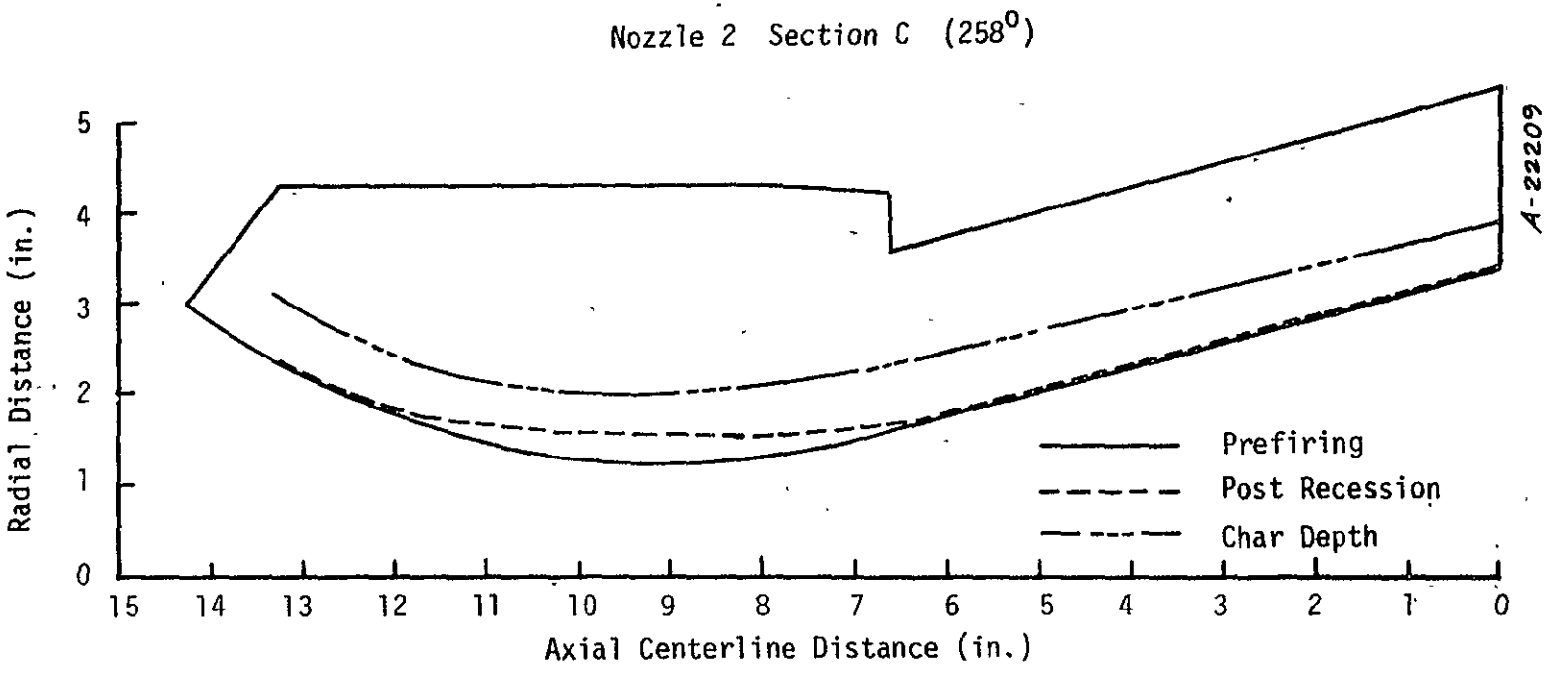
Nozzle 2 Section C (258°)
A-22209
Radial Distance (in.)
5
4
3
2
1
0
15
14
13
12
11
10
9
8
7
6
5
4
3
2
1
0
Axial Centerline Distance (in.)
Prefiring
Post Recession
Char Depth

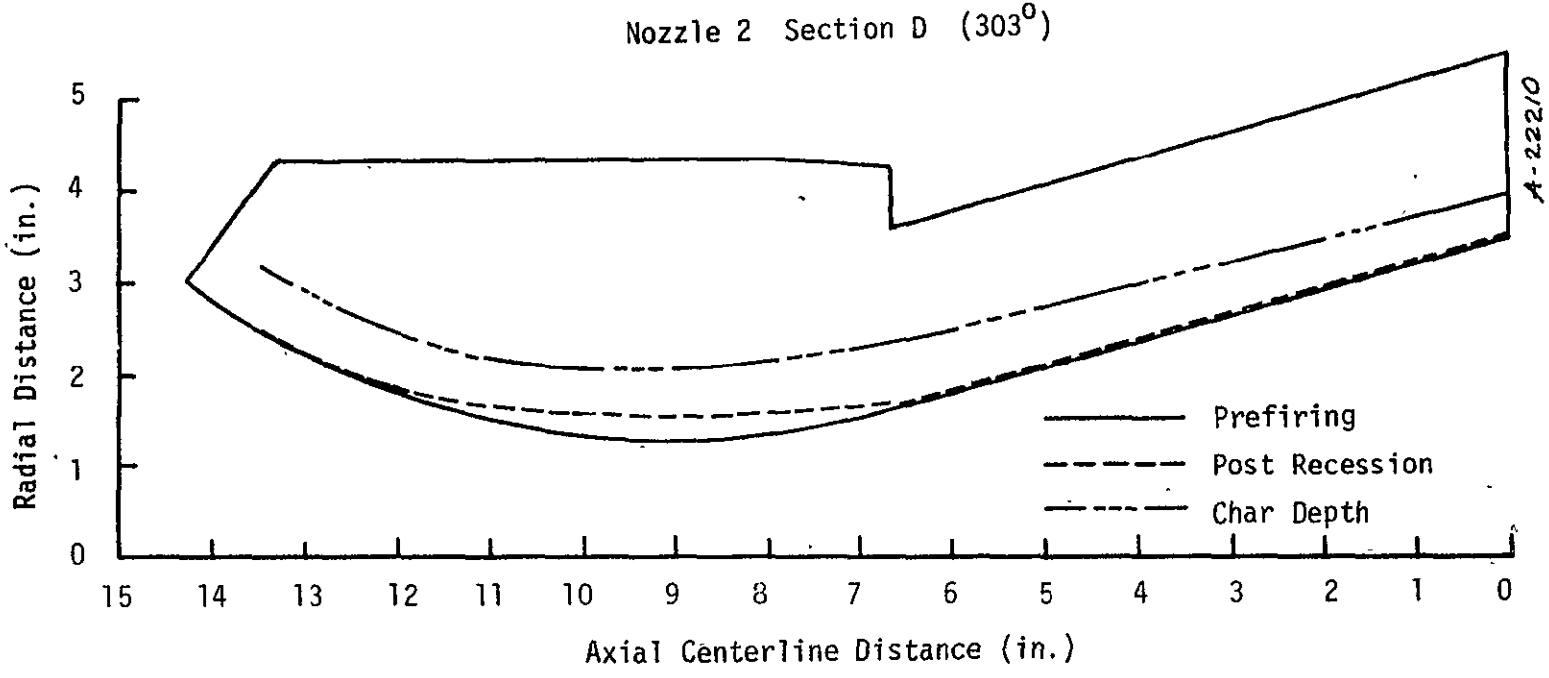
Nozzle 2 Section D (303°)
A-22210
Radial Distance (in.)
5
4
3
2
1
0
15 14 13 12 11 10 9 8 7 6 5 4 3 2 1 0
Axial Centerline Distance (in.)
Prefiring
Post Recession
Char Depth

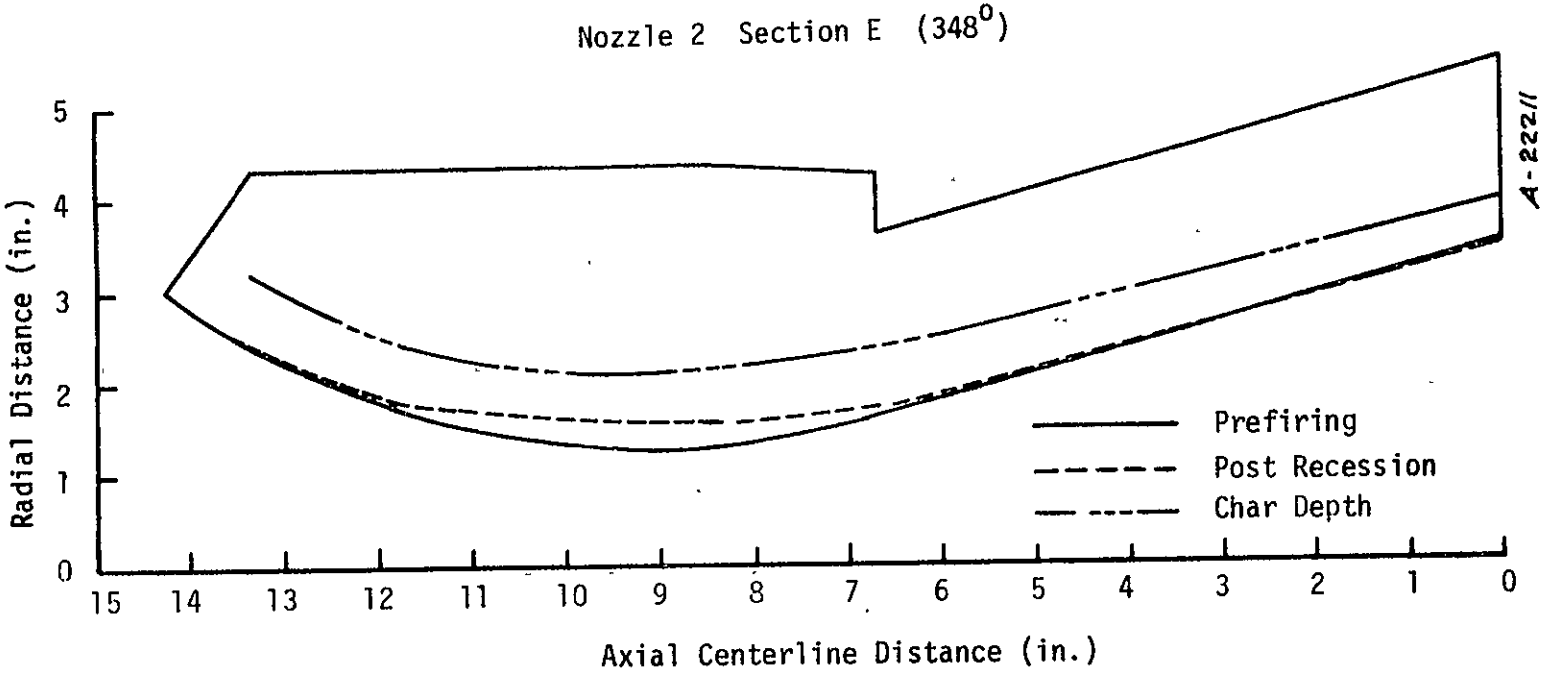
Nozzle 2 Section E (348°)
Radial Distance (in.)
5
4
3
2
1
0
15 14 13 12 11 10 9 8 7 6 5 4 3 2 1 0
Axial Centerline Distance (in.)
Prefiring
Post Recession
Char Depth
A-22211

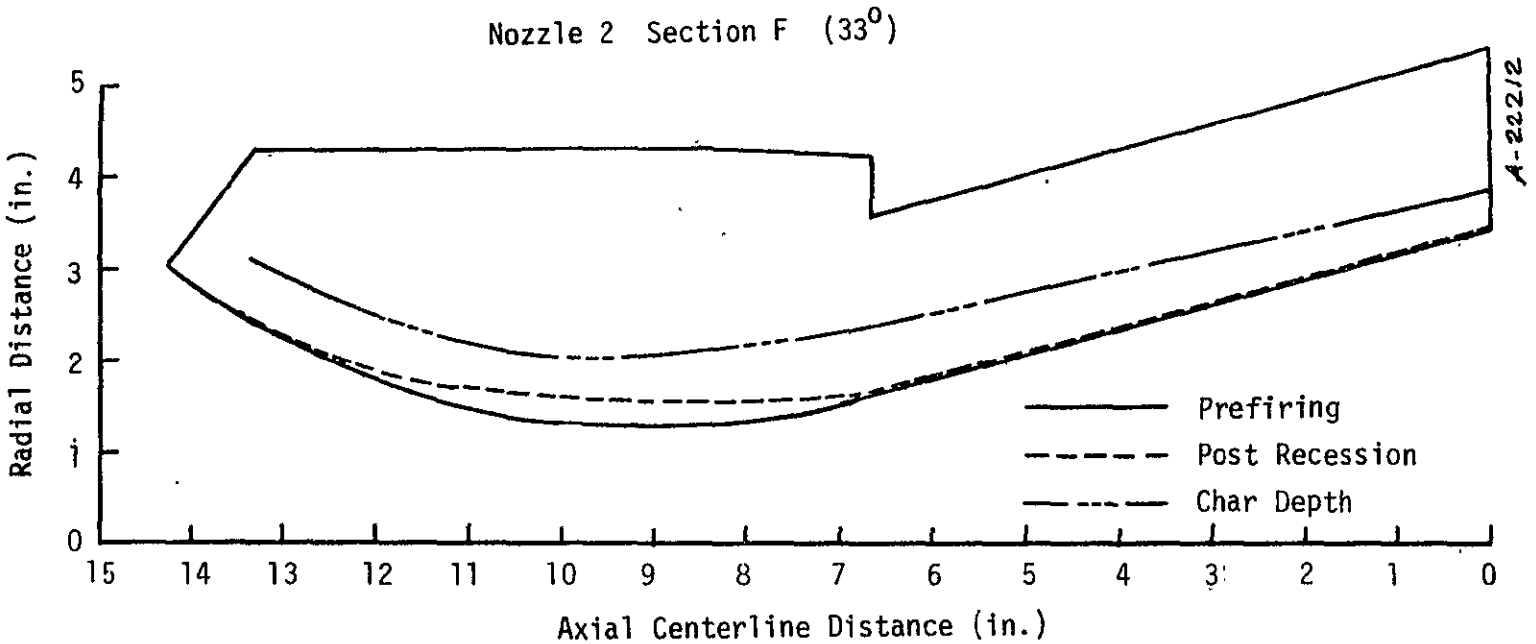
Nozzle 2 Section F (33°)
Radial Distance (in.)
5
4
3
2
1
0
15 14 13 12 11 10 9 8 7 6 5 4 3 2 1 0
Axial Centerline Distance (in.)
Prefiring
Post Recession
Char Depth
A-22212

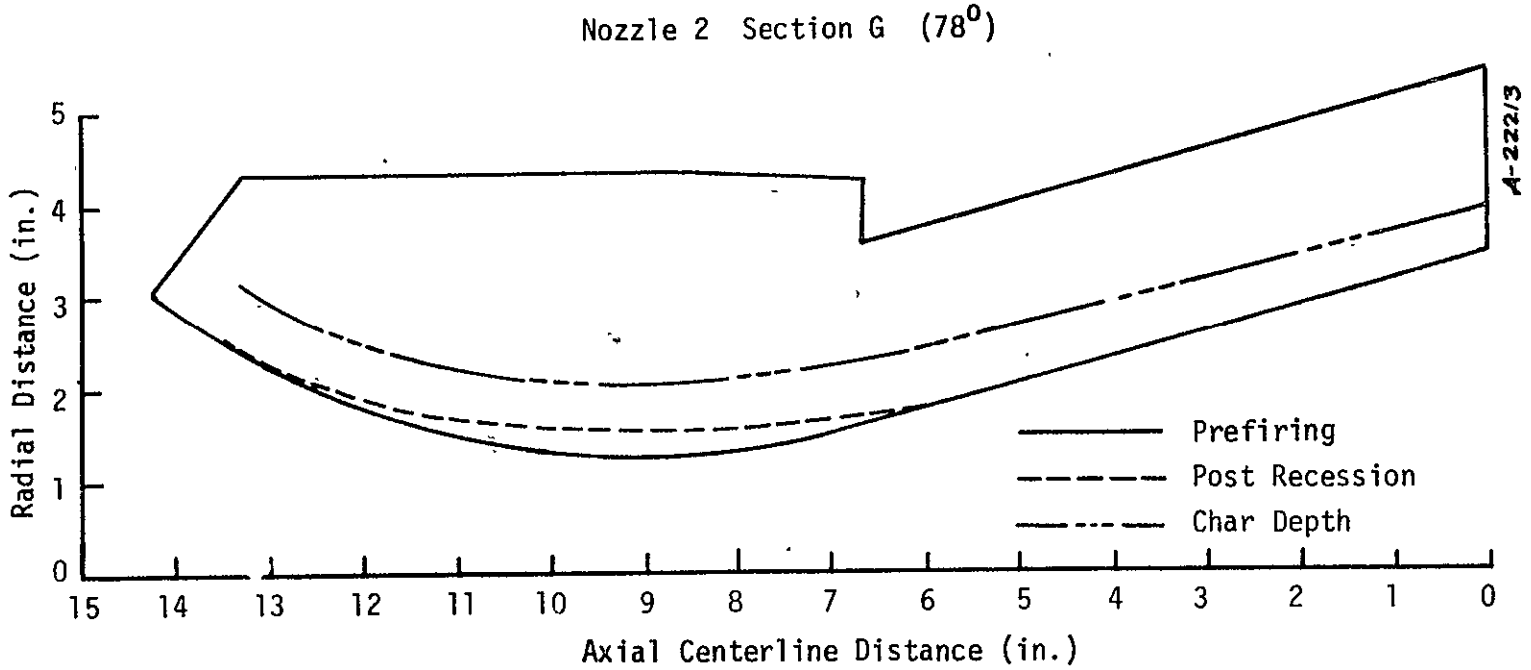
Nozzle 2 Section G (78°)
Radial Distance (in.)
5
4
3
2
1
0
15 14 13 12 11 10 9 8 7 6 5 4 3 2 1 0
Axial Centerline Distance (in.)
Prefiring
Post Recession
Char Depth
A-222/3

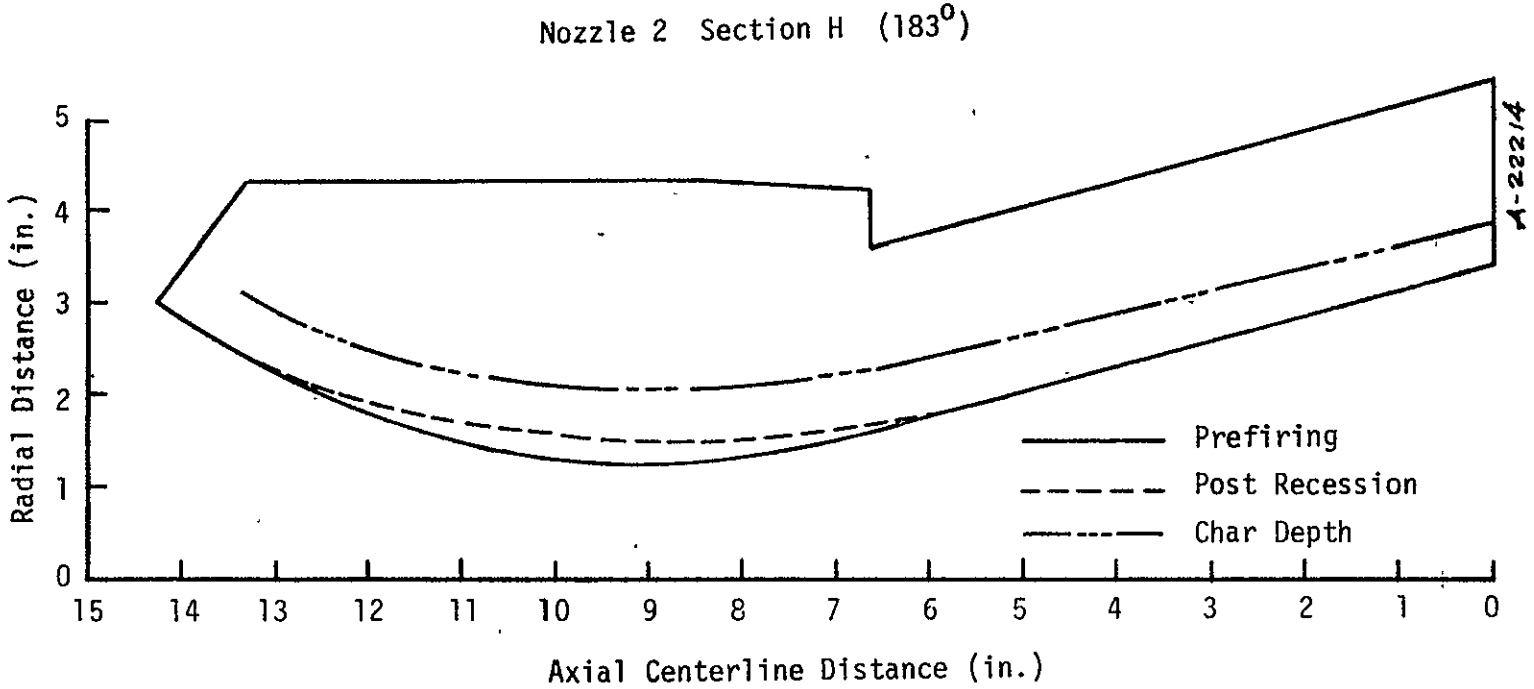
Nozzle 2 Section H (183°)
Radial Distance (in.)
5
4
3
2
1
0
15 14 13 12 11 10 9 8 7 6 5 4 3 2 1 0
Axial Centerline Distance (in.)
Prefiring
Post Recession
Char Depth
A-22214

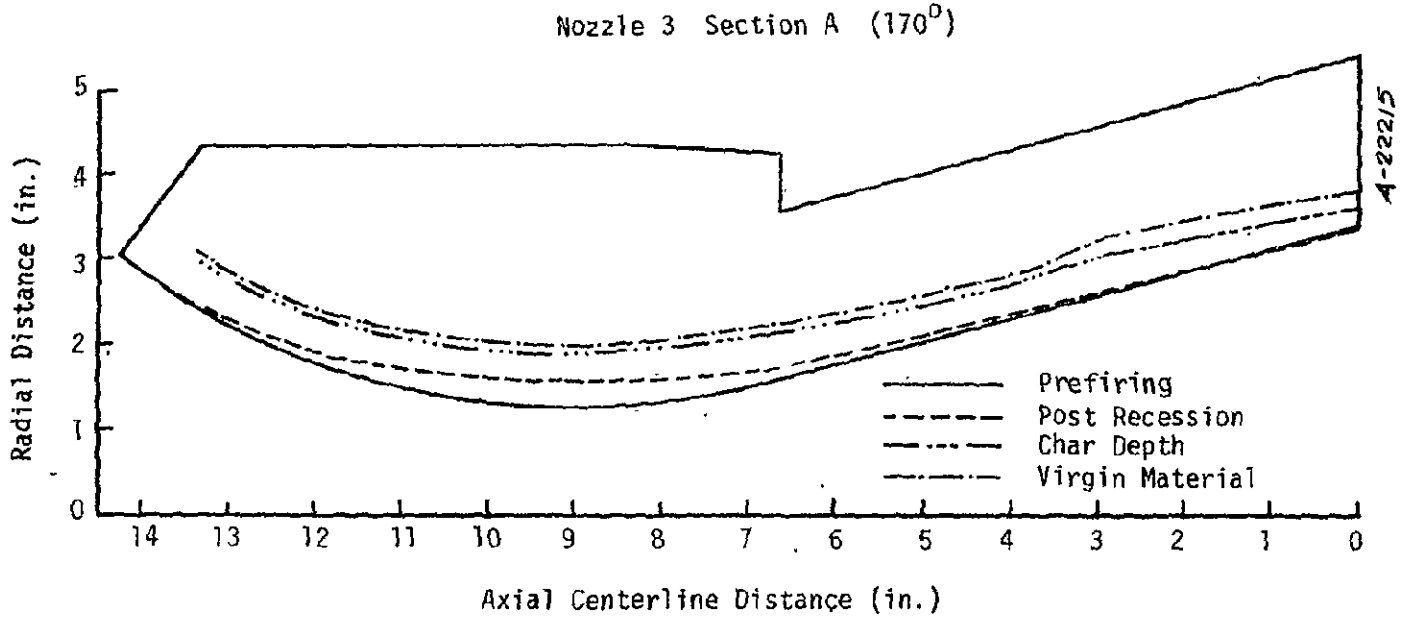
Nozzle 3 Section A (170°)
Radial Distance (in.)
Axial Centerline Distance (in.)
Prefiring
Post Recession
Char Depth
Virgin Material
A-222/5

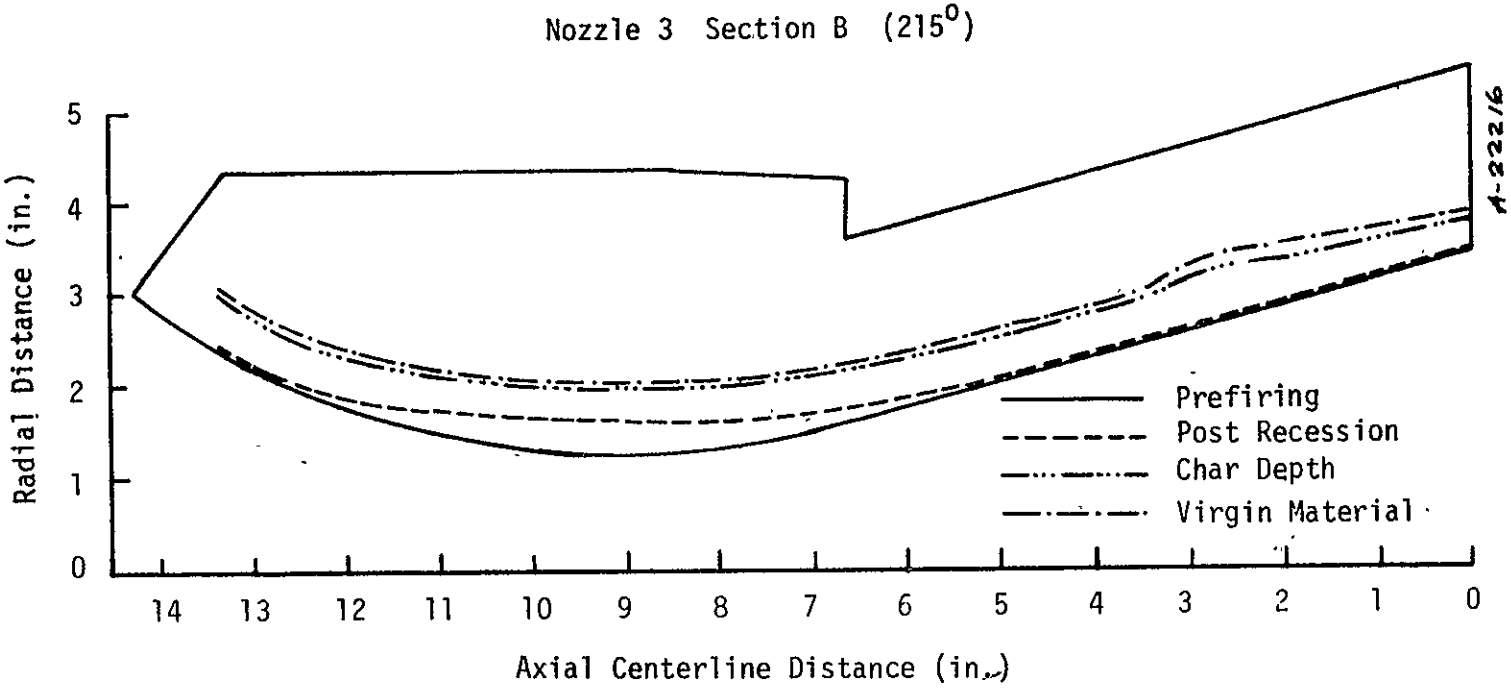
Nozzle 3 Section B (215°)
Radial Distance (in.)
5
4
3
2
1
0
14
13
12
11
10
9
8
7
6
5
4
3
2
1
0
Axial Centerline Distance (in.)
Prefiring
Post Recession
Char Depth
Virgin Material
A-22216

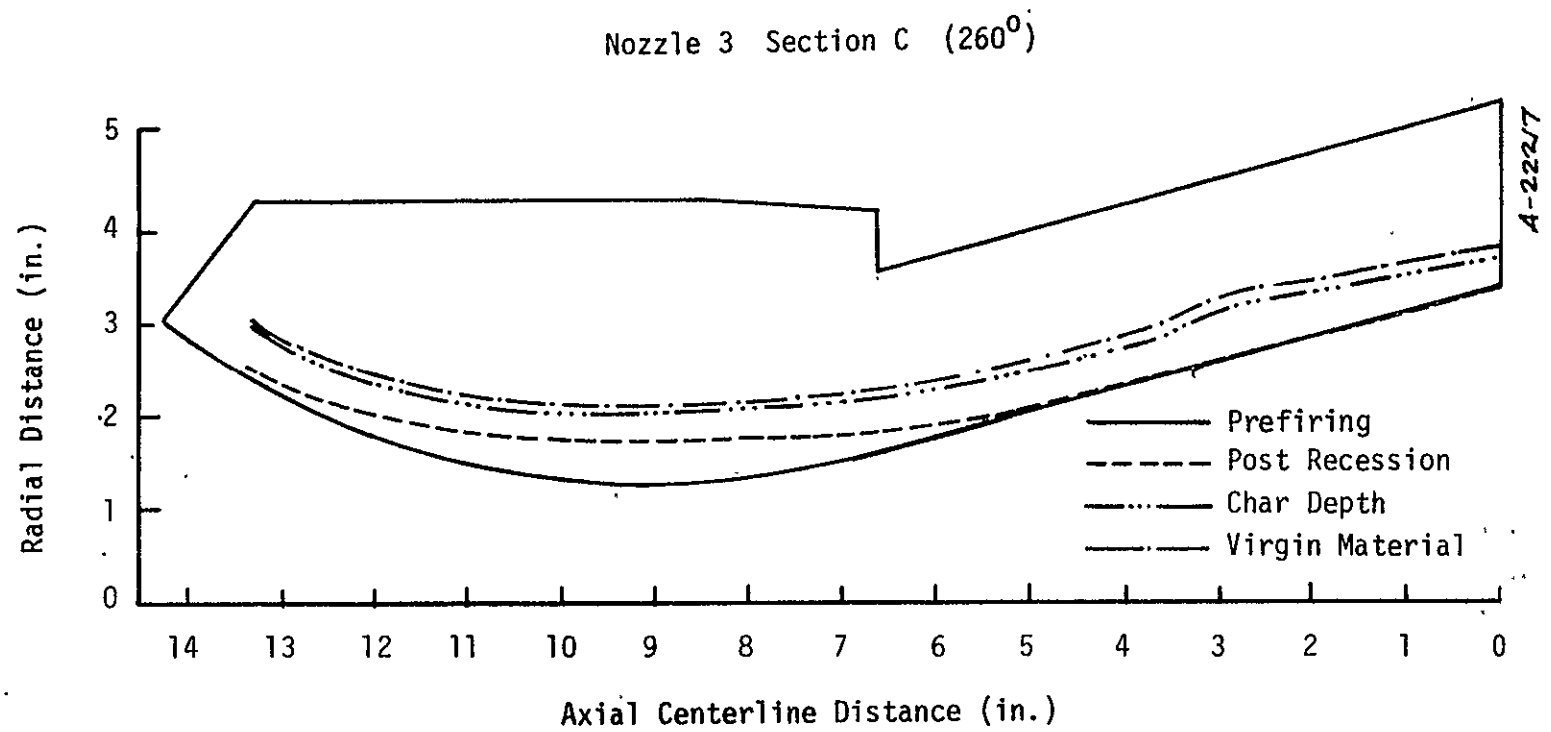
Nozzle 3 Section C (260°)
Radial Distance (in.)
5
4
3
2
1
0
14
13
12
11
10
9
8
7
6
5
4
3
2
1
0
Axial Centerline Distance (in.)
Prefiring
Post Recession
Char Depth
Virgin Material
A-222/7

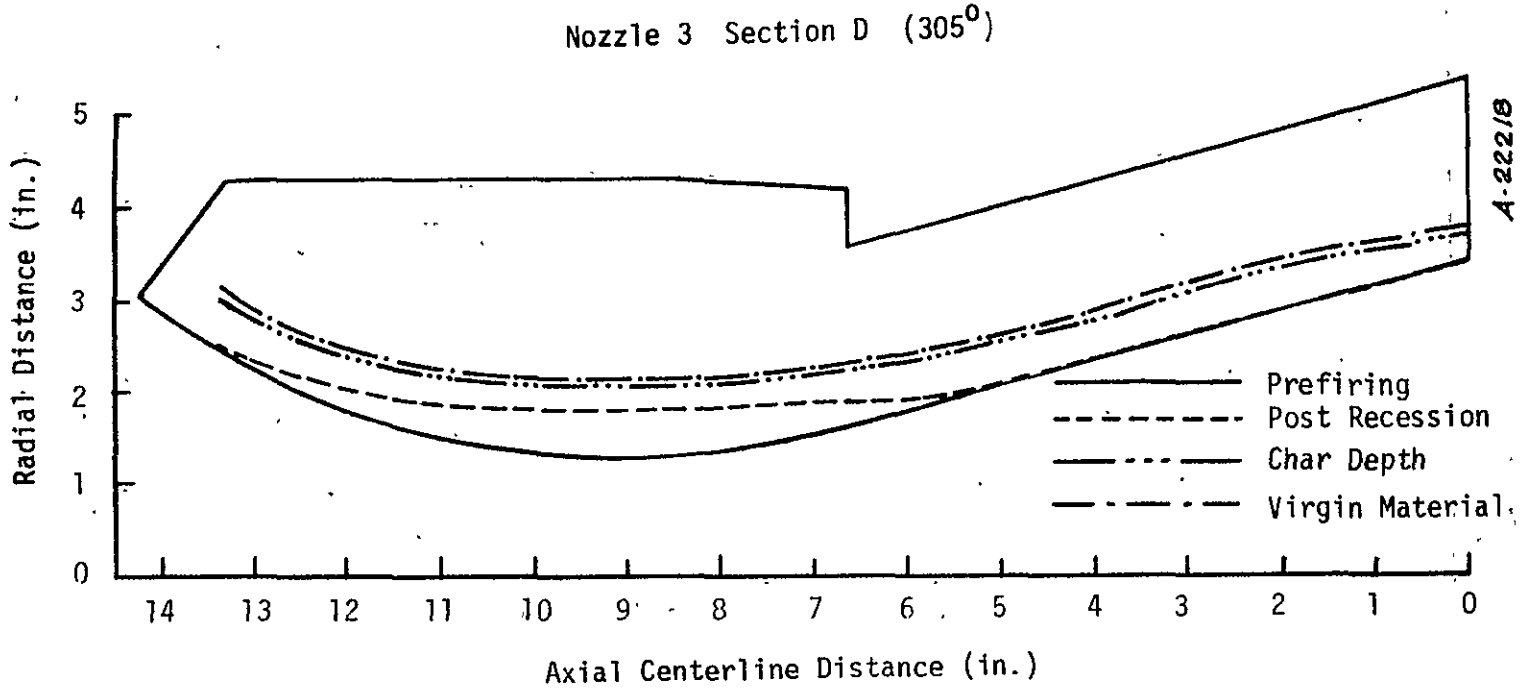
Nozzle 3 Section D (305°)
Radial Distance (in.)
5
4
3
2
1
0
14
13
12
11
10
9
8
7
6
5
4
3
2
1
0
Axial Centerline Distance (in.)
Prefiring
Post Recession
Char Depth
Virgin Material
A-22218

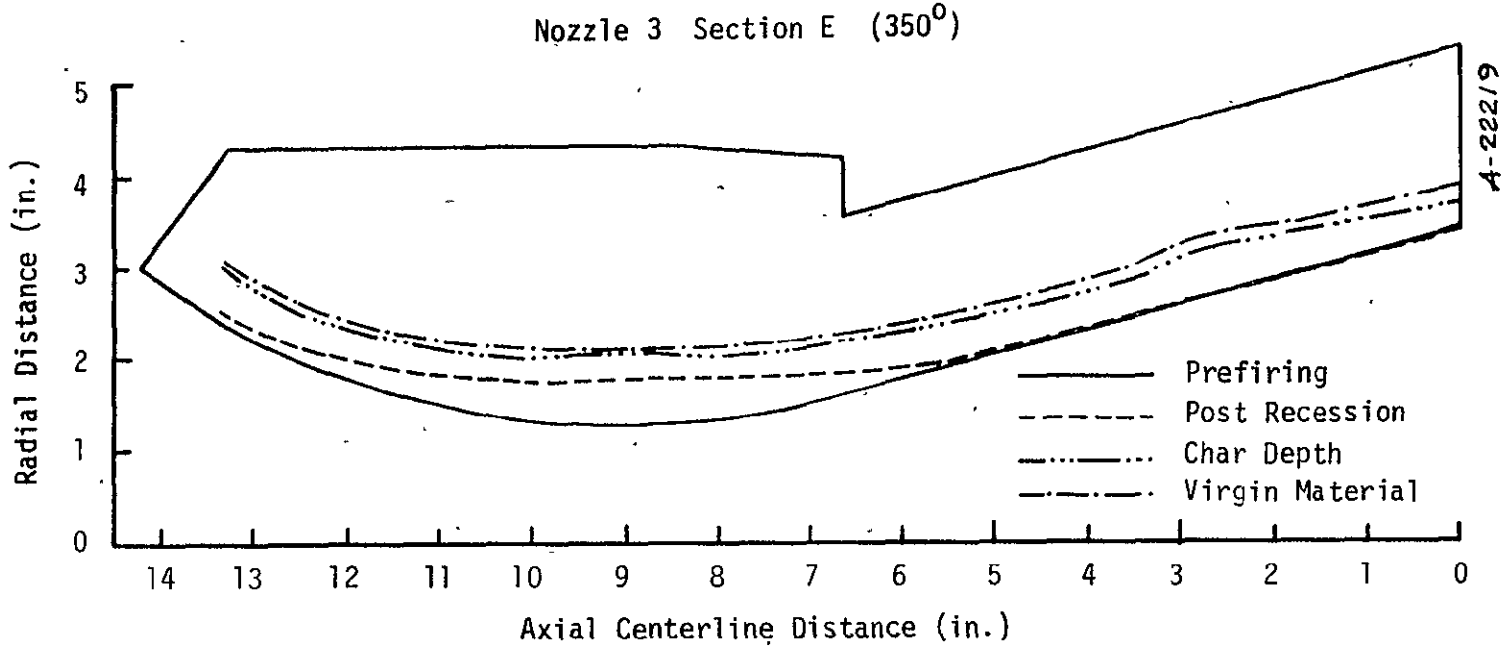
Nozzle 3 Section E (350°)
Radial Distance (in.)
5
4
3
2
1
0
14
13
12
11
10
9
8
7
6
5
4
3
2
1
0
Axial Centerline Distance (in.)
Prefiring
Post Recession
Char Depth
Virgin Material
A-22219

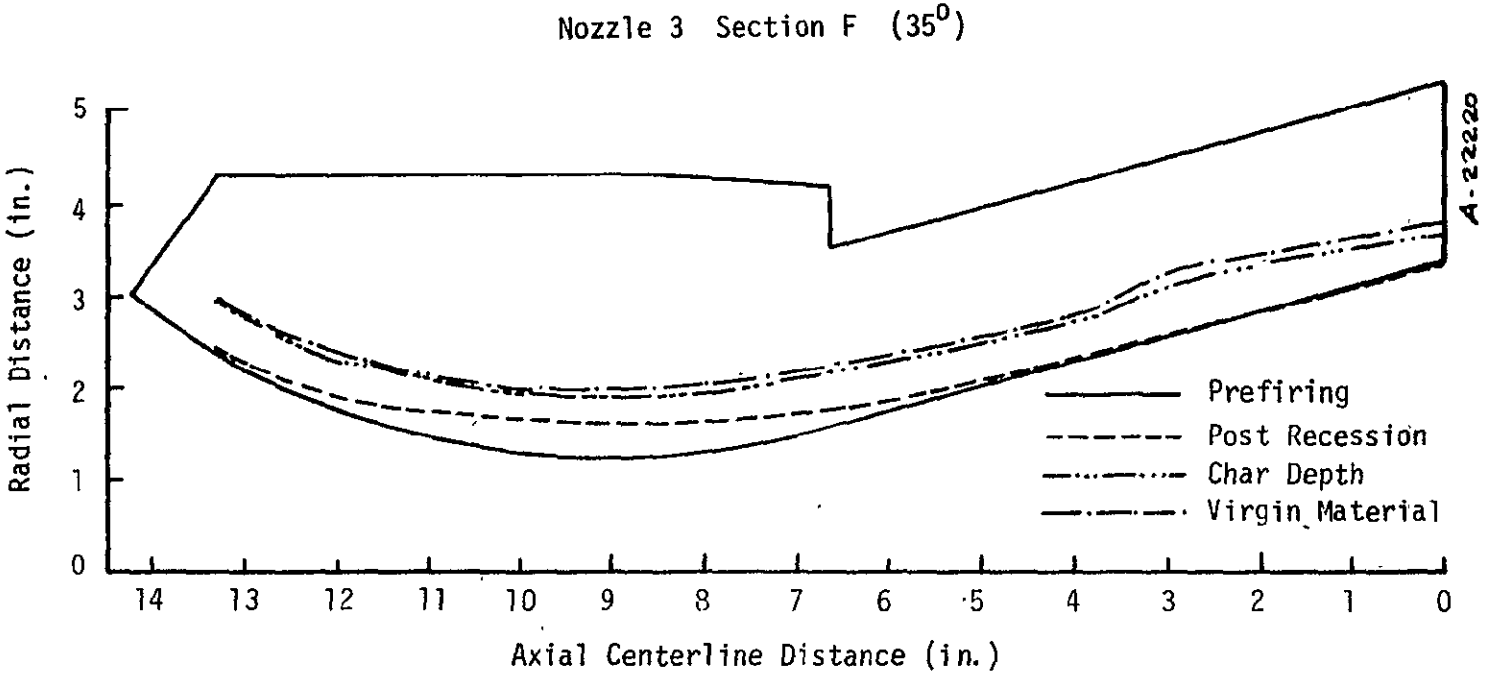
Nozzle 3 Section F (35°)
Radial Distance (in.)
5
4
3
2
1
0
14
13
12
11
10
9
8
7
6
5
4
3
2
1
0
Axial Centerline Distance (in.)
Prefiring
Post Recession
Char Depth
Virgin Material
A-22220

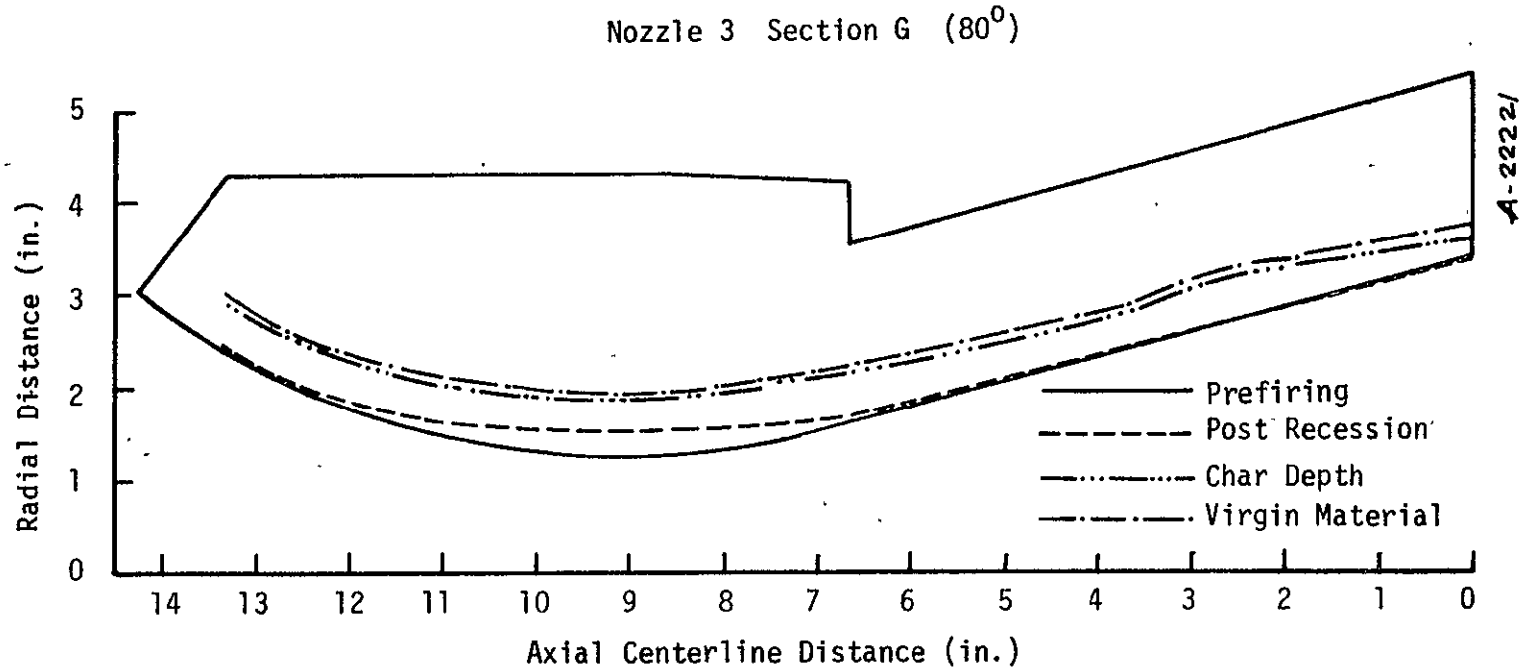
Nozzle 3 Section G (80°)
Radial Distance (in.)
5
4
3
2
1
0
14
13
12
11
10
9
8
7
6
5
4
3
2
1
0
Axial Centerline Distance (in.)
Prefiring
Post Recession
Char Depth
Virgin Material
A-2222

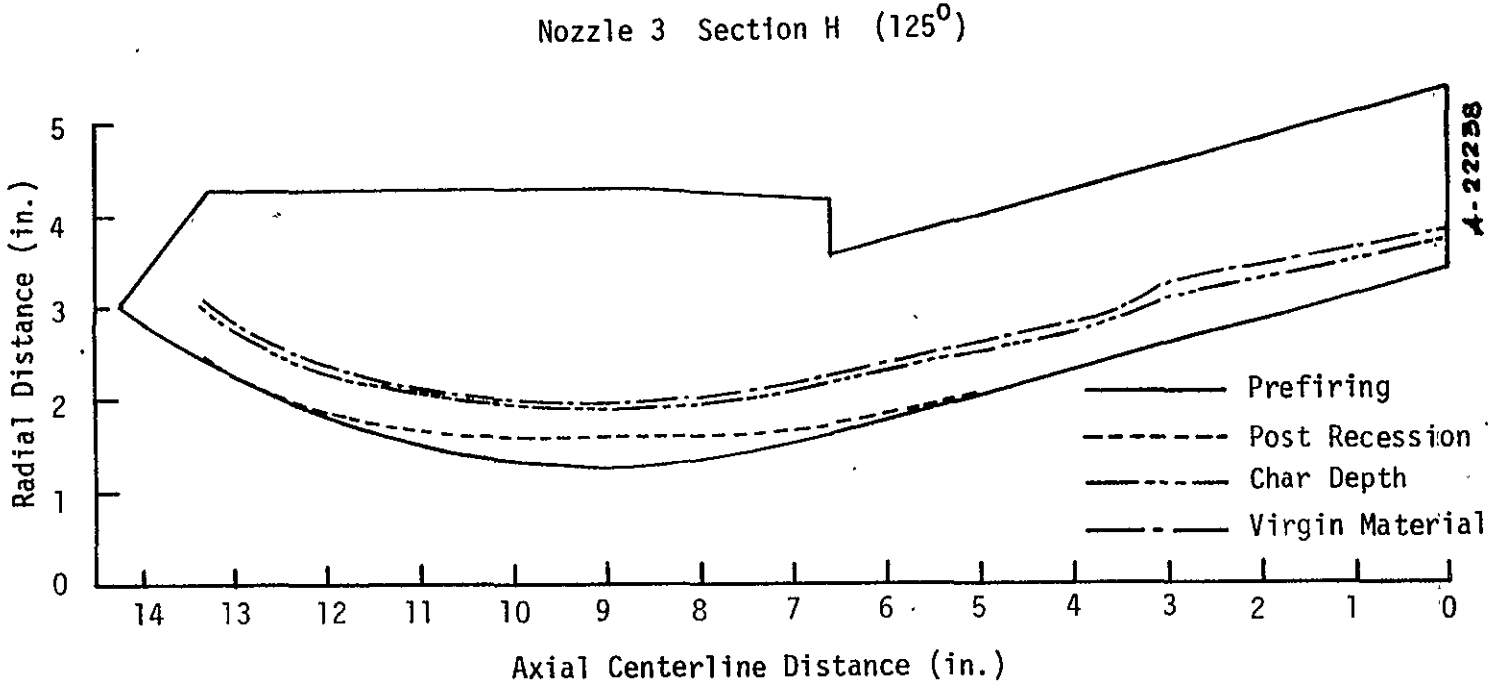
Nozzle 3 Section H (125°)
Radial Distance (in.)
5
4
3
2
1
0
14
13
12
11
10
9
8
7
6
5
4
3
2
1
0
Axial Centerline Distance (in.)
Prefiring
Post Recession
Char Depth
Virgin Material
4-22238

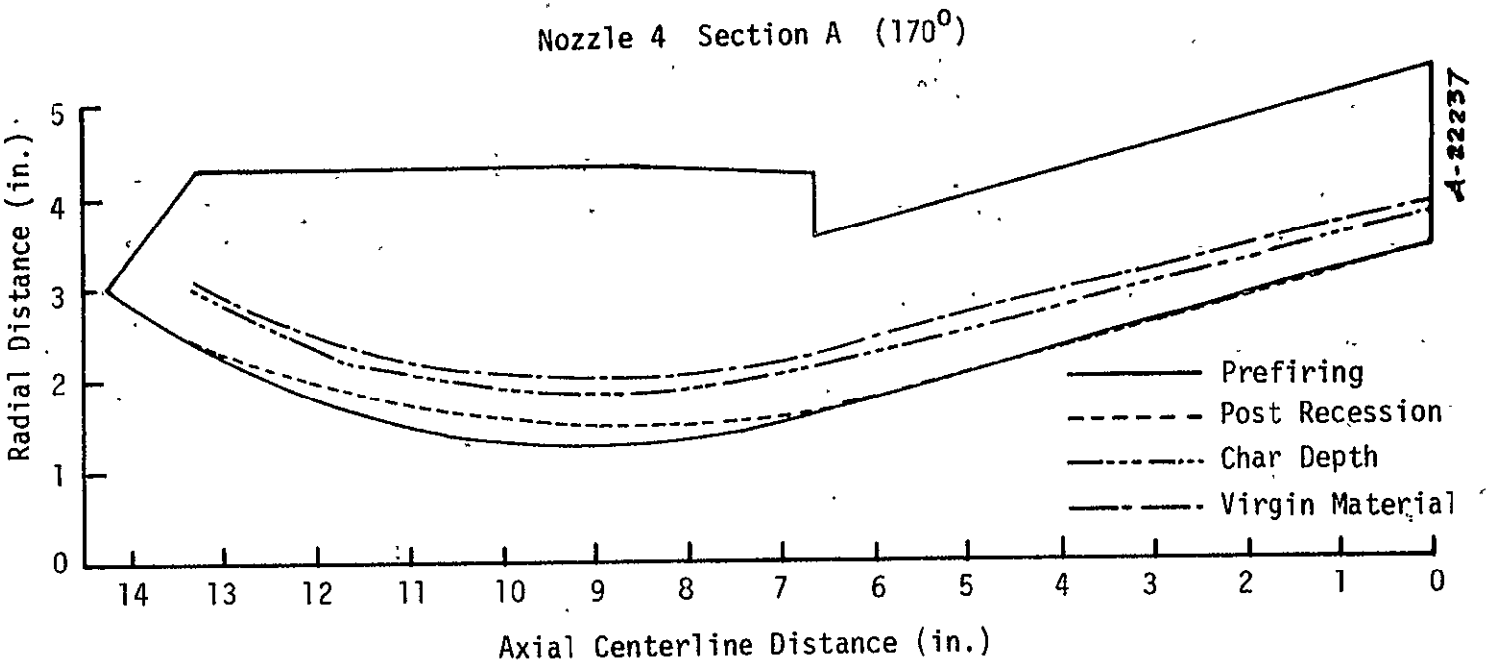
Nozzle 4 Section A (170°)
Radial Distance (in.)
5
4
3
2
1
0
14
13
12
11
10
9
8
7
6
5
4
3
2
1
0
Axial Centerline Distance (in.)
Prefiring
Post Recession
Char Depth
Virgin Material
A-22237

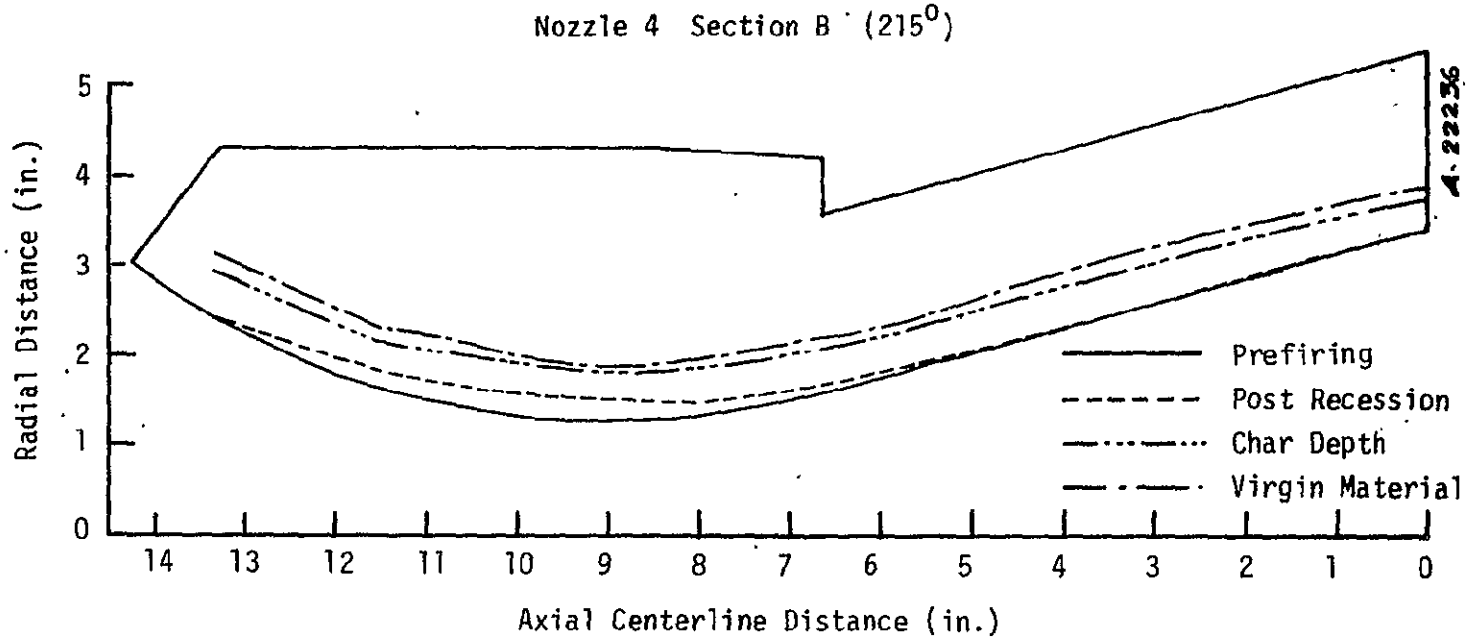
Nozzle 4 Section B (215°)
Radial Distance (in.)
5
4
3
2
1
0
14
13
12
11
10
9
8
7
6
5
4
3
2
1
0
Axial Centerline Distance (in.)
Prefiring
Post Recession
Char Depth
Virgin Material
4.22236

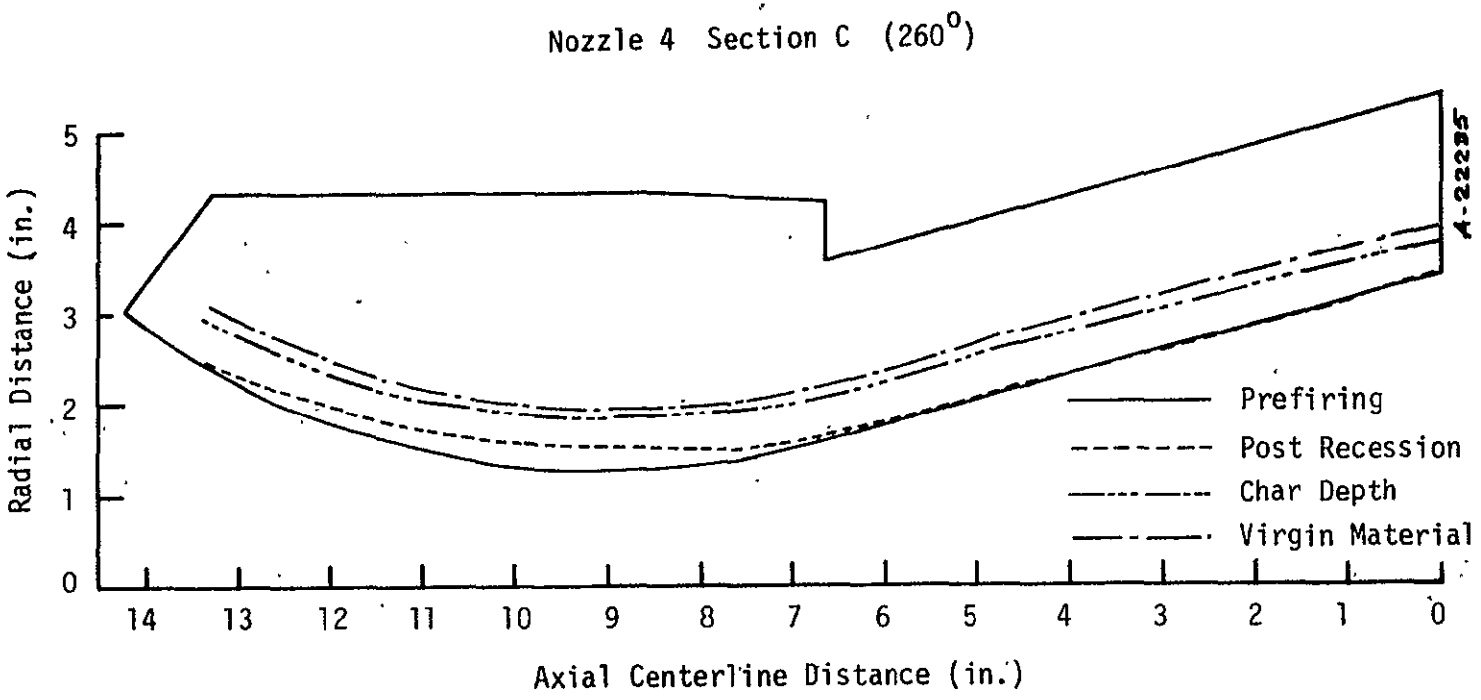
Nozzle 4 Section C (260°)
Radial Distance (in.)
5
4
3
2
1
0
14
13
12
11
10
9
8
7
6
5
4
3
2
1
0
Axial Centerline Distance (in.)
Prefiring
Post Recession
Char Depth
Virgin Material
4-22295

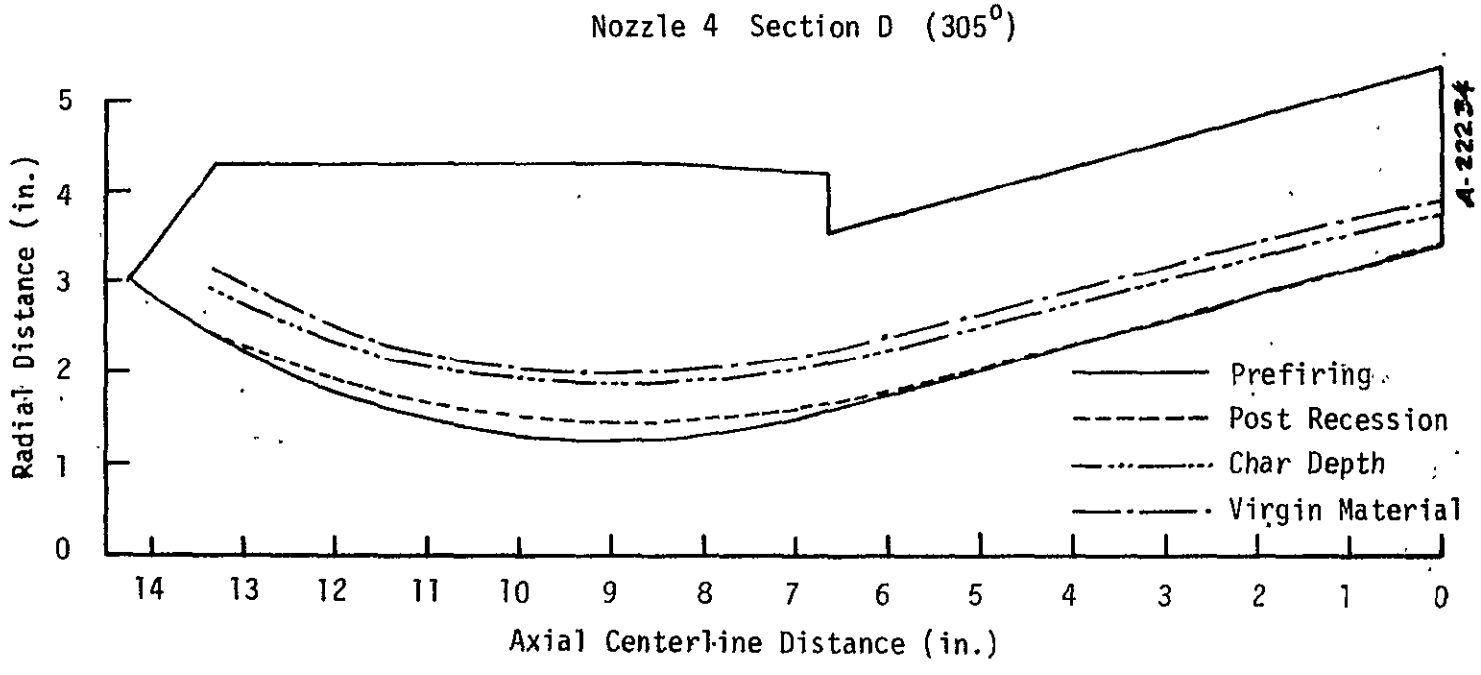
Nozzle 4 Section D (305°)
Radial Distance (in.)
5
4
3
2
1
0
14
13
12
11
10
9
8
7
6
5
4
3
2
1
0
Axial Centerline Distance (in.)
Prefiring
Post Recession
Char Depth
Virgin Material
A-22234

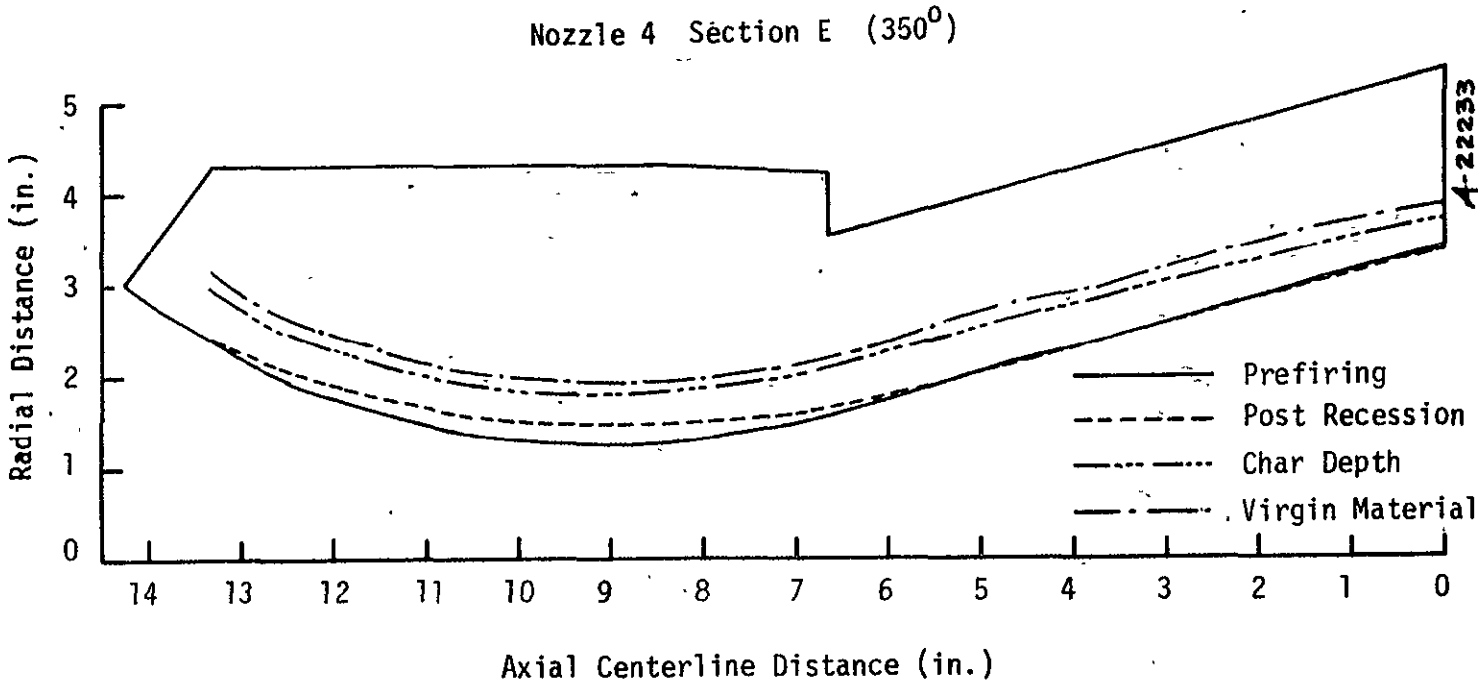
Nozzle 4 Section E (350°)
Radial Distance (in.)
5
4
3
2
1
0
14
13
12
11
10
9
8
7
6
5
4
3
2
1
0
Axial Centerline Distance (in.)
Prefiring
Post Recession
Char Depth
Virgin Material
A-22233

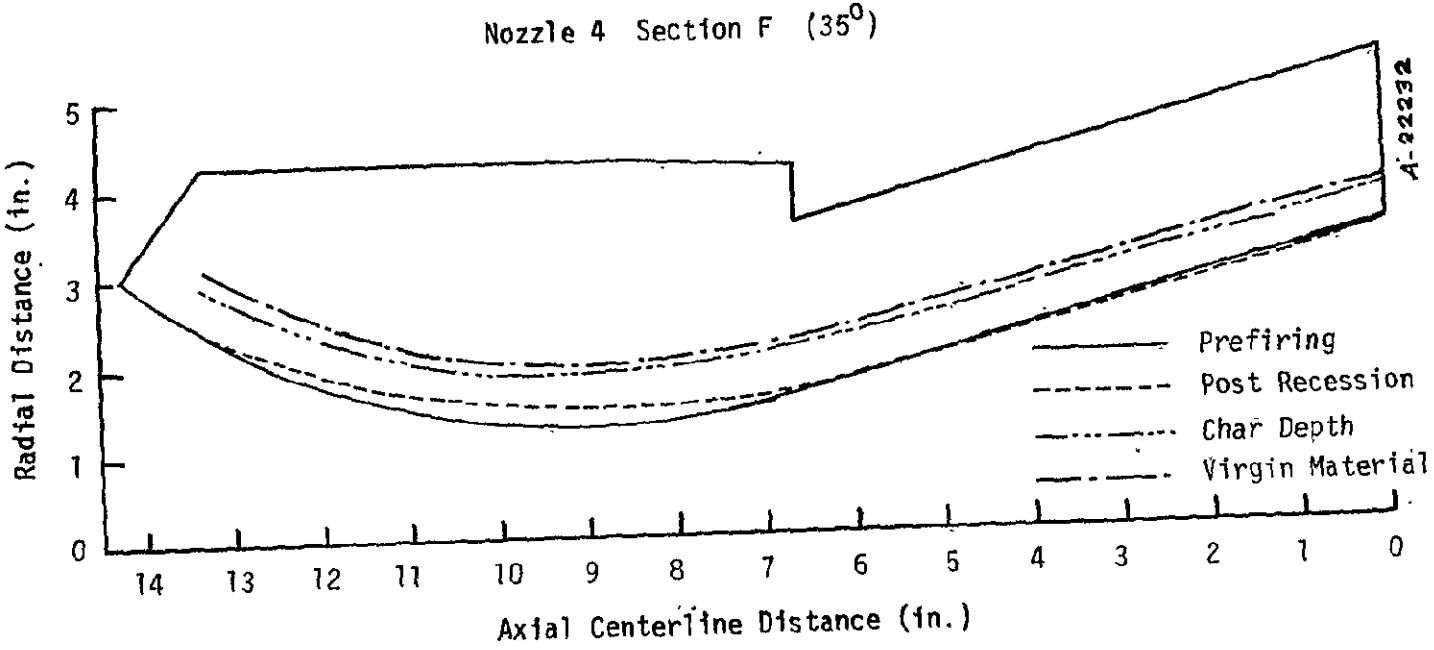
Nozzle 4 Section F (35°)
A-22232
Radial Distance (in.)
5
4
3
2
1
0
14
13
12
11
10
9
8
7
6
5
4
3
2
1
0
Axial Centerline Distance (in.)
Prefiring
Post Recession
Char Depth
Virgin Material

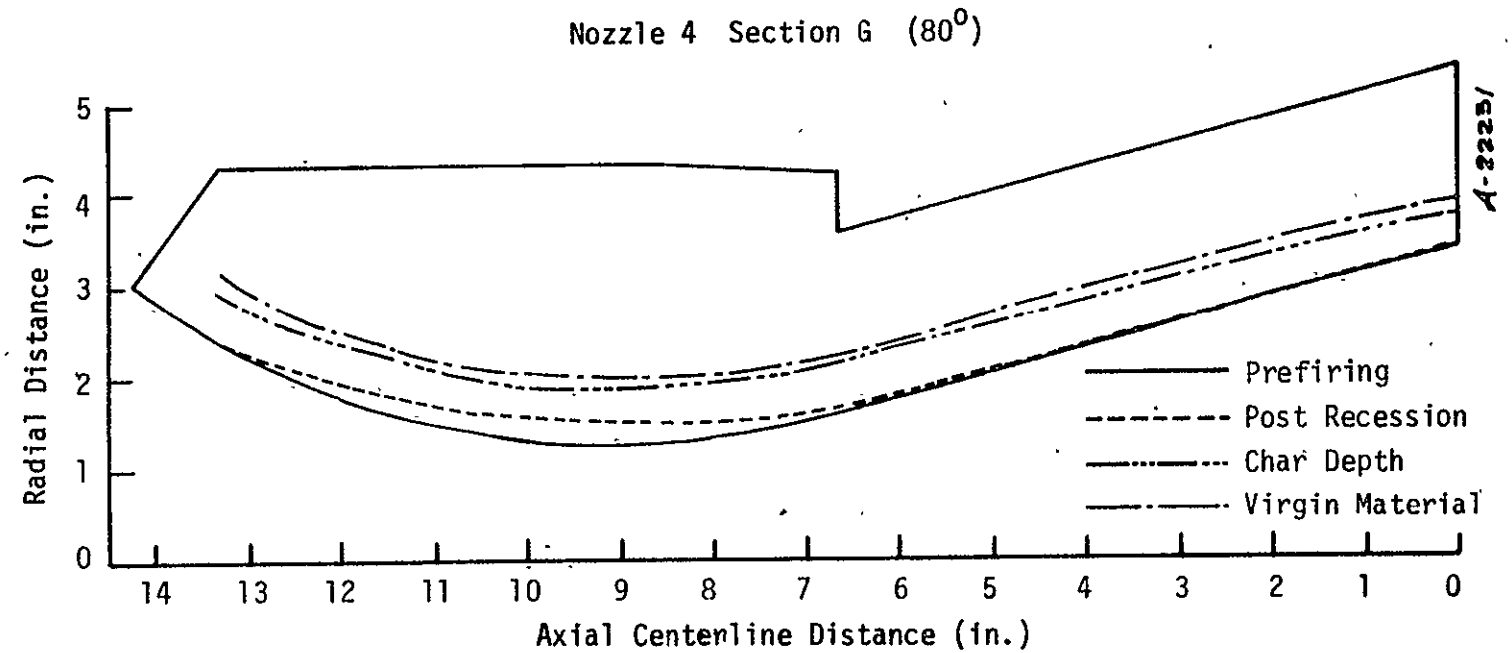
Nozzle 4 Section G (80°)
A-2225I
Radial Distance (in.)
0
1
2
3
4
5
14
13
12
11
10
9
8
7
6
5
4
3
2
1
0
Axial Centerline Distance (in.)
Prefiring
Post Recession
Char Depth
Virgin Material

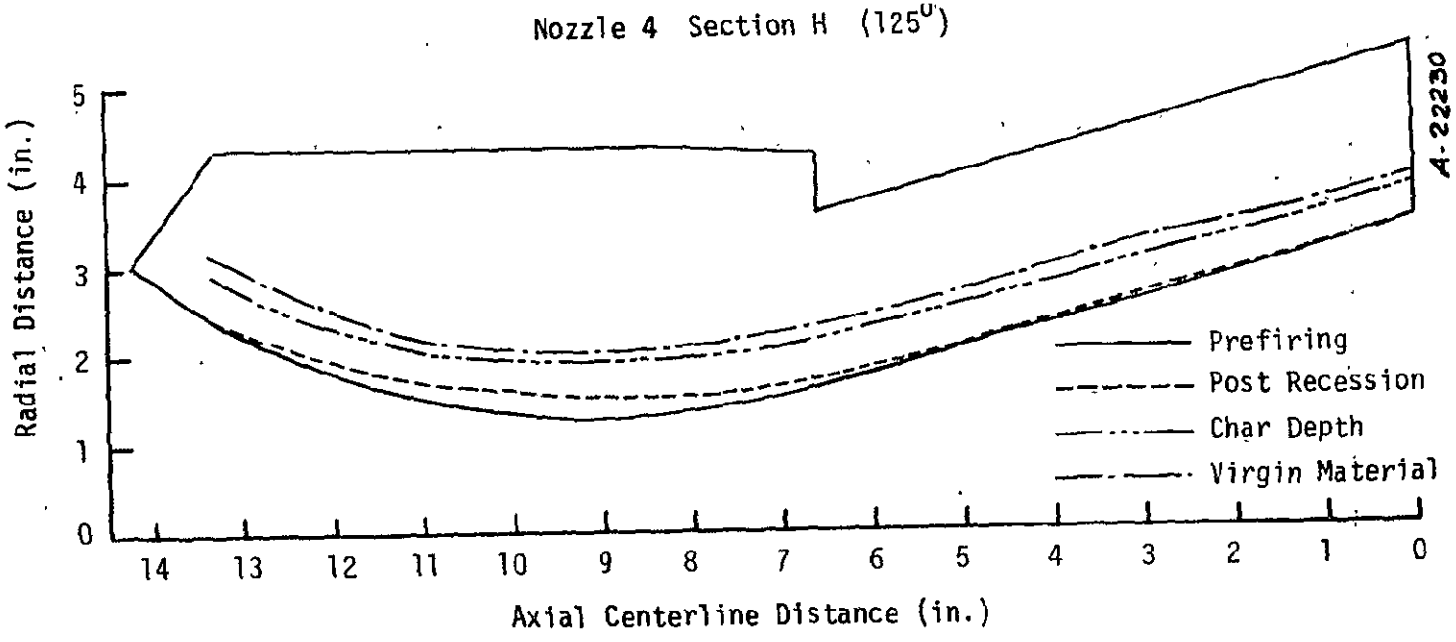
Nozzle 4 Section H (125°)
Radial Distance (in.)
5
4
3
2
1
0
14
13
12
11
10
9
8
7
6
5
4
3
2
1
0
Axial Centerline Distance (in.)
Prefiring
Post Recession
Char Depth
Virgin Material
A-22230

the virgin material depth, thus providing a measurement of the pyrolysis layer thickness. The pyrolysis layer thickness indicates the amount of virgin material available for the remainder of an SRM firing in the event the char layer is lost.

Figures 2-5 through 2-8 present each nozzle's throat recession profile plotted on polar graphs. These profiles are plotted at the throat center station of 9.00 inches.

2.2 7-INCH CHAR MOTOR NOZZLE

2.2.1 Design and Fabrication

The design of the 7-inch CHAR motor nozzle was the responsibility of Acurex. Because of cost and previous experience with the fabrication of large nozzles, HITCO Corporation was selected to fabricate the 7-inch CHAR motor nozzle. The design was provided to HITCO by Acurex personnel who followed the fabrication closely and provided consultation for solving problems encountered during fabrication.

The 7-inch nozzle assembly is shown schematically in Figure 2-9. This nozzle was a submerged configuration of the following components and materials:

1. Forward ring: pitch fabric (FM 5788)
2. Throat ring: pitch fabric (FM 5788) and rayon fabric (HITCO CCA-3)
3. Exit cone: staple rayon fabric (HITCO CCA-28)
4. Submerged section insulator: stable rayon fabric (HITCO CCA-28) over silica cloth phenolic (FM 5504)

The fabric orientation with respect to the nozzle centerline for each section is designated in the figure.

There was concern whether the areas of the exit cone forward station adjacent to the throat ring and at the aft end of the exit cone

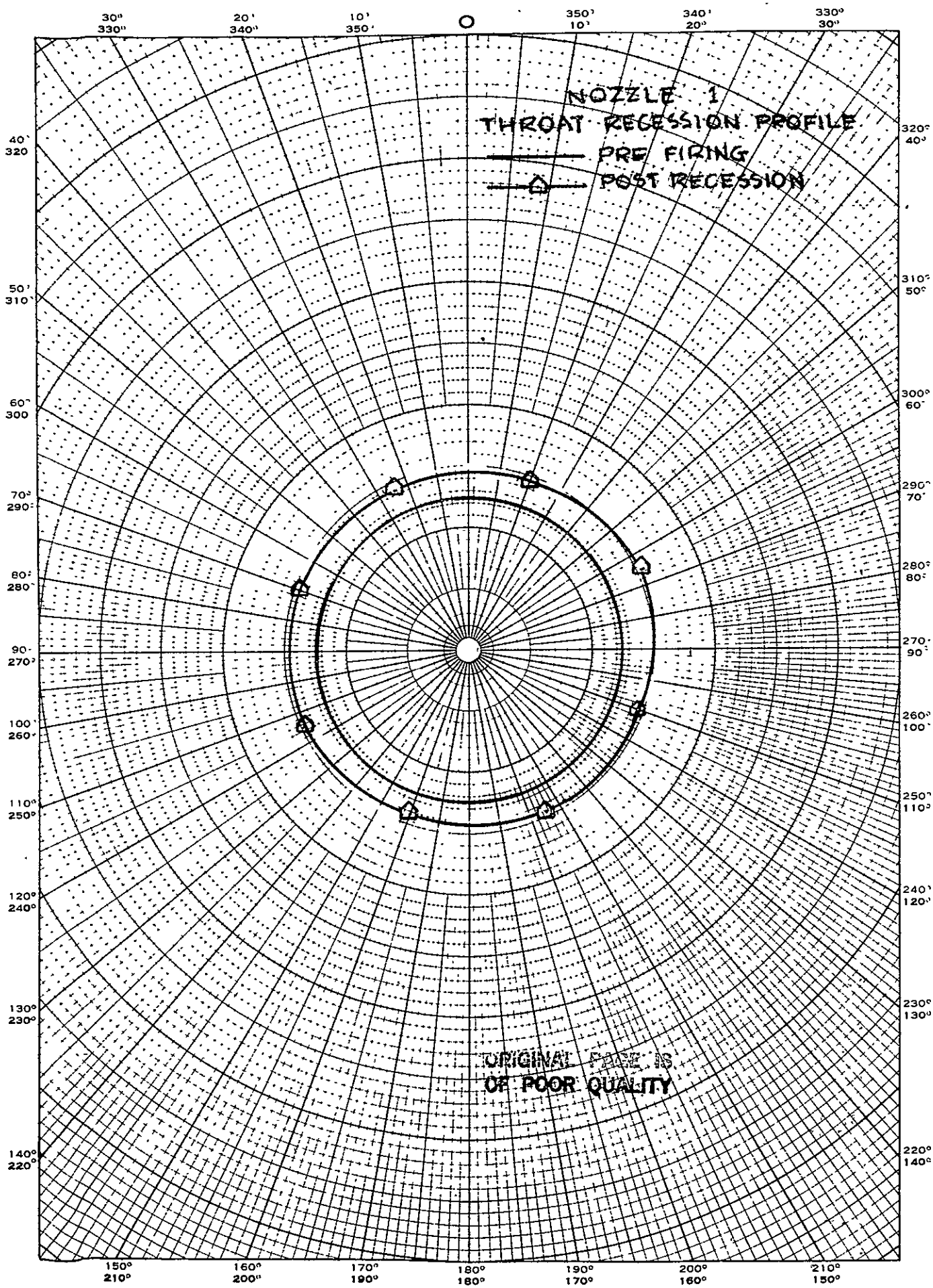

Figure 2-5. Nozzle 1 throat recession profile.

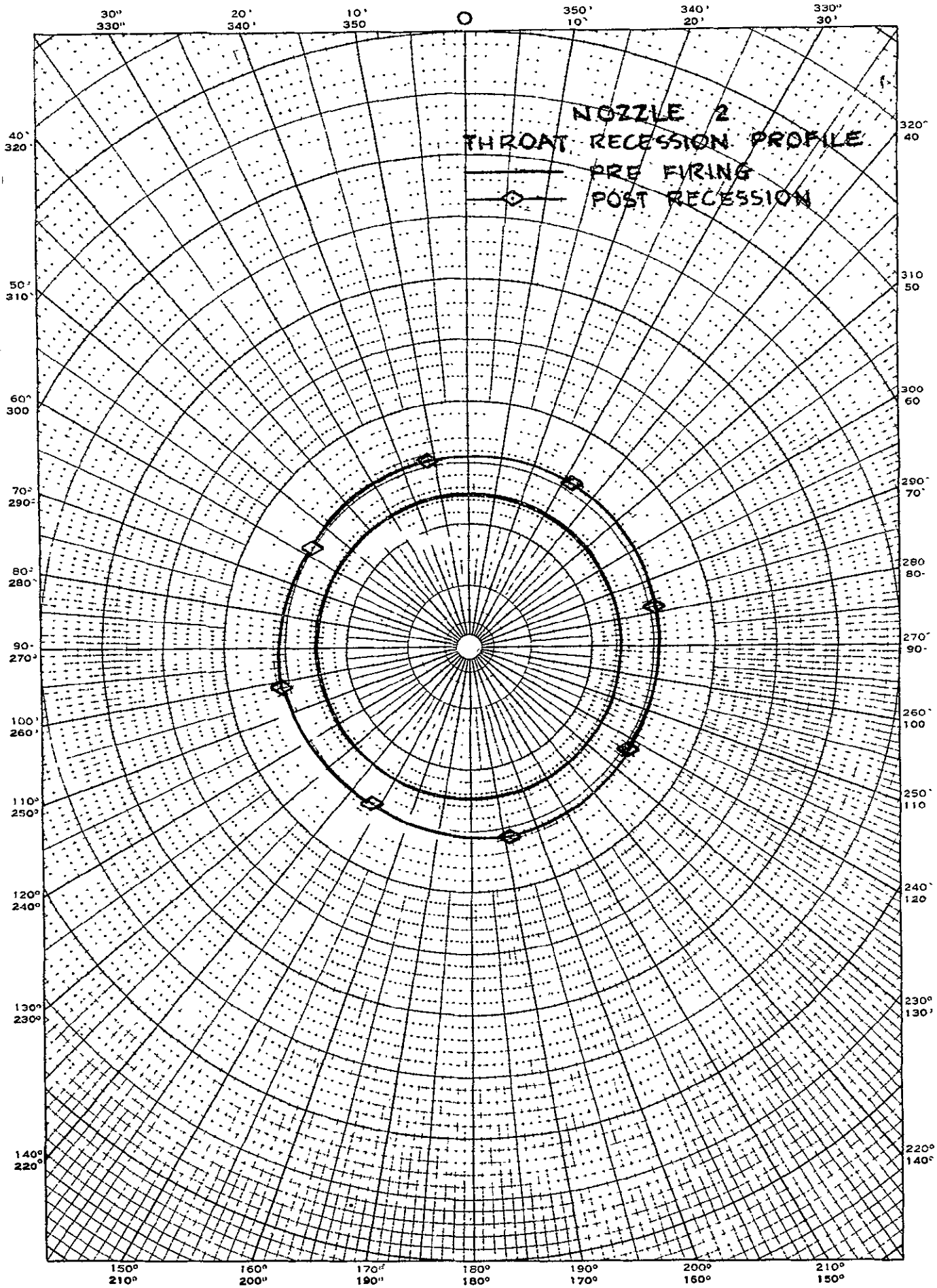

Figure 2-6. Nozzle 2 throat recession profile.

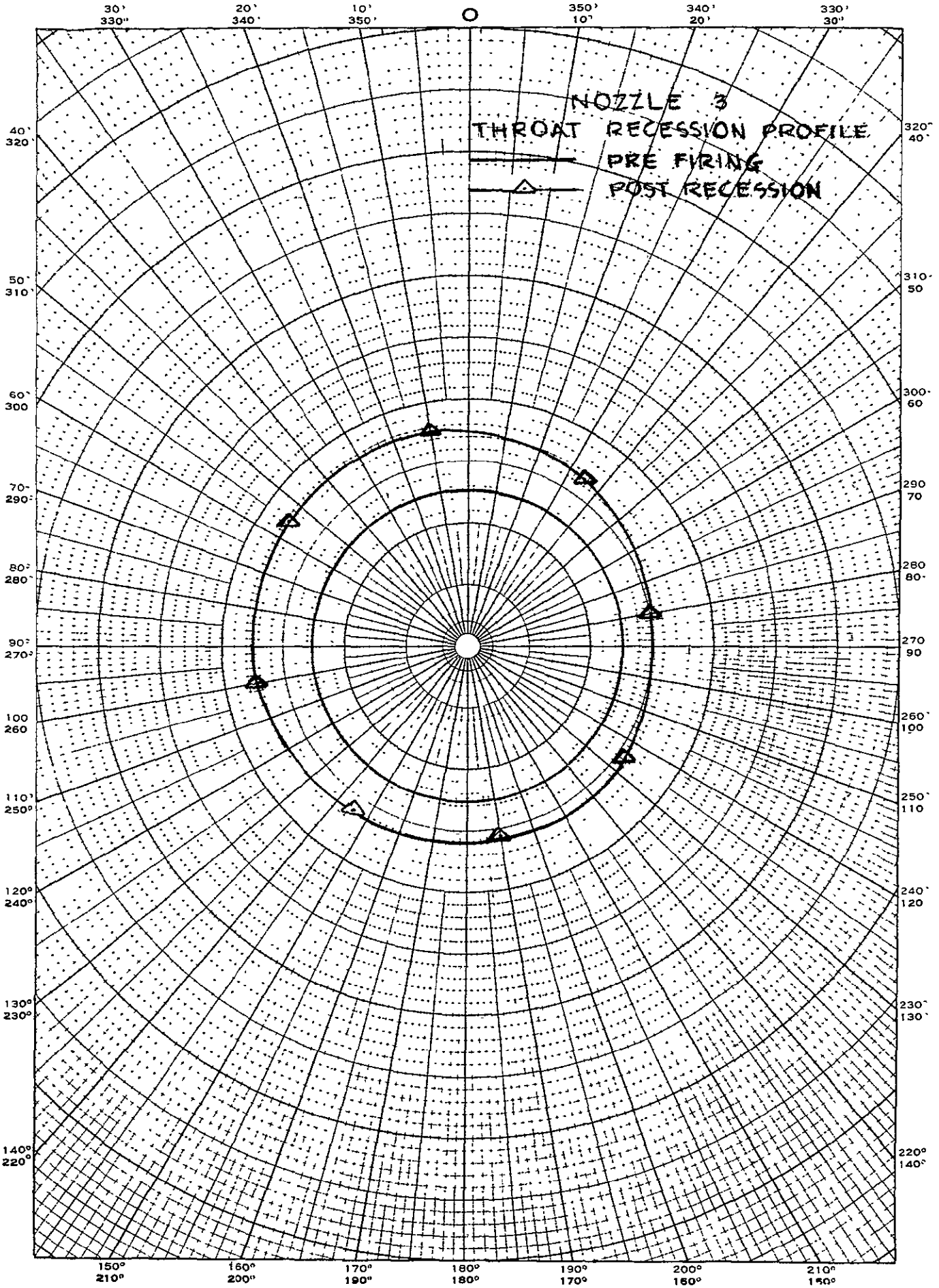

Figure 2-7. Nozzle 3 throat recession profile.

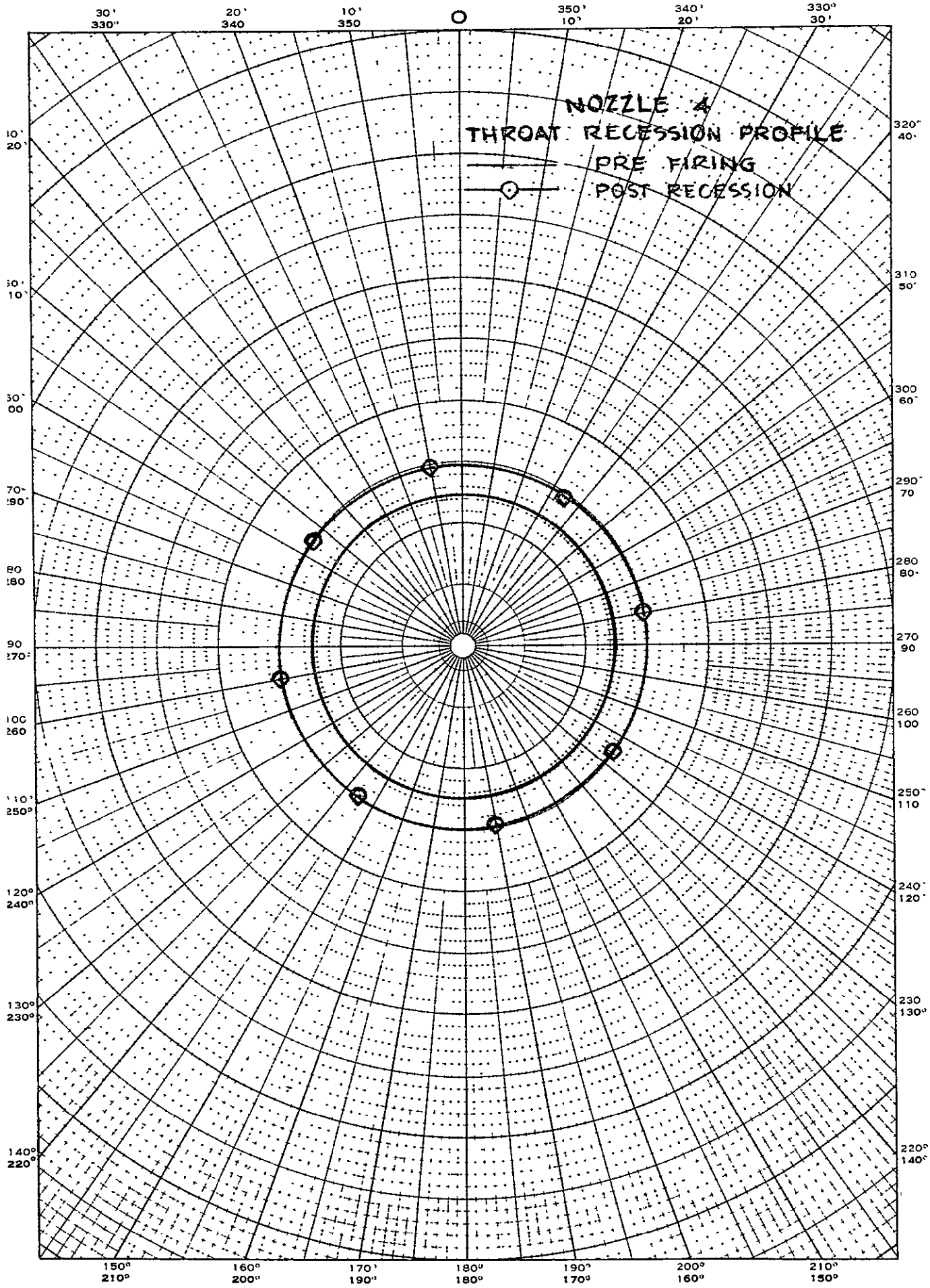

Figure 2-8. Nozzle 4 throat recession profile.

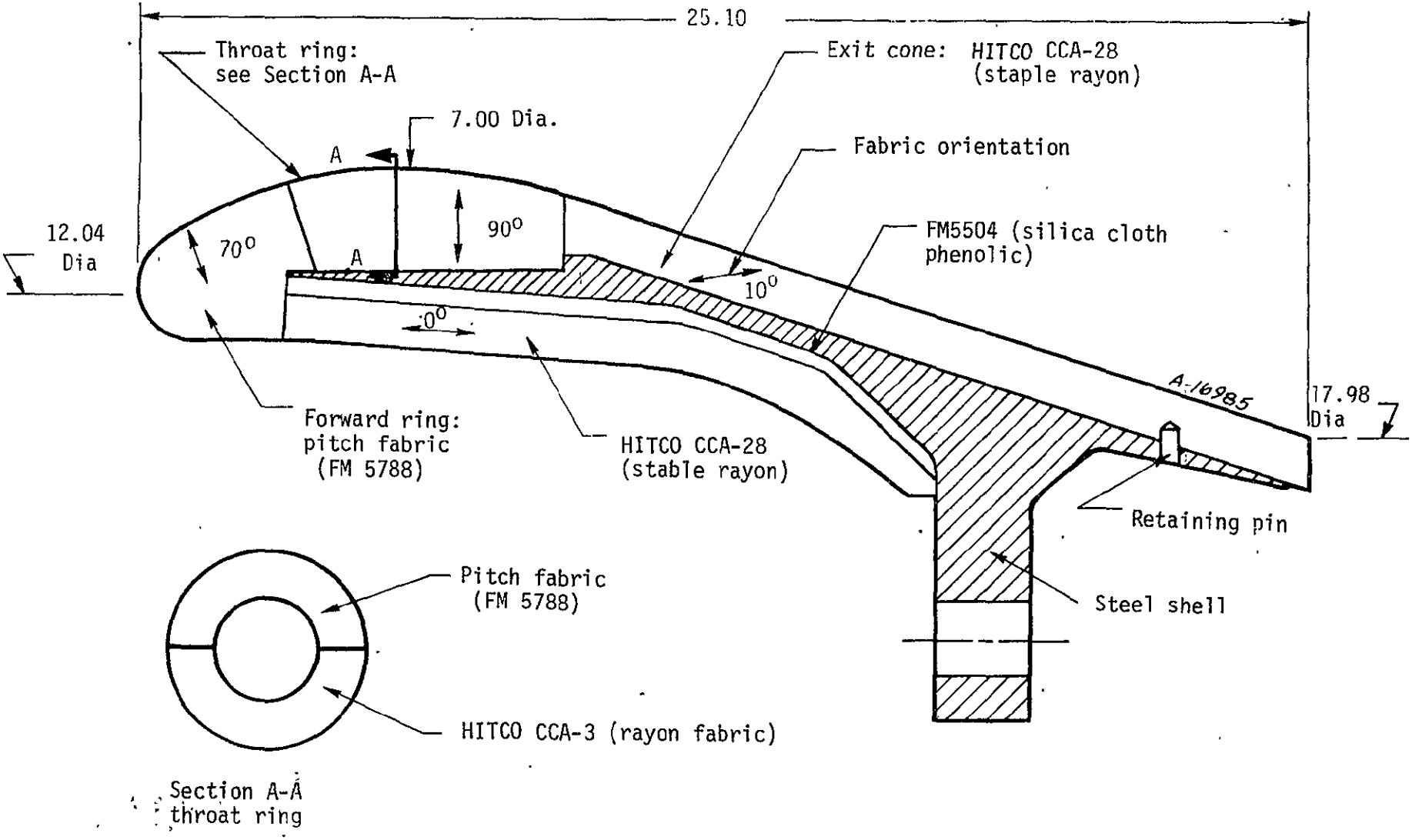

Figure 2-9. Schematic of 7-inch throat diameter CHAR motor nozzle.

were of adequate thickness to prevent debonding from the steel shell due to heat conduction during firing. Therefore, an analysis was conducted to determine the design thickness required for thermal protection.

The analysis was performed to evaluate the thermal adequacy of an existing preliminary design for the 7-inch CHAR motor test nozzle. Thermal performance predictions were made only at two stations representative of those locations with minimum liner thickness. The first station is just aft of the throat, and the second station is in the exit cone near the exit plane as shown in Figure 2-10. The analysis followed the procedures outlined in Reference 2.

The composition of the Shuttle solid propellant was obtained from Reference 3. Table 2-11 summarizes these data and includes an evaluation of the enthalpy of the propellant.

Since the propellant composition was not available in elemental mass fractions (or mole fractions), it had to be determined from the composition of the constituents. The first step was to determine the mass fraction of each element in each constituent as shown in Table 2-12. The elemental composition of the propellant was obtained by summing the product of the mass fraction of each constituent and the mass fraction of each element in the constituent. The resultant elemental composition of the propellant is presented in Table 2-13. The trace amount of iron was neglected in subsequent analyses.

Definition of the properties of the propellant exhaust throughout the nozzle are necessary to evaluate the boundary conditions and surface thermochemistry at the locations of interest. This definition is obtained with ACE (Reference 4) by performing an isentropic expansion from an

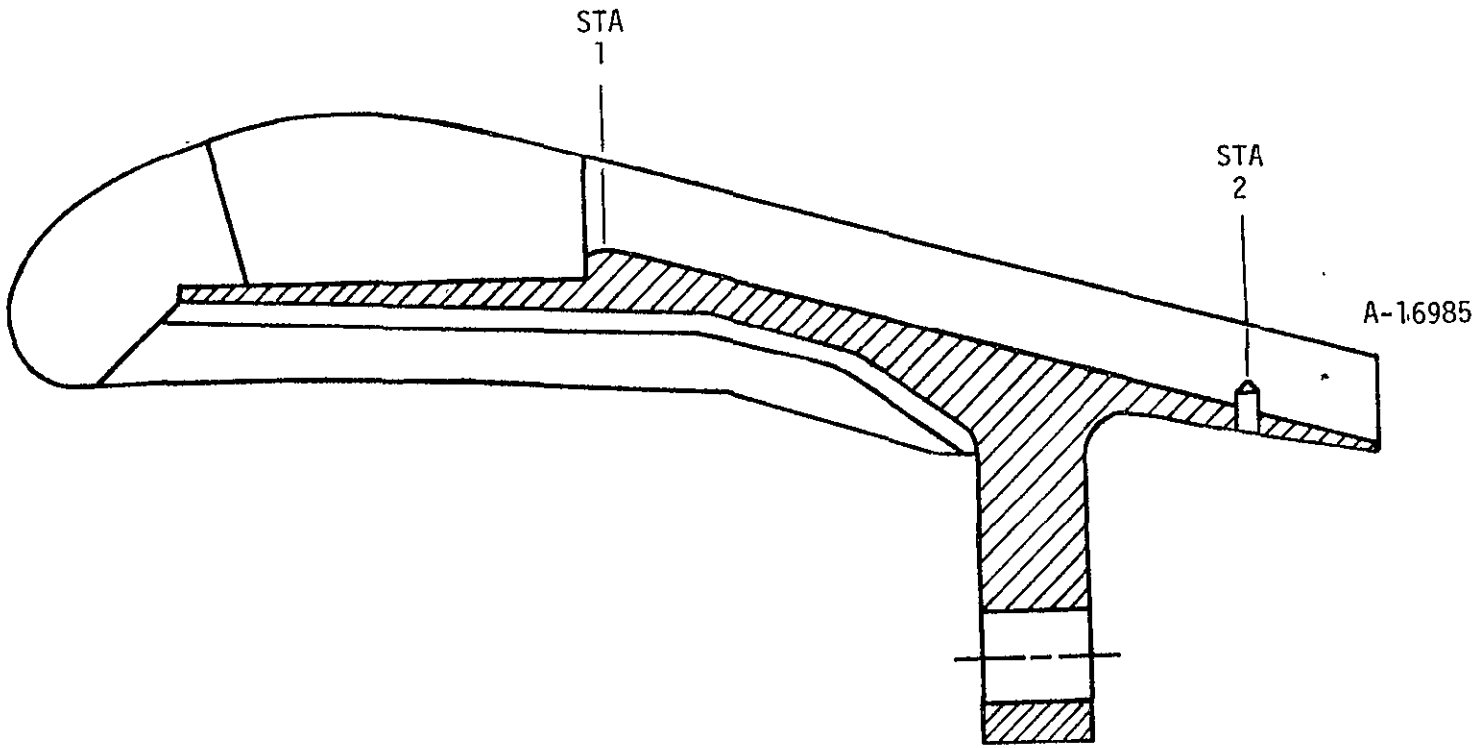

Figure 2-10. Stations for CHAR motor analysis.

TABLE 2-11. PROPELLANT CONSTITUENTS AND PROPERTIES

Constituent	Formula	MW_i	ρ_i	H_{fi}	K_i	$K_i H_{fi}/MW_i$
		gm/mole	gm/cc	Kcal/mole	gms_i/gms_{total}	cal/gm
Ammonium Perchlorate	$NH_4Cl O_4$	117.496	1.95	- 70.69	0.6999	-421.086
Ferric Oxide	Fe_2O_3	159.700	5.12	-184.182	0.0001	- 0.115
Aluminum	Al	26.97	2.699	0.00	0.1600	0.000
PBAN Binder	$C_{6.884}H_{10.089}O_{0.278}N_{0.264}$	100.0[a]	0.93	- 12.000	0.1204	14.448
Epoxy Curing Agent	$C_{6.15}H_{6.97}O_{1.17}N_{0.03}$	100.0[a]	1.129	- 28.300	0.0196	- 5.547
Totals					1.0	-441.196

[a]Effective

AS-T-0006

$$H_{fuel} = \sum_i K_i H_{fi}/MW_i = -441.20 \text{ cal/gm} = -794.15 \text{ Btu/lbm}$$

TABLE 2-12. CONSTITUENT ELEMENTAL COMPOSITION

Constituent	K_i	Element	Stoichiometric Coefficient, ν_{ji}	MW_i	$\nu_{ji}\ MW_i$	$\nu_{ji}\ MW_i/\Sigma$	$K_i(\nu_{ji}\ MW_i/\Sigma)$
			(moles/mole$_{total}$)	(gm/mole)	(gm/mole)	(gm/gm^{total})	(gm/gm$_{total}$)
Ammonium Perchlorate	0.6999	N	1.0	14.007	14.007	0.11921	0.08343
		H	4.0	1.008	4.032	0.03432	0.02402
		Cl	1.0	35.457	35.457	0.30177	0.21121
		O	4.0	16.000	64.000	0.54470	0.38123
					Σ = 117.496	1.00000	0.69989
Ferric Oxide	0.0001	Fe	2.0	55.850	111.70	0.69943	0.0000699
		O	3.0	16.000	48.00	0.30056	0.0000300
					Σ = 159.70	0.99999	0.0000999
Aluminum	0.1600	Al	1.0	26.97	26.97	1.00	0.1600
PBAN Binder	0.1204	C	6.884	12.011	82.6837	0.81865	0.09856
		H	10.089	1.008	10.1697	0.10069	0.01212
		O	0.278	16.000	4.4480	0.04404	0.00530
		N	0.264	14.007	3.6978	0.03661	0.00441
					Σ = 100.9992	0.99999	0.12039
Epoxy Curing Agent	0.0196	C	6.15	12.011	73.8676	0.73842	0.01447
		H	6.97	1.008	7.0258	0.07023	0.00138
		O	1.17	16.000	18.7200	0.18714	0.00367
		N	0.03	14.007	0.4202	0.00420	0.00008
					Σ = 100.0336	0.99999	0.01960

AS-T-0005

TABLE 2-13. PROPELLANT ELEMENTAL COMPOSITION

Element	Symbol	MW_j	$\tilde{K}_j$
Hydrogen	H	1.008	0.03752
Carbon	C	12.001	0.11303
Nitrogen	N	14.007	0.08792
Oxygen	O	16.000	0.39023
Aluminum	Aℓ	26.970	0.16000
Chlorine	Cℓ	35.457	0.21121
Iron	Fe	55.850	0.00007
			$\sum_j$ = 0.99998

where $\tilde{K}_j = \sum_j \nu_{ji} MW_i K_i / \sum_i$

average chamber condition. The average chamber conditions were obtained from Reference 3 and are shown in Table 2-14. The freestream properties of the propellant exhaust (pressure, temperature, enthalpy, and velocity) are illustrated in Figure 2-11 as a function of the local-to-throat area ratio. The locations of interest are downstream of the throat and correspond to radii of 4.2 inches and 8.27 inches, respectively. The local freestream conditions at these stations are summarized in Table 2-15.

Thermal performance predictions require a detailed definition of the thermochemical properties of the propellant exhaust and the ablating surface for the conditions existing at the stations of interest. The local gas properties were obtained from ACE by performing calculations for the local gas composition in the temperature range from the boundary layer edge to the nozzle surface. The surface thermochemistry tables were obtained by performing open system ACE calculations (assuming unequal diffusion coefficients) which evaluate surface temperature and enthalpy as a function of nondimensional char and pyrolysis gas injection rates, B'_c and B'_g.

The ACE expansion calculations indicate a significant amount of condensed phase Al_2O_3 in the propellant exhaust (typical of aluminized propellants). Under certain conditions, thermochemical equilibrium would predict Al_2O_3 condensing on the ablating surface, a phenomenon which has not been physically observed. To preclude this possibility, the elemental composition of the edge gases was modified by reducing the mass fraction of aluminum and oxygen by the amount of each element in the condensed phase prior to computing the surface thermochemistry. The modified composition was calculated by the following procedure.

TABLE 2-14. AVERAGE CHAMBER CONDITIONS

Symbol	Definition	Value
P_c	Average chamber pressure	650 psia
T_c	Propellant flame temperature	5858°F

TABLE 2-15. LOCAL FREESTREAM CONDITIONS

Station	R (in)	A/A*	P_e (atm)	T_e (°R)	H_e (Btu/lbm)	U_e (ft/sec)	$\frac{\text{Mass } Al_2O_3}{\text{Mass}_{gas}}$
1	4.2	1.44	9.70	5372.	-1270.6	5578.	0.41874
2	8.27	5.58	1.35	4190.	-1917.5	7968.	0.43269

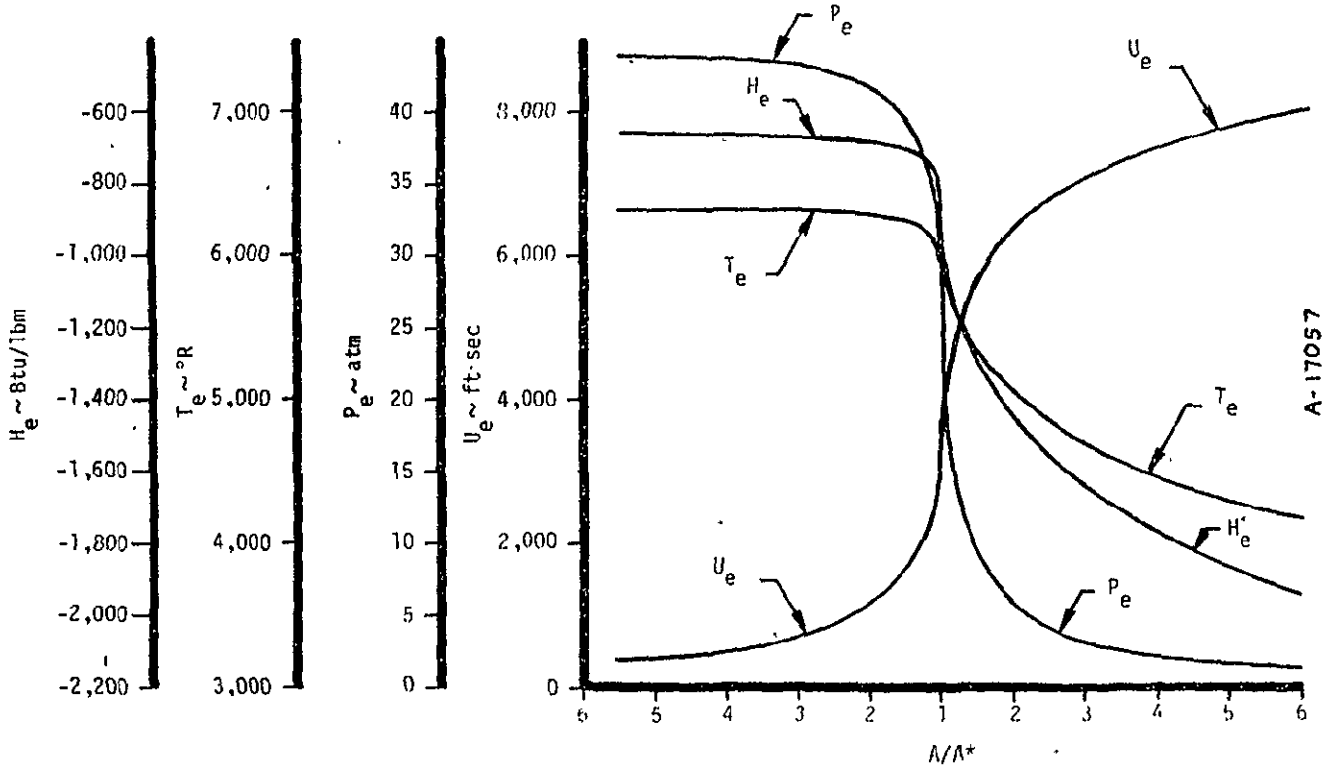

Figure 2-11. Propellant freestream properties.

Let $$x = \frac{\text{Mass}_{Al_2O_3}}{\text{Mass}_{gas}}$$

then $1 + x$ = total mass of propellant exhaust (gas + condensed)

and $$\frac{x}{x+1} = \frac{\text{Mass}_{Al_2O_3}}{\text{Mass}_{total}}$$

The mass fraction of each element in the condensed phase was obtained by multiplying this ratio by the mass fraction of the particular element in Al_2O_3:

$$\text{Mass}_{Al\ \text{condensed phase}} = \left(\frac{x}{x+1}\right)\left[\frac{2 * AW_{Al}}{MW_{Al_2O_3}}\right]$$

$$\text{Mass}_{O\ \text{condensed phase}} = \left(\frac{x}{x+1}\right)\left[\frac{3 * AW_{O}}{MW_{Al_2O_3}}\right]$$

These mass fractions were subtracted from the original composition given in Table 2-13. The results at the two locations under consideration are shown in Table 2-16.

The surface thermochemical tables were calculated by ACE, utilizing the elemental compositions of the edge gas given in Table 2-16 and the elemental composition of the pyrolysis gas and char phases commonly used for MX4926 carbon phenolic, as given in Table 2-17. The predicted B' maps for the two locations under consideration are illustrated in Figures 2-12 and 2-13.

TABLE 2-16. GAS PHASE ELEMENTAL COMPOSITION

Element	Mass Fraction Station 1	Mass Fraction Station 2
H	0.03752	0.03752
C	0.11303	0.11303
N	0.08792	0.08792
O	0.25125	0.24802
A	0.00382	0.000194
C	0.21121	0.21121

TABLE 2-17. MX4926 ELEMENTAL COMPOSITION (BY MASS)

Element	Pyrolysis Gas	Char
H	0.10710	0.0
C	0.60957	1.0
O	0.28333	0.0

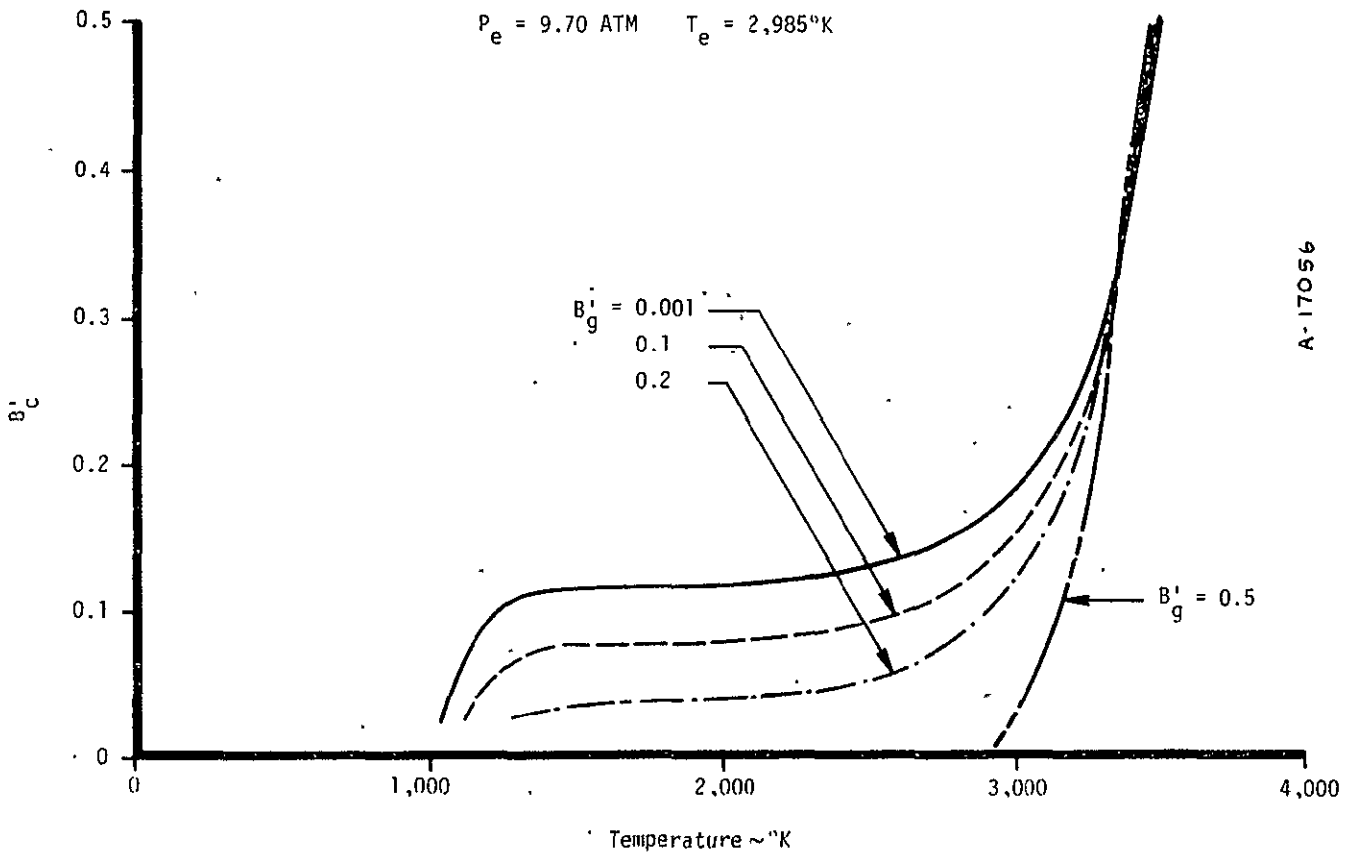

Figure 2-12. Nondimensional mass loss for MX4926 at Station 1.

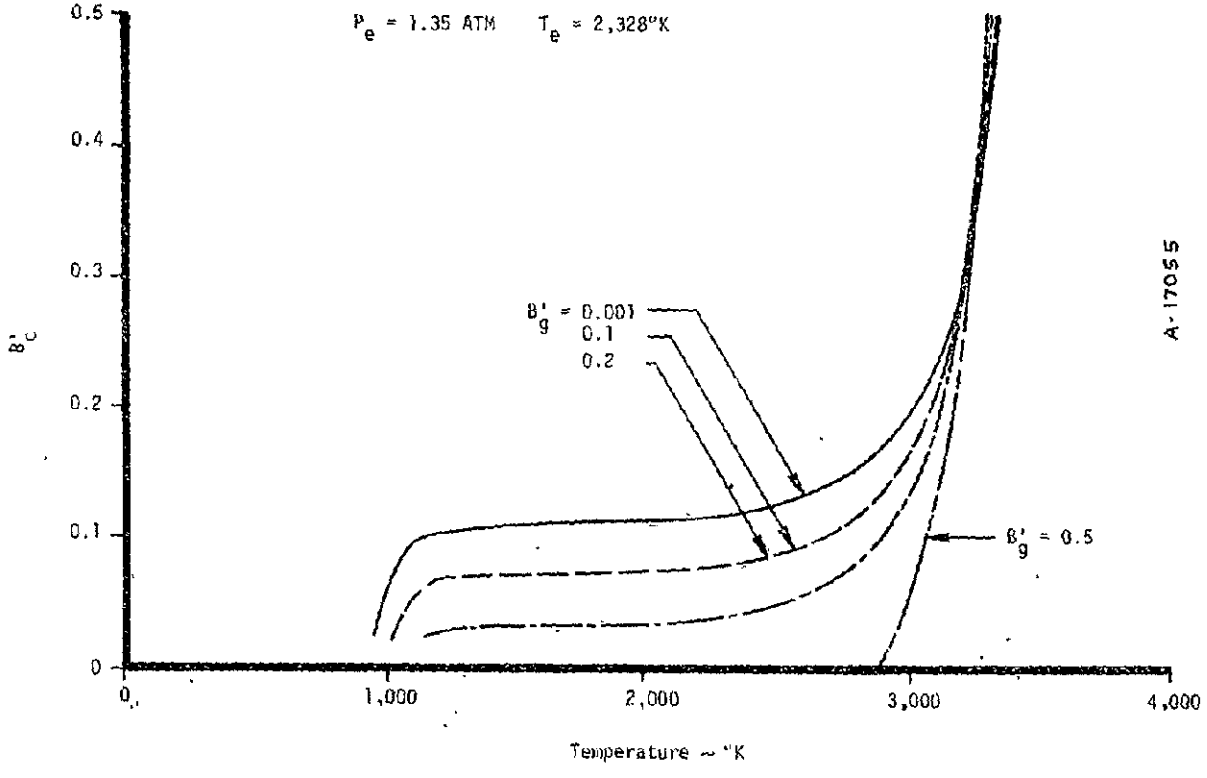

Figure 2-13. Nondimensional mass loss for MX4926 at Station 2.

Heat transfer coefficients throughout the nozzle were calculated with the ARGEIBL energy integral code (Reference 5). The ARGEIBL procedure requires input of Mollier data representative of the propellant composition and the pressure and temperature ranges throughout the nozzle. These Mollier data were generated with ACE, assuming that an average propellant composition throughout the nozzle can be represented by the composition at throat conditions with all Al_2O_3 removed. Some sensitivity of the heat transfer coefficient to surface temperature required an accurate estimate of the surface temperature (actually wall enthalpy) during the firing. It was assumed that the quasi-steady surface temperature at Station 1 is 4,900°R, and at Station 2 is 4,050°R. There is some difference in the wall enthalpy at these respective temperatures, dependent upon whether one takes the enthalpy as that of the equilibrium composition near the wall or that of the equilibrium composition of the freestream evaluated at the wall temperature (frozen). This small effect on transfer coefficient is shown in Figure 2-14 which illustrates the variation of heat transfer coefficient throughout the nozzle.

Transfer coefficients were also estimated using the Bartz equation (Reference 6) at the two locations. The Bartz equation can be written as:

$$\rho_e u_e C_H = \frac{0.026}{D^{*0.2}} \left(\frac{\mu^{0.2} C_p}{Pr^{0.6}} \right)_o (\rho_e u_e)^{0.8} \sigma \left(\frac{D^*}{r_c} \right)^{0.1} \qquad (2\text{-}1)$$

where

$$\sigma = \left(\frac{\rho_{am}}{\rho_e} \right)^{0.8} \left(\frac{\mu_{am}}{\mu_o} \right)^{0.2} \qquad (2\text{-}2)$$

The Bartz results, as well as the ARGEIBL results, must be reduced 25 percent to be consistent with experimental data. A comparison of the Bartz and ARGEIBL heat transfer coefficients at the two stations under analysis is given in Table 2-18. The agreement is quite good. The other

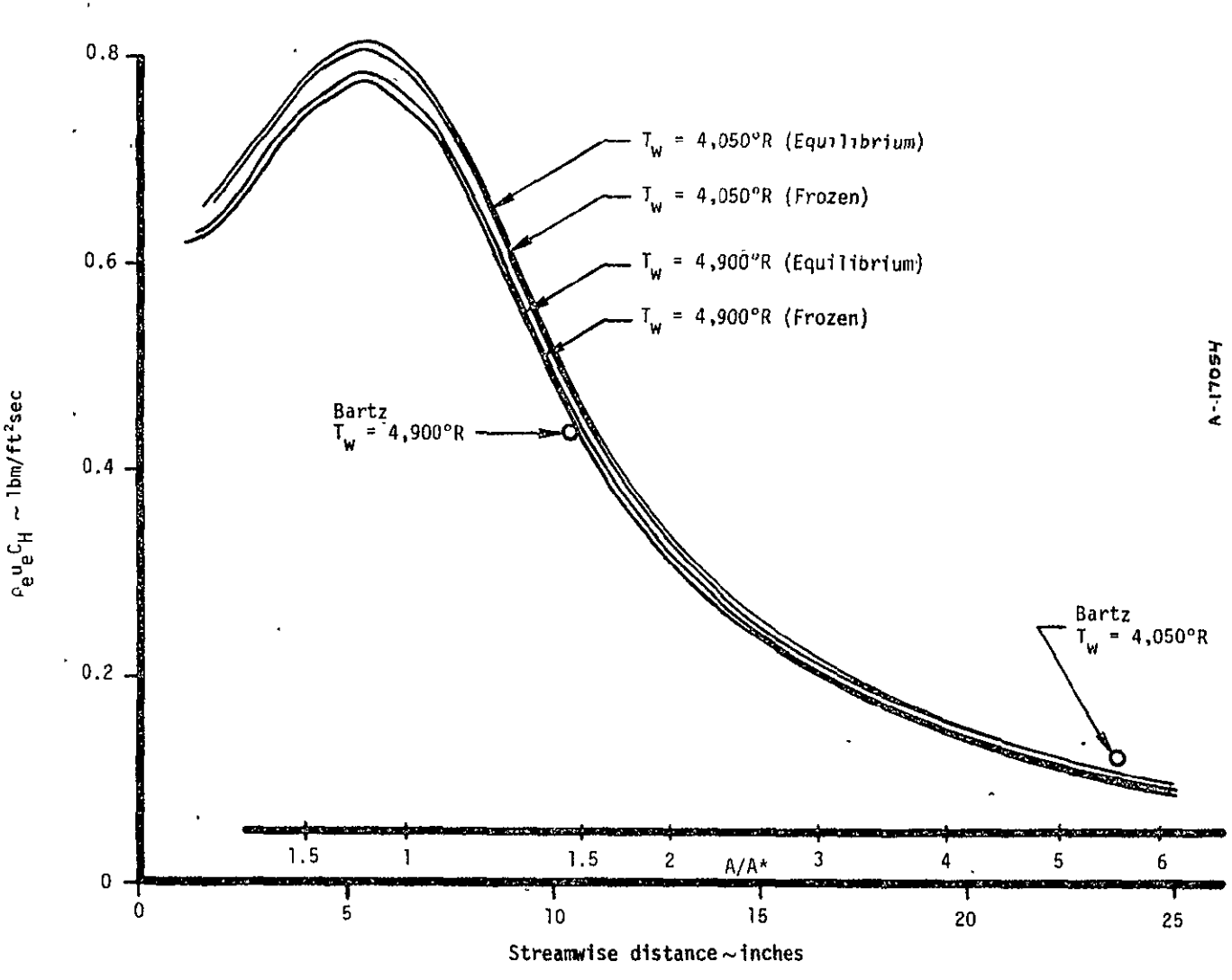

Figure 2-14. Heat transfer coefficient.

quantities in Table 2-18 are the remaining values required to completely specify the surface boundary conditions as discussed below.

TABLE 2-18. SURFACE BOUNDARY CONDITIONS

Station	T_e (^oR)	Assumed T_w (^oR)	H_R (Btu/lbm)	ϵ_{eff}	$\dot{q}_{RAD}$ (Btu/ft^2 sec)	C_M/C_H	$\rho_e u_e C_{H_{ARGEIBL}}$ (lbm/ft^{2}sec)	$\rho_e u_e C_{H_{BARTZ}}$ (lbm/ft^2 sec)
1	5372	4900	808.62	0.382	396.28	0.73976	0.4443	0.4374
2	4190	4050	612.98	0.158	146.69	0.74660	0.1060	0.1228

AS-T-0007

The local recovery enthalpy is calculated from known stream properties, assuming a turbulent boundary layer, by:

$$H_R = H_e + (Pr)^{1/3} \frac{u_e^2}{2gJ} \qquad (2\text{-}3)$$

It is worth noting that the Prandtl number of the particle-free stream is higher than that of the particle-laden stream. This is due to the fact that aluminum and its compounds have a low value of heat capacity, and removing them from the propellant exhaust stream results in an increase in the specific heat of the remaining gas. Since the local static enthalpy used in Equation 2-3 is for a particle-free stream, it is consistent to evaluate the Prandtl number for the identical stream composition.

The char emissivity used for the analysis must be modified since the exhaust gas is partially transparent, allowing the nozzle liner surface to view radiation from other areas of the nozzle. An effective emissivity is calculated assuming the parallel plate analogy for radiant heat transfer:

$$\varepsilon_{eff} = \frac{1}{1/\varepsilon_{stream} + 1/\varepsilon_{char} - 1} \qquad (2\text{-}4)$$

where ε_{stream} is the emissivity of the actual particle-laden stream and ε_{char} is the emissivity of the charred liner surface. For MX4926 carbon phenolic, the char emissivity was taken as 0.85. The emissivity of the stream is calculated from:

$$\varepsilon_{stream} = 1 - EXP\left(\frac{-0.808\rho Dn}{16}\right) \qquad (2\text{-}5)$$

where ρ is the density of the particle-laden stream (gas and condensed) in units of lbm/ft^3, D is the local nozzle diameter in inches, and n is the percent by mass of aluminum in the actual propellant (16 percent for this analysis).

The black body radiant heat flux is simply given by:

$$\dot{q}_{RAD} = \sigma T_e^4 \qquad (2\text{-}6)$$

where σ is the Stefan-Boltzmann constant, and T_e is the local stream temperature.

The ratio of the Stanton numbers for mass and heat transfer is calculated for nonunity Lewis number (typical of unequal diffusion problems) by:

$$C_M/C_H = L_e^{2/3} \qquad (2\text{-}7)$$

where the Lewis number is the ratio of the Prandtl to Schmidt numbers. As discussed previously, the Prandtl and Schmidt numbers are evaluated for the particle-free stream for consistency.

Thermal analysis of the ablative liner at the two locations of interest was performed using properties of MX4926 for the carbon phenolic. These properties are summarized in Tables 2-19 and 2-20. The preliminary design employs a 0^o layup, and the thermal conductivity given in Table 2-20 is consistent with that design. All thermal performance predictions were made with the CMA code (Reference 7).

Thermal response predictions were made for a 60 second firing time (Reference 3). The results (time histories of surface temperature, char erosion, recession rate, char thickness, and char penetration depth) for the two stations under consideration are shown in Figures 2-15 and 2-16, respectively. More recent information defined the actual firing time as 50 seconds.

The safety factor criterion normally employed in rocket nozzle design requires:

$$\delta_i \geq 2\delta_e + 1.25\ \delta_c = \delta_{sf} \qquad (2\text{-}8)$$

TABLE 2-19. MX4926 CHEMICAL PROPERTIES

Symbol	Units	Value
Virgin	Lb virgin/ft^3 virgin	91.30
Char	Lb char/ft^3 char	73.22
Effective resin molecule	-	C_6H_6O
Effective reinforcement molecule	-	C*
$\rho A1$	Lb initial A/ft^3 resin	60.75
$\rho A2$	Lb final A/ft^3 resin	32.40
$\rho B1$	Lb initial B/ft^3 resin	20.25
$\rho B2$	Lb final B/ft^3 resin	0.0
$\rho C1$	Lb initial C/ft^3 reinforcement	97.40
$\rho C2$	Lb final C/ft^3 reinforcement	97.40
K_r	Lb resin/lb virgin	0.330
	ft^3 resin/ft^3 virgin	0.372
k_A	sec^{-1}	4.48×10^9
k_B	sec^{-1}	1.40×10^4
k_C	sec^{-1}	0.0
$-E_A/R$	^oR	3.68×10^4
$-E_B/R$	^oR	1.54×10^4
$-E_C/R$	^oR	0.0
n_A	-	3.0
n_B	-	3.0
n_C	-	0.0
ΔHf_v	Btu/lb virgin	-363.0
ΔHf_c	Btu/lb char	0.0

TABLE 2-20. MX4926 THERMOPHYSICAL PROPERTIES

Temperature (^{O}R)	Virgin Material		Char		Pyro Gas
	C_{p_v} (Btu/lbm-^{O}R)	$k_v \times 10^4$ (Btu/ft-sec-^{O}R)	C_{p_c} (Btu/lbm-^{O}R)	$k_c \times 10^4$ (Btu/ft-sec-^{O}R)	H_g (Btu/lbm)
500	0.210	1.39	0.210	1.83	----
800	0.360	1.58	---	---	----
1,000	---	---	0.430	1.90	-1,687
1,160	0.360	1.83	---	---	-1,536
1,500	0.472	1.83	0.472	1.95	-1,214
2,000	0.484	1.83	0.484	2.35	- 690
3,000	0.493	1.83	0.493	5.40	833
4,000	0.498	1.83	0.498	11.65	2,809
5,000	0.500	1.83	0.500	18.80	4,175
6,000	0.500	1.83	0.500	26.50	5,620

AS-T-0008

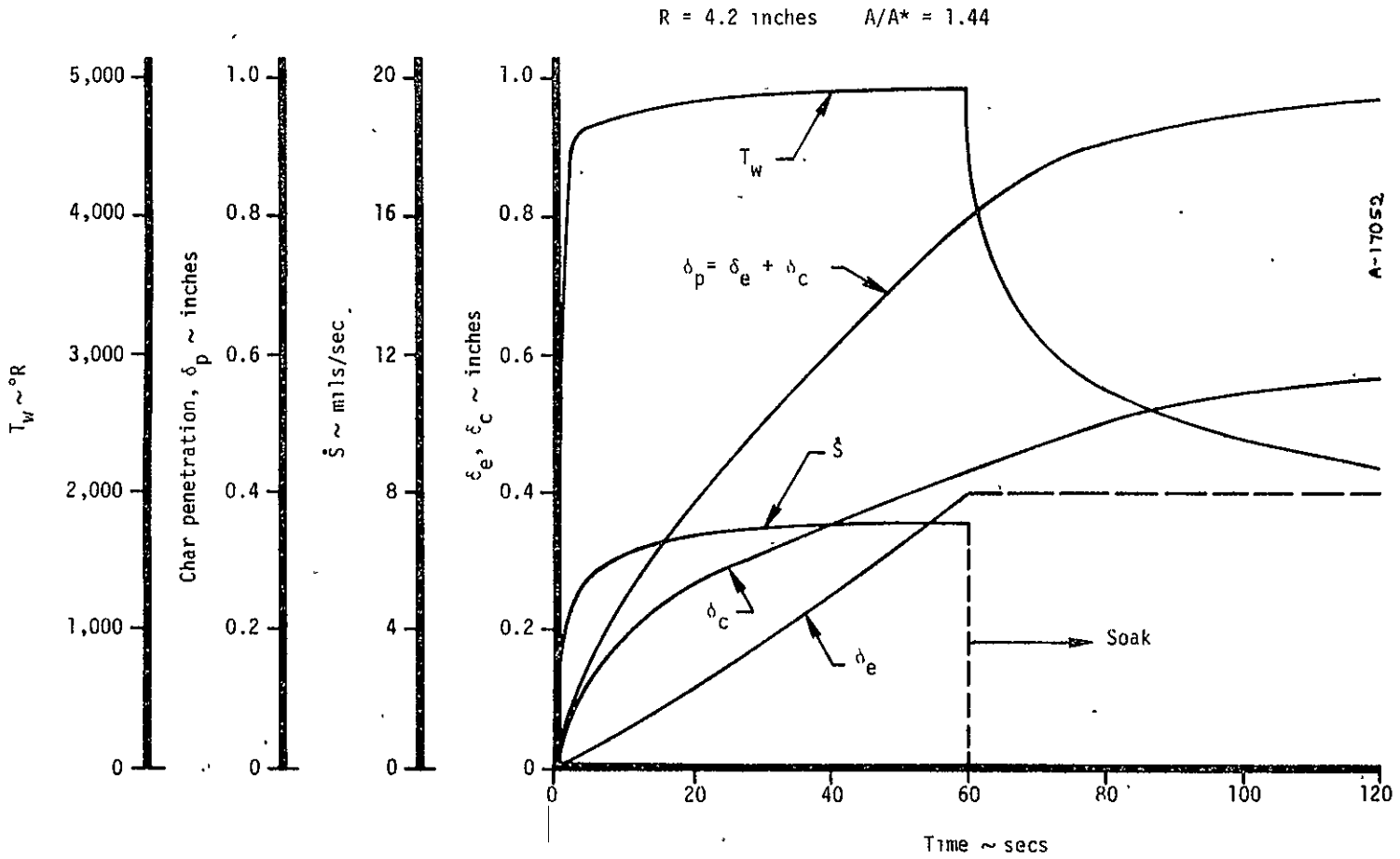

Figure 2-15. Carbon phenolic thermal performance at Station 1.

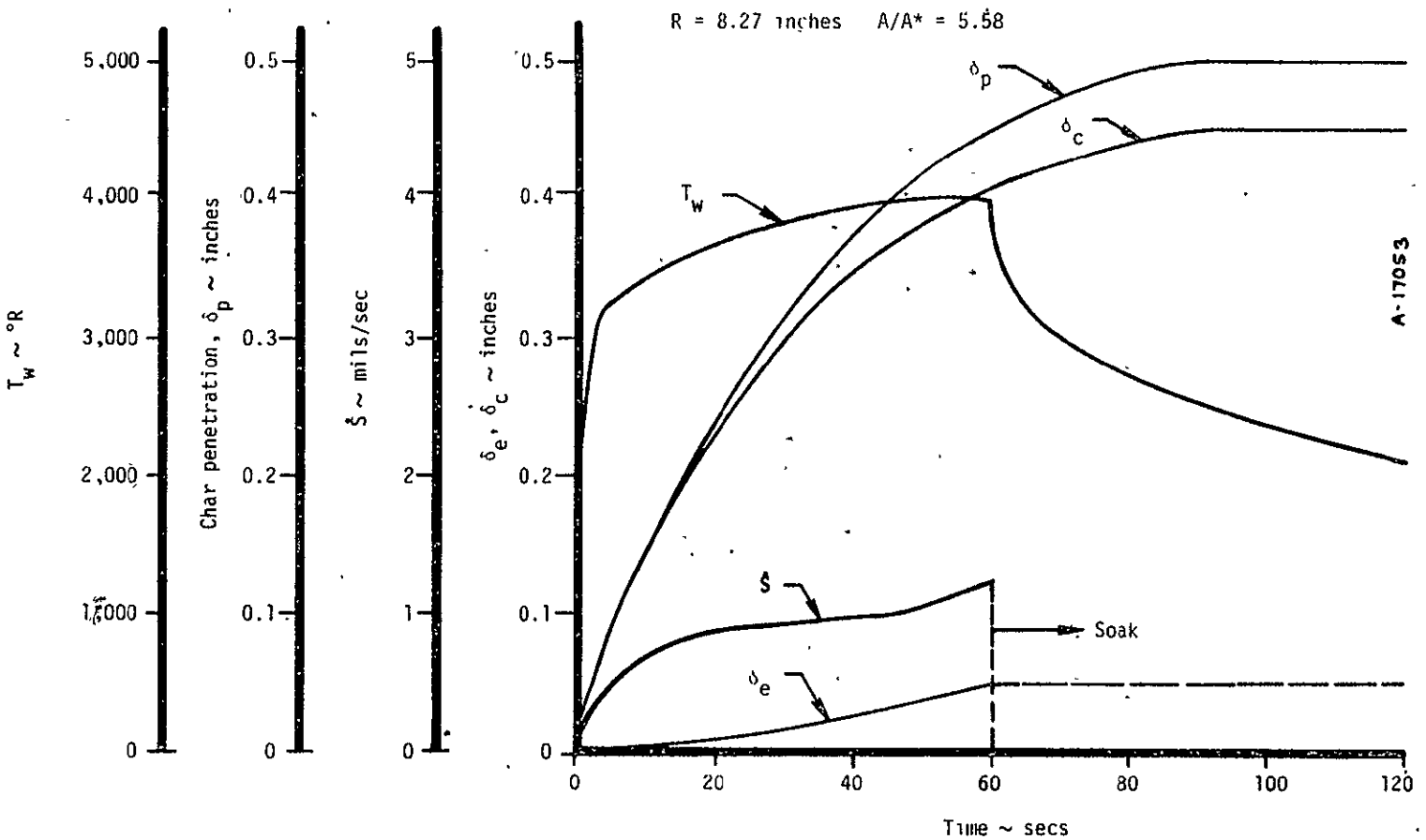

Figure 2-16. Carbon phenolic thermal performance at Station 2.

where δ_e is the amount of erosion at the end of the firing, δ_c is the char thickness at the end of the firing, and δ_i is the initial design thickness of the liner at the particular location. Table 2-21 summarizes the results for a 50-second firing which was the total firing time predicted for the CHAR motor propellant. It is seen that the liner thickness for the preliminary design does not meet the safety factor criteria, and additional liner thickness is required. This additional thickness was incorporated in the final design.

Table 2-21 also shows the depth of penetration of the char front, δ_p, the depth at which resin decomposition is just beginning. For phenolic resins, incipient charring occurs at approximately $900^{\circ}R$. Thus, it is obvious that, even if the char front had penetrated to the steel structure, the integrity of the structure would not be threatened. The difference between δ_p and δ_{sf} illustrates the conservatism of the safety factor criterion. This is graphically illustrated in Figure 2-17 for the two locations considered.

2.2.2 Test Program

The 7-inch nozzle assembly was sent to test area 1-52C of the RPL facility at Edwards AFB for testing in the 84-inch CHAR motor configuration. Upon receipt of the nozzle at the facility, a detailed dimensional and visual inspection was conducted. The nozzle was then mounted into the aft closure. The entire nozzle/aft closure assembly was mounted onto the motor case immediately following propellant loading. The nozzle was tested on July 27, 1977.

Figure 2-18 presents the CHAR motor chamber pressure history for the firing. Peak chamber pressure was 770 psig which was well within the predicted range. The time of firing was 46 seconds to the start of tailoff and 50 seconds to complete burn time.

TABLE 2-21. CARBON PHENOLIC RESPONSE AT 50 SECONDS -- 7-INCH NOZZLE DESIGN CRITERIA

Station	R (in)	A/A*	δ_i (in)	δ_e (in)	δ_c (in)	δ_p (in)	δ_{sf} (in)
1	4.20	1.44	1.05	0.329	0.376	0.705	1.128
2	8.27	5.58	0.50	0.039	0.382	0.421	0.555

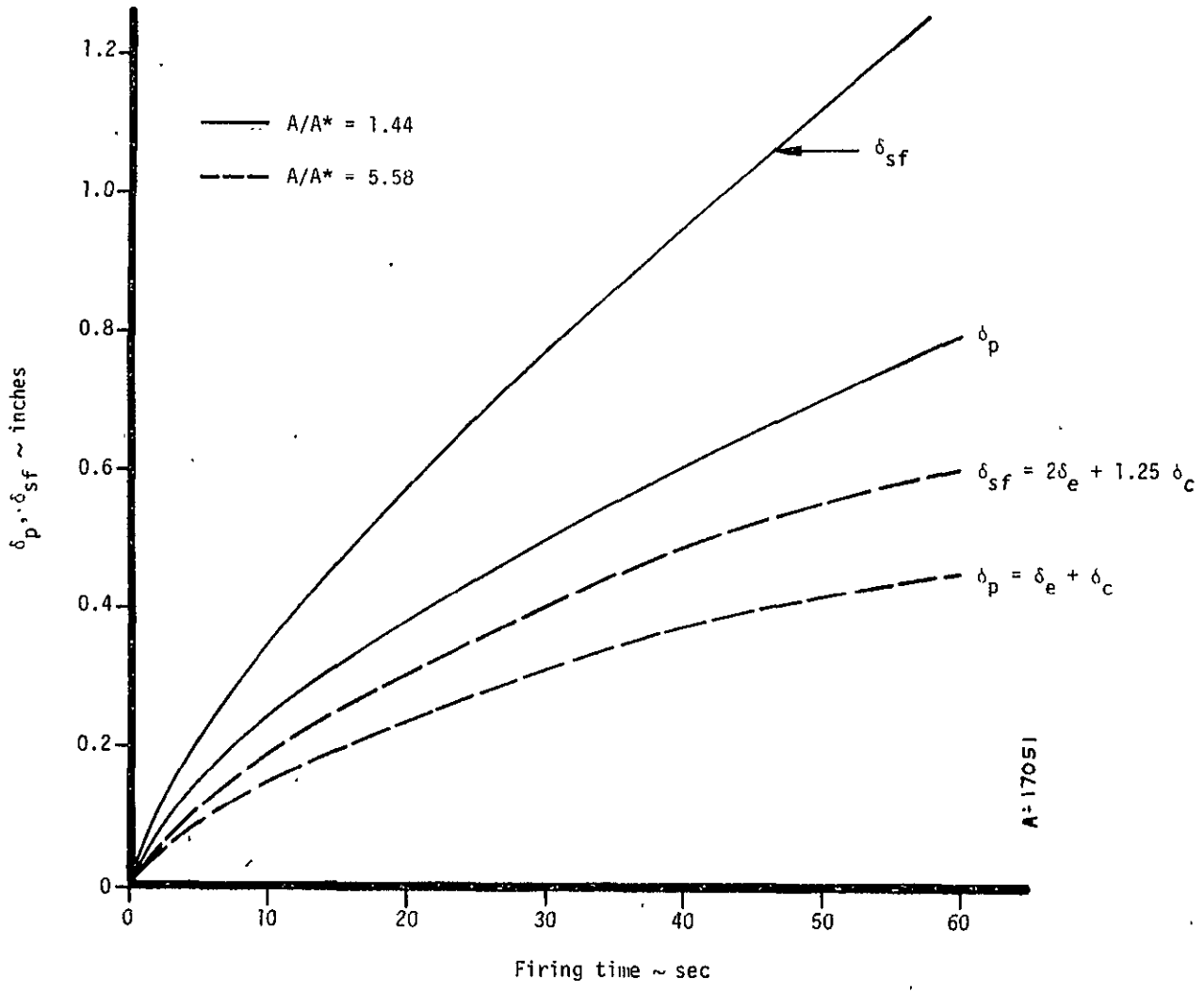

Figure 2-17. Liner thickness requirements versus firing time.

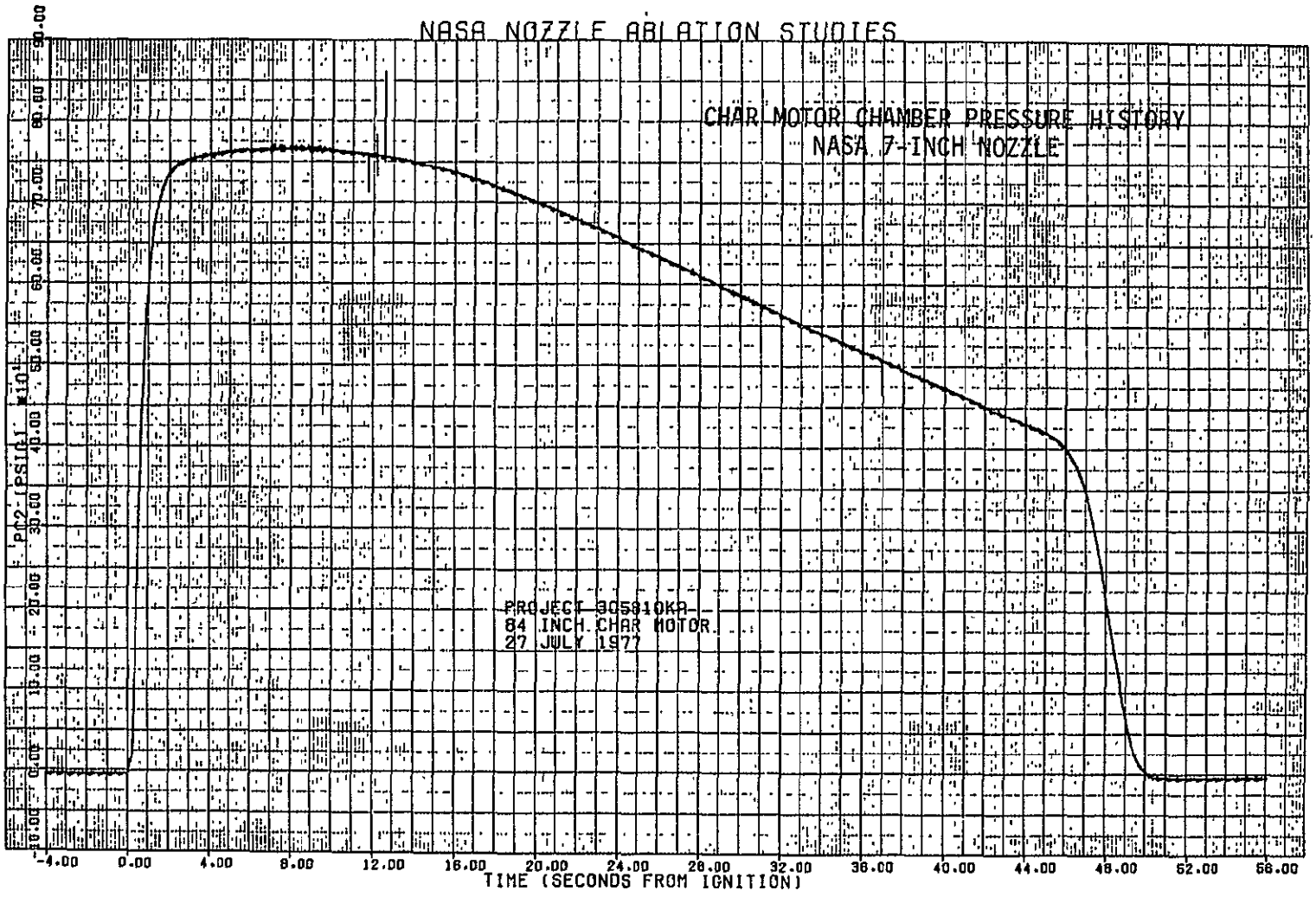

Figure 2-18. CHAR motor chamber pressure history, 7-inch nozzle.

2.2.3 Test Results

As was done with the 2.5-inch HIPPO nozzles, the 7-inch nozzle throat diameter was measured using a dial micrometer and then shipped to Acurex for a thorough post-test characterization. The throat measurement made at the test site was 8.87 inches and represents only an average.

At Acurex, the 7-inch nozzle was sliced into eight sections, as was done with the 2.5-inch nozzles. These sections were designated A through H, as shown in Figure 2-19. The section angles with respect to 0^0 (pre- and post-test marking) were selected at 45^0 increments, which placed the intersection of pitch and rayon fabric throat sections in the center of Sections B and F. The axial locations designated for measurement are also shown in Figure 2-19 and were selected based on visual inspection of the nozzle's erosion pattern to enable the most accurate contour map of the nozzle's performance. The end of the exit cone was designated as Station 0.0 inch. The forward end is Station 25.101 inches, and the throat center is Station 19.60 inches. The local nozzle slope with respect to the nozzle centerline at each axial location is given in Table 2-22.

Detailed measurements were made of the recession and char depth at each axial location (or station). These measurements are presented in Tables 2-23 and 2-24. They are also plotted in Figure 2-20 as profiles compared to the original nozzle contour. These profiles are plotted for each nozzle section and provide a visual examination of the nozzle's performance. Figures 2-21 through 2-26 present circumferential recession profiles at critical locations at or near the nozzle throat. They are plotted on polar graphs for immediate visual observation of the post-test recession compared to the original nozzle profile.

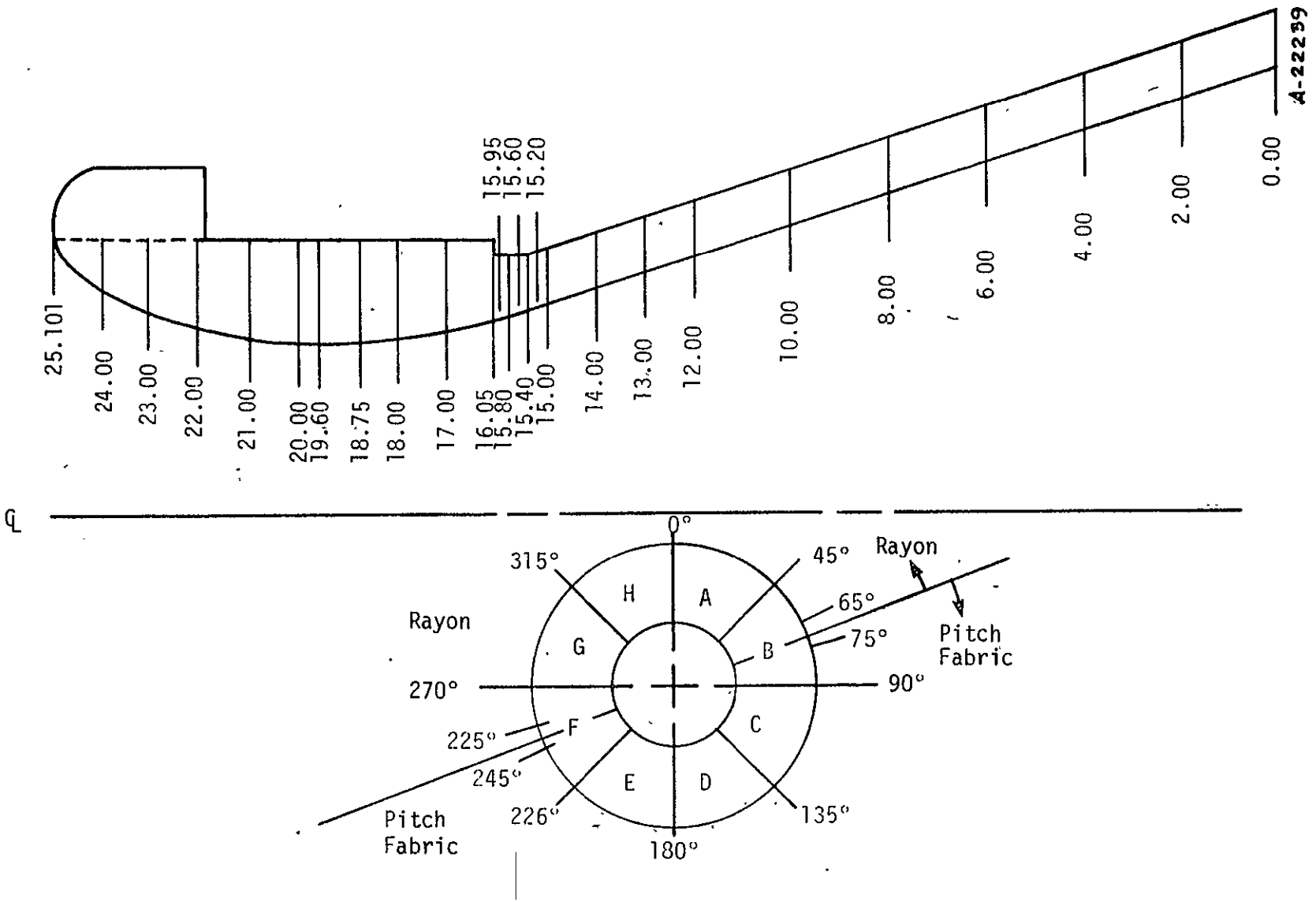

Figure 2-19. 7-Inch CHAR motor nozzle, axial and circumferential measurement locations.

TABLE 2-22. 7-INCH CHAR MOTOR NOZZLE MEASUREMENT LOCATIONS

Axial Location[a]	Local Nozzle Slope
0.00	17°27'
2.00	17°27'
4.00	17°27'
6.00	17°27'
8.00	17°27'
10.00	17°27'
12.00	17°27'
13.00	17°27'
14.00	17°27'
15.00	17°27"
15.20	17°27'
15.40	17°27'
15.60	16°31'
15.80	15°42'
15.95	15°5'
16.05	14°40'
17.00	10°44'
18.00	6°36'
18.75	3°29'
19.60	0°
20.00	2°34'
21.00	8°56'
22.05	16°1'
23.00	21°40'
24.00	28°2'

[a]Refer to Figure 2-18

TABLE 2-23. 7-INCH CHAR MOTOR NOZZLE — RECESSION MEASUREMENTS

Axial Location[a] (in)	Circumferential Location															
	0°		45°		90°		135°		180°		225°		270°		315°	
	⊥[b] to ℄	⊥ to Surface	⊥ to ℄	⊥ to Surface	⊥ to ℄	⊥ to Surface	⊥ to ℄	⊥ to Surface	⊥ to ℄	⊥ to Surface	⊥ to ℄	⊥ to Surface	⊥ to ℄	⊥ to Surface	⊥ to ℄	⊥ to Surface
8.0	0.042	0.040	0.062	0.059	0.057	0.054	0.043	0.041	0.028	0.027	0.053	0.051	0.041	0.039	0.053	0.051
10.0	0.059	0.056	0.042	0.040	0.060	0.057	0.041	0.039	0.050	0.048	0.053	0.051	0.054	0.052	0.071	0.068
12.0	0.107	0.102	0.019	0.018	0.103	0.098	0.114	0.109	0.100	0.095	0.116	0.111	0.075	0.072	0.118	0.113
13.0	0.138	0.132	0.030	0.029	0.093	0.089	0.074	0.071	0.084	0.080	0.112	0.107	0.076	0.073	0.107	0.102
14.0	0.172	0.164	0.055	0.052	0.120	0.114	0.104	0.099	0.120	0.114	0.133	0.127	0.113	0.108	0.140	0.134
15.0	0.252	0.240	0.185	0.176	0 139	0.133	0.121	0.115	0.125	0.119	0.132	0.126	0.151	0.144	0.169	0.161
15.2	0.254	0.242	0.190	0.181	0.132	0.126	0.135	0.129	0.128	0.122	0.153	0.146	0.160	0.153	0.168	0.160
15.4	0.252	0.240	0.209	0.199	0.142	0.135	0.132	0.126	0.135	0.129	0.153	0.146	0.178	0.170	0.141	0.135
15.6	0.275	0.264	0.197	0.189	0.142	0.136	0.106	0.102	0.157	0.151	0.140	0.134	0.179	0.172	0.157	0.151
15.8	0.312	0.300	0.235	0.226	0.146	0.141	0.131	0.126	0.166	0.160	0.152	0.146	0.203	0.195	0.214	0.206
15.95	0.387	0.374	0.272	0.263	0.240	0.232	0.183	0.177	0.187	0 181	0.171	0.165	0 243	0.235	0.291	0.281
16.05	0.453	0.438	0.245	0.237	0.113	0.109	0.098	0.095	0.101	0.098	0.111	0.107	0.197	0.191	0.278	0.269
17.0	0.545	0.535	0.344	0.338	0.242	0.238	0.205	0.201	0.209	0.205	0.210	0.206	0 286	0.281	0.432	0.424
18.0	0.614	0.610	0.513	0.510	0.345	0.343	0.283	0.281	0.313	0.311	0.319	0.317	0.367	0.364	0.540	0 536
18.75	--	--	0.646	0.645	0.420	0.419	0.348	0.347	0.370	0.369	0.371	0.370	0.451	0.450	--	--
19.6	0.547	0.547	0.638	0.638	0.457	0.457	0.376	0.376	0.401	0.401	0.443	0.443	0.455	0.455	0.500	0.500
20.0	0.505	0.504	0.612	0.611	0.482	0.482	0.398	0.398	0.438	0.438	0.457	0.457	0.456	0.456	0.481	0.481
21.0	0.484	0.478	0.588	0.581	0.464	0.458	0.382	0.377	0.438	0.432	0.464	0.458	0.466	0.460	0.451	0.446
22.05	0.456	0.438	0.574	0.552	0.512	0.501	0.409	0.393	0.480	0.461	0.486	0.467	0.418	0.402	0.287	0.276
23.0	0.447	0.415	0.465	0.432	0.450	0.418	0.384	0.357	0.452	0.420	0.431	0.401	0.412	0.383	0.273	0.258
24.0	0.349	0.308	0.319	0.282	0.306	0.270	0.274	0.242	0.331	0.292	0.341	0.301	0 305	0.269	0.187	0.165

T-640

[a] Refer to Figure 2-19; Stations 0 through 6.0-inch omitted since recession was negligible

[b] ⊥ denotes perpendicular

TABLE 2-24. 7-INCH CHAR MOTOR NOZZLE — CHAR DEPTH MEASUREMENTS

Axial Location[a] (in)	Circumferential Location															
	0°		45°		90°		135°		180°		225°		270°		315°	
	⊥[b] to ℄	⊥ to Surface	⊥ to ℄	⊥ to Surface	⊥ to ℄	⊥ to Surface	⊥ to ℄	⊥ to Surface	⊥ to ℄	⊥ to Surface	⊥ to ℄	⊥ to Surface	⊥ to ℄	⊥ to Surface	⊥ to ℄	⊥ to Surface
0.0	0.699	0.677	0.477	0.455	0.518	0.494	0.534	0.509	0.573	0.642	0.442	0.422	0.486	0.464	0.458	0.437
2.0	0.573	0.547	0.439	0.419	0.400	0.382	0.428	0.408	0.545	0.520	0.431	0.411	0.442	0.422	0.408	0.389
4.0	0.520	0.496	0.438	0.418	0.420	0.401	0.446	0.425	0.507	0.484	0.384	0.366	0.422	0.403	0.414	0.395
6.0	0.480	0.458	0.437	0.417	0.448	0.428	0.417	0.398	0.576	0.549	0.397	0.379	0.446	0.425	0.423	0.404
8.0	0.493	0.470	0.413	0.394	0.413	0.394	0.438	0.418	0.526	0.502	0.350	0.334	0.395	0.377	0.420	0.401
10.0	0.526	0.502	0.494	0.471	0.440	0.420	0.529	0.505	0.549	0.524	0.390	0.372	0.438	0.418	0.388	0.370
12.0	0.443	0.423	0.441	0.421	0.448	0.427	0.541	0.516	0.483	0.461	0.403	0.384	0.489	0.466	0.402	0.383
13.0	0.461	0.440	0.467	0.446	0.460	0.439	0.527	0.508	0.473	0.451	0.441	0.421	0.528	0.504	0.383	0.365
14.0	0.387	0 369	0.457	0.436	0.436	0.416	0.509	0.486	0.500	0.477	0.421	0.402	0.493	0.470	0.414	0.395
15.0	0.404	0.385	0.458	0.437	0.424	0.404	0.490	0.467	0.477	0.455	0.420	0.401	0.428	0.408	0.362	0.345
15.2	0.391	0.373	0.439	0.419	0.424	0.404	0.509	0.486	0.517	0.493	0.447	0.426	0.418	0.399	0.374	0.457
15.4	0.442	0.422	0.444	0.424	0.435	0.415	0.505	0.482	0.497	0.474	0.466	0.445	0.397	0.379	0.397	0.379
15.6	0.405	0.388	0.436	0.418	0.464	0.445	0.486	0.466	0.495	0.475	0.488	0.468	0.413	0.396	0.415	0.398
15.8	0.431	0.415	0.416	0.400	0.495	0.477	0.518	0.499	0.521	0.502	0.505	0.486	0.441	0.425	0.368	0.372
15.95	0.429	0.414	0.462	0.446	0.532	0.514	0.558	0.539	0.620	0.599	0.574	0.554	0.453	0.437	0.388	0.375
16.05	0.433	0.419	0.531	0.514	0.803	0.777	0.781	0.756	0.746	0.722	0.733	0.709	0.500	0.484	0.486	0.470
17.0	0.404	0.397	0.460	0.452	0.822	0.808	0.717	0.704	0.718	0.705	0.757	0.744	0.467	0.459	0.483	0.475
18.0	0.401	0.398	0.433	0.430	0.745	0.740	0.738	0.733	0.618	0.614	0.648	0.644	0.463	0.460	0.424	0.421
18.75	--	--	0.396	0.395	0.612	0.611	0.688	0.687	0.588	0.587	0.712	0.711	0.410	0.409	--	--
19.6	0.464	0.464	0.401	0.401	0.773	0.773	0.639	0.639	0.597	0.597	0.657	0.657	0.466	0.466	0.469	0.469
20.0	0.426	0.426	0.405	0.405	0.695	0.694	0.790	0.789	0.565	0.564	0.584	0.583	0.410	0.410	0.449	0.449
21.0	0.414	0.409	0.381	0.376	0.657	0.649	0.715	0.706	0.587	0.580	0.623	0.615	0.418	0.413	0.462	0.456
22.05	0.378	0.363	0.384	0.369	0.353	0.339	0.263	0.253	0.256	0.246	0.228	0.219	0.325	0.312	0.309	0.297
23.0	0.335	0.311	0.408	0.379	0.344	0.320	0.247	0.230	0.222	0.206	0.226	0.210	0.329	0.306	0.350	0.325
24.0	0.349	0.308	0.456	0.402	0.382	0.337	0.234	0.207	0.291	0.257	0.163	0.144	0.345	0.305	0.305	0.269

T-641

[a] Refer to Figure 2-19

[b] ⊥ denotes perpendicular

Figure 2-20. 7-inch CHAR motor nozzle pre- and post-test profiles.

(Pages 2-89 through 2-96)

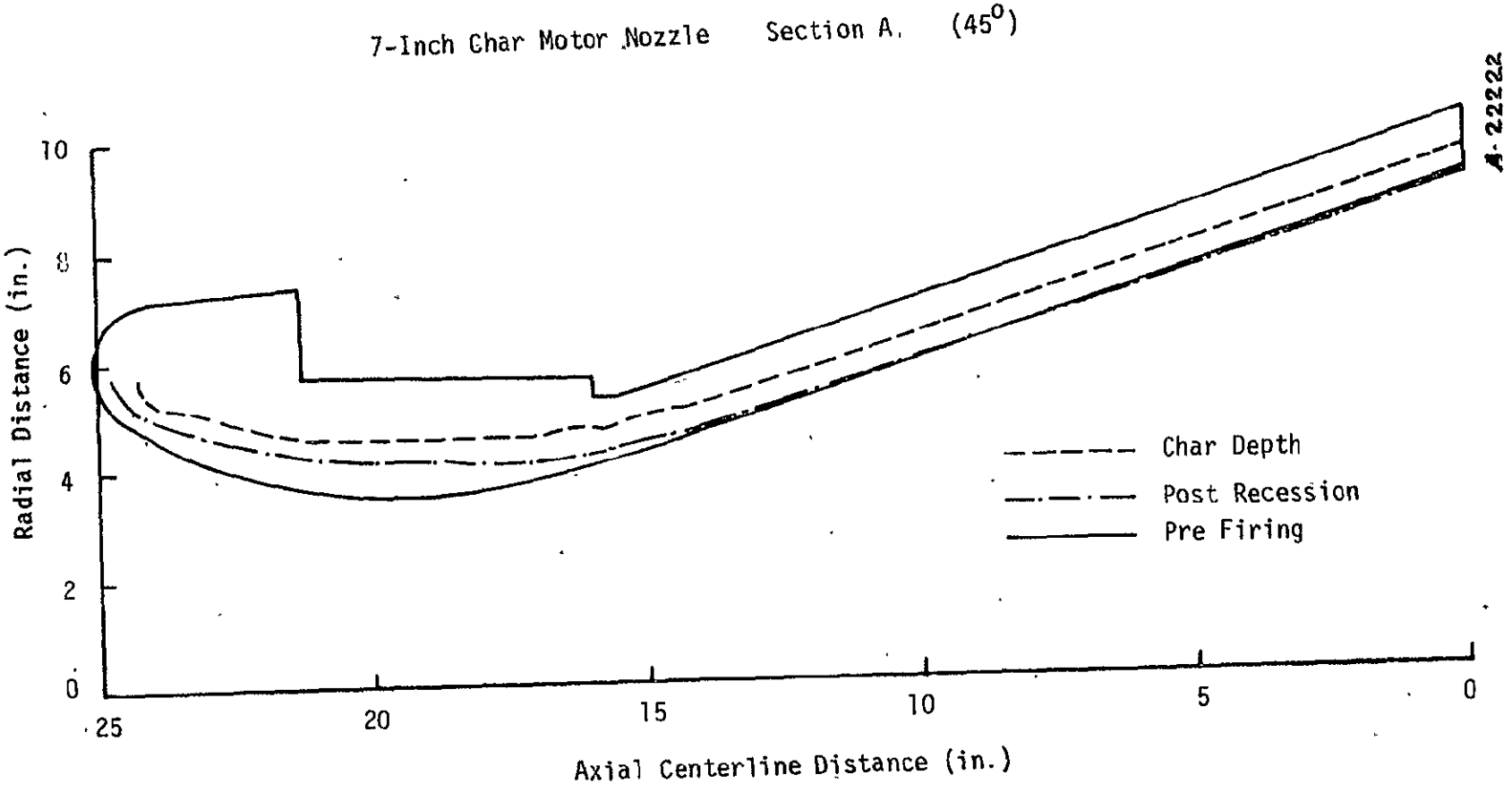
7-Inch Char Motor Nozzle Section A. (45°)
A-22222
Radial Distance (in.)
10
8
6
4
2
0
25
20
15
10
5
0
Axial Centerline Distance (in.)
Char Depth
Post Recession
Pre Firing

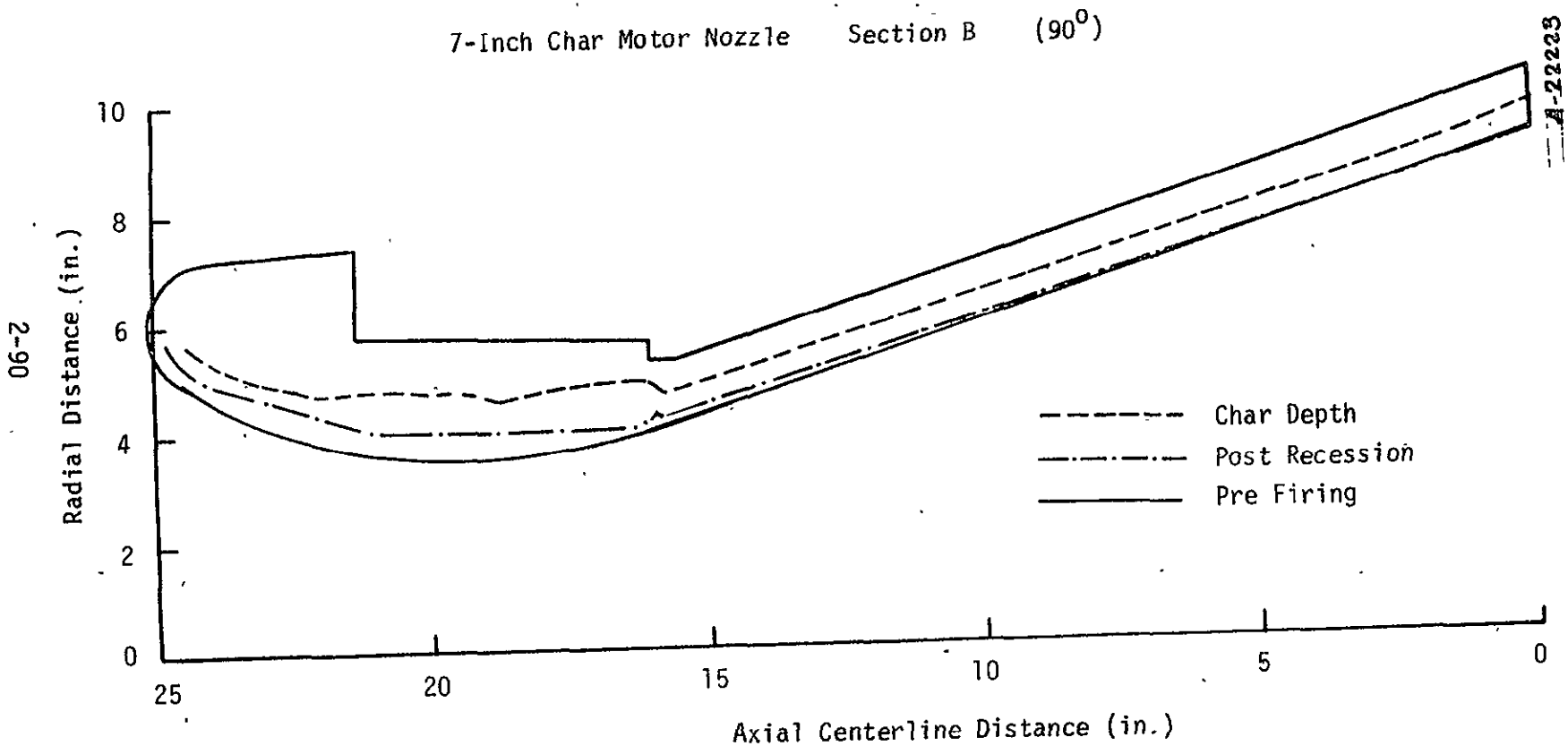
7-Inch Char Motor Nozzle Section B (90°)
A-22223
Radial Distance (in.)
10
8
6
4
2
0
25
20
15
10
5
0
Axial Centerline Distance (in.)
Char Depth
Post Recession
Pre Firing

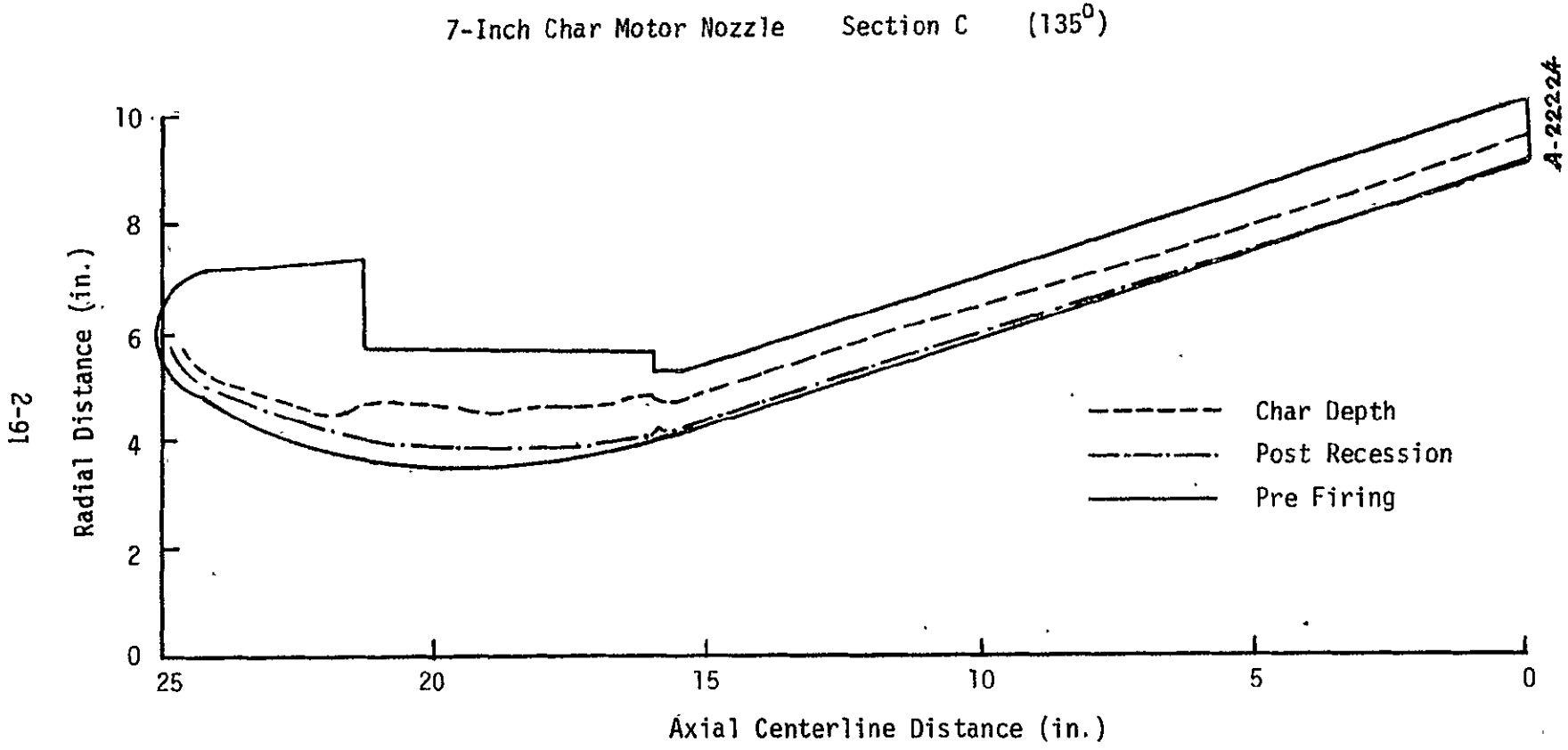
7-Inch Char Motor Nozzle Section C (135°)
A-22224
Radial Distance (in.)
10
8
6
4
2
0
25
20
15
10
5
0
Axial Centerline Distance (in.)
Char Depth
Post Recession
Pre Firing

7-Inch Char Motor Nozzle Section D (180°)

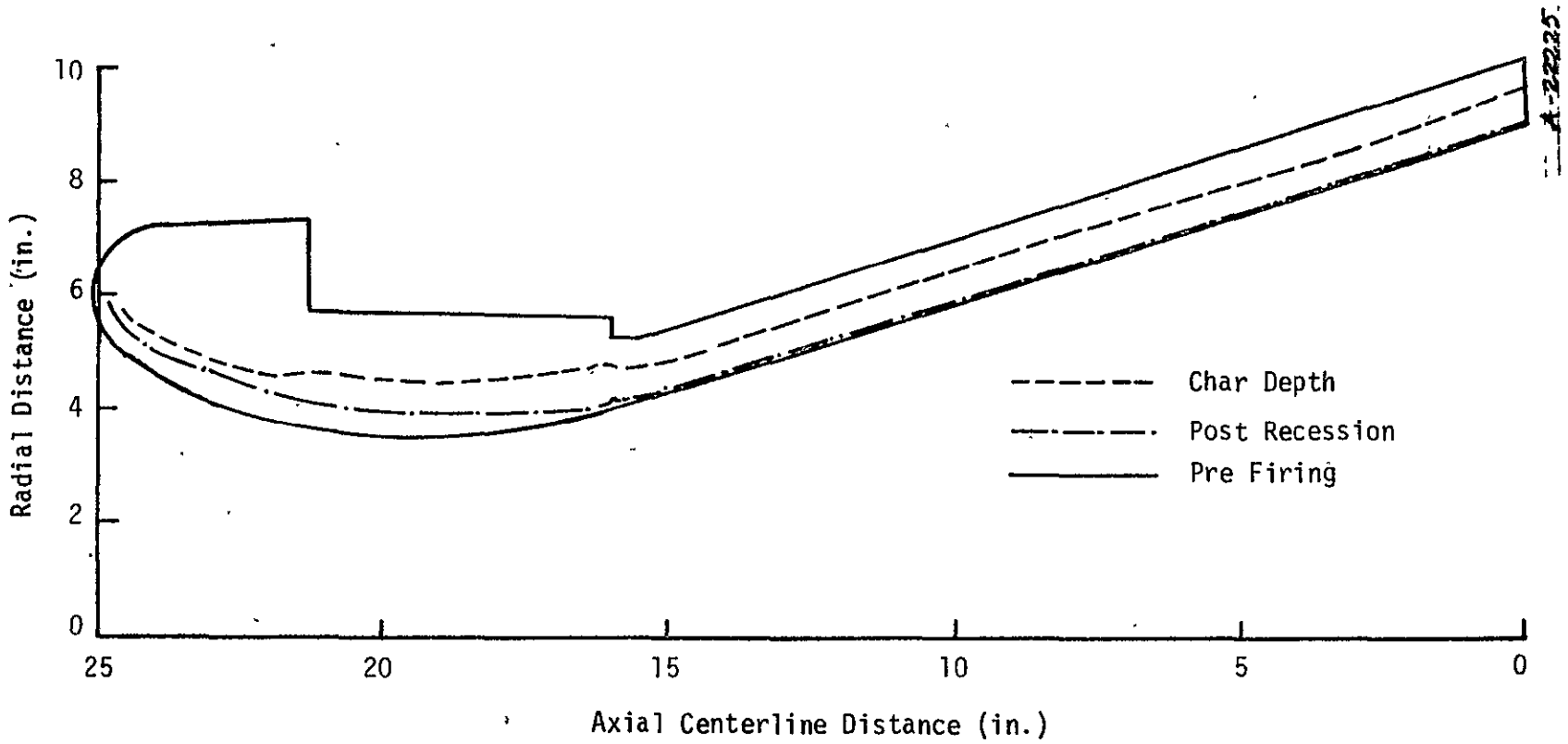

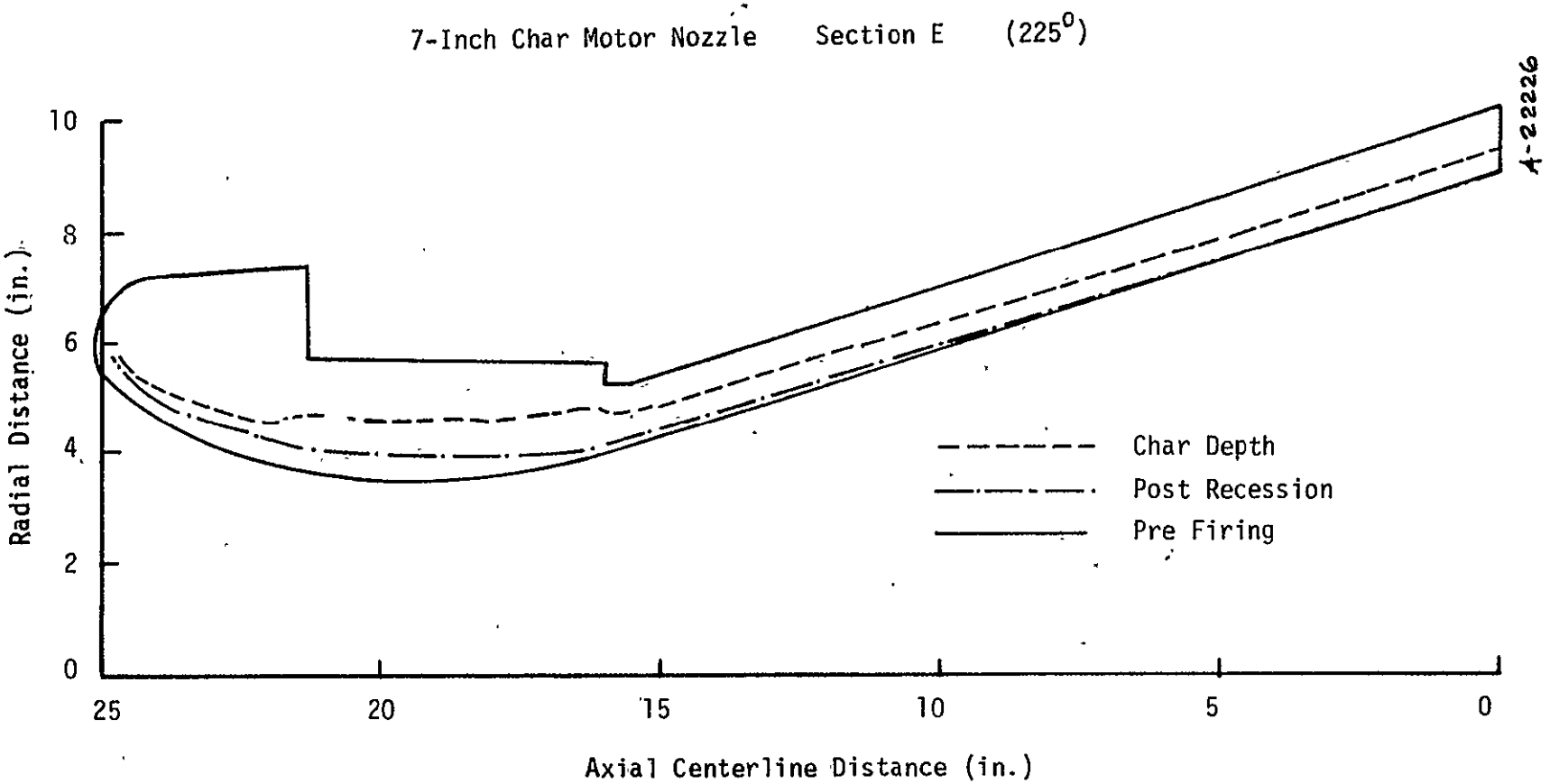
7-Inch Char Motor Nozzle Section E (225°)
4-22226
Radial Distance (in.)
10
8
6
4
2
0
25
20
15
10
5
0
Axial Centerline Distance (in.)
Char Depth
Post Recession
Pre Firing

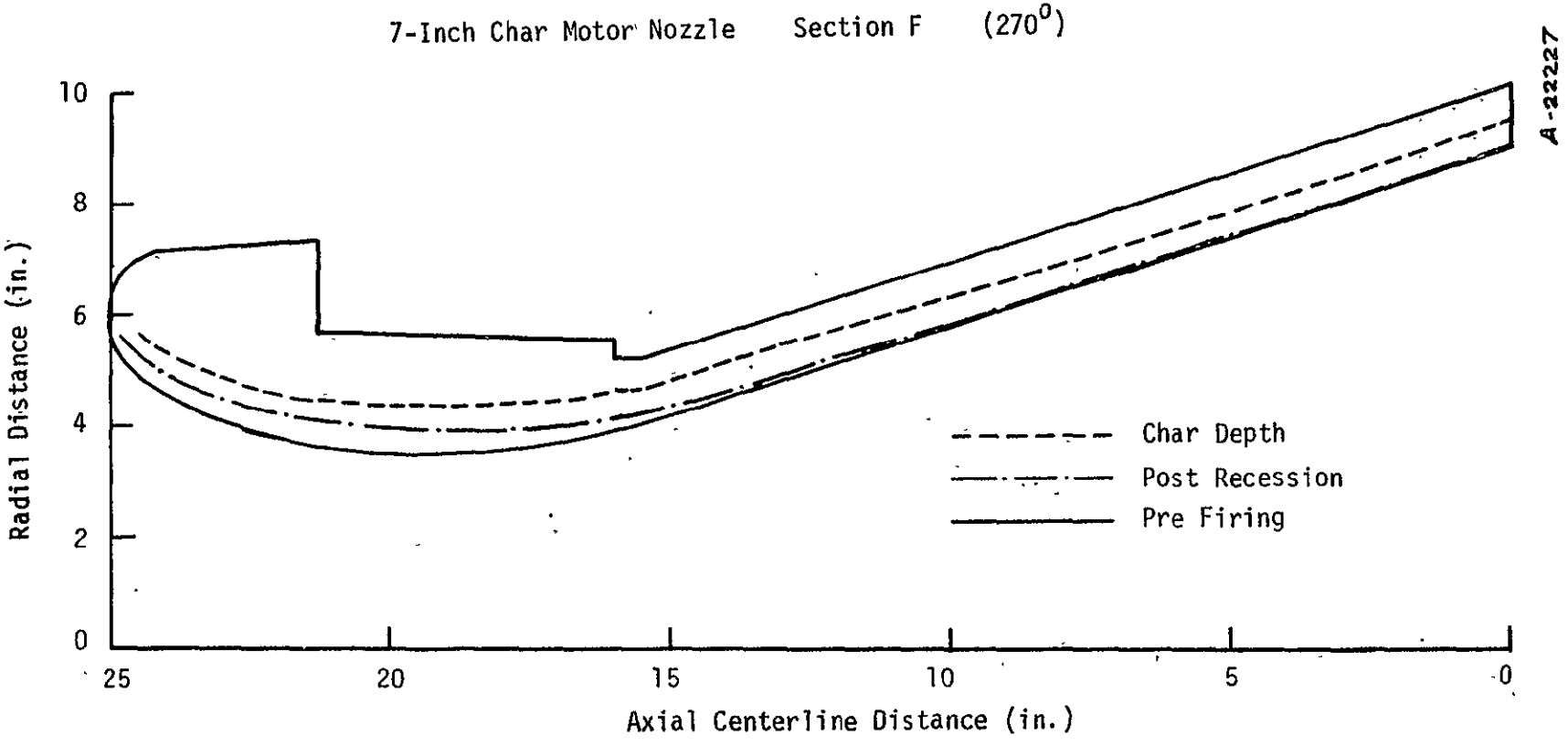
7-Inch Char Motor Nozzle Section F (270°)
A-22227
Radial Distance (in.)
10
8
6
4
2
0
25
20
15
10
5
0
Axial Centerline Distance (in.)
Char Depth
Post Recession
Pre Firing

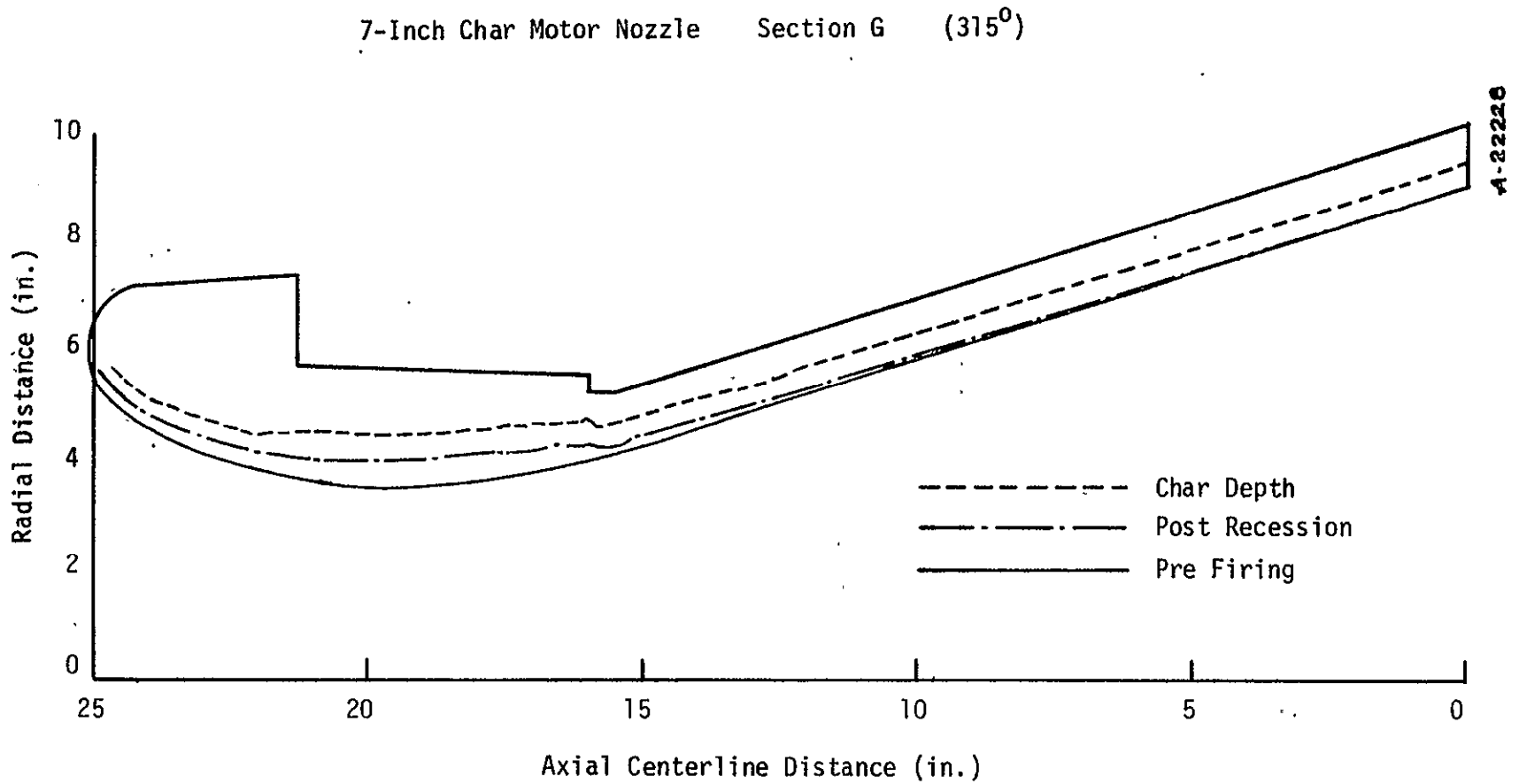
7-Inch Char Motor Nozzle Section G (315°)
A-22226
Radial Distance (in.)
10
8
6
4
2
0
25
20
15
10
5
0
Axial Centerline Distance (in.)
Char Depth
Post Recession
Pre Firing

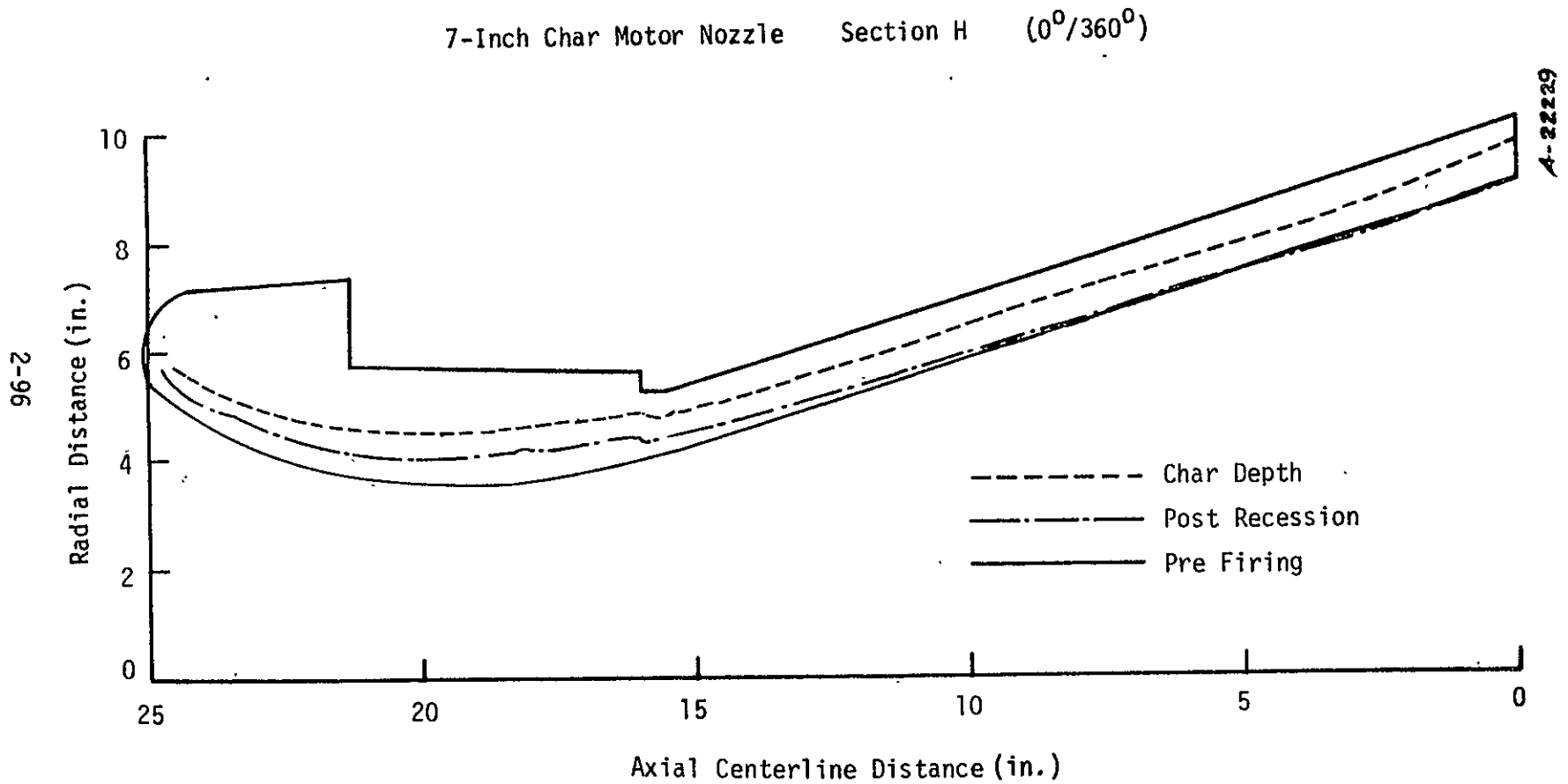
7-Inch Char Motor Nozzle Section H (0°/360°)
A-22229
Radial Distance (in.)
10
8
6
4
2
0
25
20
15
10
5
0
Axial Centerline Distance (in.)
Char Depth
Post Recession
Pre Firing

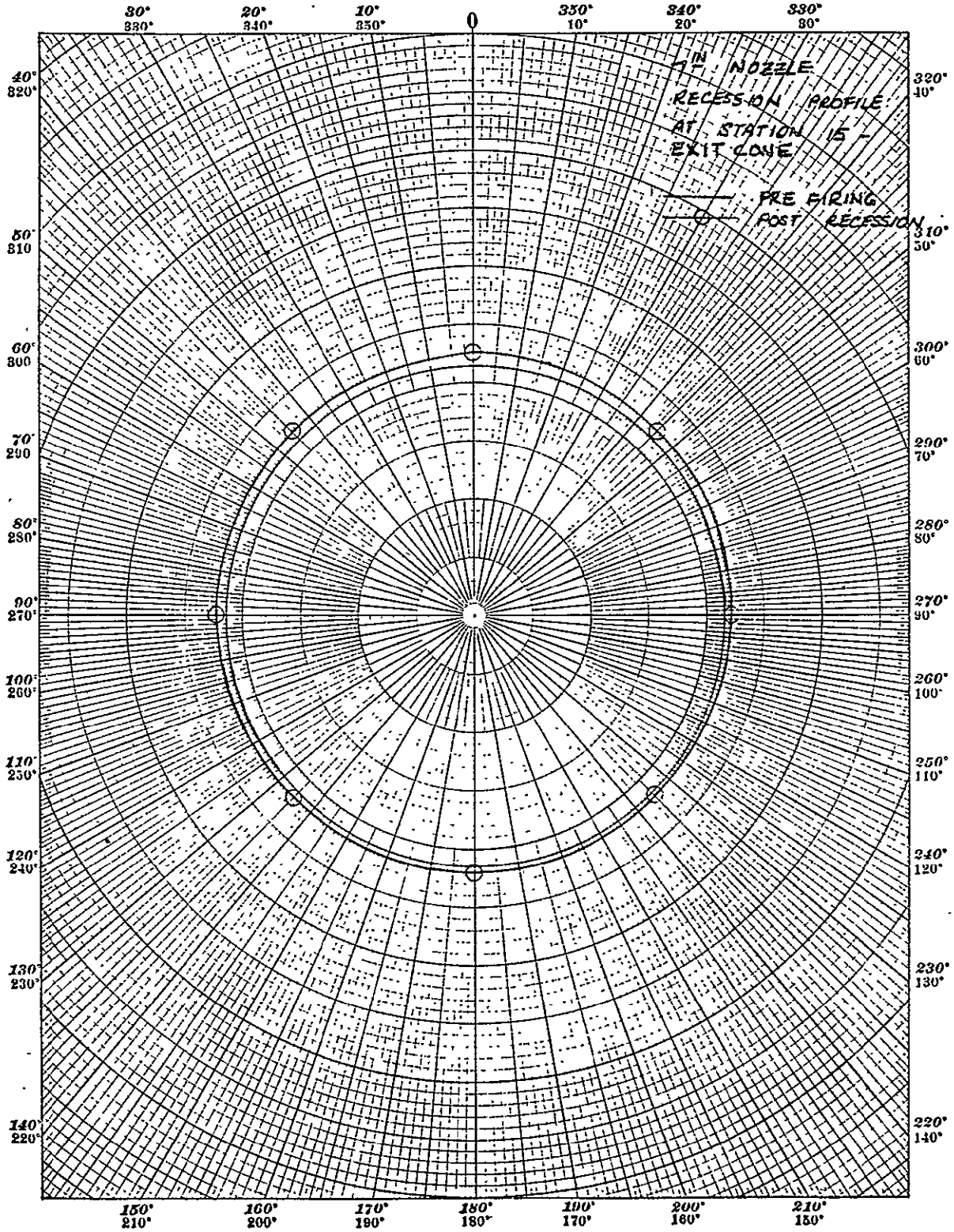

Figure 2-21. 7-inch nozzle recession profile at Station 15 -- exit cone.

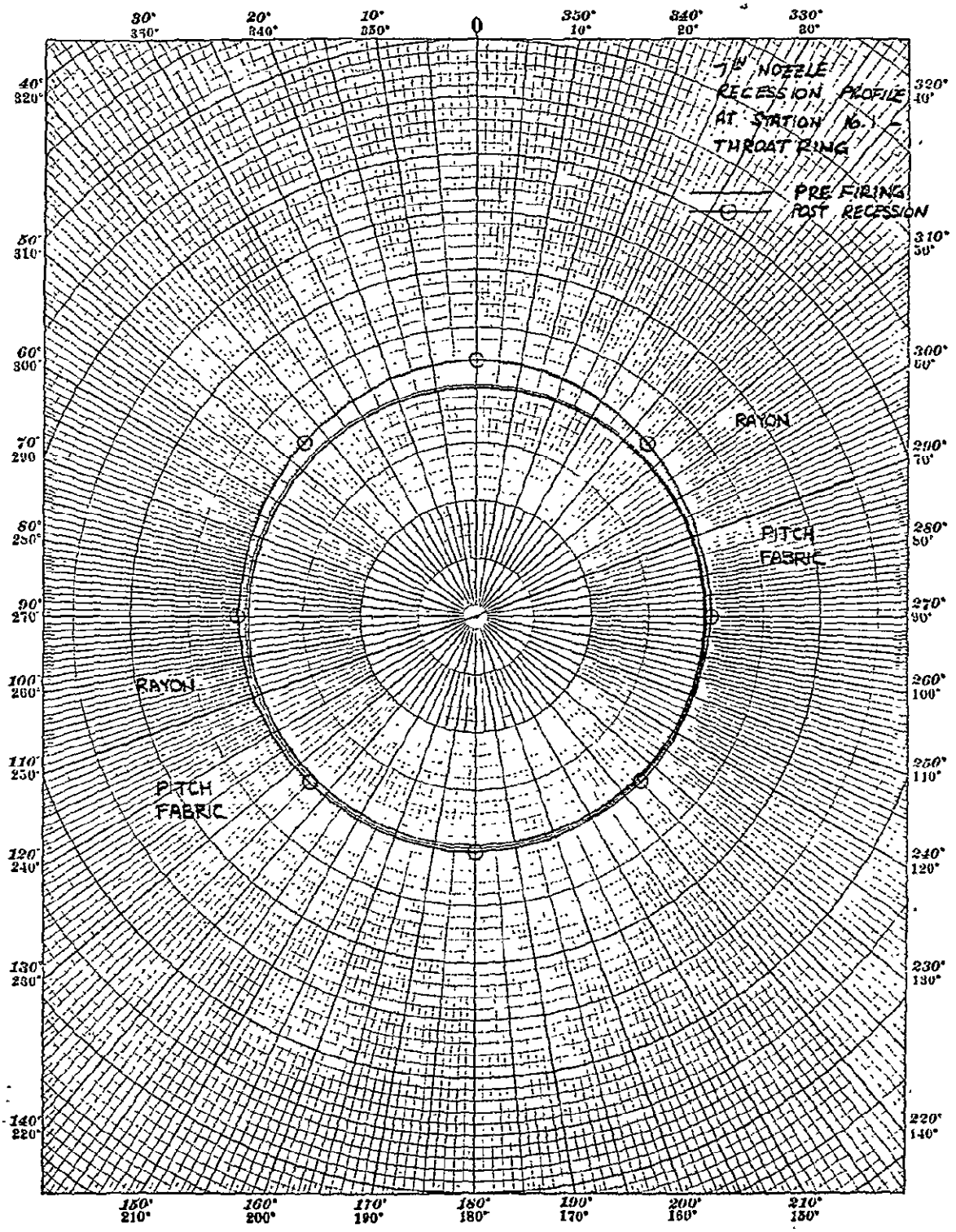

Figure 2-22. 7-inch nozzle recession profile at Station 16.1 -- throat ring.

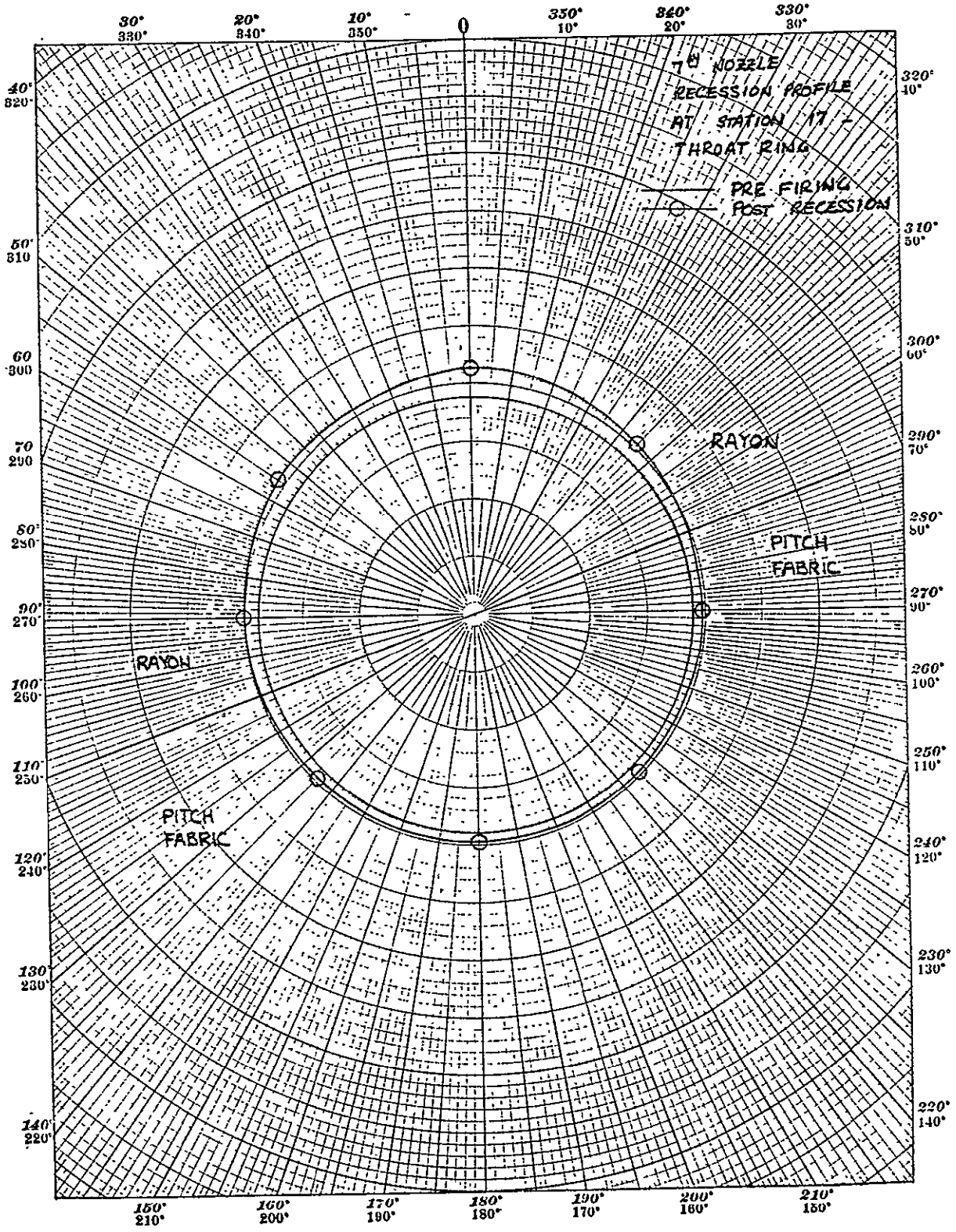

Figure 2-23. 7-inch nozzle recession profile at Station 17 -- throat ring.

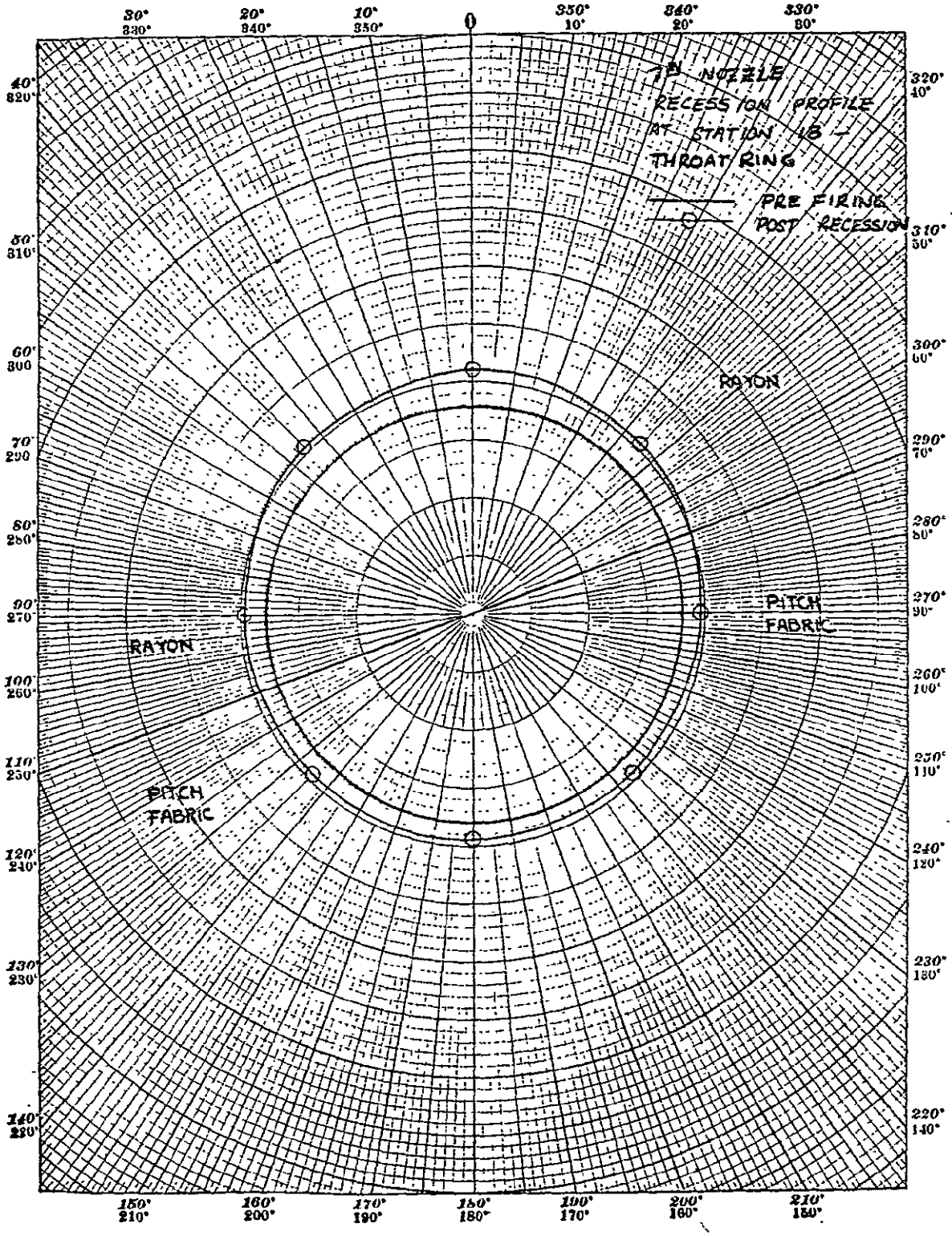

Figure 2-24. 7-inch nozzle recession profile at Station 18 -- throat ring.

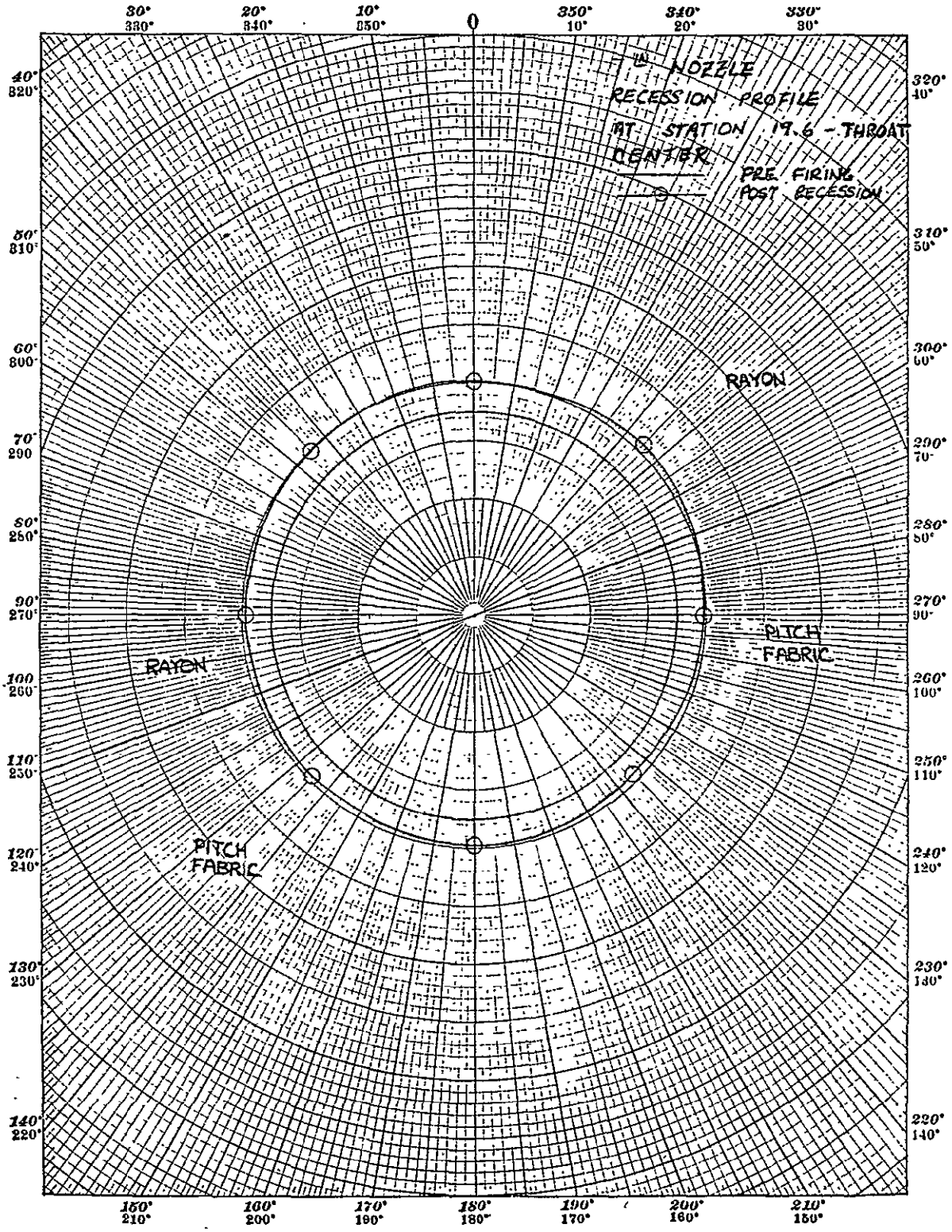

Figure 2-25. 7-inch nozzle recession profile at Station 19.6 -- throat center.

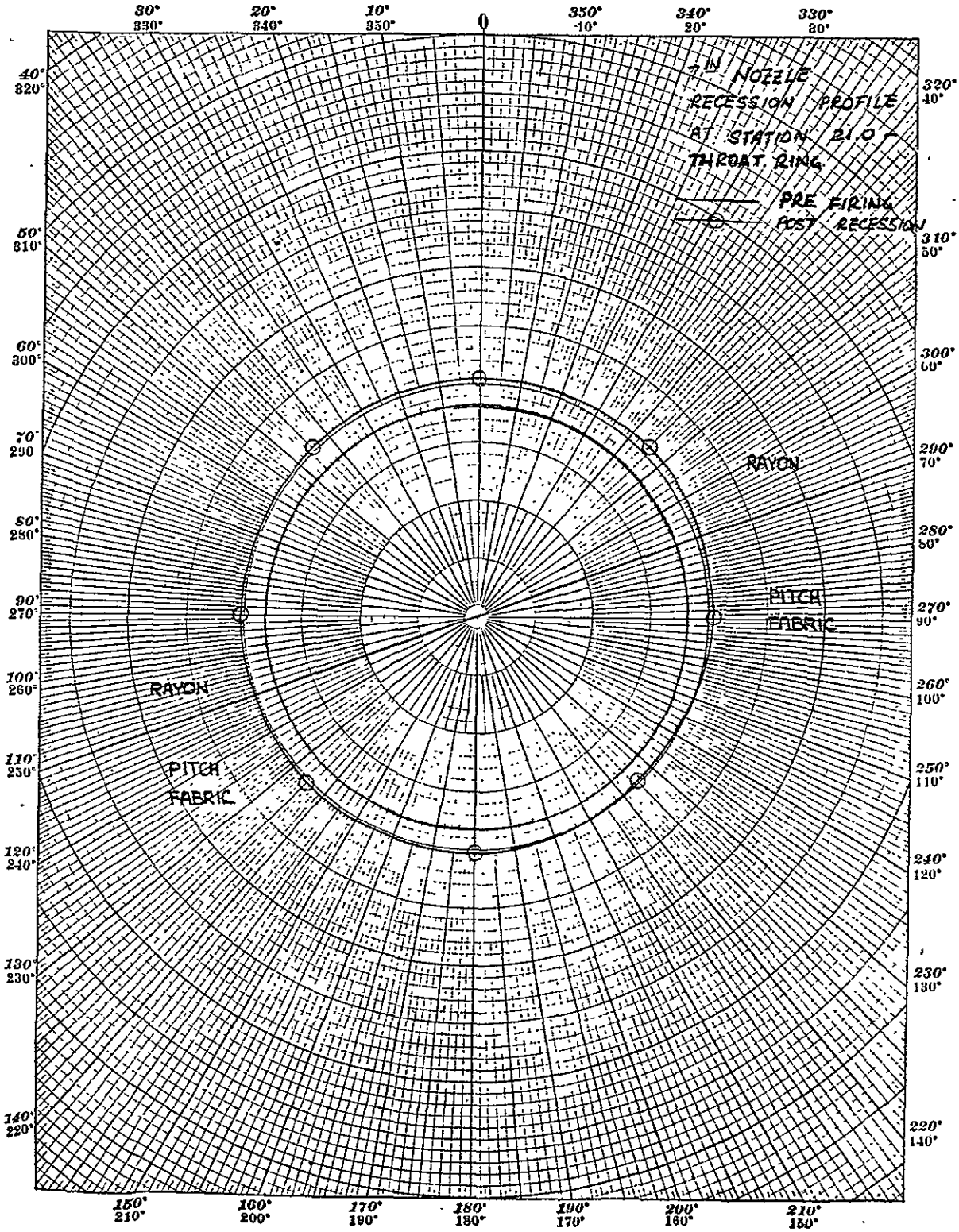

Figure 2-26. 7-inch nozzle recession profile at Station 21.0 -- throat ring.

Photographs were taken of the disassembled 7-inch nozzle prior to cutting slices for detailed recession measurements. The forward nose ring, exit cone, and submerged section insulator are shown in Figure 2-27. The holes in the exit cone are from removal of the retaining pins, and the cut in the insulator was made for ease of removal from the steel shell. Figure 2-28 shows the throat ring following disassembly. Note that the rayon side is severely gouged; this will be discussed in the summary section. The pitch side appears smooth, and the junction is well-defined.

Figure 2-29 shows a rayon, pitch, and a junction section of the throat ring and exit cone following the cutting of the nozzle into slices. The rayon section is shown in more detail in Figure 2-30, and as can be seen, the gouging is quite evident in Section H, as opposed to the smoother surface of Section A. Figure 2-31 shows the pitch rayon junction, and the difference in erosion and post-test structure is evident. Finally, Figure 2-32 shows a pitch section with its corresponding nose ring section also composed of pitch fabric. Note that the recession is smooth and the structure is reasonably intact; there was no indication of an anomalous performance by the pitch fabric throat section.

2.3 SUBSCALE NOZZLE TEST SUMMARY

The four 2.5-inch throat diameter nozzle tests were successful, and the test objectives were satisfactorily attained. One anomaly, however, occurred with nozzle No. 1. Post-test observation of the throat ring showed an area of irregular erosion (gouging). This irregularity was not anticipated in nozzle No. 1 since it was the baseline rayon fabric nozzle (FMC MX-4926). Following nozzle sectioning at Acurex, slices of material

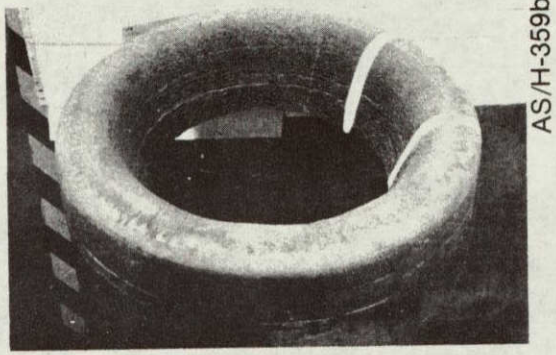

Forward nose ring -- pitch fabric

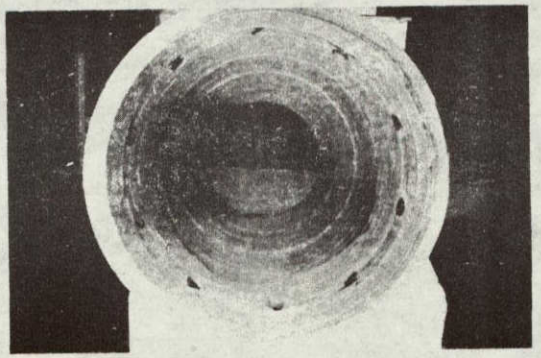

Exit cone -- rayon

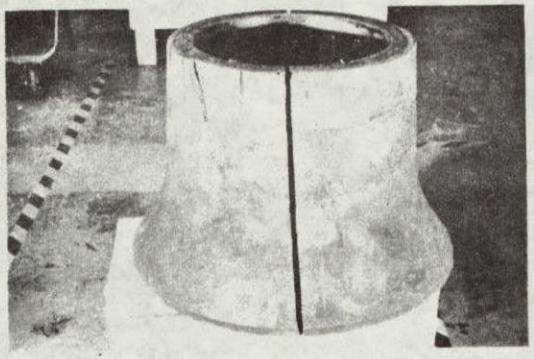

Submerged section insulator -- rayon/silica cloth

Figure 2-27. Post-test condition of 7-inch nozzle forward nose ring, exit cone and submerged insulator following disassembly from steel shell.

Pitch side

Rayon side

Rayon/pitch junction

Figure 2-28. Post-test surface condition of 7-inch nozzle throat ring following disassembly from steel shell.

AS/H-358b

Section H -- rayon

Section D -- pitch

Section B -- rayon/pitch

Figure 2-29. Post-test condition of 7-inch nozzle throat and exit cone sections.

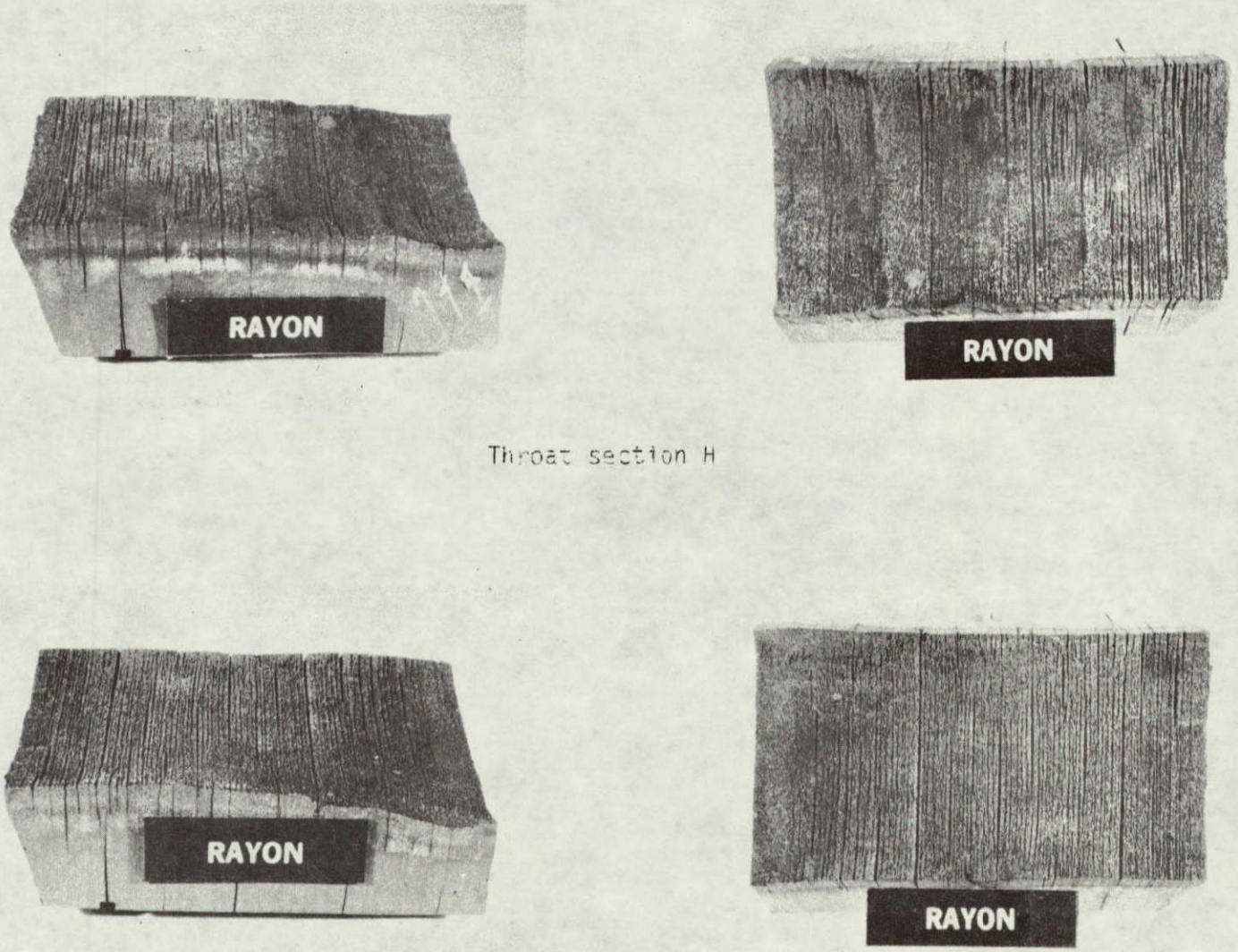

Figure 2-30. Post-test condition of 7-inch nozzle rayon fabric throat sections A and H.

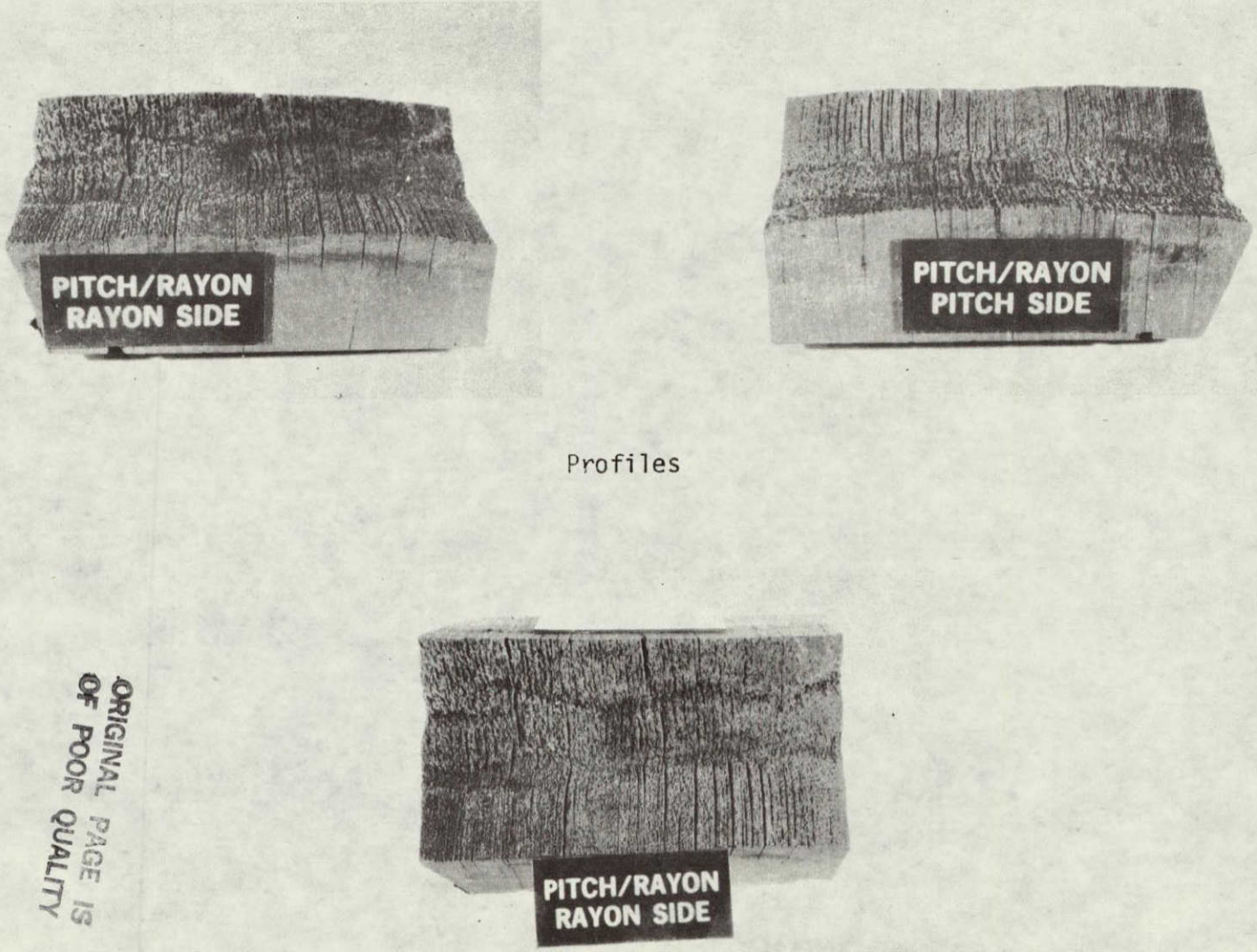

Figure 2-31. Post-test condition of 7-inch nozzle throat section at junction of pitch fabric and rayon fabric.

AS/H-365b

Section D

Nose ring section D

Figure 2-32. Post-test condition of 7-inch nozzle pitch fabric throat section and corresponding nose ring section.

found for the gouging, and the overall performance of the nozzle was not affected.

The pitch fabric sections, the forward nose ring and one-half of the throat ring, performed as well as the rayon section. The erosion depth was approximately the same with the exception of the gouged area, in which case, the rayon erosion was much greater than the pitch fabric (see Figures 2-22 and 2-23). The char depth in the pitch fabric, however, was greater than in the rayon side. Finally, note that some minor gouging occurred in the exit cone just below the gouged area in the rayon throat ring. Again, no explanation was found for the gouging.

SECTION 3

SURVEY, SELECTION, AND CHARACTERIZATION OF ALTERNATE LOW COST NOZZLE MATERIALS

This section describes the testing procedures and results of a materials screening process, conducted under Phase V, to define alternate carbon phenolic fabric ablative materials as candidates for the Shuttle SRM nozzle. Section 3.1 discusses the survey for candidate materials; the screening tests are described in Section 3.2. Full characterization of the two most promising materials is presented in Section 3.3, and the necessary data for a full-scale nozzle design using these two materials is presented in Section 3.4.

3.1 MATERIAL SURVEY

A material survey was conducted to identify low cost ablative fabrics which have potential application for use in the NASA Shuttle SRM nozzle. These fabrics were then evaluated by conducting ablation tests in the Acurex Arc Plasma Generator (APG). This survey was made necessary by the uncertain availability of continuous filament rayon which has been the widely used precursor (baseline) for ablative fabrics in rocket nozzle applications, including the NASA Shuttle nozzle.

Fabric selection criteria were governed by two Shuttle nozzle requirements: low cost and long-term availability. Low cost was dictated by the large size of the Shuttle nozzle, as each nozzle requires

approximately 12,160 pounds of carbon phenolic to obtain a final machined configuration. Thus, a reduction in carbon phenolic prepreg cost by one dollar could effect a $12,160 savings for each nozzle.

Long-term availability is mandatory for carbon fabrics in Shuttle nozzles because:

1. Current flight plans extend through 1992.
2. Material requalification is expensive.

As a result of the survey of candidate ablative materials for the Shuttle nozzle, 13 fabrics were recommended for ablative tests in Acurex's APG. These fabrics are identified in Table 3-1 and include the following precursor types:

- Staple PAN
- Staple rayon
- Pitch
- Continuous filament rayon

The continuous filament rayon precursor fabric was included to provide a reference from which to compare the other fabrics. Many other fabrics were reviewed as possible candidates but were rejected, primarily due to the cost and availability criteria. Rejected materials are reviewed in Section 3.1.2.

3.1.1 Survey Scope

The survey included four elements of fabric production: precursor manufacturers, fiber/fabric manufacturers, specialty weavers, and prepreggers. Organizations within each category were selected to represent typical capabilities in production of ablative grade precursors, fabrics, and prepregs. Table 3-2 summarizes the companies surveyed and identifies their respective capabilities.

TABLE 3-1. SHUTTLE NOZZLE CANDIDATE MATERIALS

Reinforcement Fabric				Reinforcement Precursor			Laminate Supplier Identity		Matrix Identities (Phenolic Resin)		Estimated 1980 Fabric Cost[a] ($/lb)
Supplier	Identity	Style	Filaments	Type	Source	Treatment	Fiberite	U.S. Polymeric	Fiberite	U.S. Polymeric	
Fiberite	W-502	8H-S	Staple	Pitch	Foreign	Carbonized	Karbon 419	Not received	HT 494C	N/A	--
Hercules	(Unknown)	8H-S	Staple	Pan	Foreign	Carbonized	Karbon 425	Not received	HT 562	N/A	38
HITCO	CCA-3[b]	8H-S	Continuous	Rayon	Domestic	Carbonized	MX 4926	FM 5055	HT 428A	U.S.P. 95	38
	CCA-28	8H-S	Staple	Rayon	Domestic	Carbonized	MX 4940	FM 5829	HT 428A	U.S.P. 95	--
	G-2252	8H-S	Staple	Rayon	Domestic	Graphitized	Not expected	FM 5746	N/A	U.S.P. 95	--
	SS-2231	8H-S	Staple	Pan	Domestic	Carbonized	Not expected	FM 5748	N/A	U.S.P. 95	--
Polycarbon	CSAS	8H-S	Staple	Rayon	Domestic	Carbonized	MX 4940	Not received	HT 428A	N/A	25
	CSAS	8H-S	Staple	Rayon	Domestic	Graphitized	Karbon 433	Not received	HT 494C	N/A	--
Stackpole	KFB	Knit	Staple	Pan	Foreign	Carbonized	Karbon 421	Not received	HT 494C	N/A	<30
	PWB-6	Plain	Staple	Pan	Foreign	Carbonized	Karbon 414	Not received	HT 494C	N/A	<32
	SWB-8	8H-S	Staple	Pan	Foreign	Carbonized	Karbon 411	Not received	HT 494C	N/A	<32
Union Carbide	VC-0149	8H-S	Continuous	Pitch	Domestic	Carbonized	Karbon 408P	FM 5749	HT 494C	U.S.P. 95	17
	VC-0150	8H-S	Continuous	Pitch	Domestic	Graphitized	Karbon 418	FM 5750	HT 494C	U.S.P. 95	18

[a]Based on 1977 dollars
[b]Baseline Shuttle fabric

TABLE 3-2. COMPANIES SURVEYED

Capability	Company
Precursor Production[a]	Avtex Beaunit
Fiber/Fabric Production[b]	Celanese Great Lakes Carbon Hercules HITCO Polycarbon Stackpole Union Carbide
Weavers[b]	Fiberite Woven Structures
Prepreg Production	Fiberite Hexcel U.S. Polymeric

[a]Continuous filament rayon
[b]Carbon and graphite fibers and fabrics

3.1.2 Screening and Selection

This section will review the screening conducted to select the fabrics for thermal testing. The primary criteria will be reviewed, followed by an additional criterion, state of development, for one material only.

3.1.2.1 Availability

A large number of fabrics which are cited in reports and producer literature were eliminated during screening due to the unavailability of:

- Precursor fibers
- Specific form of an available precursor
- A fabric under a given designation

Typical fabrics eliminated for these reasons are presented in Table 3-3. Some examples are:

- Union Carbide's VCX, eliminated because its precursor was a continuous filament rayon which is no longer available
- Union Carbide's VC-0139 pitch precursor fabric, eliminated because of a change in pitch filament diameter
- HITCO's staple rayon fabric identified as SS-2228, now sold under the CCA-28 designation.

3.1.2.2 Cost

Cost considerations resulted in the elimination of additional candidate fibers and fabrics, even though they are expected to be available on a long-term basis. Candidates eliminated due to cost are grouped in the following categories:

1. Fabrics which are woven from carbonized or graphitized yarns
2. Fabrics which have inherent production cost limitations

TABLE 3-3. FABRICS ELIMINATED DUE TO AVAILABILITY CRITERIA

Precursor Type	Manufacturer	Identity	Fabric Description	Comments
Rayon	Union Carbide	VCX	Carbonized, 8 HS	Discontinued, rayon precursor unavailable
		VCL	Carbonized, 8 HS	
		WCJ	Graphitized, plain	
		WCG	Graphitized, plain	
	HITCO	CCA-2	Carbonized, 8 HS	Discontinued, American Enka rayon precursor unavailable
		G-1965	Graphitized, plain	
		G-1966	Graphitized, plain	
		SS-2237	Carbonized, 8 HS	Discontinued, foreign continuous rayon precursor
		CCA-1	Carbonized, 8 HS	Discontinued, IRC rayon precursor
Pitch	Union Carbide	VC-0139	Carbonized, 8 HS	Discontinued, change in precursor diameter

AS-0010

3. Potential fabrics which could be woven from well-characterized yarns having long-term availability.

Schematics of the various routes available for production of fabrics from rayon, PAN, and pitch precursors are shown in Figures 3-1 and 3-2. An example of the first category, which is illustrated by the upper path in Figure 3-1, is Fiberite's W-133 fabric. This fabric is woven from Thornel-300 which is a carbonized yarn. Thornel-300 has an excellent potential for long-term availability and is being produced in substantial quantities. The potential for using this fabric in nozzles is, however, limited due to cost. The $40 per pound cost of Thornel-300 yarns places this fabric at a cost disadvantage compared to other candidates.

An example from the second category, fabrics which have an inherent production cost limitation, is Stackpole's SWB-3 fabric. Although this fabric is produced from readily available precursors, SWB-3 has a lower weight compared to other fabrics produced from the same precursor, such as SWB-8. The lower weight of SWB-3 inherently limits the total fabric production volume for given processing costs. Thus, SWB-3 would have a higher cost than SWB-8 for a given production volume and was, therefore, eliminated.

A typical yarn in the third category, fabrics that could be woven from carbonized or graphitized yarns, is Hercules 1000 Filament HM Fiber. This fiber is being increasingly committed to ablative use in the Department of Defense reentry vehicle applications. Therefore, long-term availability is anticipated. However, the HM Fiber has a limited production volume and is processed to a graphitized yarn. As a result, cost of the 1000 Filament HM Fiber is extremely high (approximately $300/pound), and fabrics using this fiber were eliminated from consideration on a cost basis.

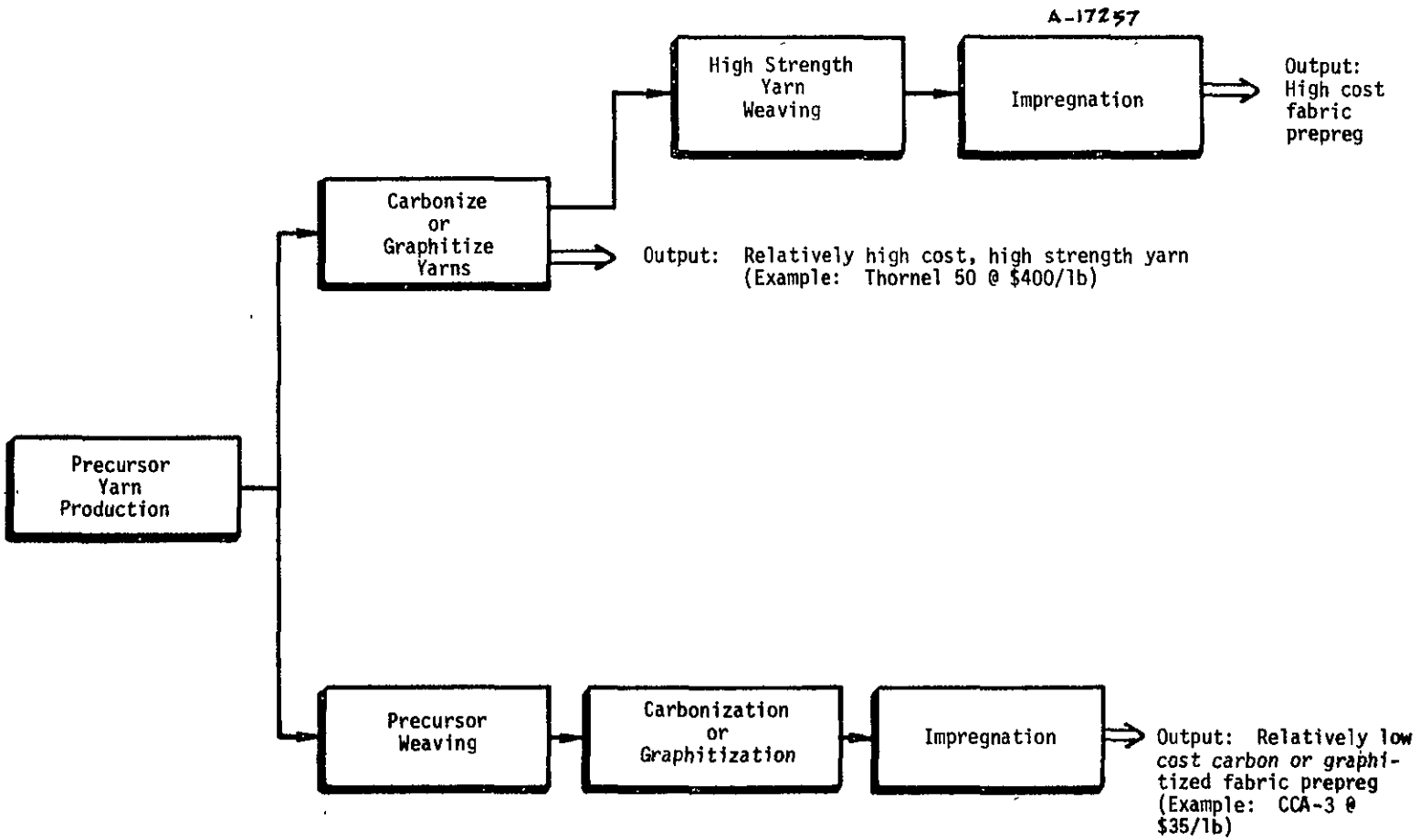

Figure 3-1. - Basic rayon or PAN precursor fabric production approaches.

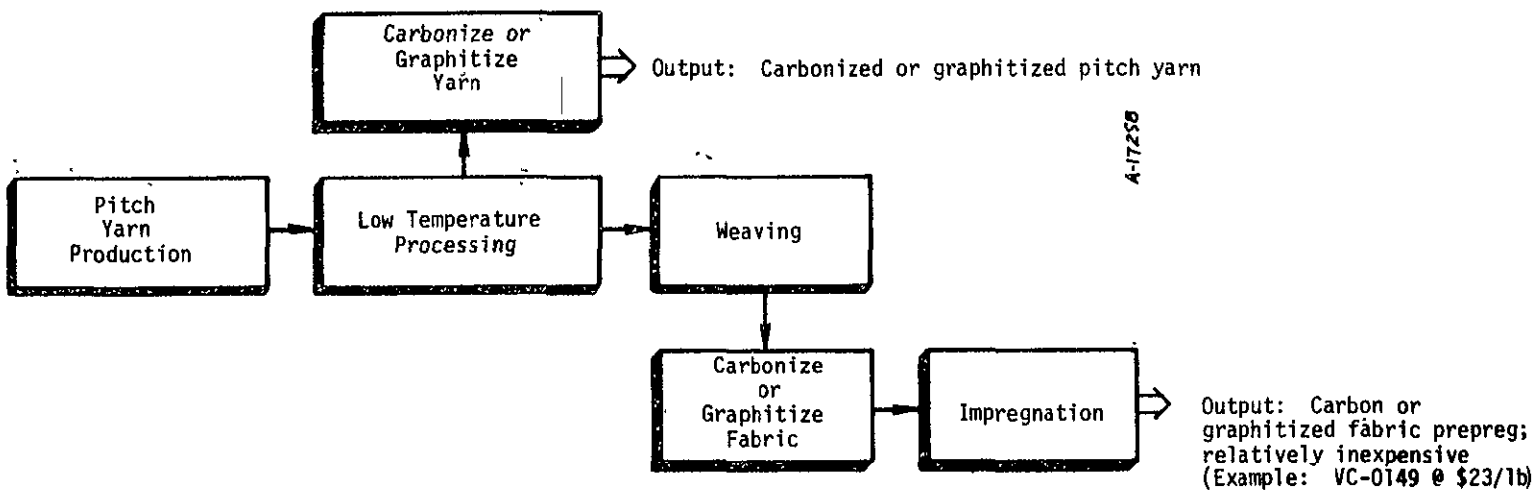

Figure 3-2. Basic pitch fabric production sequence.

3.1.2.3 State of Development

Fabrics used on the Shuttle nozzle must be at an advanced state of development, in addition to having long-term availability and low cost. This criteria resulted in the elimination of the Beaunit precursor. Beaunit manufactures a continuous filament rayon fiber, and long-term availability and low cost are anticipated. However, a limited search has revealed that no thermal, physical, mechanical, or ablative performance data exists for carbonized fabric produced from the Beaunit precursor. Since generation of such data is not warranted under this program, the Beaunit precursor was eliminated from consideration.

3.1.3 Projected Costs

This section first reviews the basis on which the projected cost data were developed. Second, effects of selected production methods on projected costs for large quantity fabric procurements are reviewed. Finally, projected costs for fabrics from alternate precursors are discussed. All costs are based on 1977 dollars.

3.1.3.1 Cost Projection Basis

Projected costs were based upon the following data:

- 5857 pounds of carbon phenolic are used in each finished machined nozzle
- A 52 percent material loss is experienced in the production cycle to obtain a finished part
- A total of 19 nozzles are required through June 1980
- A total of 42 nozzles are required from June 1980 through 1984
- 836 nozzles will be needed from 1985 through 1992

In order to provide a common base for cost comparison, the assumption was made that prepregs used in nozzle production would contain 35 percent resin.

Fabrics represent the major cost element in nozzle prepregs. The Fiberite Company estimated that 1977 costs were $20 per pound and $18 per pound, based on delivery of 3000 pounds or 12,000 pounds, respectively, per month. Very little cost reduction in fabrics is anticipated at the present time. It should be pointed out that all prepreggers are subject to the same fluctuations in resin costs.

3.1.3.2 Production Method Cost Effects

As noted earlier, some fabrics were eliminated from consideration due to cost effects arising from production methods which include fabric graphitization and conversion of fibers into fabric. Processing fabrics through graphitization provides some improvement in performance but at potentially higher costs. Thus, only graphitized fabrics with an anticipated high production volume would be cost-effective. An example of such a fabric is Union Carbide's VC-0150 which is a graphitized form of VC-0149. As shown in Figure 3-3, graphitization at high production rates has only a small effect on fabric cost. Therefore, VC-0150 is considered acceptable even though it is graphitized.

A predominant number of fabrics are produced by weaving. However, some fabrics are also produced by a lower cost knitting process. The savings possible from knitting can lead to a one to two dollar a pound cost advantage, according to Stackpole. Consequently, Stackpole's KFB carbonized, knit fabric was selected based on cost. Typical cost for woven and knit fabrics produced from the same PAN precursors are shown in Figure 3-4.

3.1.3.3 Precursor Comparative Cost Projections

Cost projections obtained during the survey are presented in this section. The projections include typical fabrics for each precursor type. The precursors and fabrics include:

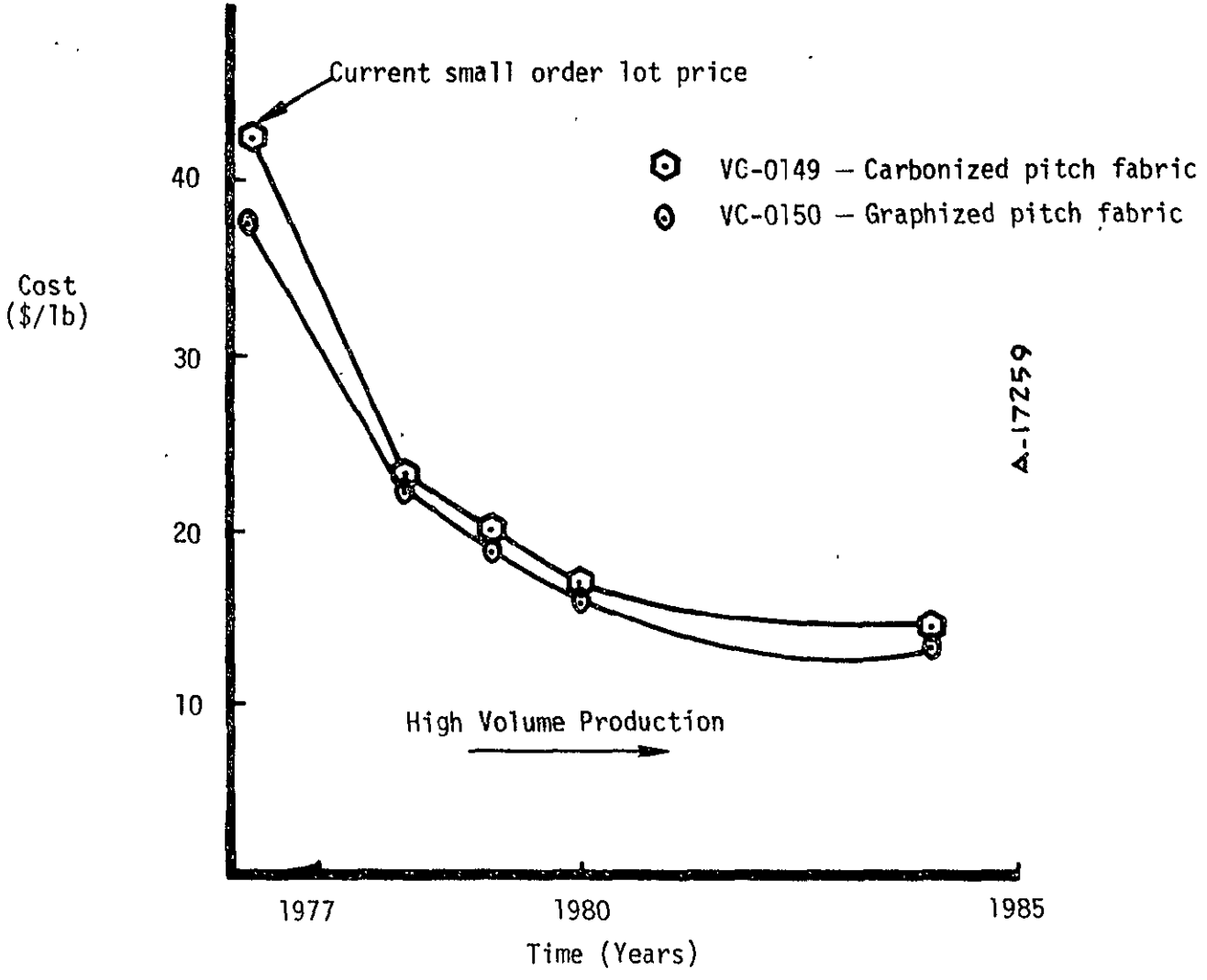

Figure 3-3. Cost effects of alternate processing on high volume production.

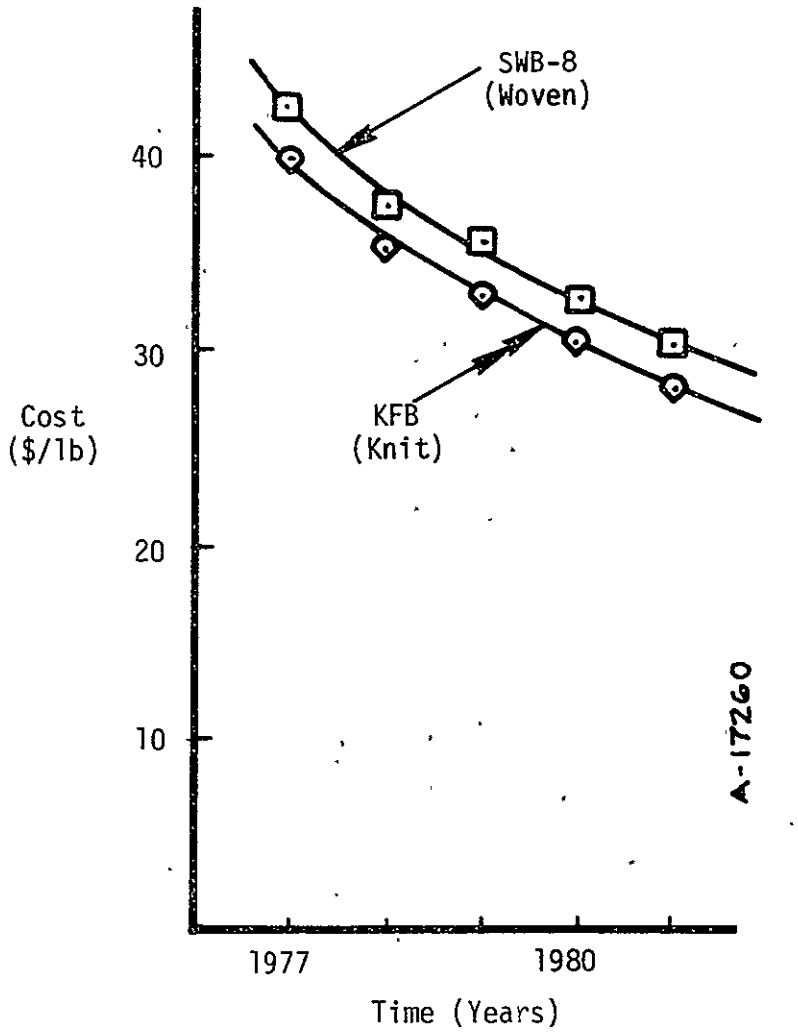

Figure 3-4. Effect of fabric production method on cost.

- Staple PAN (SWB-8) -- Figure 3-5
- Pitch (VC-0149) -- Figure 3-6
- Staple rayon (CCA-28) -- Figure 3-7

No extrapolations are presented beyond the time span in which supplier projections were available.

Figure 3-8 compares these cost trends with the continuous rayon precursor fabrics now used in the Shuttle nozzle (CCA-3). The figure also includes cost projections for two additional fabrics: a Hercules staple PAN and a Polycarbon staple rayon product (CSAS).

From the available projections, anticipated cost for the precursors surveyed are ranked as follows:

- Lowest cost -- pitch fabrics
- Intermediate costs -- staple rayon fabrics, staple PAN fabrics
- Highest cost -- continuous filament rayon fabrics

3.2 MATERIALS SCREENING TESTS

The thermal performance of the low cost candidate materials was evaluated by a screening test program using the Acurex 1-MW Arc Plasma Generator (APG) as a convective heat source. The materials in this program (Table 3-1) included pitch, PAN, and rayon fabrics. The major emphasis of the screening program was on pitch and PAN fabric carbon phenolics since these materials show great promise for very significant reductions in materials costs and have long-term availability, as was discussed in the previous section.

The test conditions for the APG materials screening program are discussed in Section 3.2.1. The model and test configurations, and the test matrix are presented in Section 3.2.2. Section 3.2.3 presents the

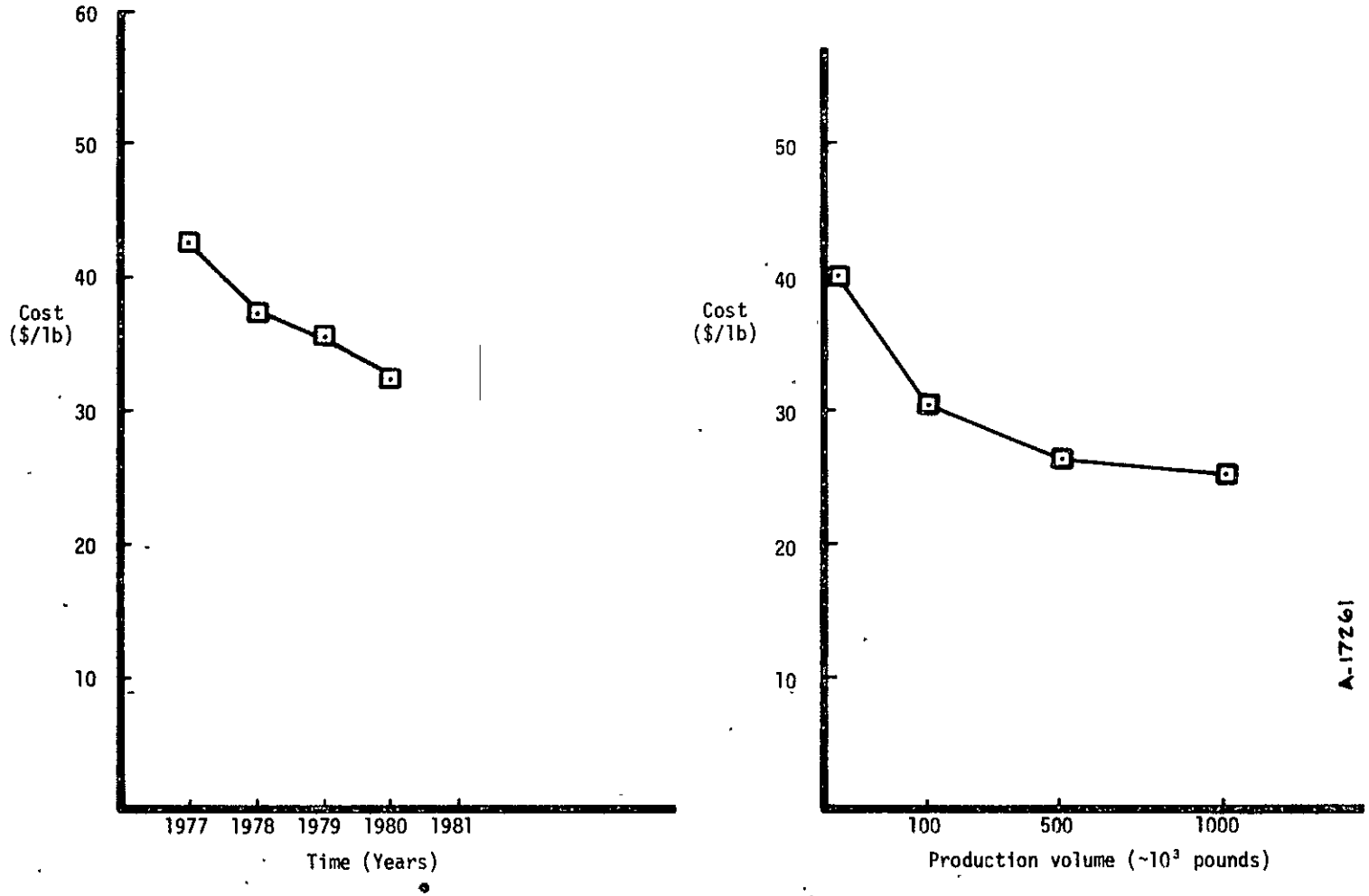

Figure 3-5. Cost projections for typical PAN fabric (Stackpole SWB-8).

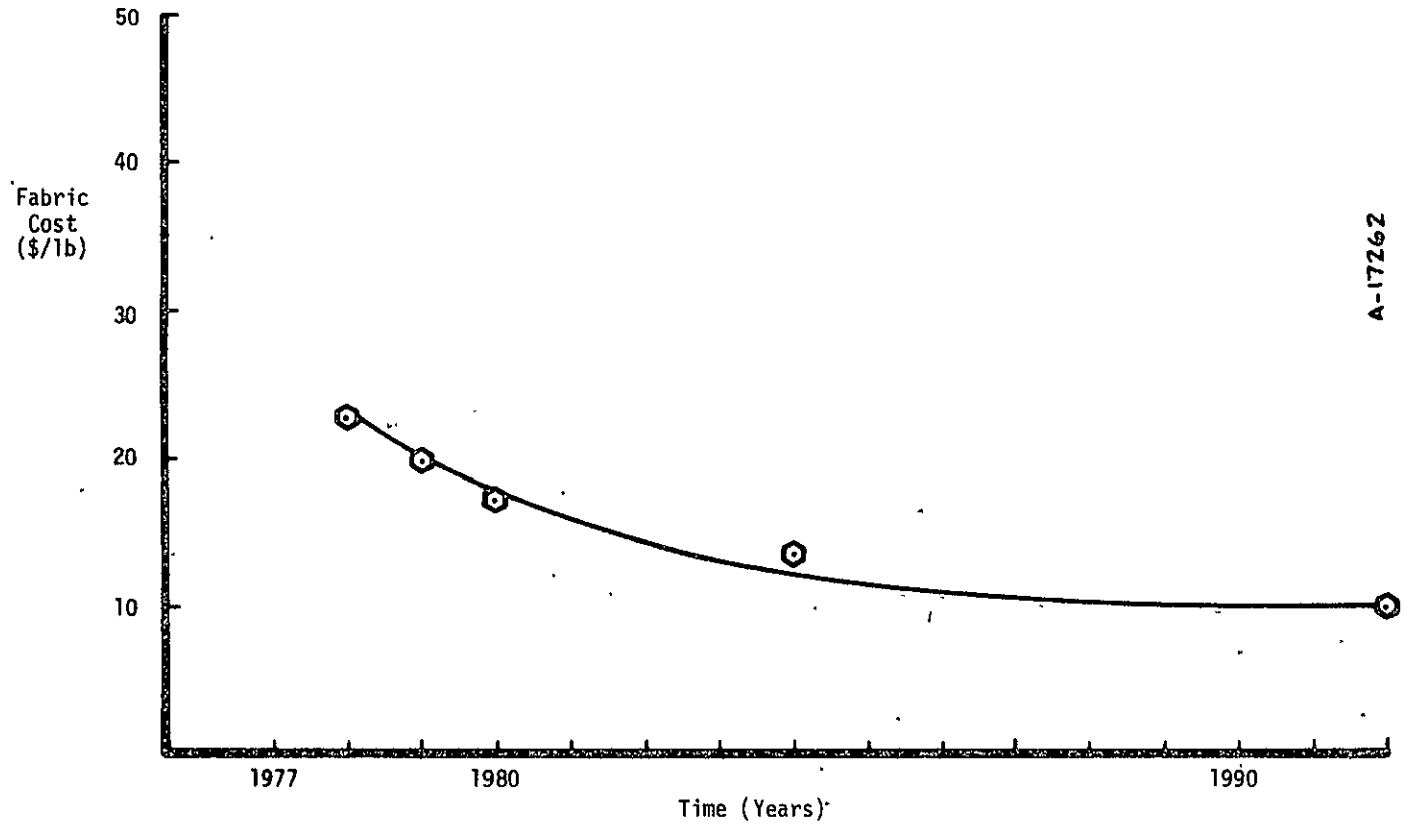

Figure 3-6. Cost projections for pitch precursor fabrics (Union Carbide VC-0149).

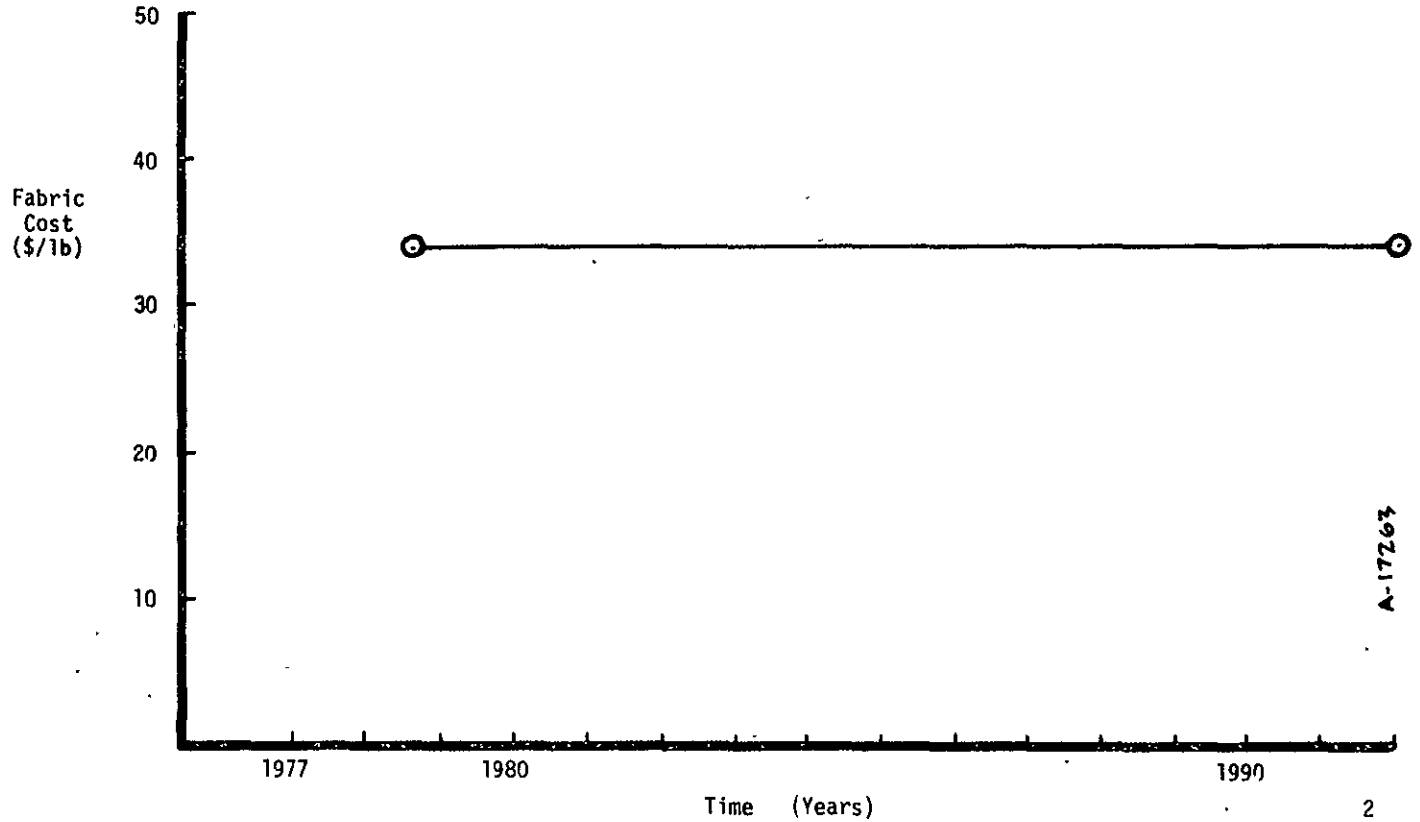

Figure 3-7. Projected costs for staple rayon precursor fabrics (HITCO CCA-28).

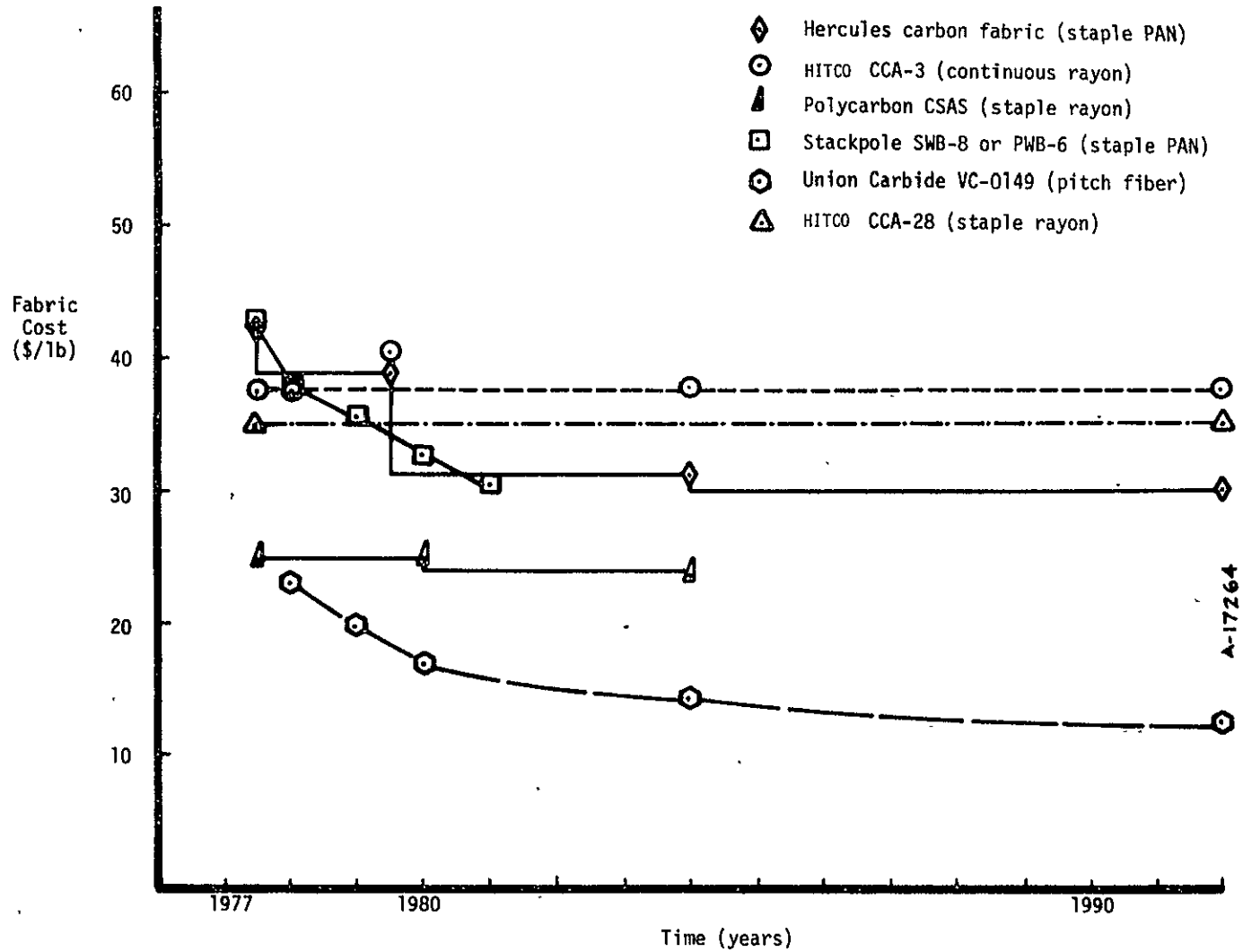

Figure 3-8. Comparison of projected costs.

test results and selection of the two candidate materials for full characterization.

3.2.1 Test Conditions

The screening test conditions were designed to simulate actual rocket motor firing conditions as closely as possible. Since the major emphasis was on the thermal performance of a material in a rocket nozzle, simulation of the following parameters was considered important:

- Heat flux to the material ($\dot{q}$)
- Reactive chemical species (H,O) composition

These two parameters were chosen because the former represents the simulation of in-depth temperature profile and the latter represents the simulation of surface chemical erosion. An exact simulation, of course, would not be possible, so some compromises were necessary for testing in the APG. Tables 3-4 and 3-5 compare screening test conditions and representative rocket motor firing conditions.

3.2.2 Model and Test Configurations -- Test Matrix

Models of the low cost candidate materials were machined from as-received billets into 90° and 20° ply orientations. The test model configuration is shown in Figure 3-9. The models with the composite plies in the 90° orientation were for nozzle throat materials simulation, and those with the 20° orientation were for exit cone material simulation. Two models for each ply orientation were made from the baseline rayon fabric (CCA-3) billets, MX 4926 and FM 5055 designations, to provide a repeatable data base.

The materials were tested in the APG, which is shown schematically in Figure 3-10, in a planar 2D nozzle configuration. In this configuration, as shown in Figure 3-11, two models were tested

TABLE 3-4. COMPARISON OF ROCKET MOTOR AND APG ENVIRONMENTS

Rocket Motor Convective Environment

$\frac{A}{A^*}$	λ (ft)	P_e (atm)	u_e (ft/sec)	h_e (Btu/lbm)	$\rho_e u_e C_H$ (lbm/ft^{2}sec)	$\dot{q}$ Btu/ft^2-sec)
1.0	3.1	26	3430	595	0.78	1170

ARC Plasma Generator Environment

$\frac{A}{A^*}$	P_e (atm)	h_e (Btu/lbm)	$\rho_e u_e C_H$ (lbm/ft^2-sec)	$\dot{q}_{cw}$ (Btu/ft^2-sec)
1.0	2.14	8742	0.163	920

TABLE 3-5. COMPARISON OF APG TEST GAS AND TYPICAL NOZZLE EXHAUST GAS EQUILIBRIUM COMPOSITION

Test Gas Equilibrium Composition
$2\ H_2O + CO + 8.3\ H_2$
Typical Nozzle Exhaust Gas H, C, O Equilibrium Composition
$2\ H_2O + CO$

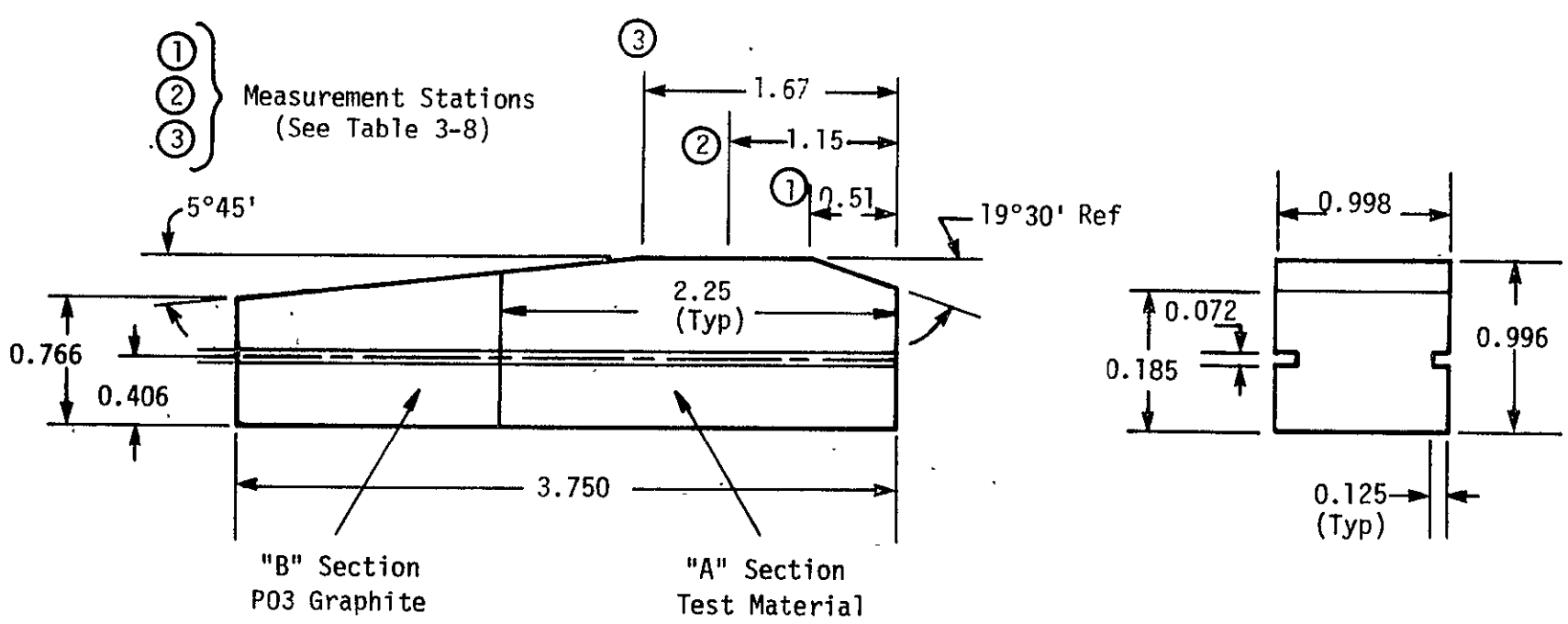

NOTE: All measurements are in inches

Figure 3-9. Typical screening test model.

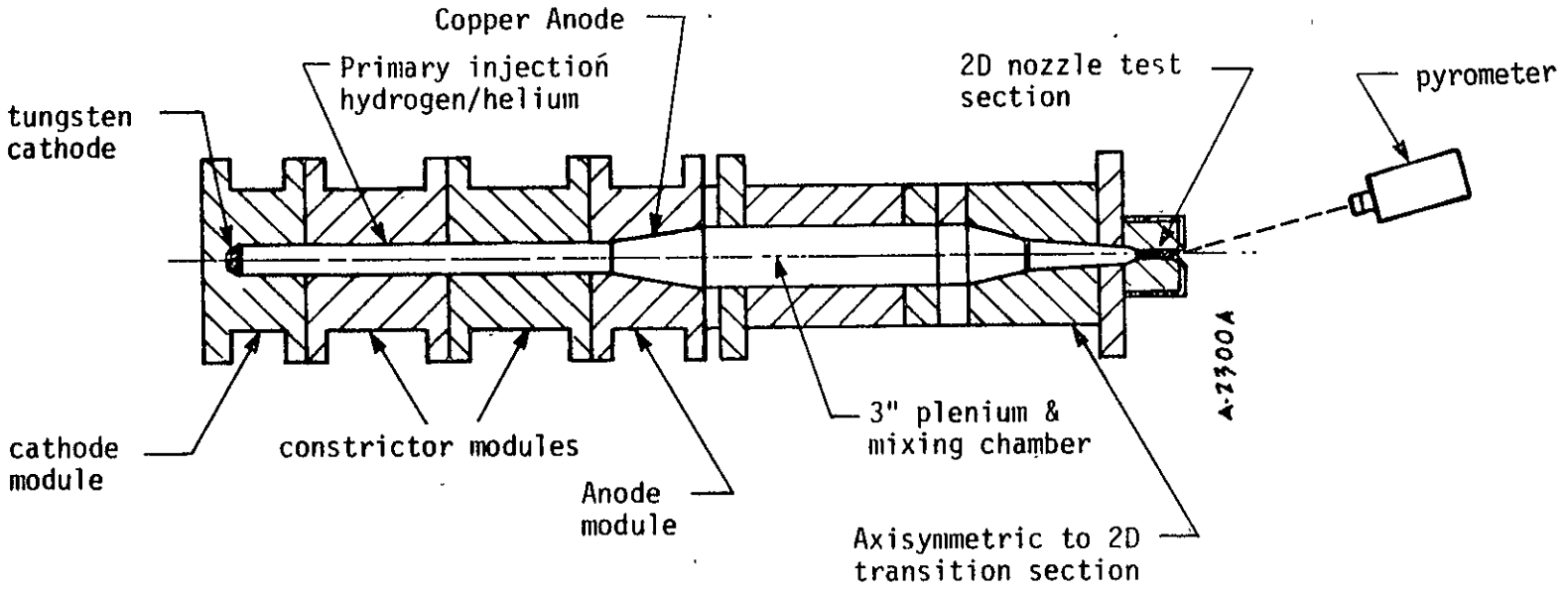

Figure 3-10. Acurex constrictor arc, rocket simulator configuration.

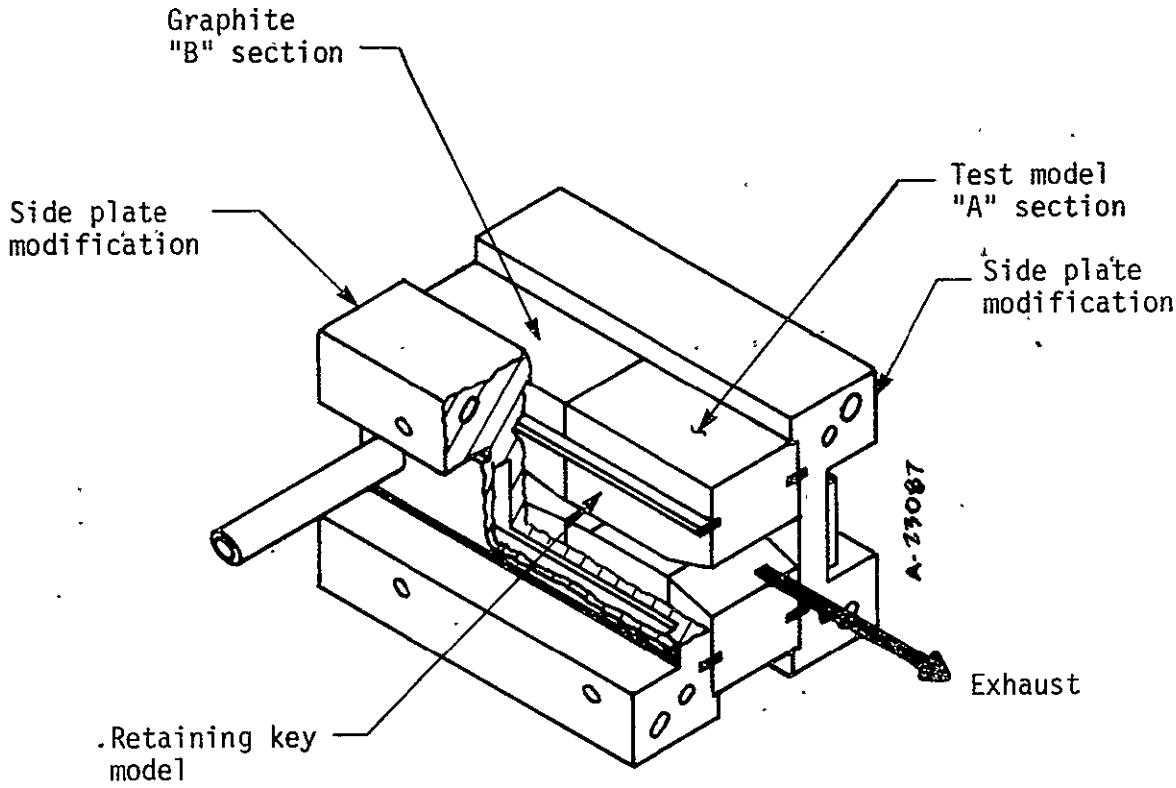

Figure 3-11. Test configuration.

simultaneously. Due to limited material supplied by the vendors, the throat entrance sections (Section B) were fabricated from pyrolytic graphite. Prior to testing, the volatile and cured resin contents were determined for each material and are presented in Table 3-6.

The test matrix for the screening program is presented in Table 3-7. Materials of the same generic class and ply orientation were arranged to be tested simultaneously on the premise that their performance would be similar. In some cases it was necessary to test one model with a dummy graphite model on the opposite wall.

3.2.3 Test Results

The materials screening test results are presented in Table 3-8. The performance data are presented as recession rate (in/sec) and mass loss rate (gm/sec). The recession of each model was obtained from pre- and post-test measurements taken at three locations (see Figure 3-9) and averaged. The mass loss data was, of course, determined from pre- and post-test model weights.

The recession and mass loss rate data were plotted in bar chart form for each material and ply orientation. These charts are presented in Figures 3-12, 3-13, 3-14 and 3-15, and provide an overall visual comparison of the ablation performance of the low cost materials with the baseline material: continuous rayon fabric carbon phenolic. The continuous rayon data have high, average, and low values since two models of each material were tested. As can be seen from the charts, the performance of most of the materials appears to be superior, or at least equal, to the baseline material. This is true especially for the PAN and one or two of the pitch fabric materials.

TABLE 3-6. PREPREG AND CURED RESIN CONTENT DATA

Laminate Supplier	Laminate Identity	Prepreg Resin Content (%)	Prepreg Volatile Content (%)	Cured Resin Content (%)
Fiberite	Karbon 419	36.3	4.2	29.0
Fiberite	Karbon 425	37.0	5.1	39.0
Fiberite	MX 4926	34.4	5.0	38.0
Fiberite	MX 4940 (CCA-28)	33.6	5.0	28.0
Fiberite	MX 4940 (CSAS)	36.5	5.0	38.0
Fiberite	Karbon 433	35.3	4.8	52.0[b]
Fiberite	Karbon 421	35.1	4.1	33.0
Fiberite	Karbon 414	34.1	4.2	32.0
Fiberite	Karbon 411	32.8	4.9	38.0
Fiberite	Karbon 408P	34.1	4.9	35.0
Fiberite	Karbon 418	33.1	3.6	43.0
U.S. Polymeric	FM 5055	30.2	3.0	50.0[b]
U.S. Polymeric	FM 5829	54.5	4.7	55.0
U.S. Polymeric	FM 5746	56.0	3.3	58.0
U.S. Polymeric	FM 5748	47.1	2.6	48.0
U.S. Polymeric	FM 5749[a]	31.5	4.2	54.0[b]
U.S. Polymeric	FM 5750[a]	35.4	3.5	44.0

[a]U.S. Polymeric also reports (with 150 psig achieved by press) a resin flow of 31.3% for the FM 5749 system and 18.7% for the FM 5750 material. All other U.S.P. prepreg systems are low flow (less than 5% by weight of the uncured prepreg).

AS-0012

[b]These data, based upon reported prepreg information, are suspect.

TABLE 3-7. NOZZLE MATERIAL SCREENING TEST MATRIX

Test No.	Prepreg/Laminate Identity	Fabric Designation	Ply Orientation	Precursor
1	MX4926-FIB[a]	CCA-3	90°	Rayon
2	MX4926-FIB	CCA-3	20°	
3	MX4926-FIB MX4940-FIB	CCA-3 CCA-28	90° 90°	
4	MX4940-FIB	CSAS	90°	
5	MX4940-FIB	CSAS	20°	
6	FM5055-USP[b]	CCA-3	90°	
7	FM5055-USP	CCA-3	20°	
8	FM5055-USP FM5829-USP	CCA-3 CCA-28	90° 90°	
9	FM5746-USP KARBON 433-FIB	G-2252 GSAS	90° 90°	
10	MX4926-FIB MX4940-FIB	CCA-3 CCA-28	20° 20°	
11	FM5055-USP FM5829-USP	CCA-3 CCA-28	20° 20°	
12	FM5746-USP KARBON 433-FIB	G-2252 GSAS	20° 20°	Rayon
13	KARBON 411-FIB KARBON 421-FIB	SWB-8 KFB	90° 90°	PAN

[a]FIB: denotes Fiberite
[b]USP: denotes U.S. Polymeric
[c]UNK: denotes unknown

TABLE 3-7. Concluded

Test No.	Prepreg/Laminate Identity	Fabric Designation	Ply Orientation	Precursor
14	FM5748-USP KARBON 425-FIB	SS2231 UNK[c]	90° 90°	PAN
15	KARBON 411-FIB KARBON 421-FIB	SWB-8 KFB	20° 20°	
16	FM5748-USP KARBON 425-FIB	SS2231 UNK	20° 20°	PAN
17	KARBON 408P-FIB KARBON 418-FIB	VC-0149 VC-0150	90° 90°	Pitch
18	FM5749-USP FM5750-USP	VC-0149 VC-0150	90° 90°	
19	KARBON 408P-FIB KARBON 418-FIB	VC-0149 VC-0150	20° 20°	
20	FM5749-USP FM5750-USP	VC-0149 VC-0150	20° 20°	
21 22	KARBON 419-FIB KARBON 419-FIB	W-502 W-502	90° 20°	Pitch
23 24	KARBON 414-FIB KARBON 414-FIB	PWB-6 PWB-6	90° 20°	PAN PAN

NOTES: 1. Runs 1, 2, 4, 5, 6, and 7 will be run with graphite dummy on opposite side; all others will be tested together.
2. Runs 23 and 24 will be additional runs to be made if time permits.

TEST CONDITION: P_e = 2.93 atm
h_e = 8713 Btu/lbm
q_{cw} = 982 Btu/ft^2-sec

TABLE 3-8. MATERIALS SCREENING TEST RESULTS

TEST NUMBER (MATRIX)	MODEL NO.	TEST NO. (ARC)	PREPREG/LAMINATE IDENTITY	FABRIC DESIG.	PLY ORIENT. (DEG)	MASS LOSS (GM)	TEST TIME (SEC)	MASS LOSS RATE (GM/SEC)	SURFACE RECESSION[a] 1	2 (IN)	3	AVE (IN)	RECESSION RATE (10^{-3} IN/SEC)
1	101	2977-01	MX 4926 -FIB	CCA-3	90	6.369	36.8	.173	.044	.055	.105	.068	1.848
2	201	2977-02	MX 4926 -FIB	CCA-3	20	6.024	36.8	.164	.021	.061	.082	.055	1.545
3	102	2978-01	MX 4926 -FIB	CCA-3	90	7.993	44.2	.181	.051	.075	.127	.084	1.900
3	103	2978-01	MX 4940 -FIB	CCA-28	90	9.066	44.2	.205	.036	.061	.116	.071	1.606
4	105	2978-02	MX 4940 -FIB	CSAS	90	7.985	38.3	.209	.030	.045	.116	.064	1.673
5	206	2978-03	MX 4940 -FIB	CSAS	20	7.397	38.0	.195	.013	.039	.098	.050	1.318
6	107	2978-04	FM 5055 -USP	CCA-3	90	5.880	29.0	.203	.025	.033	.104	.062	2.138
7	202	2979-01	FM 5055 -USP	CCA-3	20	6.248	35.9	.174	.014	.021	.095	.085	2.368
8	106	2979-02	FM 5055 -USP	CCA-3	90	7.184	33.9	.212	.030	.050	.110	.063	1.858
8	108	2979-02	FM 5829 -USP	CCA-3	90	7.147	33.9	.211	.030	.044	.111	.062	1.829
10	203	2979-03	MX 4926 -FIB	CCA-3	20	6.232	35.8	.174	.026	.057	.065	.049	1.371
10	204	2979-03	MX 4940 -FIB	CCA-28	20	6.832	35.8	.193	.034	.049	.056	.046	1.287
9	109	2979-04	FM 5746 -USP	G-2252	90	6.381	35.5	.180	.056	.066	.068	.065	1.834
9	110	2979-04	KARBON 433 -FIB	GSAS	90	9.976	35.5	.281	.080	.118	.100	.099	2.793
11	207	2979-05	FM 5055 -USP	CCA-3	20	6.570	37.3	.176	.023	.031	.038	.031	.831
11	208	2979-05	FM 5829 -USP	CCA-28	20	7.285	37.3	.195	.031	.060	.074	.055	1.475
12	209	2979-06	FM 5746 -USP	G-2252	20	7.600	36.3	.210	.063	.080	.105	.083	2.290
12	210	2979-06	KARBON 433 -FIB	GSAS	20	6.326	36.3	.174	.038	.044	.057	.046	1.269
14	113	2985-01	FM 5748 -USP	SS2231	90	7.364	29.6	.249	.014	.019	.026	.0197	.666
13	112	2985-02	KARBON 421 -FIB	KFB	90	7.152	31.1	.230	.023	.030	.038	.0303	.976
15	211	2985-03	KARBON 411 -FIB	SWB-8	20	5.730	31.9	.180	.011	.018	.023	.0173	.543
15	212	2985-03	KARBON 421 -FIB	KFB	20	6.21	31.9	.195	.025	.037	.046	.036	1.130
16	213	2986-01	FM 5748 -USP	SS2231	20	4.514	24.8	.182	.008	.012	.013	.011	.444
16	214	2986-01	KARBON 425 -FIB	PAN	20	5.106	24.8	.206	.014	.022	.026	.021	.847
17	115	2988-01	KARBON 408P -FIB	VC-0149	90	6.041	37.3	.162	.025	.025	.034	.028	.752
17	116	2988-01	KARBON 418 -FIB	VC-0150	90	8.653	37.3	.232	.023	.030	.035	.029	.779
18	117	2988-02	FM 5749 -USP	VC-0149	90	10.067	36.2	.278	.014	.017	.022	.018	.497
18	118	2988-02	FM 5750 -USP	VC-0150	90	8.347	36.2	.231	.037	.043	.048	.043	1.188
19	215	2988-03	KARBON 408P -FIB	VC-0149	20	4.723	31.8	.149	.011	.017	.027	.018	.567
19	216	2988-03	KARBON 418 -FIB	VC-0150	20	8.865	31.8	.279	.015	.022	.038	.025	.787
20	217	2988-04	FM 5749 -USP	VC-0149	20	6.830	33.0	.207	.042	.051	.056	.050	1.517
20	218	2988-04	FM 5750 -USP	VC-0150	20	4.869	33.0	.148	.021	.031	.043	.032	.971
21	119	2989-01	KARBON 419 -FIB	W-502	90	6.964	34.5	.202	.043	.043	.050	.045	1.304
22	219	2989-02	KARBON 419 -FIB	W-502	20	5.505	33.8	.163	.006	.021	.036	.021	.622
23	120	2989-03	KARBON 414 -FIB	PWB-6	90	6.723	32.9	.204	.023	.032	.046	.034	1.033
25	111A	2989-04	KARBON 411 -FIB	SWB-8	90	6.247	33.0	.190	.029	.029	.036	.031	.941
25	114A	2989-04	KARBON 425 -FIB	PAN	90	5.787	33.0	.176	.035	.043	.050	.043	1.305
24	220	2989-05	KARBON 414 -FIB	PWB-6	20	5.382	31.3	.172	.021	.026	.035	.027	.863

[a]See Figure 3-9

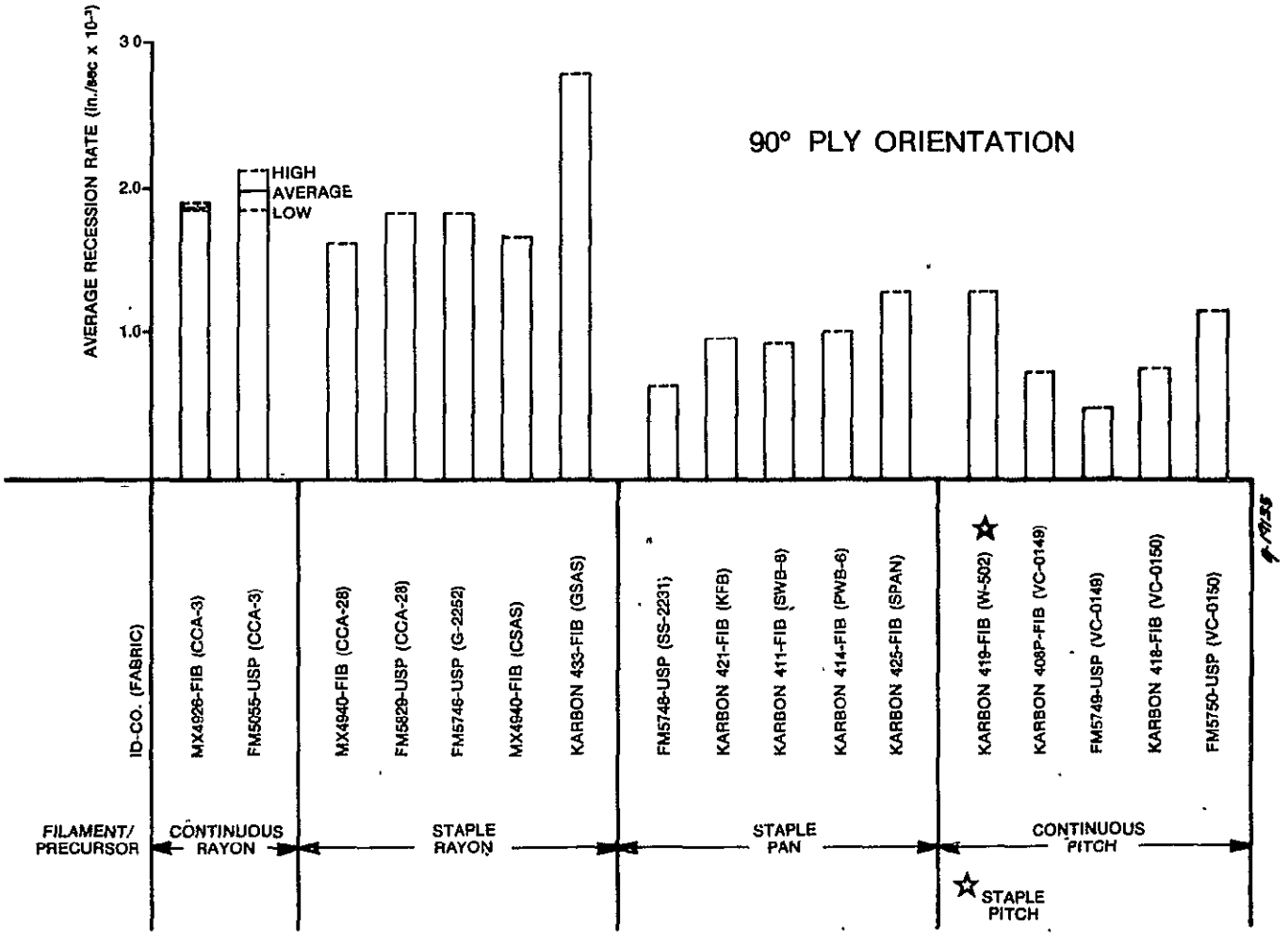

Note: FIB denotes Fiberite; USP denotes U.S. Polymeric.

Figure 3-12. Summary of recession rate data from screening tests for 90° ply orientation.

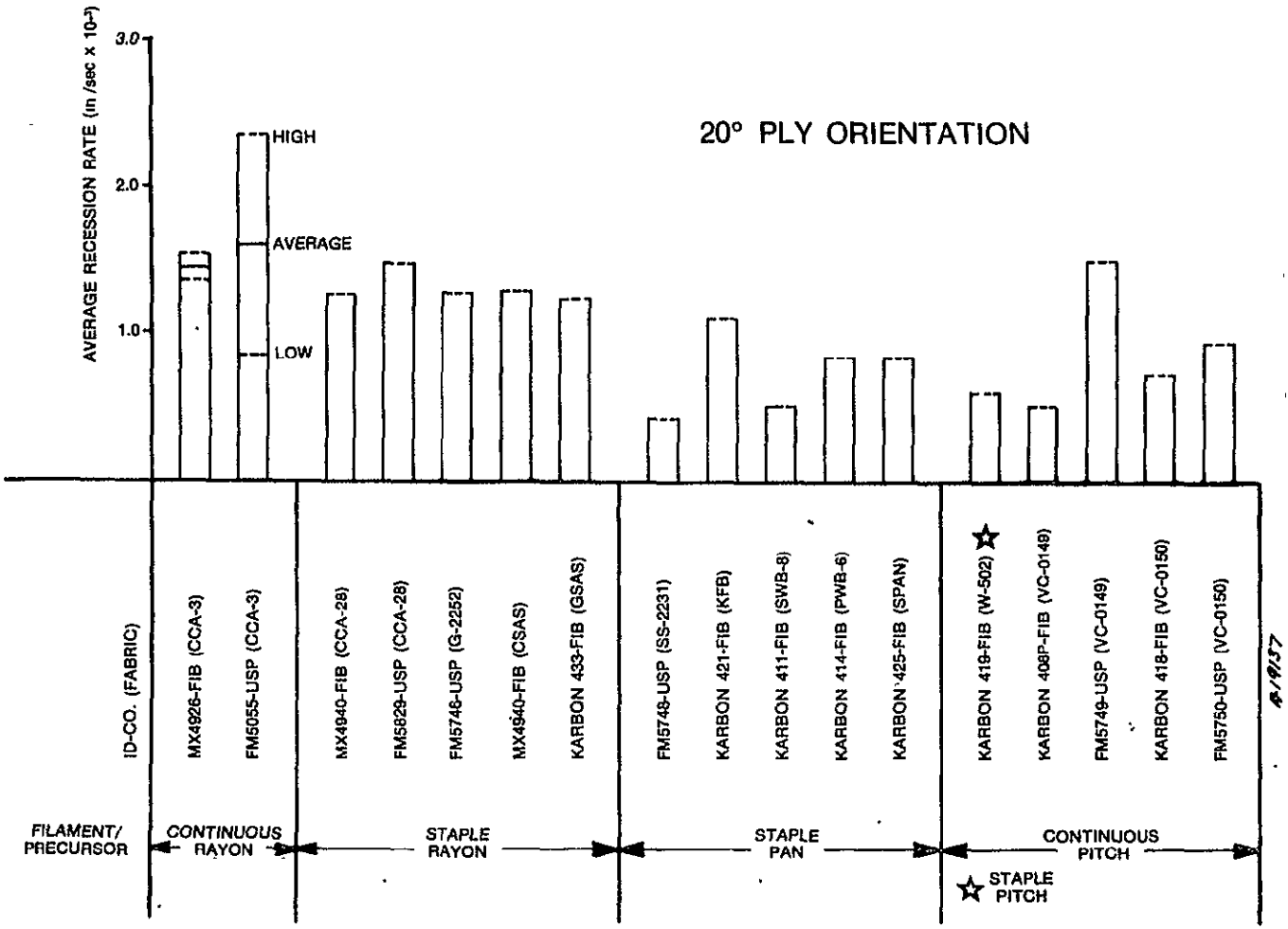

Note: FIB denotes Fiberite; USP denotes U.S. Polymeric.

Figure 3-13. Summary of recession rate data from screening tests for 20° ply orientation.

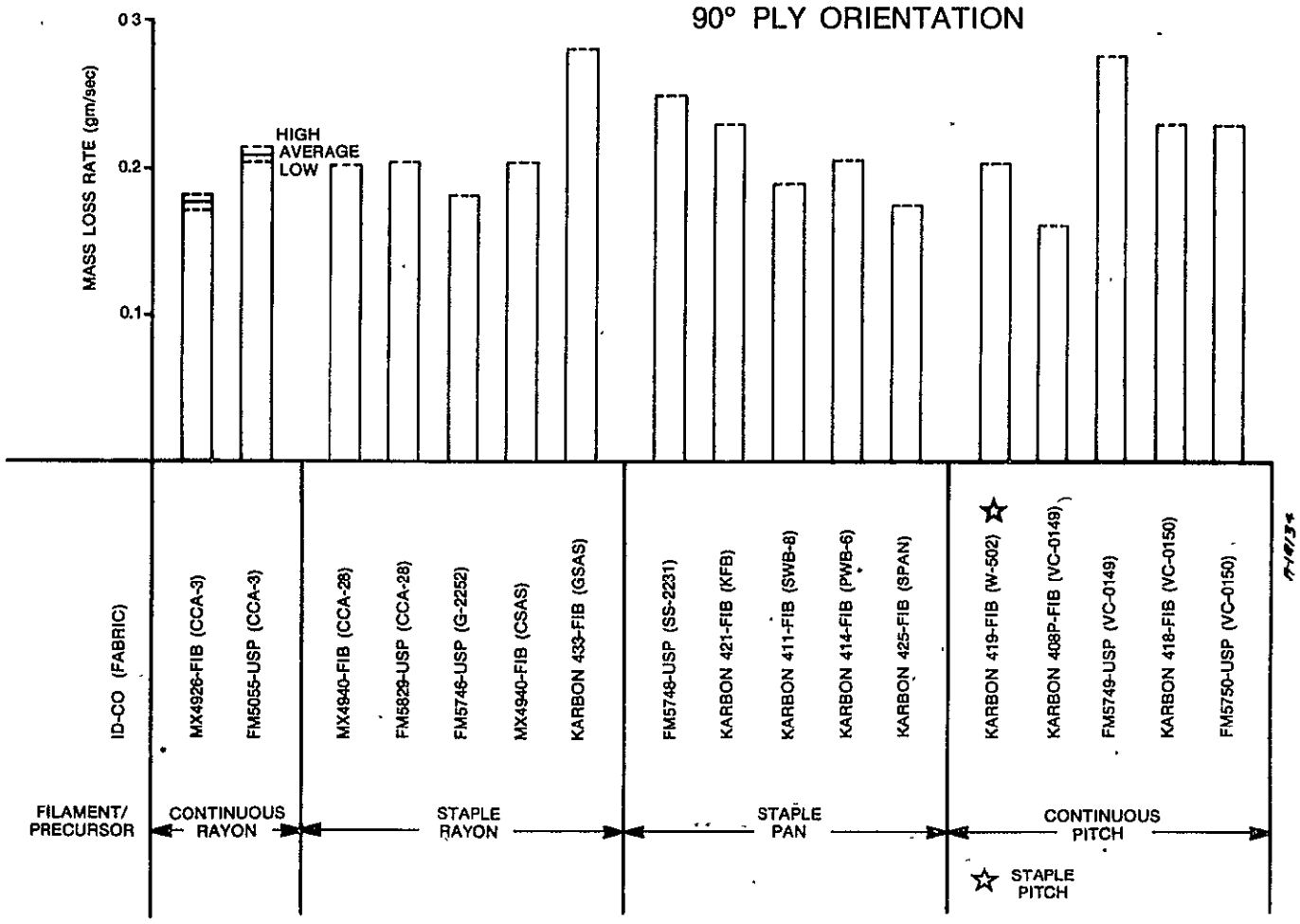

Note: FIB denotes Fiberite; USP denotes U.S. Polymeric.

Figure 3-14. Summary of mass loss rate data from screening tests for 90° ply orientation.

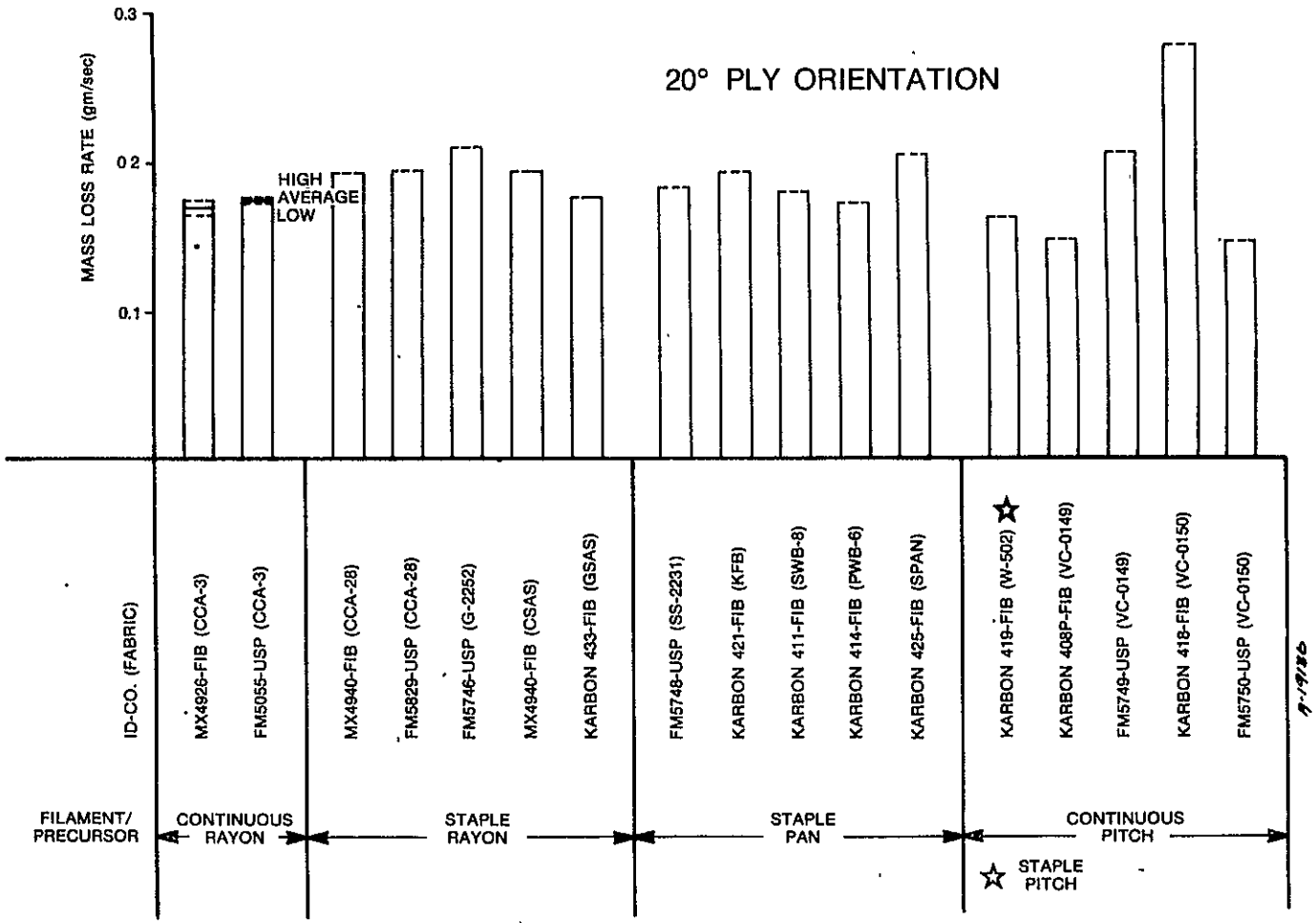

Note: FIB denotes Fiberite; USP denotes U.S. Polymeric.

Figure 3-15. Summary of mass loss rate data from screening tests for 20° ply orientation.

Post-test photographs were taken of each material class tested. Typical post-test surface conditions for these materials are shown in Figure 3-16.

From the screening test results, two generic materials were selected for full thermophysical property characterization. The main objective of this program was to study low cost materials; however, the selection was based on ablation performance and material availability as well as cost. The two materials chosen were Fiberite's Karbon 408P (pitch precursor, VC-0149) and Karbon 411 (PAN precursor, SWB-8). Staple rayon performed almost equally as well but was not selected due to the questionable availability of rayon fabrics and the high cost of rayon.

Table 3-9 compares the ablation performance and cost of the two selected materials with the baseline continuous rayon fabric (CCA-3). As can be seen, the pitch-based material not only performed well, but the cost is significantly lower.

3.3 MATERIALS FULL CHARACTERIZATION PROGRAM

Since the properties for charring ablative materials are dependent upon fabric orientation and thermodynamic state (T and ρ), material properties were evaluated for both virgin and charred composites of the two selected materials from the screening tests in two fabric orientations (90° and 0°). The properties determined were:

- Decomposition kinetics
- Elemental composition
- Heat of formation
- Density
- Specific heat capacity
- Thermal conductivity

Figure 3-16. Typical post-test photographs of APG screening material specimens.

(Pages 3-37 through 3-43)

AS/H-357b

Post-test surface condition of continuous rayon fabric/phenolic baseline nozzle material.

Post-test surface condition of staple rayon fabric/phenolic nozzle candidate materials.

Material used for full characterization
(SWB-8 fabric)

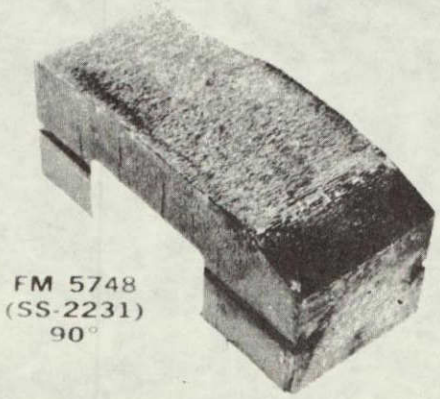

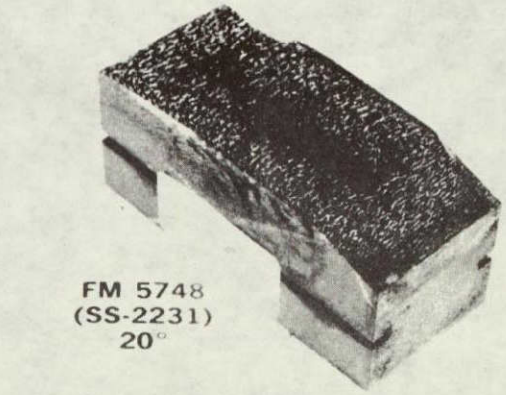

Alternate material (SS-2231 fabric)

Post-test surface condition of staple PAN fabric/phenolic nozzle material candidates.

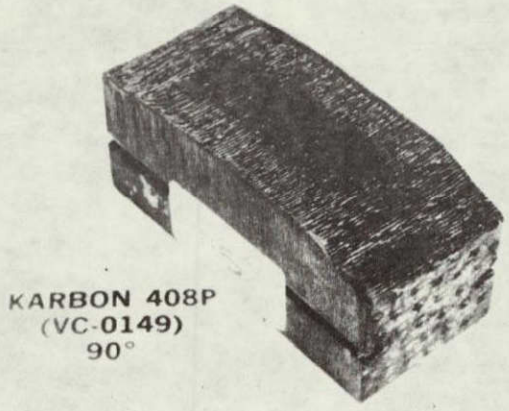

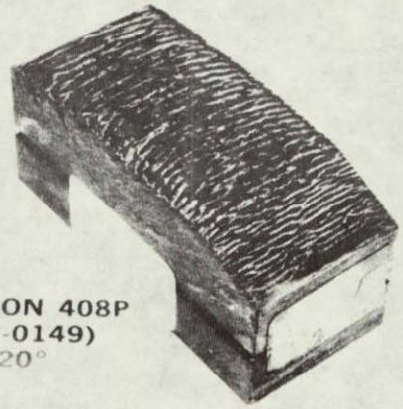

Material used for full characterization
(VC-0149 fabric)

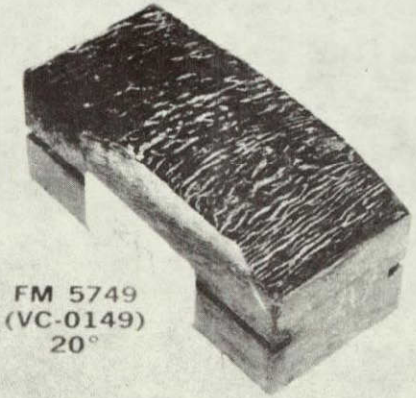

Alternate material (VC-0149 fabric)

Post-test surface condition of continuous pitch fabric/phenolic nozzle material candidates.

The above properties are discussed in Sections 3.3.1 through 3.3.6, respectively. The materials for which these properties were determined are:

- Fiberite -- Karbon 408P (pitch fabric)
- Fiberite -- Karbon 411 (PAN fabric)

3.3.1 Decomposition Kinetics

Resinous materials degrade in a highly complex manner. These complex degradation mechanisms are generally not understood sufficiently to formulate exact analytical expressions. Therefore, empirical homogeneous kinetics are normally used to describe the degradation.

The thermal degradation reactions, if assumed to be irreversible, may be described by a psuedo-order classical rate expression:

$$\left(\frac{\partial \rho_i}{\partial \theta}\right)_y = - B_i \exp\left(-\frac{E_{a_i}}{RT}\right) \rho_{o_i} \left(\frac{\rho_i - \rho_{r_i}}{\rho_{o_i}}\right)^{\psi_i} \qquad (3\text{-}1)$$

The kinetic parameters (activation energy E_{a_i}, frequency factor B_i, and reaction order ψ_i), can be determined by reducing thermogravimetric analysis (TGA) data.

The multiple-linear-regression analysis is one of the procedures which can be used to reduce TGA data. This analysis has the capability to evaluate the three kinetic parameters simultaneously and also to curve fit the input data in a theoretically optimal manner.

The evaluation procedure is straightforward. Equation (3-1) is first linearized to yield the following form:

$$\ln\left(-\frac{d\,\rho_i/\rho_{o_i}}{d\theta}\right) = \ln B_i - \frac{E_{a_i}}{R}\left(\frac{1}{T}\right) + \psi_i \ln\left(\frac{\rho_i - \rho_{r_i}}{\rho_{o_i}}\right) \qquad (3\text{-}2)$$

The bracketed terms in Equation (3-2) can be obtained from TGA data. As the number of data points is larger than three, the equations will overdetermine the values of kinetic constants. Hence, an optimum curve fitting procedure is required. If we write Equation (3-2) in matrix notation, it has the form:

$$B = AX \qquad (3\text{-}3)$$

where B and A are matrices whose elements are determined from the TGA data and X is the matrix of best fit parameters. The curve fitting procedure is then applied by multiplying Equation (3-3) by the transpose of A:

$$A^T B = A^T A X \qquad (3\text{-}4)$$

where $A^T A$ is square and determinate. Hence, the X matrix can be evaluated by Gaussian elimination from the transformed normal equations.

The experimental data used for data reduction are obtained from thermogravimetric analysis (TGA). TGA is an experimental procedure to measure the pyrolysis mass loss history at a prescribed heating rate. The TGA analyses are a necessary step in determining a material's decomposition constants which are used in Acurex's Charring Material Ablation (CMA) code (Reference 7). The TGA testing was conducted at the Acurex materials laboratory using a Dupont thermal analyzer. The heating agent used was nitrogen to prevent any surface chemical reaction. A heating rate of 10^{o}C per minute was used to obtain TGA data since the higher the heating rate, the lower the accuracy of the data. This rate of 10^{o}C per minute is a value that has yielded reliable data in the past. In addition, the

pyrolysis kinetics of charring materials behave almost linearly with respect to heating rate. The results from the TGA tests are presented in Figures 3-17 and 3-18 as percent weight retention versus temperature (^{o}C).

The Acurex CMA model requires the instantaneous density of the composite to obey the relationship:

$$\rho = \Gamma\ (\rho_A + \rho_B) + (1-\Gamma)\rho_C \qquad (3\text{-}5)$$

where A and B represent components of the resin, C represents the reinforcement material, and Γ is the resin volume fraction. Each of the three components can decompose following the relation in Equation (3-1), where ρ_{ri} is the residual density of component i, and ρ_{oi} is the original density of component i. The density of phenolic (81.0 lbm/ft^3) is well known and was employed for the initial density of the resin components A and B while the residual densities were computed from the TGA data employing Equation (3-5 The kinetic constants were calculated by the multiple-linear-regression analys described above. However, a set of kinetic constants for phenolic resin that has been in use at Acurex for many years was found to be quite representative of the data for Karbon 411 and were adopted for that material. Table 3-10 presents the decomposition constants for the two candidate materials: Karbon 408P and Karbon 411. Figures 3-17 and 3-18 illustrate a comparison of the predicted weight loss behavior using these kinetics with the original TGA data for Karbon 408P and Karbon 411, respectively. The predictions were obtained by integrating Equation (3-1) using the decomposition constants.

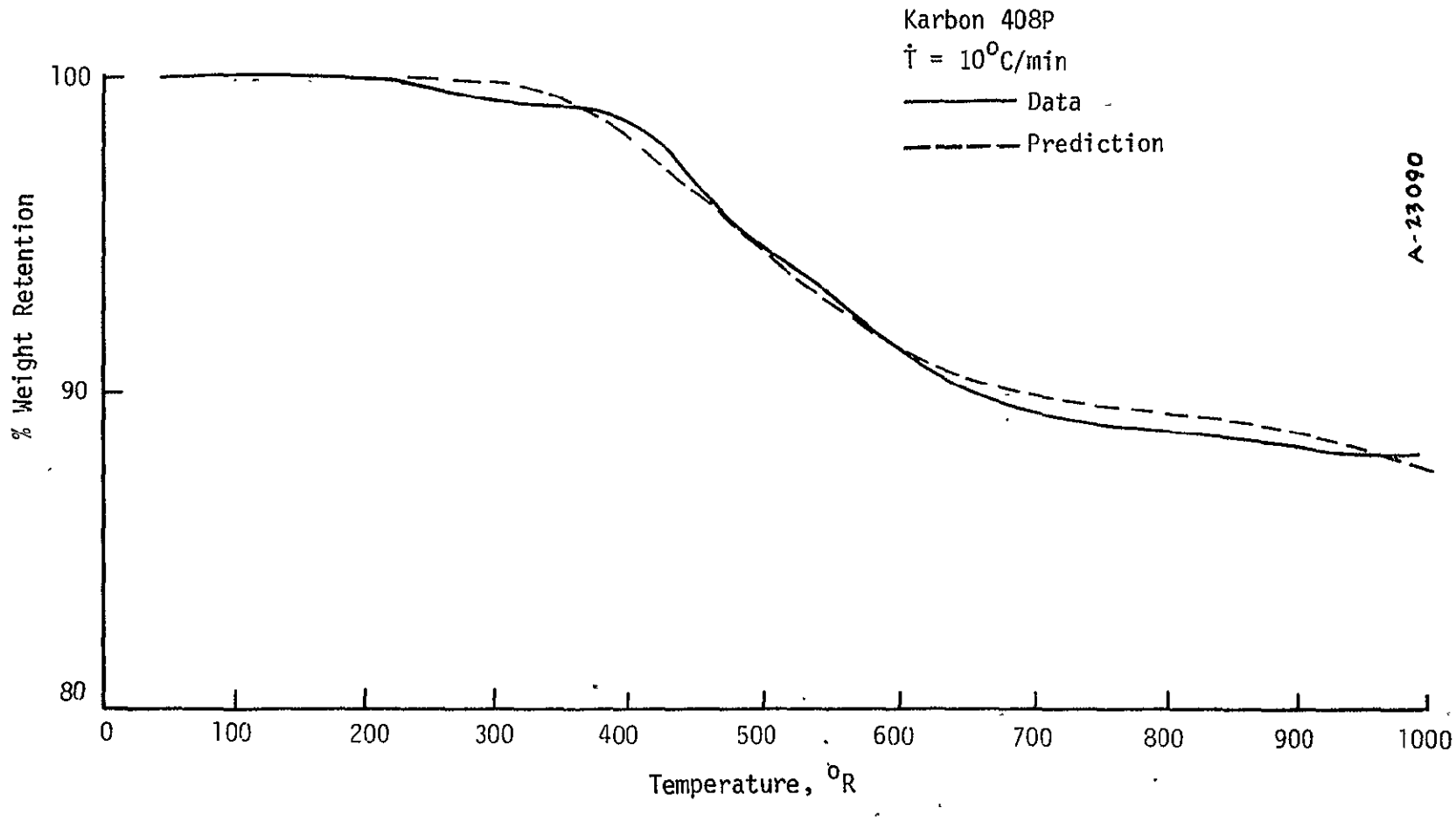

Figure 3-17. Comparison of TGA data and CMA prediction for Karbon 408P.

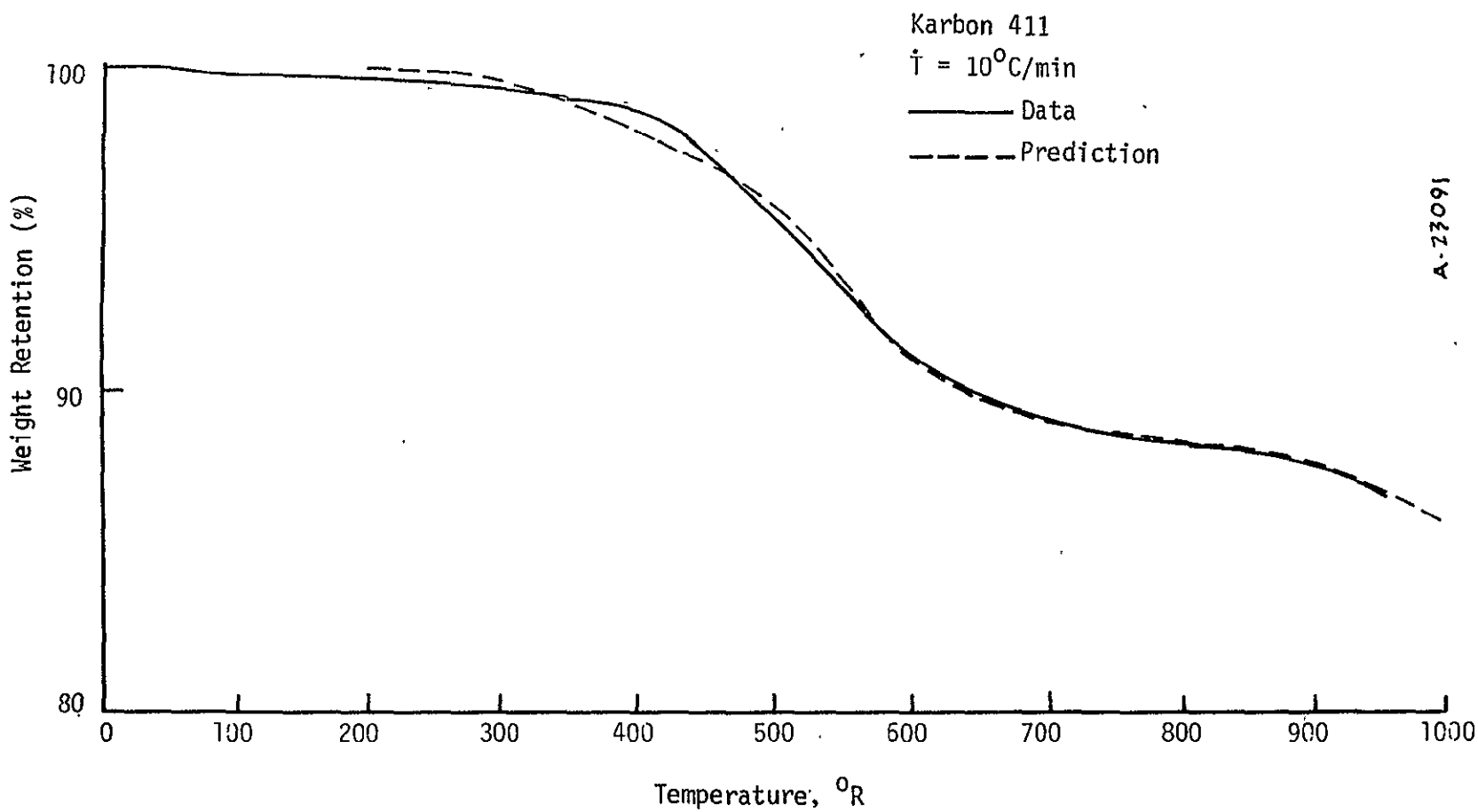

Figure 3-18. Comparison of TGA data and CMA prediction for Karbon 411.

TABLE 3-10. DECOMPOSITION CONSTANTS FOR KARBON 408P AND KARBON 411

Material	Reaction	ρ_{o_i} (lbm/ft^3)	ρ_{r_i} (lbm/ft^3)	B_i (sec^{-1})	E_{a_i}/R (^oR)	ψ_i	T_{react_i} (^oR)	Γ
KARBON 408P	A	81.00	54.388	6.922×10^1	1.235×10^4	2.232	640	0.4397
	B	0.0	0.0	0.0	0.0	0.0	10,000	
	C	118.05	115.326	2.334×10^7	8.194×10^4	2.943	1,950	
KARBON 411	A	20.25	12.00	1.40×10^4	15.4×10^3	3.0	600	0.4539
	B	60.75	43.954	4.48×10^9	36.8×10^3	3.0	600	
	C	109.86	102.684	1.576×10^7	43.84×10^3	2.0	1,962	

AS-0013

3.3.2 Elemental Composition

The elemental composition of the pyrolysis gas and char must be known in order to generate surface thermochemistry tables and determine the pyrolysis gas enthalpy. The char composition for carbon phenolic materials is easy to determine as it is merely carbon residue. To determine the pyrolysis gas composition, however, requires a knowledge of both the virgin material composition and the residual mass fraction. The virgin material composition is usually provided by the manufacturers, and the residual mass fraction is known from TGA. With this information, the elemental composition of pyrolysis gas can then be evaluated by the following equations:

$$K_{py_i} = \frac{K_{v_i}}{1 - r} \tag{3-6}$$

$$K_{py_c} = \frac{K_{v_c} - r}{1 - r} \tag{3-7}$$

where K is the elemental mass fraction; r is the residual mass fraction; subscripts py and v denote pyrolysis gas and virgin material, respectively; c and i refer to carbon and other elements that are present (e.g., H, N, O), respectively.

The evaluated pyrolysis gas elemental compositions of the two candidate materials are presented in Table 3-11.

TABLE 3-11. ELEMENTAL COMPOSITION OF PYROLYSIS GAS

Type of Material	Mass Fraction		
	H	C	O
Karbon 408P	0.19559	0.28696	0.51745
Karbon 411	0.20783	0.24236	0.54981

3.3.3 Heat of Formation

The virgin material heat of formation is determined from:

$$\Delta H_{f_{virgin}} = K(\Delta H_{f_{resin}}) + (1 - K)(\Delta H_{f_{reinf}}) \qquad (3\text{-}8)$$

where K is the resin mass fraction.

Both test specimens were comprised of a carbon reinforcement and a phenolic resin. The heat of formation of the resin ($\Delta H_{f_{resin}}$) is -1080 Btu/lbm, while the carbon reinforcement has a heat of formation ($\Delta H_{f_{reinf}}$) of zero Btu/lbm.

Table 3-12 presents the evaluated heats of formation for the Karbon 408P and Karbon 411 materials.

TABLE 3-12. VIRGIN HEATS OF FORMATION

Material	H_f (Btu/lbm)
Karbon 408P	-378.0
Karbon 411	-410.4

3.3.4 Density

The virgin material density was determined by precise weight and dimension measurement of samples which have regular geometric shapes. The char density is evaluated by multiplying the virgin material density by the residual mass fraction which was obtained from the TGA data.

The measured or evaluated densities are shown in Table 3-13.

TABLE 3-13. DENSITIES OF CANDIDATE MATERIALS

Materials	Virgin Density	Char Density
Karbon 408P	101.759	88.531
Karbon 411	96.760	81.472

3.3.5 Specific Heat Capacity

The specific heat of the virgin material was determined by graphical differentiation of specific enthalpy versus temperature curves. The enthalpy was measured using an ice mantle calorimeter. The calorimeter consists of a copper well, a distilled water vessel surrounding the copper well, an ice bath surrounding the vessel, and an insulation-filled container surrounding the ice bath. An ice mantle is formed on the outer surface of the copper well.

The material sample is heated to the desired uniform temperature in a muffle furnace and then dropped directly from the furnace into the calorimeter. The energy lost by the sample as it cools results in a volume change in the distilled water due to the partial melting of the ice mantle. This volume change is quantitatively related to the original energy of the sample.

The enthalpy results of the ice calorimeter tests conducted for the two materials are shown in Figures 3-19 and 3-20. The best fit of the data was a constant specific heat of 0.39 Btu/lbm-^{o}R for Karbon 408P and 0.45 Btu/lbm-^{o}R for Karbon 411 in the temperature range tested.

Table 3-14 presents the specific heat of these materials to 6000^{o}R. The values at higher temperatures were extrapolated from previous data for similar carbon phenolics. The char specific heat, however, need not be determined since the specific heat capacity of carbon is known.

TABLE 3-14. VIRGIN MATERIAL SPECIFIC HEAT CAPACITY

Materials	Temperature (^{o}R)	C_p (Btu/lbm-^{o}R)
Karbon 408P	530	0.390
	800	0.390
	1000	0.390
	1160	0.390
	2000	0.390
	3000	0.493
	4000	0.498
	5000	0.500
	6000	0.500
Karbon 411	530	0.450
	800	0.450
	1000	0.450
	1160	0.450
	1500	0.450
	2000	0.450
	3000	0.493
	4000	0.498
	5000	0.500
	6000	0.500

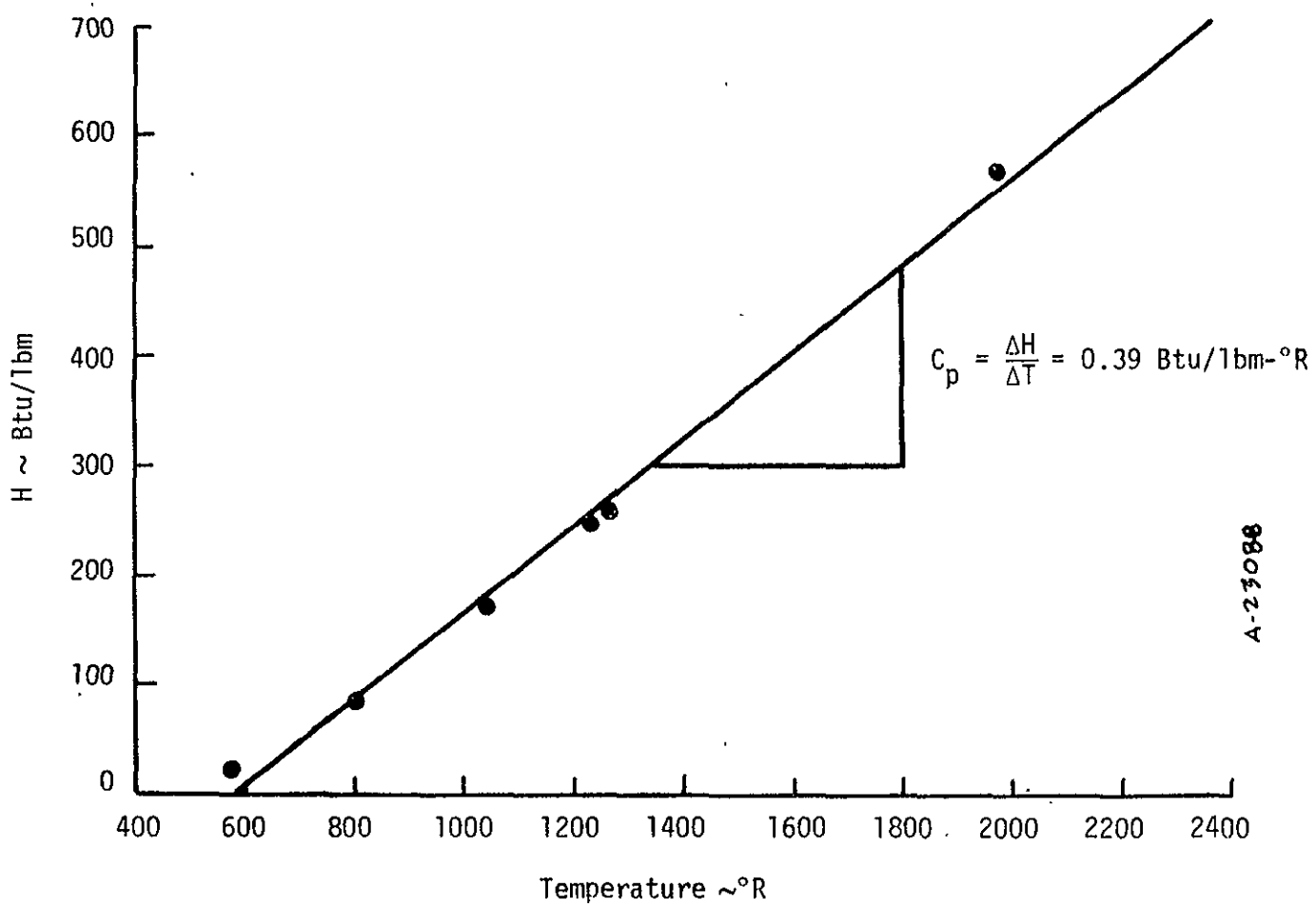

Figure 3-19. Ice calorimeter data for Karbon 408P.

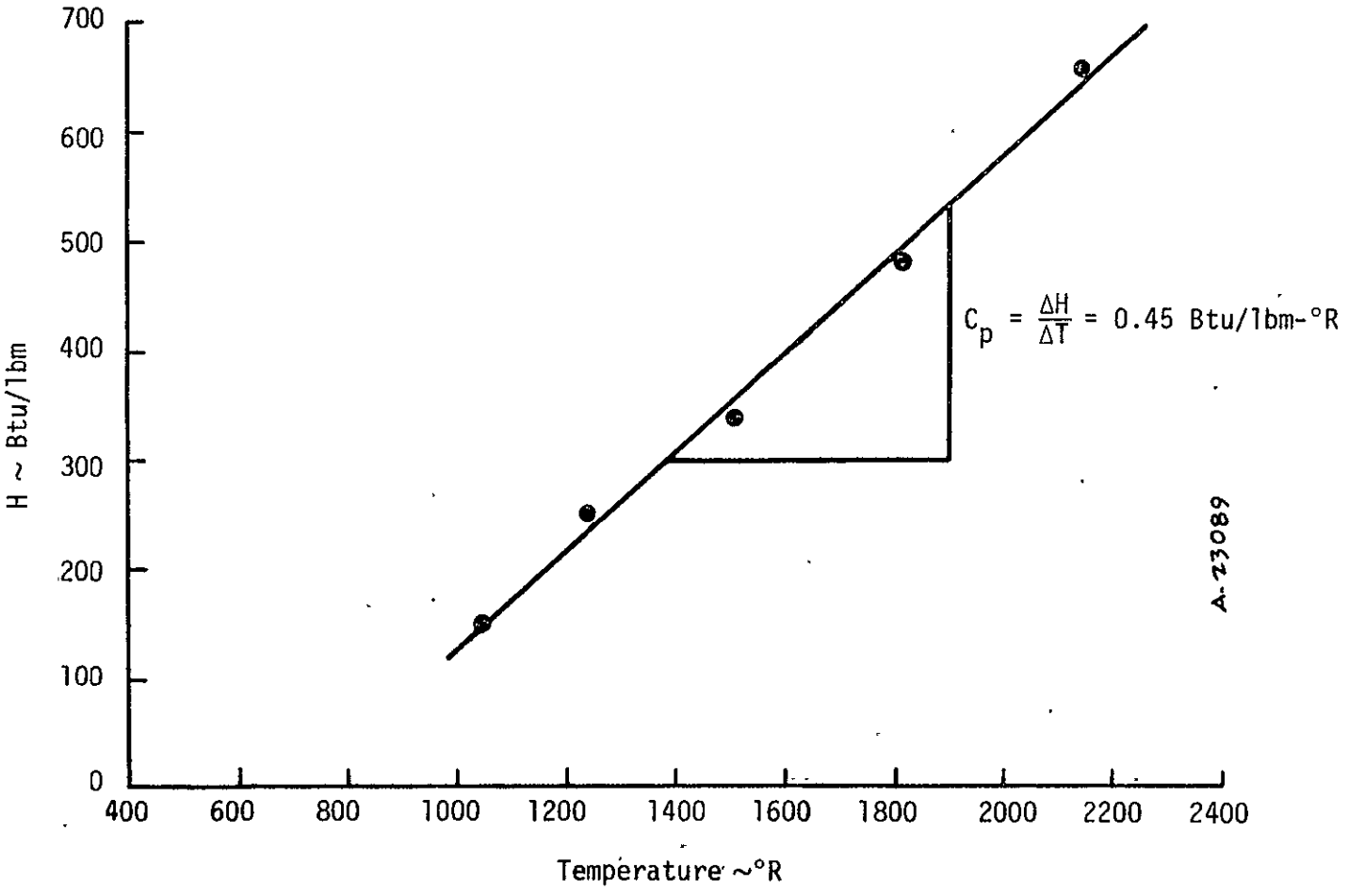

Figure 3-20. Ice calorimeter data for Karbon 411.

3.3.6 Thermal Conductivity

The material thermal conductivity was determined by two separate techniques. The applicability of each technique is dependent on the temperature and state of the material. The conventional technique is applicable for the virgin material over the temperature range from room temperature to approximately 700°F. The dynamic technique is applicable for the virgin, partially charred, or fully charred material over the temperature range from 700°F to approximately 4000°F.

3.3.6.1 Virgin Thermal Conductivity

The virgin material thermal conductivity test procedure consists of sandwiching a test specimen (2-inch diameter by 1/2-inch thick) between two pieces of a reference material with known thermal properties. A heat source is applied to one piece of the reference material, and a water cooled heat sink is impressed on the other side. Thermocouples are placed at material interfaces to measure the temperature differences across the materials.

The basic thermal conductivity unit was the Dynatech Model TCFCM-N20 located at McDonnell-Douglas Astronautics Company (MDAC). This apparatus was tied into an Autodata 9 type unit to monitor and print the temperature data. The output was fed into a computer, generating the thermal conductivity as a function of temperature. The temperature range for the thermal conductivity test was approximately 545°R to 1200°R. Both 90° and 0° layup angles were tested.

The virgin material thermal conductivity test results were much higher than anticipated for the materials tested. Therefore, at the request of Acurex, MDAC checked their apparatus and found a defective heater which caused the data to be high. MDAC then ran a series of

calibration tests and generated correction factors which were a function of conductivity level and temperature. The corrected conductivities for Karbon 408P and Karbon 411 are presented in Figures 3-21 and 3-22, respectively. Unfortunately, these corrected data did not agree well with the values determined analytically with the CMA code when generating dynamic conductivities using the arc test thermocouple data (Section 3.3.6.2). Consequently, the MDAC data is considered suspect and was not relied upon in the material characterization.

3.3.6.2 Dynamic Thermal Conductivity

The dynamic thermal conductivity technique is a combined experimental and analytical technique which has the inherent advantage that the char characteristics of the materials are accurately duplicated. This technique has been described in detail in References 8 through 11, and thus, will only be summarized in the paragraphs below.

The analysis portion of this procedure involves solving the governing equation for transient one-dimensional heat conduction in a charring ablating material. Incorporated within this equation is the model for defining the thermal conductivity of the partially-charred and fully-charred materials. This model is represented by the equation:

$$k = (1 - \chi)\, k_c + \chi k_v \qquad (3\text{-}9)$$

where χ is the mass fraction of virgin material, and k_c and k_v are the thermal conductivities for charred and virgin materials, respectively. The analytical procedure for defining the thermal conductivity of in-depth charring materials involves solving the governing one-dimensional conservation of energy and mass equations for an impressed surface

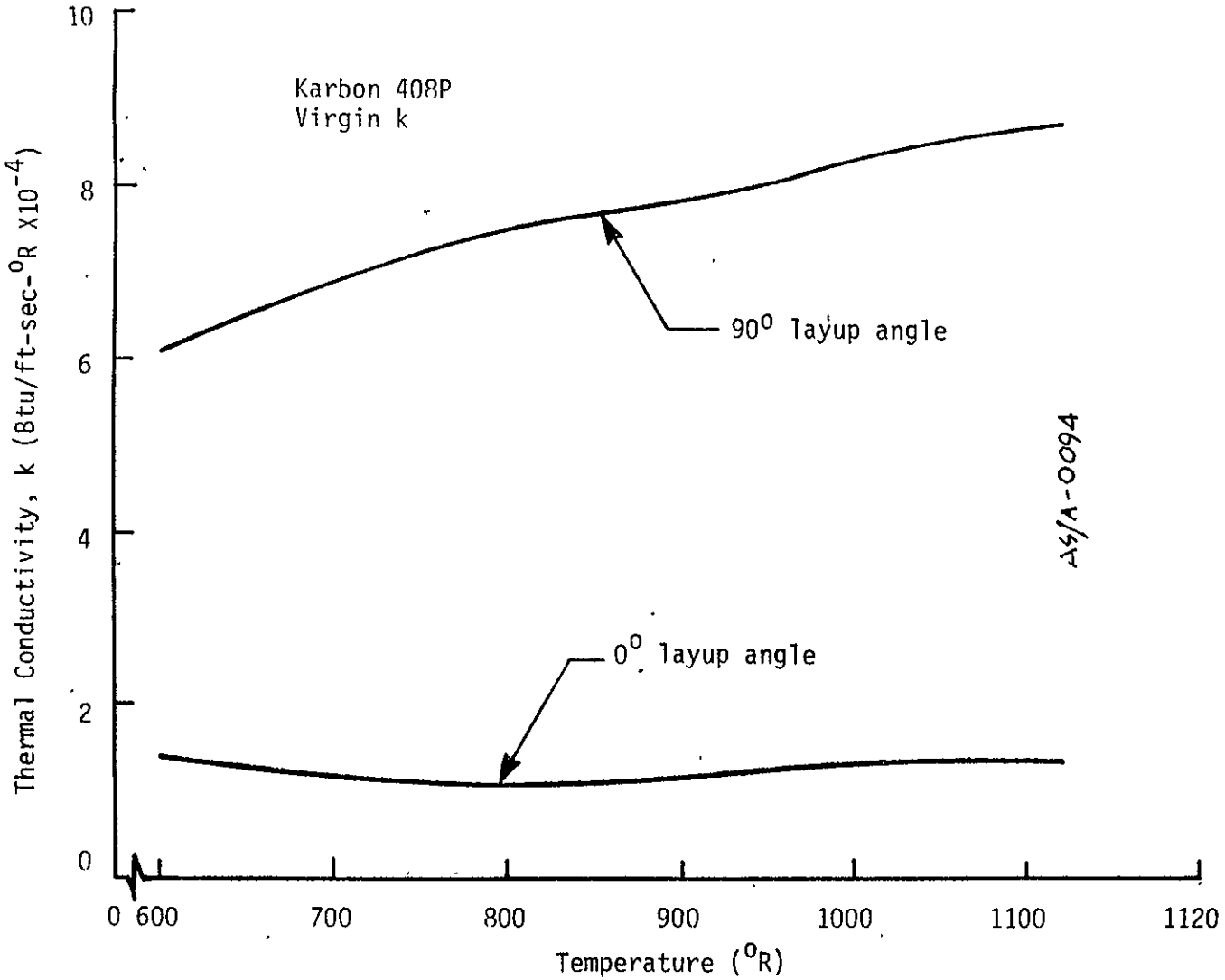

Figure 3-21. Virgin conductivity data for Karbon 408P.

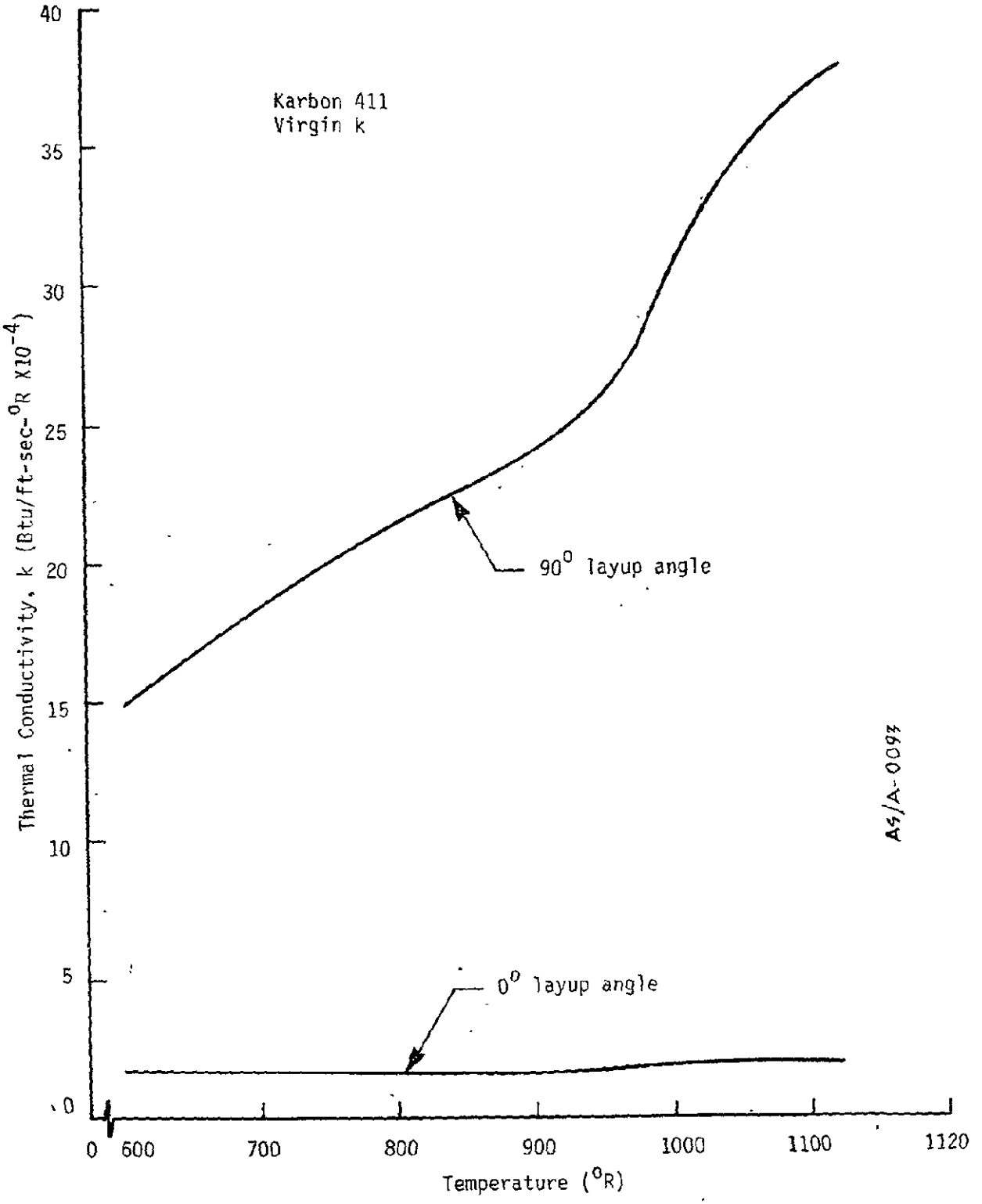

Figure 3-22. Virgin conductivity data for Karbon 411.

boundary condition. The flux terms considered in these equations are illustrated in Figure 3-23.

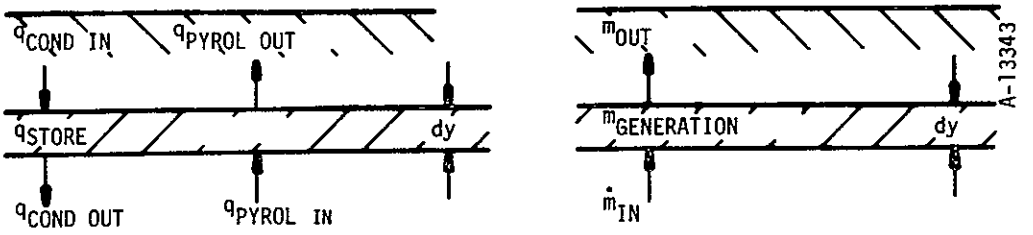

Figure 3-23. Control volumes for in-depth energy and mass balances.

If it is assumed that the pyrolysis gases do not react chemically with the char, but pass immediately out through the char, then the conservation of energy equation becomes:

$$\frac{\partial}{\partial t}(\rho h A)_y = \frac{\partial}{\partial y}\left(KA\frac{\partial T}{\partial y}\right)_t + \frac{\partial}{\partial y}\left(\dot{m}_g h_g\right)_t \tag{3-10}$$

where

A = area

h = total material enthalpy (chemical plus sensible)

h_g = total pyrolysis gas enthalpy

$\dot{m}_g$ = pyrolysis gas flowrate

t = time

T = temperature

y = distance

ρ = density

and the conservation of mass equation becomes:

$$\left(\frac{\partial \dot{m}_g}{\partial y}\right)_t = A \left(\frac{\partial \rho}{\partial t}\right)_y \tag{3-11}$$

The first term in Equation (3-10) accounts for the change in energy stored within the element; the second term accounts for the net thermal heat conduction across the element; and the third term accounts for the net transfer of thermal energy due to the flow of pyrolysis gases. Equation (3-11) describes the degradation of the material. The decomposition rate $(\partial\rho/\partial t)_y$ is defined as an Arrhenius type expression of the form:

$$\left(\frac{\partial \rho}{\partial t}\right)_y = - \sum_{i=1}^{3} B_i e^{-E_{ai}/RT} \rho_{o_i} \left(\frac{\rho_i - \rho_{r_i}}{\rho_{o_i}}\right)^{\psi_i} \tag{3-12}$$

where B = frequency factor

E_a = activation energy

R = gas constant

ρ_o = original density of component i

ρ_i = instantaneous density of component

ρ_r = residual density of component i

Ψ = reaction order

For most materials, it is sufficient to consider three different decomposing constituents, two describing the resin and one describing the reinforcement. Equations (3-10) through (3-12) are solved by the CMA program which is described in detail in Reference 7.

Equations (3-10) through (3-12) can be solved for the thermal conductivity by using measured in-depth and surface transient temperatures if the following material thermal and chemical properties are known:

- Virgin and char specific heat
- Virgin thermal conductivity
- Virgin and char density
- Resin mass fraction
- Virgin and char heat of formation
- Decomposition kinetics of the resin system

The method for obtaining the in-depth and surface temperatures is described in the following paragraphs.

To determine dynamic char thermal conductivity of the two candidate materials, specimens were tested in the Acurex 1-MW APG. The test gases and test conditions were chosen to yield a material thermal response typical of that encountered in rocket nozzles. In addition, chemically inert test gases were used to eliminate surface thermochemical ablation. This assured that the surface boundary condition (which is required in the data reduction process) was accurately known. The selected test gas, which is shown below, was chemically inert to most materials at high temperatures and also approximated the specific heat of rocket motor combustion products (Reference 8).

Species	Mass Fraction
He	0.232
N_2	0.768

The test configuration used was a two-dimensional (2-D) supersonic nozzle in which the conductivity test section formed one wall as shown in Figure 3-24. The measurement station was the nozzle throat which was of-

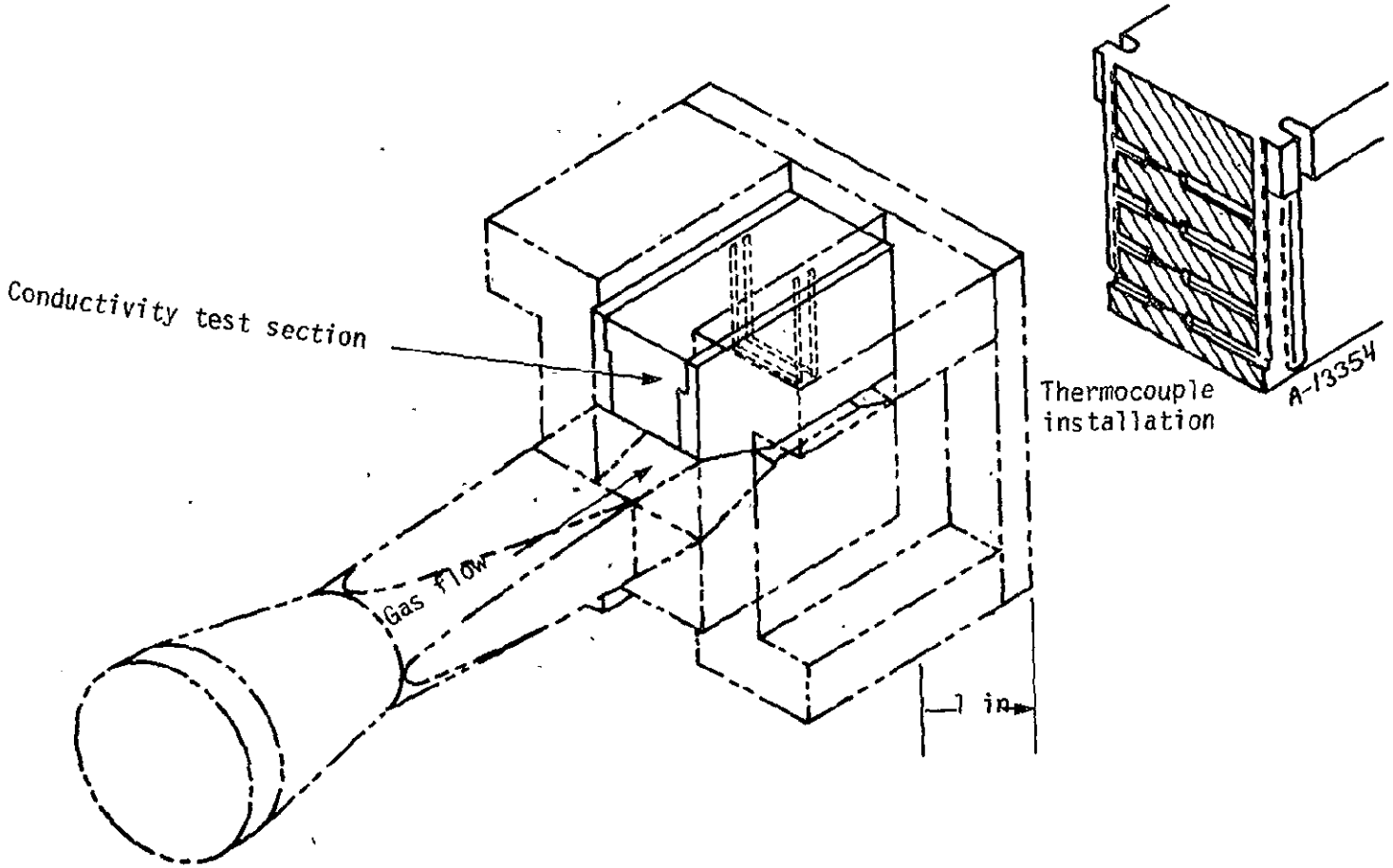

Figure 3-24. Typical instrumented duct flow test section.

finite length and yielded a significant region of well-defined, constant test conditions. The 2-D configuration allowed the test section to be obtained from parts fabricated by virtually any technique (flat laminate or tape-wrapped at any layup angle). The 2-D configuration also allowed an accurate thermocouple instrumentation technique and provided an approximately one-dimensional heat flux path.

The surface temperature boundary condition was measured continuously with an infrared optical pyrometer during each test. The in-depth temperatures were measured continuously during each test at four in-depth locations and, together with the measured surface temperature, provided the data for evaluating thermal conductivity. Tungsten 5 percent rhenium thermocouples were used for temperature measurements at the two locations nearest the surface, while chromel/alumel thermocouples were used at the other two locations. The thermocouple installation technique, illustrated in Figure 3-24, used a stepped hole to assure intimate contact of the thermocouple with the material. The thermocouple wires were brought down the side walls through alumina sleeving to prevent shorting across the electrically conductive char and/or virgin material. The thermocouple wire size was 0.005 inch, which is compatible with the capabilities of thermocouple hole drilling. The nominal thermocouple depths were 0.075, 0.150, 0.250, and 0.400 inches as shown in Figure 3-25, but the actual thermocouple depths were accurately determined with X-rays. The details and techniques for drilling the stepped holes and for thermally instrumenting the model are presented in Reference 9.

Tests were conducted in the 20^{o} and 90^{o} orientations. A 20^{o} rather than a 0^{o} orientation was used to avoid delamination of the test

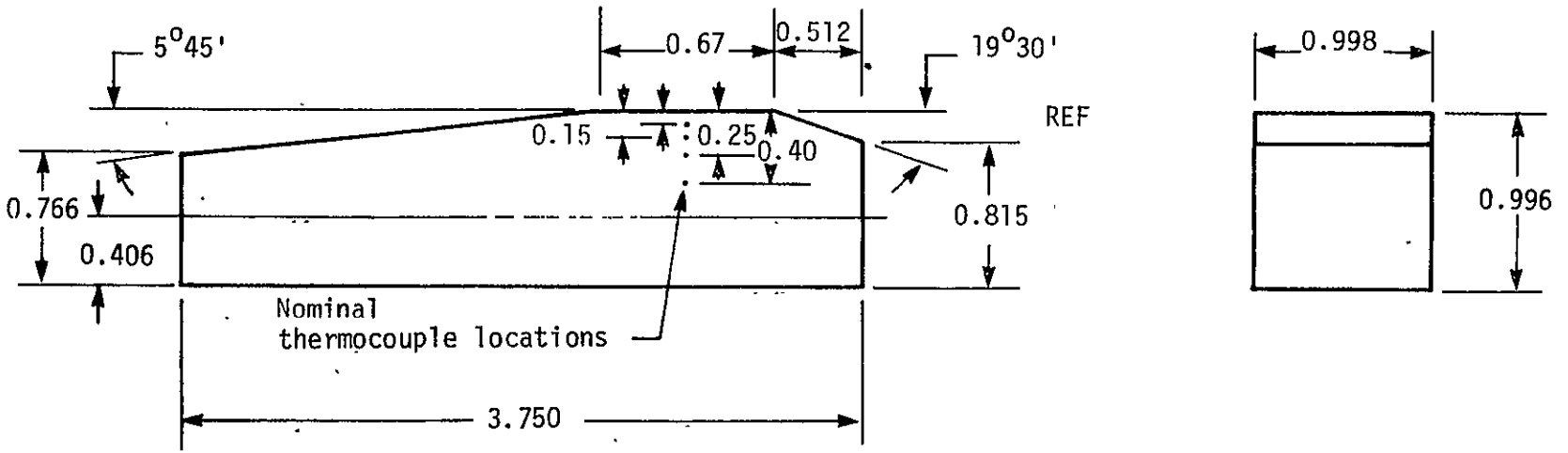

NOTE: All non-angular measurements are in inches.

Figure 3-25. Typical test model with in-depth thermocouples.

specimens. Since 20^{o} and 90^{o} layup models were tested, the following equation was applied to back out the 0^{o} orientation conductivity:

$$k_{0^{o}} = \frac{k_{20^{o}} - k_{90^{o}} \sin^{2} 20^{o}}{1 - \sin^{2} 20^{o}} \qquad (3\text{-}13)$$

The evaluated virgin and char conductivities for 0^{o} and 90^{o} orientations are shown in Figure 3-26 for Karbon 408P and Figure 3-27 for Karbon 411. The accuracy of the calculated char conductivity can be judged by comparing the calculated and measured in-depth temperature histories (see Figures 3-28 through 3-31). Except for a few anomalies, probably due to thermocouple breakage or separation from the char, the comparisons are very good. The actual in-depth thermocouple locations are necessary to make this calculation. The thermocouple locations measured from X-rays are shown in Table 3-15.

3.3.7 Characterization Summary

The full characterization data are summarized in Tables 3-16 and 3-17 and provide the information required for a thermal analysis of Karbon 408P and Karbon 411, respectively, for a Shuttle nozzle design. Since the MDAC virgin conductivity data for these two materials are considered questionable, dynamic conductivities are presented in these tables for the virgin material range.

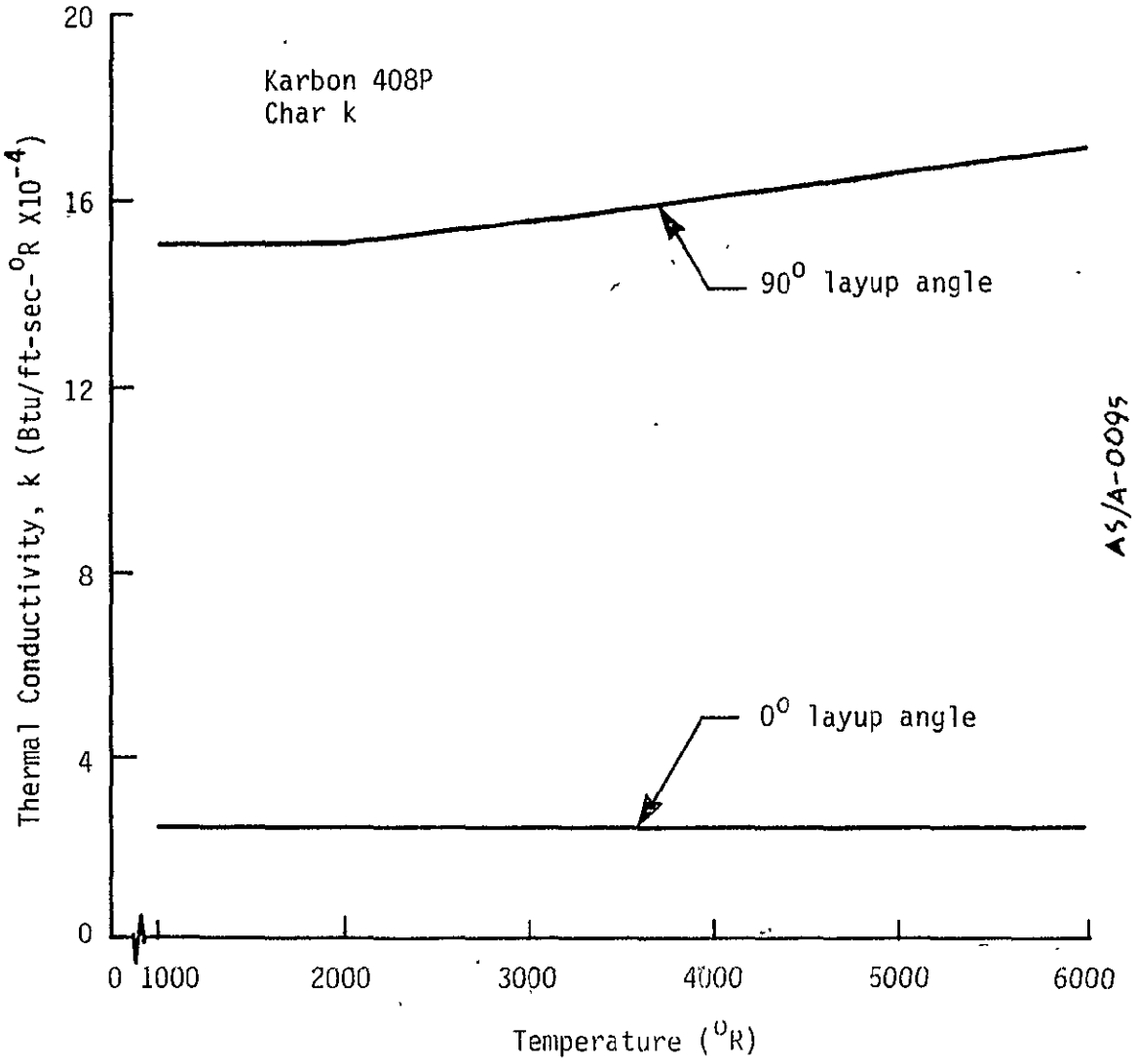

Figure 3-26. Char conductivity for Karbon 408P.

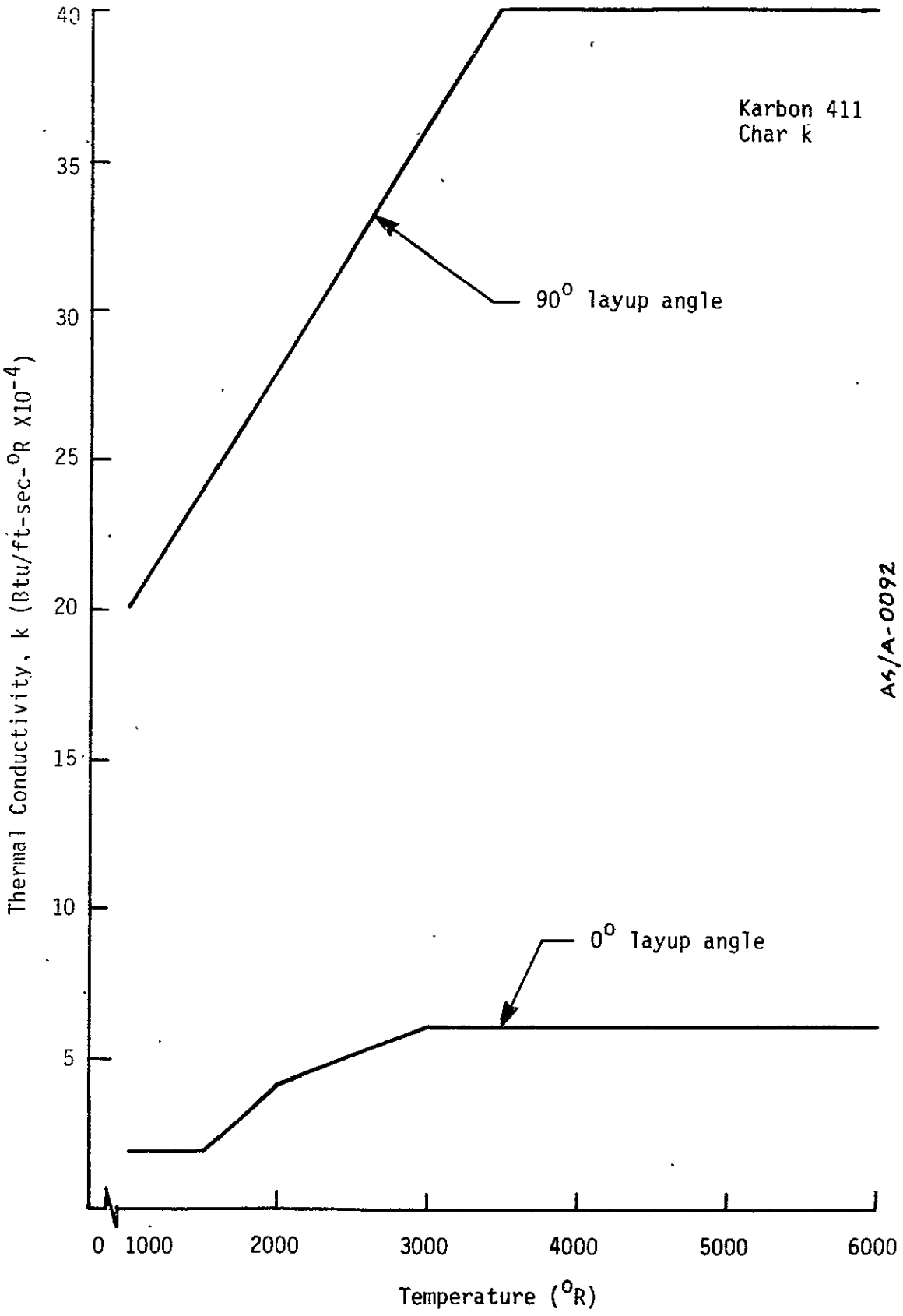

Figure 3-27. Char conductivity for Karbon 411.

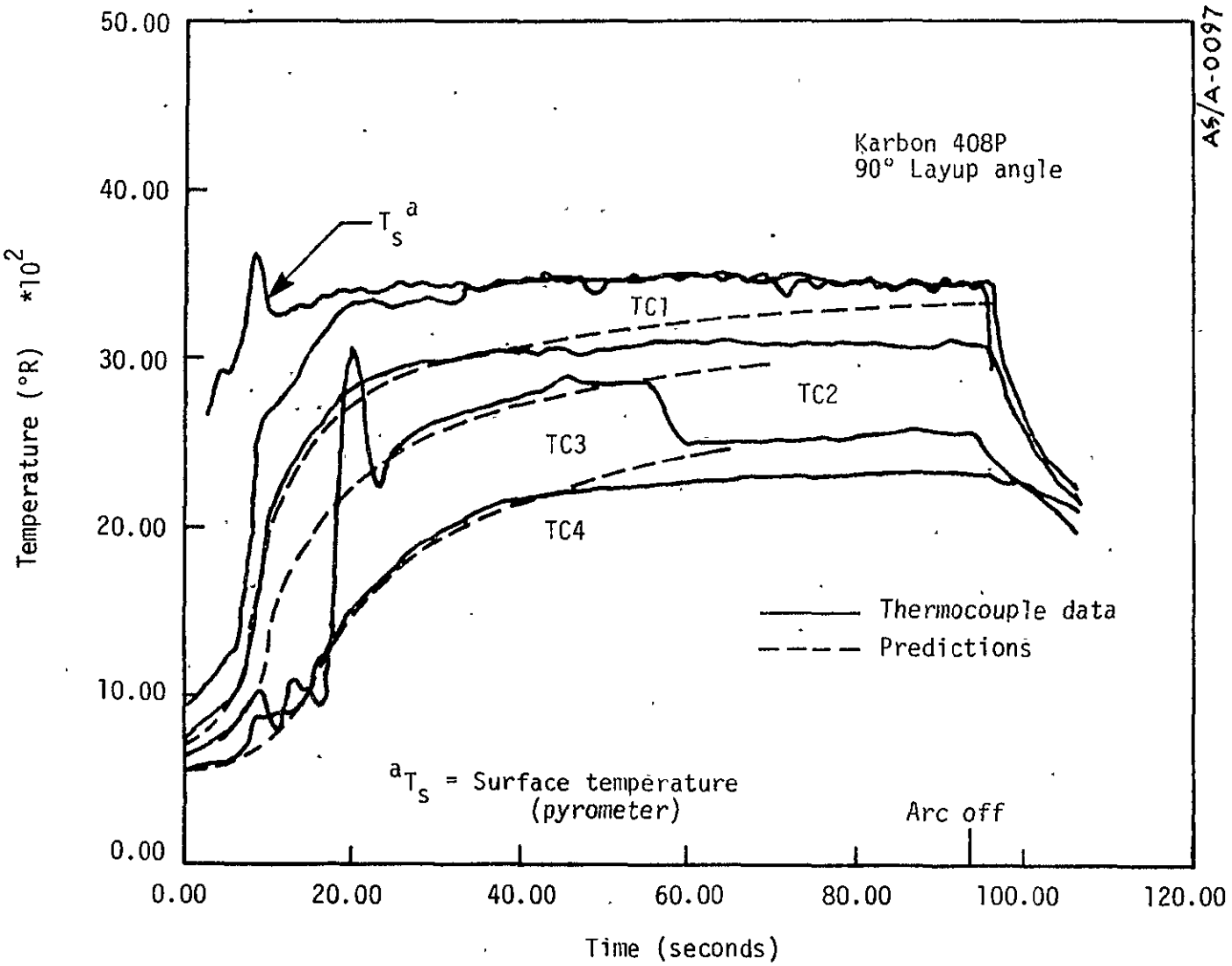

Figure 3-28. Comparison of in-depth thermocouple measurements and CMA predictions for Karbon 408P (90°).

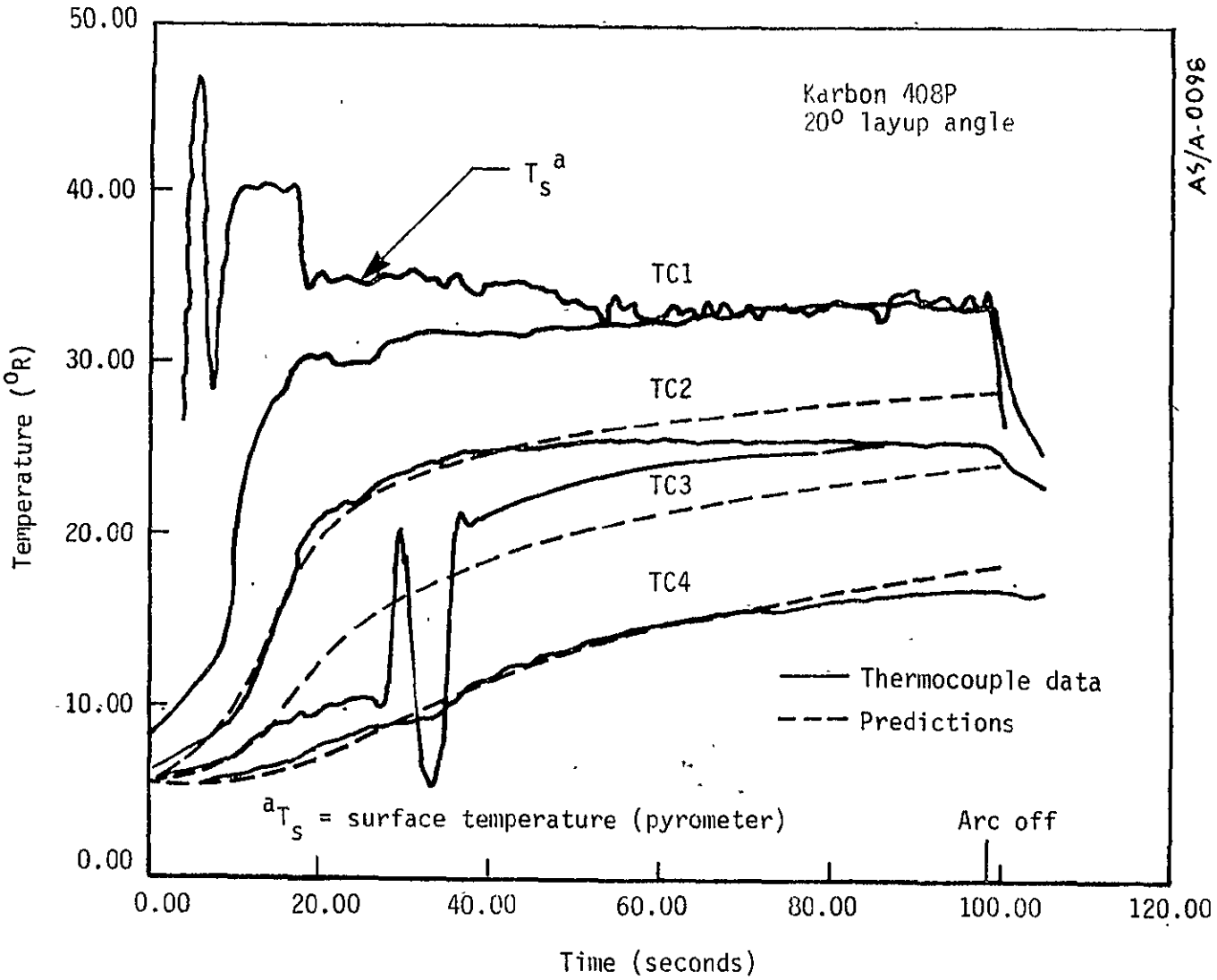

Figure 3-29. Comparison of in-depth thermocouple measurements and CMA predictions for Karbon 408P (20^{o}).

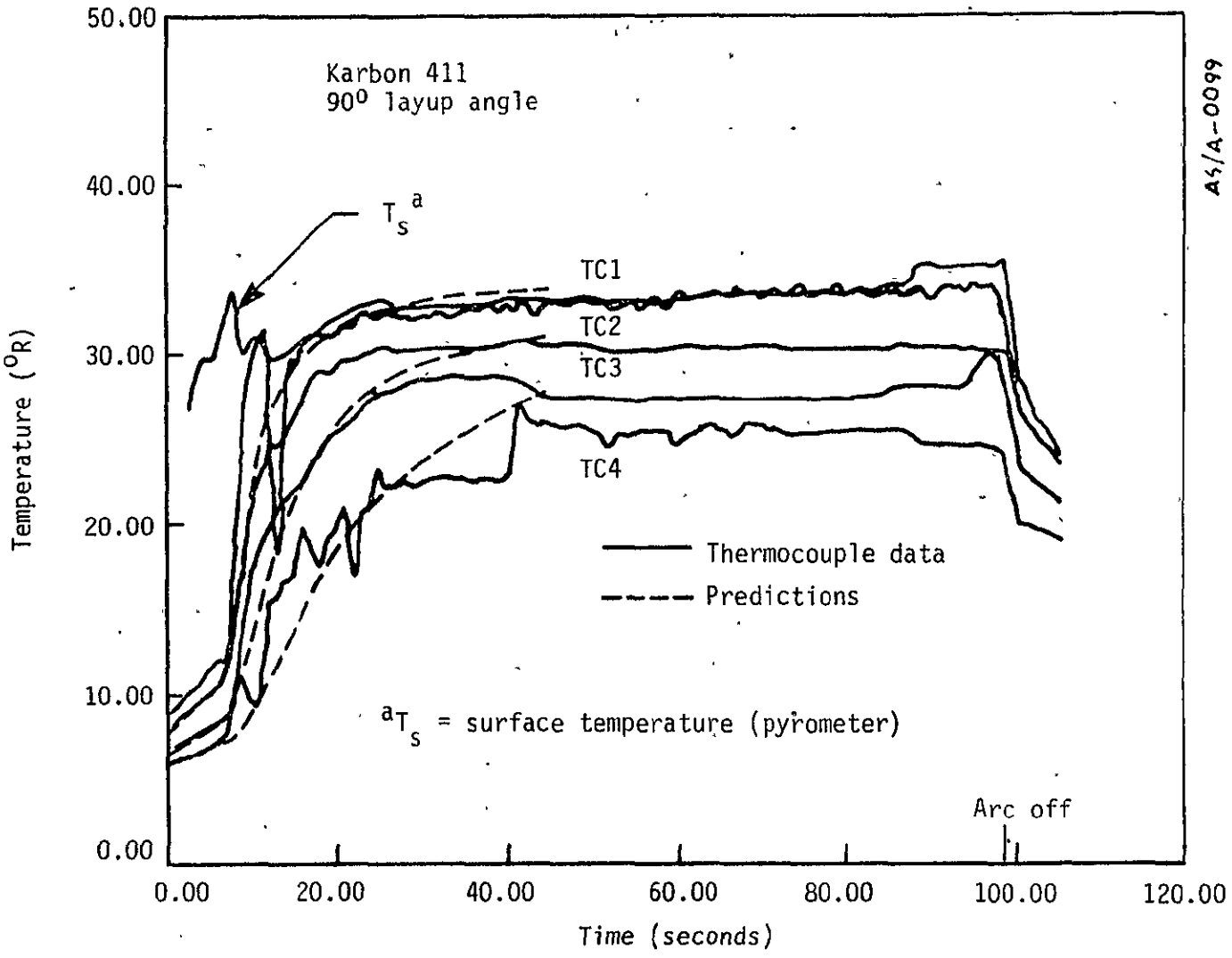

Figure 3-30. Comparison of in-depth thermocouple measurements and CMA predictions for Karbon 411 (90°).

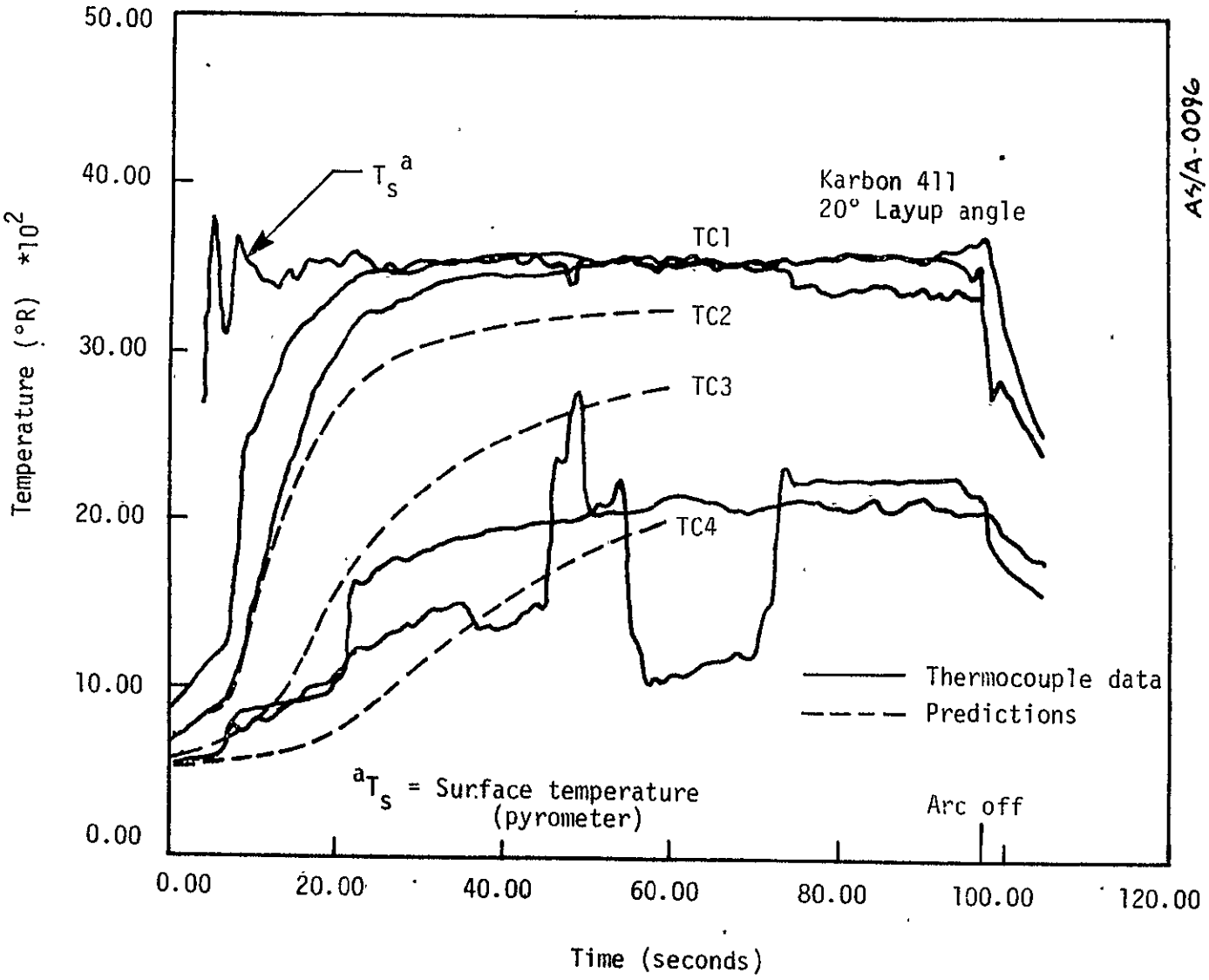

Figure 3-31. Comparison of in-depth thermocouple measurements and CMA predictions for Karbon 411 (20°).

TABLE 3-15. LOCATION OF IN-DEPTH THERMOCOUPLES BY X-RAY

Material	Layup Angle (Deg)	Distance from Surface (in)			
		TC1	TC2	TC3	TC4
Karbon 408P	90	0.073	0.152	0.242	0.410
	20	0.070	0.158	0.253	0.408
Karbon 411	90	0.075	0.144	0.262	0.411
	20	0.068	0.140	0.248	0.405

TABLE 3-16. THERMAL AND PHYSICAL PROPERTIES OF KARBON 408P

Nominal Density	Resin Mass Fraction	Resin Elemental Formula	Resin Residual	Char Density (lbm/ft^3)	Virgin Material				Char Material			Emissivity
					Temp (^oR)	Specific Heat (Btu/lbm-^oR)	Thermal Conductivity (Btu/ft-sec-^oR) x 10^4		Specific Heat (Btu/lbm-^oR)	Thermal Conductivity (Btu-ft-sec-^oR) x 10^4		
							0^o Layup	90^o Layup		0^o Layup	90^o Layup	
101.76	0.350	C_6H_6O	0.67145	88.53	530	0.390	2.50	7.50	0.390	2.50	15.00	0.85
					800	0.390		8.57	--			
					1000	--		--	0.390			
					1160	0.390		10.00	--			
					1500	0.390		12.00	0.390			
					2000	0.390		15.00	0.390			
					3000	0.493			0.493		15.50	
					4000	0.498			0.498		16.00	
					5000	0.500			0.500		16.50	
					6000	0.500			0.500		17.00	

AS-0014

a) The decomposition kinetic constants are tabulated below

Reaction	ρ_{o_i} (lbm/ft^3)	ρ_{r_f} (lbm/ft^3)	B_i (sec^{-1})	E_{a_i}/R (^oR)	ψ_i	T_{react_i} (^oR)	Γ
A	81.00	54.3875	6.922 x 10	1.2347×10^4	2.2322	640.0	
B	0.0	0.0	0.0	0.0	0.0	10000.0	0.43970
C	118.05	115.3257	2.334×10^{17}	8.194×10^4	2.9427	1950.0	

b) The following equation is suggested for layup angles other than 0^o and 90^o

$$k_\theta = k_{0^o}\left\{1 + \left(\frac{k_{90^o}}{k_{0^o}} - 1\right)\sin^2\theta\right\}$$

where θ is the layup angle referenced to a tangent to the surface.

c) The conductivity is given by

$$k = x\,k_p(T) + (1 - x)k_c(T)$$

where x is the virgin material mass fraction, and k_p and k_c are the virgin material and char conductivity, respectively.

C-3

TABLE 3-17. THERMAL AND PHYSICAL PROPERTIES OF KARBON 411

Nominal Density (lbm/ft^3)	Resin Mass Fraction	Resin Elemental Formula	Resin Residual	Char Density (lbm/ft^3)	Virgin Material				Char Material			Emissivity
					Temp (^oR)	Specific Heat ($Btu/lbm-^oR$)	Thermal Conductivity ($Btu/ft-sec-^oR$) x 10^4 0^o Layup	Thermal Conductivity ($Btu/ft-sec-^oR$) x 10^4 90^o Layup	Specific Heat ($Btu/lbm-^oR$)	Thermal Conductivity ($Btu/ft-sec-^oR$) x 10^4 0^o Layup	Thermal Conductivity ($Btu/ft-sec-^oR$) x 10^4 90^o Layup	
96.76	0.380	C_6H_6O	0.69079	81.47	530	0.450	1.88	20.00	0.450	1.88	20.0	0.85
					800	0.450			--			
					1000	--			0.450			
					1160	0.450			--			
					1500	0.450			0.450			
					2000	0.450			0.450	4.14		
					3000	0.493			0.493	6.02	40.0	
					4000	0.498			0.498			
					5000	0.500			0.500			
					6000	0.500			0.500			

AS-0015

a) The decomposition kinetic constants are tabulated below

Reaction	ρ_{o_i} (lbm/ft^3)	ρ_{r_i} (lbm/ft^3)	B_i (sec^{-1})	E_{a_i}/R (^oR)	ψ_i	T_{react_i} (^oR)	Γ
A	20.25	12.00	1.400×10^4	1.5400×10^4	3.0	600.0	
B	60.75	43.954	4.480×10^9	3.6800×10^4	0.0	600.0	0.4539
C	109.861	102.684	1.5755×10^7	4.3835×10^4	2.0	1962.0	

b) The following equation is suggested for layup angles other than 0^o and 90^o

$$k_\theta = k_{0^o}\left\{1 + \left(\frac{k_{90^o}}{k_{0^o}} - 1\right)\sin^2\theta\right\}$$

where θ is the layup angle referenced to a tangent to the surface.

c) The conductivity is given by

$$k = x\,k_p(T) + (1 - x)k_c(T)$$

where x is the virgin material mass fraction, and k_p and k_c are the virgin material and char conductivity, respectively.

SECTION 4

PROGRAM SUMMARY

This section briefly summarizes the test and study results for Phases IV and V of the NASA nozzle design computer codes and low cost nozzle materials investigation and test programs. Conclusions and recommendations are also included for each program phase.

4.1 PHASE IV SUBSCALE NOZZLE TESTS

In general, the five subscale nozzle test firings (four HIPPO motor 2.5-inch nozzles and one CHAR motor 7-inch nozzle) were very successful and all objectives were achieved. An anomaly did occur, however, in the first 2.5-inch nozzle throat area. The throat eroded into an "egg-shaped" pattern which was unexpected since it was composed of the baseline rayon fabric carbon phenolic nozzle material. The performance of the nozzle was not affected, however, and no explanation could be given for the irregular erosion pattern. Coincidentally, an anomaly also occurred in the throat area of the 7-inch nozzle which was observed as "gouging". This area was at first thought to be the pitch fabric half of the throat ring. But post-test examination proved it to be the baseline rayon fabric half. Again, no explanation could be given for the irregular erosion pattern of the rayon, and the nozzle's overall performance was not affected. Also, no correlation could be made between the 2.5-inch nozzle rayon erosion pattern and the 7-inch nozzle rayon erosion pattern.

In conclusion, the following statements and recommendations can be made from the results of the five subscale nozzle tests:

- The two 2.5-inch baseline rayon fabric nozzles (MX-4926) performed well, as expected. The baseline rayon fabric in the 7-inch nozzle throat also performed well.
- The pitch fabric 2.5-inch nozzle (MXG-1033F) performed nearly as well as the baseline rayon with the erosion and char depth somewhat greater but very uniform. The pitch fabric nose ring and one-half throat ring of the 7-inch nozzle (FM-5788) also performed nearly as well as the rayon (FM-5055).
- The pitch mat 2.5-inch nozzle (MX-4929) did not perform as well as the pitch fabric. Erosion was greater but uniform. The char depth, however, was approximately the same as the pitch fabric nozzle.
- The staple rayon fabric exit cone of the 7-inch nozzle performed satisfactorily. Recession was minimal and uniform.
- Since the performance of the pitch fabric nozzle material was comparable to that of the baseline rayon fabric nozzle material (within the bounds of requirements) it is recommended that the pitch fabric material be considered as a replacement for rayon when the rayon is no longer available. Pitch fabric is a low cost material having long-term availability.
- The pitch mat material is questionable for use in the nozzle throat area but is recommended as an acceptable exit cone material.

4.2 PHASE V: LOW COST MATERIALS SCREENING AND CHARACTERIZATION PROGRAM

The alternate materials survey, screening, and characterization program was successfully completed with all objectives attained. As a result of the survey, a total of 17 test billets of carbon phenolic/fabric ablative materials were obtained for screening tests in the Acurex 1-MW Arc Plasma Generator (APG). The two major suppliers were Fiberite and U.S. Polymeric Corporations, whose cooperation and contributions are hereby acknowledged by Acurex. The results of the screening tests showed that most of the staple PAN and continuous pitch fabrics performed equal to and in most cases better than, both the baseline continuous rayon fabric (CCA-3) and the staple rayon fabrics. Two of the materials screened were selected for full thermophysical property characterization. The two materials characterized were a staple PAN, Karbon 411 (SWB-8 fabric) and a continuous pitch, Karbon 408P (VC-0149 fabric). The overall objective of the materials characterization was to provide the necessary data for a full-scale Shuttle solid motor nozzle design.

In conclusion, the following observations and recommendations are made for the Phase V materials screening program:

- Overall, the PAN and pitch materials exhibited the lowest ablation for both the 90^{o} and 20^{o} ply orientations compared with the continuous and staple rayon materials.
- The staple rayon materials exhibited comparable ablation regardless of supplier, Fiberite (FIB) or U.S. Polymeric (USP). The one exception was Karbon 433-FIB which showed a very high recession rate for the 90^{o} ply orientation. The staple rayons had recession rates comparable to the baseline continuous rayon.

- In comparing the staple PAN materials, Fiberite's Karbon series had comparable and uniform recession rates. The one staple PAN from USP (FM5748, SS-2231 fabric) exhibited the lowest ablation of all the PAN fabrics.
- The ablation of the pitch materials were comparable to the PAN materials but were more variable compared to each other. For example, USP's FM5749 (VC-0149) showed a higher recession rate at 20^{o} (~ factor of two) than at 90^{o} which is opposite to the general trend. Also, Fiberite's Karbon 419 (W-502), which was a staple pitch, had a recession rate for the 90^{o} ply orientation approximately twice as great as the rate for the 20^{o} ply orientation which is somewhat greater than the general trend.
- In general, the PAN and pitch fabric materials demonstrated good performances and are highly recommended as alternate nozzle materials with the advantages of low cost and long-term availability.
- Thermophysical properties data were generated for two materials: Karbon 408P (pitch) and Karbon 411 (PAN), selected for characterization by their performance in the screening tests. The data generated consisted of thermal conductivities (both 0^{o} and 90^{o} ply orientations), specific heat, density, pyrolysis kinetics, heat of formation, and pyrolysis gas elemental composition. These data can subsequently be used to perform thermal predictions and design analyses using the Acurex computer codes (ACE and CMA) for nozzle applications.

- Although the ablation performance was similar for both Karbon 408P and Karbon 411, it appears that Karbon 408P is a better insulator than Karbon 411. The densities and specific heats of the two materials are similar, but the thermal conductivity is substantially higher for Karbon 411. This conclusion is substantiated by the greater char depth observed for Karbon 411 than for Karbon 408P.
- In regard to the thermal conductivity determined for the two materials characterized, the following two conclusions are made:
  1. The original virgin thermal conductivity data generated at the McDonnell Douglas (MDAC) facility was incorrect, and the corrected data is considered suspect and should not be used. Values generated using arc test results are preferred since they provide the best overall CMA predictions of the in-depth thermocouple response, which are considered the best information regarding these materials' thermal response. The Karbon 408P and Karbon 411 virgin thermal conductivities should be measured at a facility other than MDAC to substantiate the values determined analytically with the CMA code.
  2. The decomposition constants and generated char thermal conductivities are considered satisfactory since they provide predictions that agree quite well with the TGA and in-depth thermocouple measurements.

- Based on the performance and characterization of Karbon 408P and Karbon 411, both are recommended as candidate alternate nozzle materials. It is also highly recommended that subscale nozzle tests (HIPPO and/or CHAR motors) be conducted with these materials to verify their performance under actual solid motor firing environments.

REFERENCES

1. Chu, E., Tong, H., and Bedard, R., "Unified Computer Codes Properties Data for Low Cost Nozzle Materials," NASA Contract NAS 8-30264 (Aerotherm Report TR-76-9), March 1976.

2. Suchsland, K. E., "Analytical Procedure for the Thermal Response of Solid Propellant Nozzles," Aerotherm Division/Acurex Corporation, Mountain View, California, Aerotherm Report 75-148, August 1975.

3. Private communications with Floyd Anderson, Jet Propulsion Laboratory, February 23, 1977.

4. Powars, C. A. and Kendall, R. M., "User's Manual, Aerotherm Chemical Equilibrium (ACE) Computer Program," Aerotherm Corporation, Mountain View, California, May 1968.

5. "Aerotherm Real Gas Energy Integral Boundary Layer Program (ARGEIBL), User's Manual," Aerotherm Corporation, Mountain View, California, 69-UM-6911, November 1969.

6. Bartz, K. E., "A Simple Equation for Rapid Estimation of Rocket Nozzle Convective Heat Transfer Coefficients," Jet Propulsion, p. 48, January 1957.

7. Moyer, C. B., "User's Manual, Aerotherm Charring Material Thermal Response and Ablation Program (CMA), Version 3," Aerotherm Corporation, Mountain View, California, UM-70-14, April 1970.

8. Schaefer, J. W. and Dahm, T. J., "Studies of Nozzle Ablative Material Performance for Large Solid Boosters," NASA CR-72080 (Aerotherm Report No. 66-2), December 15, 1966.

9. Baker, D. L., Wool, M. R., and Schaefer, J. W., "A Dynamic Technique for Determining the Thermal Conductivity of Charring Materials," Paper presented at the Eighth Conference on Thermal Conductivity October 7-11, 1968, Thermophysical Properties Research Center, West Lafayette, Indiana.

10. McCuen, P. A., Schaefer, J. W., Lundberg, R. E., and Kendal, R. M., "A Study of Solid-Propellant Rocket Motor Exposed Materials Behavior," Report No. AFRPL-TR-65-33 (Vidya Report No. 149), February 26, 1965.

11. Schaefer, J. W., et al., "Studies of Ablative Material Performance for Solid Rocket Nozzle Application," NASA CR-72429 (Aerotherm Report No. 68-30), March 1, 1968.